

Subarray-Based Multibeam Antenna Frontend for Millimeter-Wave Hybrid Beamforming

Nadeem Ashraf

A Thesis
In the Department
of
Electrical and Computer Engineering

Presented in Partial Fulfillment of the Requirements
For the Degree of
Doctor of Philosophy (Electrical and Computer Engineering) at
Concordia University
Montreal, Quebec, Canada

January 2021

© Nadeem Ashraf, 2021

CONCORDIA UNIVERSITY
SCHOOL OF GRADUATE STUDIES

This is to certify that the thesis prepared

By: Nadeem Ashraf

Entitled: Subarray-Based Multibeam Antenna Frontend for Millimeter-Wave Hybrid Beamforming

and submitted in partial fulfillment of the requirements for the degree of

Doctor of Philosophy (Electrical and Computer Engineering)

complies with the regulations of the University and meets the accepted standards with respect to originality and quality.

Examination Committee:

_____	Chair
Dr. Muthukumaran Packirisamy	
_____	External Examiner
Dr. Ammar B. Kouki	
_____	External to Program
Dr. Marco Bertola	
_____	Examiner
Dr. Tayeb A. Denidni	
_____	Examiner
Dr. Walaa Hamouda	
_____	Examiner
Dr. Robert Paknys	
_____	Thesis Co-supervisor
Dr. Ahmed A. Kishk	
_____	Thesis Co-supervisor
Dr. Abdel R. Sebak	

Approved by:

Dr. Wei-Ping Zhu
Graduate Program Director

January 13, 2021

Dr. Mourad Debbabi
Acting Dean, Gina Cody School of Engineering and Computer Science

Abstract

Subarray-Based Multibeam Antenna Frontend for Millimeter-Wave Hybrid Beamforming

Nadeem Ashraf, Ph.D.

Concordia University, 2021

With the paradigm shift from sub-6 GHz to millimeter-wave (mm-Wave) for wireless communications, beamforming becomes essential for mm-Wave access points to mitigate losses. Due to the small wavelength, a compact circuit could accommodate a large number of antenna elements. This favors the principle of beamforming to achieve high array-gain and spatial resolution through a large-scale $N \times M$ array. For such antenna frontends, full-digital beamforming circuitry requires $N \times M$ RF chains, which is unfeasible and energy inefficient. Likewise, a higher-order mm-Wave analog beamforming network is highly lossy to generate $N \times M$ beams. Hybrid beamforming addresses this dilemma by partitioning the beamforming between the analog and digital domains appropriately. For this purpose, the antenna frontend needs to be segmented into subarrays, such that the subarray-based analog beamspace patterns are digitally processed rather than processing element patterns individually. Thus, hybrid beamforming requires a suitable subarray-based $N \times M$ multibeam antenna frontend.

In this thesis, a study of the subarray antennas is presented for hybrid beamforming operation. A simplified model is considered in which the analog beam-switching is performed in the azimuth plane (H-plane) and the digital beamspace beamforming in the elevation plane (V-plane). This is to reduce the number of RF chains as well as to achieve fine-tuned digital beam-steering in V-plane along with predefined analog switched-beams in H-plane. In this research work, the frequency band of 28 – 32 GHz is considered for prototyping purposes. For practical use at mm-Wave, the microstrip line technology is augmented with the perfect magnetic conductor (PMC) packaging. The fixed-beam and switched-beam subarrays with an order of $n \times m = 1 \times 4$, 2×2 , and 4×4 are investigated. A dual-polarized aperture-coupled magneto-electric dipole antenna is designed as a single element with 20% bandwidth, ports' isolation better than 35 dB, cross-polarization less than -25 dB, and gain of 8 dBi. Using this element, a fixed-beam 4×4 dual-polarized subarray is designed that maintains a bandwidth of 16.7% at 30 GHz with a maximum gain of 19.3 dBi and symmetrical radiation patterns. The fixed-beam limitation of the

$2^n \times 2^m$ subarray leads to building the efficient switched-beam subarray antennas for hybrid beamforming. For this purpose, a 2×2 dual-polarized analog beamforming network is designed for 28-32 GHz. Two identical PMC packaged microstrip line networks, one for each polarization, are designed on a single substrate surface. However, to be processed for beamspace digital beamforming, this topology exhibits physical layout and array factor problems. Thus, further designs are investigated to meet the hybrid beamforming frontend requirements.

To this end, as switched-beam subarrays for hybrid beamforming, two PMC packaged 4×4 Butler matrices are presented with a longitudinal layout and a folded layout for the end-fire and broadside radiation characteristics, respectively. The former design achieves a 5 GHz (28-33 GHz) bandwidth with return loss and isolation, both better than 15 dB. At 30 GHz, the insertion loss is 0.8 ± 0.3 dB, and antenna-ports' phase distributions are $\pm 45^\circ$ and $\pm 135^\circ$. E-plane-flared horn antennas terminate the Butler matrix antenna-ports as a linear array. The double-ridge gap waveguide horn antenna is designed to reduce the scan loss within a subarray environment. The H-plane fan-beam switching covers $\pm 42^\circ$ with a maximum gain of 11.7 and 11.2 dBi for the inner (1R) and outer (2R) radiation beams. The latter novel topology of the folded Butler matrix is laid out for a compact tiled planar antenna frontend to accommodate a beamforming network beneath the antenna array's physical footprints. As compared to the conventional longitudinal layout, the size is reduced by more than 50 %. The PCB aperture-coupled antenna elements are integrated within the PMC packaged environment for a broadside radiation characteristic. The folded Butler matrix and antenna element are designed for a bandwidth of 4 GHz (28-32 GHz). The single antenna element's directivity is 5.22 dBi; whereas, for a 1×4 switched-beam subarray antenna, the directivities are 11.1 dBi and 10.6 dBi for 1R and 2R beams, respectively. Using Butler matrices-based 1×4 switched-beam subarrays, two types of multibeam antenna frontends with order $N \times M = 4 \times 4$ are constructed. Post-processing for the digital beamforming is applied over the subarray-based analog beamspace. The first hybrid beamforming model maintains a scan range of $\pm 42^\circ$ in the H-plane and $\pm 28^\circ$ in the V-plane with $B_V \times B_H = 3 \times 4 = 12$ beams. Similarly, the second model maintains a scan range of $\pm 38^\circ$ in the H-plane and $\pm 40^\circ$ in the V-plane with $B_V \times B_H = 4 \times 4 = 16$ beams. As compared to full-analog two-dimensional (2-D) beamforming, these models are capable of fine-tuned beam-steering in the V-plane because the complex beamforming coefficients are not fixed but calculated digitally. Furthermore, compared to full-digital 2-D beamforming, it reduces the number of active RF chains from $N \times M$ to N .

Acknowledgments

First of all, I would like to express my deep gratitude to Professor Sebak and Professor Kishk for their supervision and guidance. My sincere thanks to Professor Sebak for giving me the opportunity to pursue Ph.D. at Concordia University and for his kind support throughout this program. I am extremely grateful to Professor Kishk for enlightening me through his immense knowledge and research expertise.

I would like to thank my thesis committee members for their insightful comments and encouragement. Their critical review highly improved the quality of this thesis.

I am thankful to Professor Paknys for teaching the graduate course Advanced Electromagnetics. Indeed, it was a unique learning experience. Similarly, the courses of Modern Antenna Theory and Microwave Engineering taught by Professor Kishk were extremely helpful in paving the way for the subsequent research.

I am very grateful to all the members of LATAMS research group, Concordia University, for their friendly support, encouragement, and fruitful research discussions. I would also like to admire the support provided by the graduate program coordinator, Sheryl Tablan.

I am thankful to the Fonds de recherche du Québec – Nature et technologies (FRQNT), for supporting this research work through the doctoral scholarship program, under the grant number B2X 260537, from 2018 to 2020.

Last but not least, I would like to thank my beloved family and siblings. The encouragement of my parents and patience of my supportive wife and lovely kids have been exemplary. I am deeply thankful to my affectionate sisters. I could not have made it without their continuous help and support.

Dedicated to my parents

Muhammad Ashraf & Irshad Begum

for their countless sacrifices

Table of Contents

List of Figures	xi
List of Tables	xvi
List of Acronym	xvii
Chapter 1. Introduction	1
1.1 Millimeter-Wave for Wireless Communication.....	1
1.2 Beamforming Architectures	3
1.3 Motivation and Problem Statement.....	6
1.4 Objective	11
1.5 Thesis Outline	11
1.6 Contributions.....	12
1.6.1 Fixed-beam versus Switched-beam Subarray Analysis	12
1.6.2 Folded Butler Matrix Switched-beam Subarray.....	13
1.6.3 Hybrid Beamforming System Demonstration.....	13
Chapter 2. Literature Review	14
2.1 Hybrid Beamforming Systems	14
2.2 ESPAR and Frequency Scanning Subarray Antennas	15
2.3 PCB Antennas, Beamforming Components, and Multibeam Subarrays	15

2.4	Layout Miniaturization.....	17
2.5	Research Methodology.....	18
Chapter 3. PCB Packaging Techniques for mm-Wave Applications.....		20
3.1	Substrate Integrated Suspended Lines (SISLs).....	21
3.2	Printed Ridge Gap Waveguide (PRGW).....	22
3.3	Perfect Magnetic Conductor (PMC) Packaged Microstrip Lines	23
3.3.1	Principles of Microstrip Line PMC Packaging	25
3.3.1.1	Design Examples.....	30
3.4	Summary	33
Chapter 4. Fixed-Beam and Switched-Beam Subarray Antenna Designs.....		34
4.1	Fixed-Beam Dual-Polarized Subarray Antenna.....	34
4.1.1	Design Challenges.....	35
4.1.2	Proposed Subarray Implementation	36
4.1.2.1	Antenna Element Design and Performance Analysis	36
4.1.2.2	$2^n \times 2^m$ Dual-polarized Subarray.....	41
4.1.3	Summary	48
4.2	Switched-Beam Dual-Polarized Subarray Antenna	49
4.2.1	Beamforming Network for Dual-Polarized 2-D Scanning.....	50
4.2.2	Subarray Antenna Performance	53

4.2.3	Summary	54
4.3	1-D Switched-Beam End-fire Subarray Antenna.....	56
4.3.1	Butler Matrix Subarray with Longitudinal Layout	56
4.3.1.1	Stage I: Synthesis of PMC Packaged 4×4 Butler Matrix	59
4.3.1.2	Stage II: DRGW Quasi-TEM Transmission Line	69
4.3.1.3	Stage III: DRGW Horn Antenna Array.....	76
4.3.1.4	Multibeam Antenna Prototype	80
4.3.2	Summary	84
4.4	1-D Switched-Beam Broadside Subarray Antenna.....	86
4.4.1	Folded Butler Matrix Layout.....	86
4.4.2	Antenna Element	95
4.4.3	Broadside 1×4 Switched-beam Subarray	99
4.4.4	Summary	101
Chapter 5. Hybrid Analog-Digital Beamforming		102
5.1	First Model	102
5.2	Performance Limitations of First Model.....	107
5.3	Second Model.....	108
5.4	Summary	112
Chapter 6. Conclusion and Future Work		115

6.1	Conclusion.....	115
6.2	Future Work	117
	Bibliography	119
	Publications	131

List of Figures

Figure 1-1. Communication cell coverage: single versus multiple beams per-sector	2
Figure 1-2. Millimeter-wave AP with $N \times M$ large-scale antenna frontend on a physically small circuit size	2
Figure 1-3. Large-scale $N \times M$ antenna array with $N \times M$ paths for RF signals	3
Figure 1-4. Beamforming architectures for $N \times M$ antenna array: (a) Full digital beamforming, (b) Full analog beamforming.....	3
Figure 1-5. Subarray-based partially connected hybrid beamforming model for $N \times M$ receiving antenna array	5
Figure 1-6. (a) Division of $N \times M$ antenna frontend into subarrays, (b) An $N \times M = 4 \times 4$ antenna frontend, and (c) Hybrid beamforming frontend with analog beam switching in ϕ -plane and digital beamforming in V -plane.....	6
Figure 1-7. (a) Fixed-beam subarray and (b) Switched-beam subarray.....	7
Figure 1-8. Circuit footprints of a conventional multibeam subarray antenna: (a) Longitudinal layout and (b) 2-D layout	8
Figure 1-9. Discontinuous $N \times M$ array aperture due to subarray with larger beamforming network as compared to radiating aperture	8
Figure 1-10. (a) A multibeam subarray radiation pattern AFs representation and (b) AFs of subarray-based $N \times M$ antenna frontend	9
Figure 1-11. Proposed multibeam antenna frontend for mm-Wave hybrid beamforming.....	10
Figure 3-1. Microstrip circuit (a) Cross-sectional view and field distribution and (b) Three different kinds of waves in quasi-TEM structures	20
Figure 3-2. (a) SISL cross-section view, (b) Exploded model view of multi-layer SISL circuit assembly, and (c) 4×4 SISL Butler Matrix (only Sub3 layer is shown)	21
Figure 3-3. (a) Printed ridge gap waveguide and (b) 4×4 Butler Matrix	23
Figure 3-4. (a) Microstrip circuit design including PMC packaging, (b) AMC realization on printed circuit board, and (c) Isolation improvement among microwave components by using PMC packaging.....	24
Figure 3-5. (a) XZ cross-section view of a PMC-PMC bounded region with microstrip line circuit in the middle, (b) Boundaries along x-axis for a cavity, and (c) Simplified cavity model covered with a PEC or PMC at the top.....	26
Figure 3-6. Full-height-pin EBG unit cell design parameters (in mm), and its dispersion diagram. (Parameters $t = 0.254$, $h = 1$, $a = 1.5$, $d = 2.25$, and $p = 2.6$).....	27
Figure 3-7. (a) PEC packaging at height $h = 1$ mm ($h - t \approx 3 \times t$) and (b) Absolute E-fields distribution at 30 GHz	28
Figure 3-8. PMC packaging using EBG lid of nails at height $h = 1$ mm ($h - t \approx 3t$) and absolute E-fields distribution at five frequency points	28
Figure 3-9. Effect of PMC packaging over the line impedance of microstrip line circuit with different packaging gaps $h - t$. (a) across frequency and (b) at 30 GHz.....	29

Figure 3-10. (a) Exploded model view of a three-layered AMC packaged structures (RO3003 substrates), (b) Cross-section view, and (c) EBG unit cell design parameters (units in mm), and dispersion diagram.....	29
Figure 3-11. Exploded model view and design parameters of crossover and coupler (units in mm)	30
Figure 3-12. Prototypes and measurement setup: (a) Crossover and (b) Hybrid Coupler	31
Figure 3-13. S-parameters (measured/simulated): (a) Crossover, (b) Hybrid Coupler, and (c) Performance comparison with/without AMC.....	32
Figure 4-1. Fixed-beam dual-polarized antenna subarray within large-scale antenna frontend	34
Figure 4-2. (a) Stacked structure of four layers, (b) Multilayer exploded model view, and (c) ME-dipole aperture's front and back view of SCSA along with feedlines	37
Figure 4-3. Current/field vectors' presentation, and H/V-polarization identification.....	37
Figure 4-4. Surface current distributions: (a) Port#1 excitation, (b) Port#2 excitation, and (c). Perspective view for Port#2 excitation.....	37
Figure 4-5. Absolute surface current distribution at $t=0$ and $t=T/4$ for (a) Port #1 and (b) Port#2.....	38
Figure 4-6. Antenna element S-parameters and gain.....	39
Figure 4-7. (a) Electric field-source over the boundary box around the antenna for V- and H-polarization and (b) Cross-section view of electric fields along with the end-launch connectors.....	40
Figure 4-8. Impact of offset parameter “d” on port-to-port coupling (S_{21}) and Port 1 reflection coefficient (S_{11}). Port 2 reflection coefficient (S_{22}) is not plotted as it remains unaffected by this parametric variation	40
Figure 4-9. Antenna element radiation pattern for (a) V-Polarization and (b) H-Polarization	41
Figure 4-10. Scalable, dual-channel SRN topology-layout on a single surface for dual-polarized $2^n \times 2^m$ array	42
Figure 4-11. Microstrip line feed networks for 2×2 and 4×4 dual-polarized arrays	42
Figure 4-12. Cross-section view of packaged microstrip line signal routing network.....	42
Figure 4-13. Reflection and transmission coefficients (a) Port#1, 2×2 feed network, (b) Port#2, 2×2 feed network, (c) Port#1, 4×4 feed network, (d) Port#2, 4×4 feed network, and (e) Coupling coefficients for 4×4 array feed network.....	43
Figure 4-14. Feed arrangement within an array environment and S-parameters	44
Figure 4-15. Corporate dual-channel feed network for 4×4 dual-polarized ME dipole antenna array	44
Figure 4-16. PCB multi-layer exploded model of a 4×4 dual-polarized ME dipole antenna array	45
Figure 4-17. S-parameters and gain (a) Simulated and (b) Measured	45
Figure 4-18. Measured and simulated radiation patterns for V-pol excitation	46
Figure 4-19. Measured and simulated radiation patterns for H-pol excitation	47
Figure 4-20. Inter-subarray spacing and directional radiation patterns highlighted	48
Figure 4-21. Large-scale antenna frontend with 2D beam-switched subarray antenna	49
Figure 4-22. Layout schematic for a 2×2 dual-channel beamforming network.....	51
Figure 4-23. (a) XZ cross-section view of packaged beamforming network and (b) Microstrip beamforming network on single surface of XY-plane at BB' cross-section level	52
Figure 4-24. S-parameters (magnitudes and phase distribution) for port#1 excitation.....	53

Figure 4-25. (a) Dual-polarized antenna element – ME-dipole, (b) 2-D beam switching, and (c) 3-dB contours.....	54
Figure 4-26. Footprint of antenna aperture compared to beamforming network	55
Figure 4-27. Array factors of 2×2 subarray antenna.....	55
Figure 4-28. (a). A hypothetical multibeam frontend for hybrid beamforming, and (b). End-fire multibeam subarray antenna.....	57
Figure 4-29. (a) Three stages of multibeam subarray antenna, (b) XY cross-section view, (c) XZ cross-section view, and (d) Front view of 1×4 array aperture.....	58
Figure 4-30. Design parameters and performance of a patch-shape hybrid coupler.....	60
Figure 4-31. Crossover design and its crude equivalent circuit model	61
Figure 4-32. Crossover parametric study: (a) Return loss, (b) Isolation $ S_{21} $, (c) Isolation $ S_{41} $, (d) Phase variation, and (e) S-parameters for $L_S=2.4$, $W_S=0.3$ mm	62
Figure 4-33. Reflection coefficient and phase variation of Path 1 (Crossover) and Path 2 (Delay-line).....	63
Figure 4-34. Circuit configuration of (a) Path 2 and (b) Loaded line with double open circuit stubs of half-wavelength	64
Figure 4-35. Crossover reference line, a delay-line, and double open stub loaded delay-lines to conceive wideband phase shifter coherent with reference line	66
Figure 4-36. (a) Reflection coefficients, (b) Phases, (c) 0° and 45° phase shifters S-parameters, and (d) Phase variations and phase differences.....	66
Figure 4-37. 4×4 packaged Butler Matrix with extended measurement and phase compensation lines.....	67
Figure 4-38. S-parameters: magnitude and phase distributions for beam-port#1 (1R) and #2 (2L) excitation of a 4×4 Butler Matrix	68
Figure 4-39. Comparison of transmission coefficient with/Without AMC packaging	69
Figure 4-40. Parallel plate quasi-TEM transmission line, (b) Double-ridge waveguide, and (c) Desired boundary conditions	70
Figure 4-41. (a) Half-height EBG unit cell design parameters, (b) Equivalent circuit model, (c) Dispersion diagram, (d) Modes' E-fields, (e) Bandgap condition, and (f) DRGW dispersion diagram	72
Figure 4-42. (a) DRGW transmission line and S-parameters and (b) E-field distributions on AA' BB' Cross-sections	74
Figure 4-43. (a) Microstrip line to DRGW transition, (b) S-parameters, and (c) E-fields distributions across x-axis	75
Figure 4-44. Design parameters and simulated S-parameters.....	76
Figure 4-45. (a) E-plane exponentially tapered profile and (b) Corresponding impedance mapping.	77
Figure 4-46. (a) DRGW Horn antenna design parameters and (b) E-fields distribution onto the antenna aperture	77
Figure 4-47. (a) S-parameters, (b) Effect of chokes on antenna back radiation, and radiation patterns at: (c) 28 GHz, (d) 30 GHz, (e) 32 GHz, (f) 34 GHz.....	79
Figure 4-48. (a) 1×4 H-plane DRGW antenna array and (b) Radiation patterns by applying a set of phase distributions	80
Figure 4-49. H-plane beam-switched multibeam antenna design interior	81

Figure 4-50. Measured/Simulated S-parameters, gain and efficiency for (a) Beam-port#1 (1R) and (b) Beam-port#2 (2L) excitations.....	82
Figure 4-51. (a) Simulated co-/cross-beam patterns and (b) Beam patterns and single antenna element pattern 2-dB zoomed view.....	82
Figure 4-52. Simulated and measured radiation patterns at (a) 29 GHz, (b) 30 GHz, and (c) 31 GHz	83
Figure 4-53. Multibeam antenna prototype and the measurement setup. Keysight PNA (N52248) and compact range anechoic chamber	84
Figure 4-54. 16 – antenna element frontend by stacking four switched-beam subarray antennas in elevation plane..	85
Figure 4-55. Folded Butler Matrix topology layout.....	87
Figure 4-56. Folded Butler Matrix implementation with packaged microstrip line technology	88
Figure 4-57. EBG unit cell design parameters (units in mm) and its bandgap characteristics.....	88
Figure 4-58. AMC packaged microstrip line (exploded model view and cross-section view), and S-parameters.....	89
Figure 4-59. Coupler's design and S-parameters	90
Figure 4-60. Crossover's design and S-parameters	90
Figure 4-61. Two-layer packaged microstrip line transition: (a) Isometric and cross-section views and (b) Exploded model view	91
Figure 4-62. Two-layer packaged microstrip line transition S-parameters.....	92
Figure 4-63. PMC packaged 4×4 folded Butler matrix: (a) Geometry and dimensions, (b) First and second stage, and (c) Front and back views of folded microstrip traces.....	93
Figure 4-64. Folded Butler matrix S-parameters. Magnitude (a) Port#1 excitation, (b) Port#2 excitation, and (c) Phase difference at array-ports for Port#1 and Port#2 excitation	94
Figure 4-65. Defining antenna element design parameters in its perspective and isometric view.....	96
Figure 4-66. Antenna design parameters: (a) 3D exploded model view and (b) Front view	96
Figure 4-67. Reflection coefficient parametric study for (a) Length “L” and (b) Width “W”.....	97
Figure 4-68. Reflection coefficient (S_{11}) performance comparison.....	98
Figure 4-69. Cross-section views of absolute electric field distribution at antenna aperture.....	98
Figure 4-70. Antenna directivity: (a) 3D plot and (b) Polar plot at two principle planes	99
Figure 4-71. Packaged folded Butler matrix: (a) Exploded model view, (b) Antenna array aperture view, and (c) Beam-ports identification in isometric view	99
Figure 4-72. S-parameters for Port #1 and Port #2 excitation	100
Figure 4-73. Beam switching performance. (a) Cartesian plots at plane $\phi = 0^0$ and (b) 3D radiation patterns.....	100
Figure 5-1. First model of hybrid beamforming based on H-plane beam-switched subarray antenna	102
Figure 5-2. Vertically stacked subarrays to build a 4×4 antenna frontend for hybrid beamforming. Perspective views showing (a) Front and (b) Back	103
Figure 5-3. Directivity patterns from full-wave analysis of a 16-ports antenna system of first model.....	103
Figure 5-4. 3-dB radiation beams’ contours of the first model 16-ports antenna system at 30 GHz.....	104
Figure 5-5. Switched-beams in H-plane (H-Plane) and beam selection through SP4T switch.....	105

Figure 5-6. Beamspace digital beamforming operation over the H-plane beam-switched signals	105
Figure 5-7. 3-dB radiation pattern contours of hybrid beamforming for first model.....	107
Figure 5-8. Appearance of the grating lobe within 3-dB contour level	108
Figure 5-9. Second model of hybrid beamforming based on planar folded Butler Matrix subarray topology	109
Figure 5-10. Arrangement of four folded Butler matrix subarray antennas for the second model of hybrid beamforming	110
Figure 5-11. (a) Front-view and (b) Back-view of the second model of 16-antenna system.....	110
Figure 5-12. Directivity patterns from full-wave analysis of the second model of 16-ports antenna system	111
Figure 5-13. 3-dB radiation beams' contours of the second model of 16-ports antenna system at 30 GHz.....	112
Figure 5-14. A complete multibeam frontend for hybrid analog-digital beamforming	113
Figure 5-15. 3-dB radiation pattern contours of hybrid beamforming for second model	114
Figure 5-16. Process mapping of Hybrid Analog-Digital beamforming	114

List of Tables

Table 2-1. State-of-the-art multibeam antennas.....	17
Table 3-1 Cavity resonances with PEC/PMC packaging lids.....	27
Table 4-1. Progressive phase shift for horizontal polarization	52
Table 4-2. Design parameters for 0^0 (Path 4) and 45^0 (Path 5) phase shifters	65
Table 5-1. Beamforming coefficients calculated for the E-plane beamspace digital beamforming	106

List of Acronym

2G	2 nd Generation
3G	3 rd Generation
3GPP	3rd Generation Partnership Project
4G	4 th Generation
5G	5 th Generation
ADC	Analog to Digital Converter
AF	Array Factor
AMC	Artificial Magnetic Conductor
AP	Access Point
BS	Base Station
CMOS	Complementary Metal-Oxide-Semiconductor
CST MWS	Computer Simulation Technology Microwave Studio
DAC	Digital to Analog Converter
DRGW	Double-Ridge Gap Waveguide
DSP	Digital Signal Processing
EBG	Electromagnetic Band Gap
ESPAR	Electronically Steerable Parasitic Array Radiators
FR1	Frequency Range 1
FR2	Frequency Range 2
GSM	Global System for Mobile Communications
H/V-pol	Horizontal/Vertical-polarization
IC	Integrated Circuit
LNA	Low Noise Amplifier
LTCC	Low-Temperature Co-fired Ceramic
LTE	Long-Term Evolution
ME	Magneto-Electric
MIMO	Multiple-Input and Multiple-Output
mm-Wave	millimeter-Wave
NR	New Radio
PCB	Printed Circuit Board
PEC	Perfect Electric Conductor
PMC	Perfect Magnetic Conductor
PRGW	Printed Ridge gap Waveguide
PTFE	Polytetrafluoroethylene
RF	Radio Frequency
SCSA	Shared-single Cross-Slot Aperture

SISLs	Substrate Integrated Suspended Lines
SIW	Substrate Integrated Waveguide
SLL	Side Lobe Level
SP4T	Single-Pole 4-Throw
SRN	Signal Routing Network
TE	Transverse Electric
TEM	Transverse Electro-Magnetic
TM	Transverse Magnetic
UMTS	Universal Mobile Telecommunications Service
WiMax	Worldwide Interoperability for Microwave Access
x-pol	Cross-polarization

Chapter 1

Introduction

1.1 Millimeter-Wave for Wireless Communication

In the last three decades, huge milestones have been achieved in wireless communication. The advancement has recently paved its way towards the 5th generation (5G) and beyond. It succeeds 4G (LTE/WiMax), 3G (UMTS), and 2G (GSM) systems that have been operating below 6 GHz. The unprecedented bandwidth requirement is the main driving force to look for the next generation of wireless communications. Centimeter and millimeter-wave (mm-Wave) frequency bands within 24.25 ~ 52.6 GHz have been under consideration for 5G new radio frequency range 2 (NR FR2) standards [1]. Recent research and industrial development have demonstrated that mm-Wave frequency bands are feasible for future indoor/outdoor wireless communication networks [2]. To establish a base station (BS) for the legacy wireless networks, a communication cell is typically divided into three sectors for a 360^o-azimuth coverage. However, due to path losses, a single beam per-sector is not sufficient for future mm-Wave access points (APs). This path loss could be compensated by implementing multiple directional beams to cover a sector range, as shown in Figure 1-1. Furthermore, it is advantageous that with highly directional communication links, the capacity of a mm-Wave wireless system can be substantially enhanced by frequency reuse and multiple-input and multiple-output (MIMO) techniques within the same sector of a communication cell [3], [4].

This requires a mm-Wave AP frontend with beamforming capabilities in which the signal is transmitted or received preferentially in a specific direction over the others. For this purpose, electromagnetic radiation is controlled by phased array concepts. Analog and digital beamforming are the most commonly adopted wireless communication systems [5]. At mm-Wave, a physically small circuit size could be populated with a large number of radiating elements, which results in an $N \times M$ large-scale antenna system, as shown in Figure 1-2. The trait of physical miniaturization

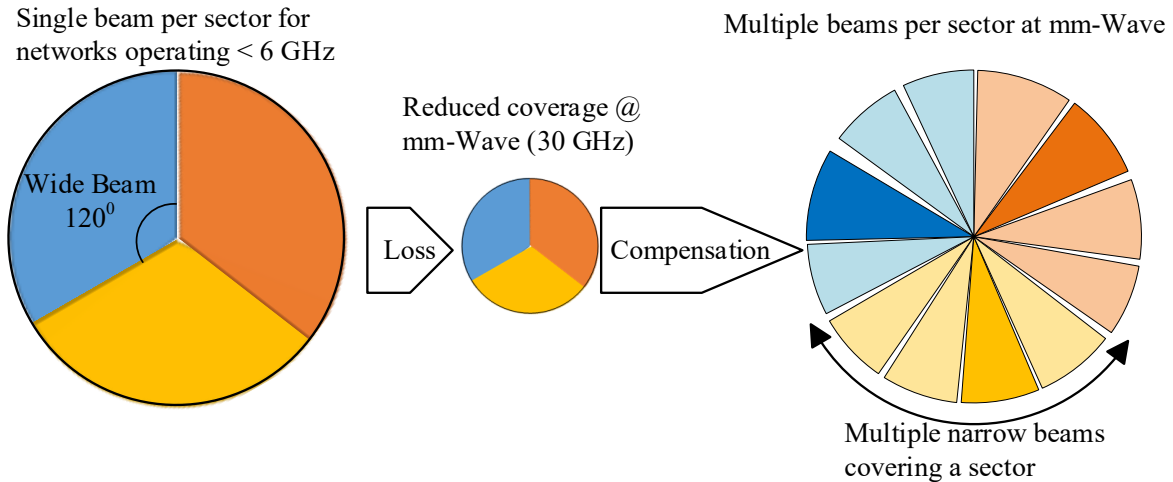


Figure 1-1. Communication cell coverage: single versus multiple beams per-sector

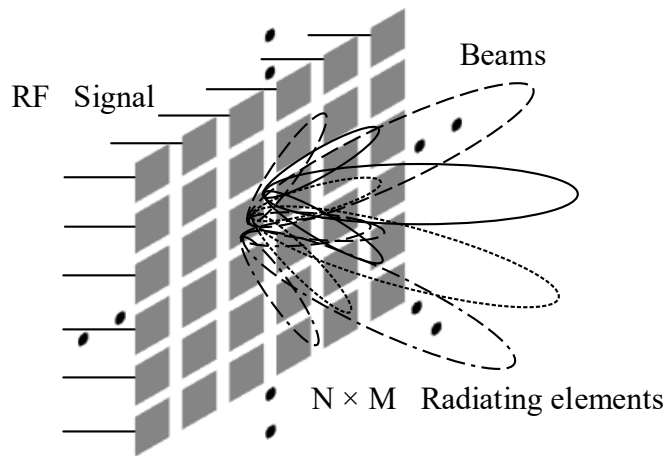


Figure 1-2. Millimeter-wave AP with $N \times M$ large-scale antenna frontend on a physically small circuit size

at mm-Wave could be effectively exploited to design multibeam antenna systems with high spatial resolution. Therefore, it is evident that beamforming capabilities are essential in future mm-Wave BS/AP designs [6].

Ideally, a highly directional antenna system with too high spatial resolution and wide scan-range would be suitable for mm-Wave APs. However, the gain and scan-range are inversely proportional to each other. Increasing the gain at the element or subarray level limits the scan-range of a large-scale $N \times M$ antenna frontend. Therefore, to minimize the scan loss and to equalize

the gain profile of a large-scale beamforming array, a large-scale antenna frontend could be divided into subarrays.

1.2 Beamforming Architectures

With the advancement of digital signal processing (DSP) techniques and the development of electronics hardware, the implementation of digital beamforming has been preferred over the analog counterpart for the last couple of decades. A smart antenna system has emerged in which the antenna array adapts its radiation pattern continuously according to the requirement [7]–[9].

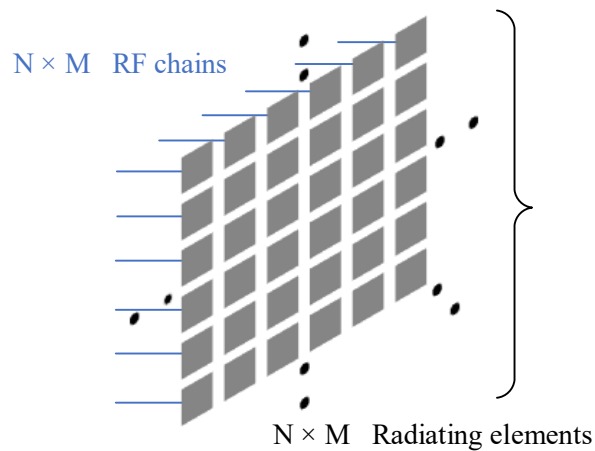


Figure 1-3. Large-scale $N \times M$ antenna array with $N \times M$ paths for RF signals

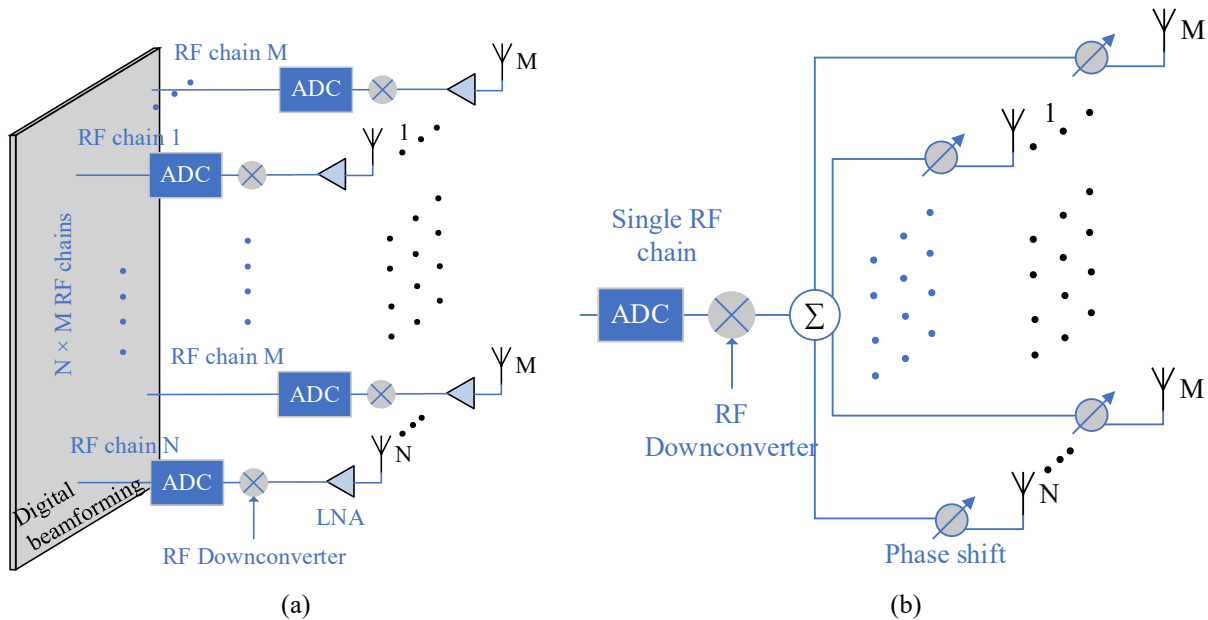


Figure 1-4. Beamforming architectures for $N \times M$ antenna array: (a) Full digital beamforming, (b) Full analog beamforming

For such systems, the antenna frontend requires a dedicated radio frequency (RF) chain for each radiating element, as shown in Figure 1-3. In receiving mode, the RF chain consists of an antenna element, low noise amplifier (LNA), frequency downconverter, and analog-to-digital converter (ADC). The digital beamforming coefficients are calculated and applied to form simultaneous digital beams at the baseband level. On the other hand, in analog beamforming architecture, the phase shifts among the array-ports are controlled within a microwave circuitry through phase shifters that result in beam formation. For an $N \times M$ antenna array, full-digital and full-analog beamforming architectures are shown in Figure 1-4 (a) and Figure 1-4 (b), respectively.

A complete implementation of digital beamforming architecture requires a dedicated RF chain for each radiating element within a large-scale $N \times M$ antenna system. It is not feasible to accommodate a large number of RF chains within a small circuit size, practically and economically. Additionally, it could result in losses, and a large amount of power dissipation from active RF chains, which leads to the problem of energy efficiency; as the total power consumption of a wireless system is the sum of the effective transmit power and the power loss in the RF chains' circuit. Therefore, a large-scale $N \times M$ digital beamforming antenna array shown in Figure 1-4 (a) could exhibit energy efficiency and hardware complexity problems. On the other hand, a large-scale amplitude/phase distributing analog RF precoder could be highly lossy. The accumulated losses could lower the system's dynamic range by transmitting fewer bits of information successfully over the channel, which results in a spectral efficiency problem. Thus, a large-scale analog beamforming architecture with a single RF chain, as modeled in Figure 1-4 (b), is not a feasible design either. Therefore, the sole implementation of either digital or analog beamforming architecture for mm-Wave large-scale BS/AP antenna system could result in system-level inadequacies.

For wireless communication, the concept of beamspace digital beamforming has been detailed in the literature long ago [10], [11]. In this scheme, a subarray pattern is taken to perform digital beamforming rather than an element pattern. The term beamspace refers to a subarray radiation pattern within a large-scale antenna system. The analog beamforming networks could generate these beamspace (subarray radiation patterns); therefore, it is also called hybrid beamforming. A paradigm shift from sub-6 GHz to mm-Wave for 5G and beyond, its effectiveness

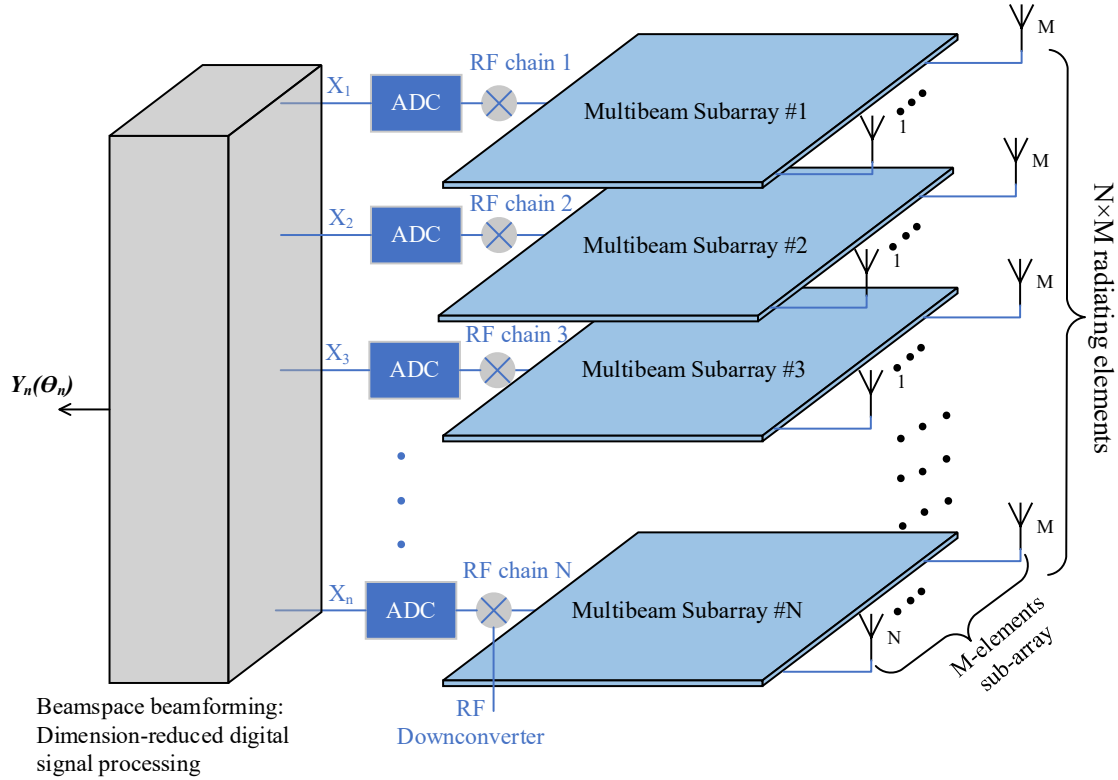


Figure 1-5. Subarray-based partially connected hybrid beamforming model for $N \times M$ receiving antenna array

has been recognized more than ever before [12]. In this regard, partially-connected and fully-connected hybrid beamforming models have been thoroughly investigated in the literature [13]. In [14], [15], it has been shown that energy-efficiency and spectral-efficiency can be achieved through the implementation of mm-Wave hybrid beamforming in which analog beamforming subarray plays a pivotal role. From the perspective of analog beamforming network order, a partially- or sub-connected model is more pragmatic, as shown in Figure 1-5. This model shows that an $N \times M$ antenna frontend can be divided into vertically stacked subarrays having individual RF chains. A limited set of predefined beams defines the horizontal spatial coverage domain. Whereas, for a finetuned digital beamspace beamforming, DSP can be applied over the subarray signals X_m to generate Y_n beams in the direction of θ_n . Thus, this model could reduce the number of RF chains from $N \times M$ (for a completely digital beamforming architecture) to N , resulting in a dimension-reduced digital signal processing. In most such studies, a hypothetical analog RF beamformer block is usually considered for analytical analysis [16]. Thus, several critical antenna

aspects remain overlooked, such as beamforming subarray configuration, choice of technology, and mutual coupling effects in an active environment.

1.3 Motivation and Problem Statement

A hybrid architecture is an efficient implementation of mm-Wave beamforming systems in which the multibeam subarray antenna is the most pivotal entity. This fact motivates the investigation of

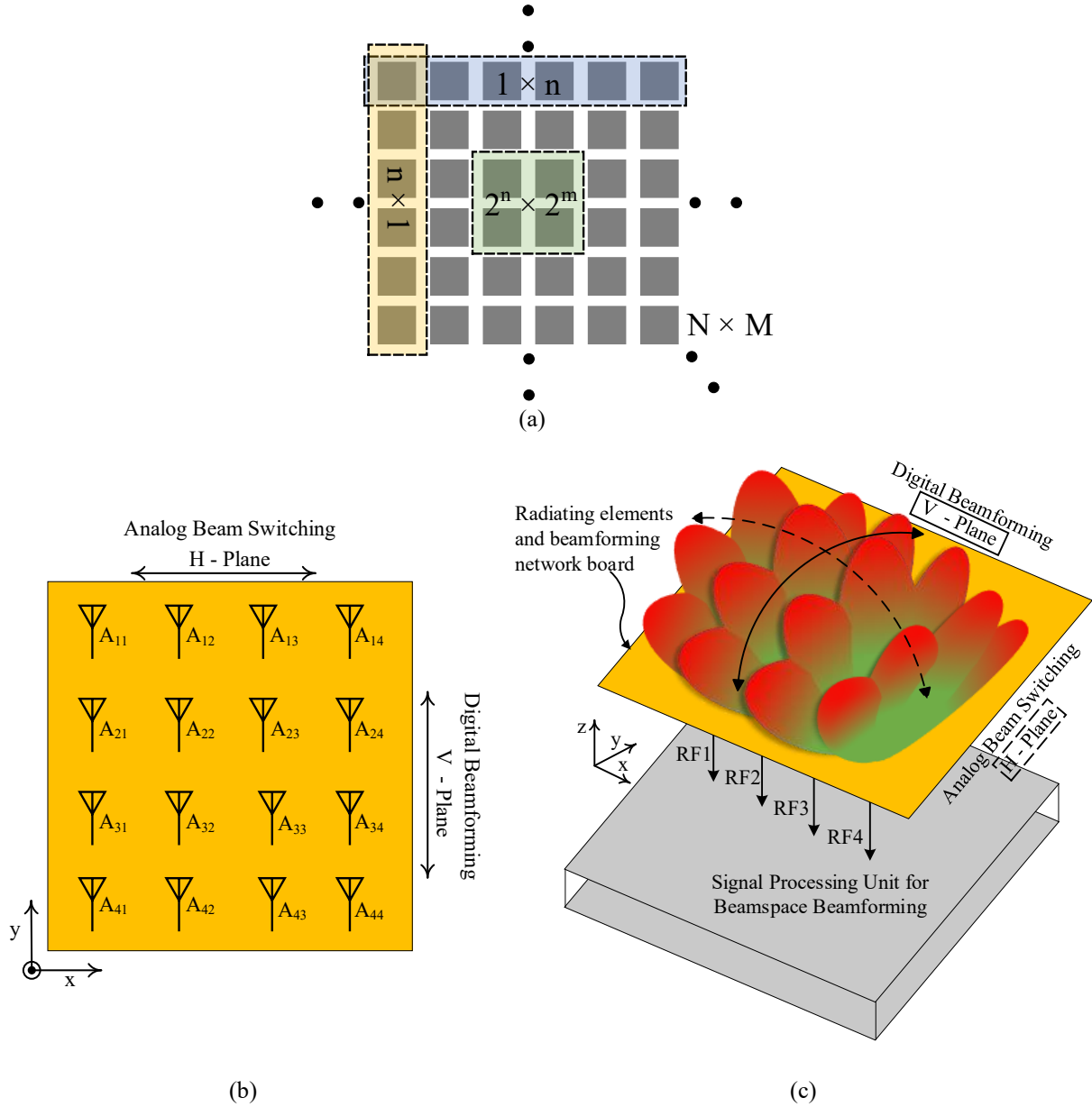


Figure 1-6. (a) Division of $N \times M$ antenna frontend into subarrays, (b) An $N \times M = 4 \times 4$ antenna frontend, and (c) Hybrid beamforming frontend with analog beam switching in ϕ -plane and digital beamforming in V-plane

multibeam subarray antenna designs as the constituents of an $N \times M$ antenna frontend, as depicted in Figure 1-6 (a). To put things in perspective, an $N \times M = 4 \times 4 = 16$ -antenna element planar geometry is defined in Figure 1-6 (b), which could perform analog beam switching in the H-plane and a finetuned digital beamforming in the V-plane. The desired hybrid beamforming functionality defined in Figure 1-6 (c) requires a subarray-based multibeam antenna frontend, which could be efficiently integrated with an integrated circuit (IC) DSP module to perform digital beamspace beamforming.

A multibeam subarray could be designed with fixed-beam or switched-beam radiation patterns to pursue the objectives mentioned above. However, either choice could have a substantial performance impact. For instance, with the fixed-beam subarray design, as shown in Figure 1-7 (a), if two wavefronts imping on a four-element subarray with a normal (θ_1) and grazing (θ_2) angle of incidence. Then, the received signal “Y” is significantly reduced for the angle of arrival, θ_2 , as the subarray SRN is designed for maximum directivity at $\theta_1 = 0^0$. This problem could be addressed by designing a switched-beam subarray antenna, as shown in Figure 1-7 (b). Rather than the SRN to generate a single fix-beam, a feeding network could be designed to generate multiple switched-beams from the same antenna aperture, such as Lens or Butler matrix-based multiple switched-beam antennas. Each striking wavefront could be received at the corresponding beam switched at θ_1 , θ_2 , and θ_3 directions. Thus, receiving the signals “ $Y_n(\theta_n)$ ” with coherent combinations for all

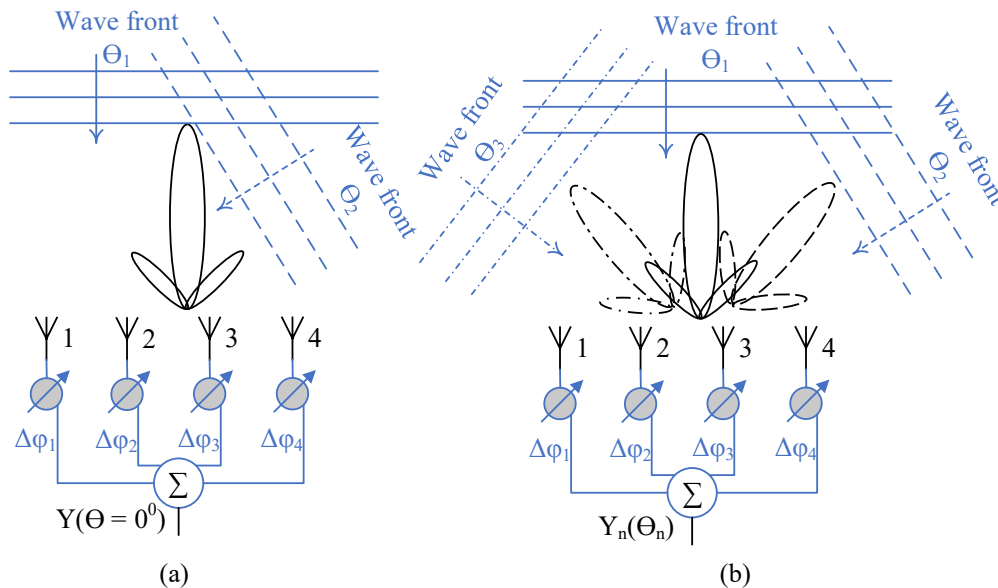


Figure 1-7. (a) Fixed-beam subarray and (b) Switched-beam subarray

striking wavefronts without loss. However, it requires a subarray antenna with an analog beamforming network.

While designing the high gain antenna with multiple switched-beams as a subarray within a large-scale $N \times M$ antenna system for hybrid beamforming, the following are the two associated problems found in the existing work.

A. Subarray Antenna Layout

The conventional layouts of the beamforming networks, such as Butler matrix [17], [18], Blass matrix [19], Nolen matrix [20], and Rotman lens [21], [22], occupy large circuit. A

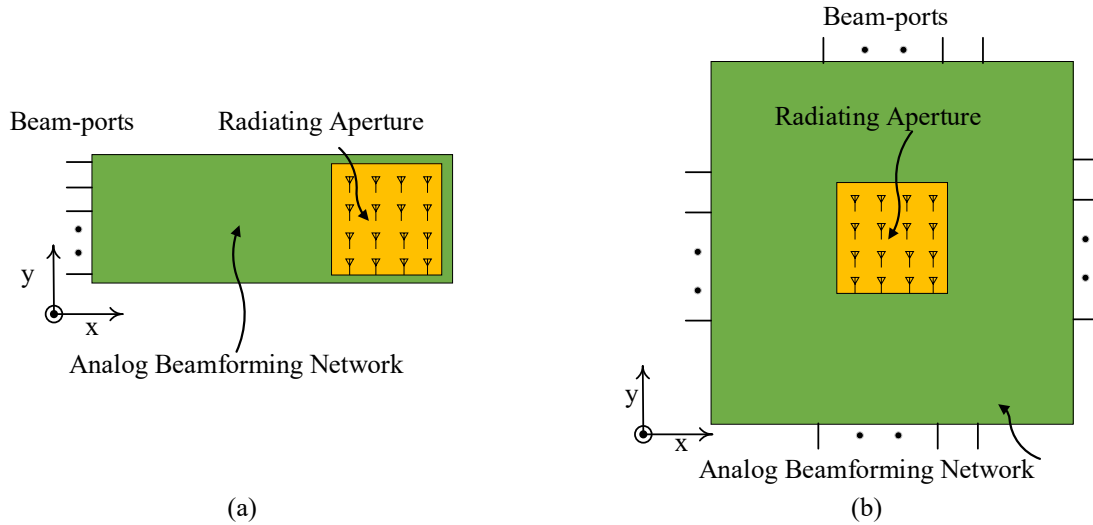


Figure 1-8. Circuit footprints of a conventional multibeam subarray antenna: (a) Longitudinal layout and (b) 2-D layout

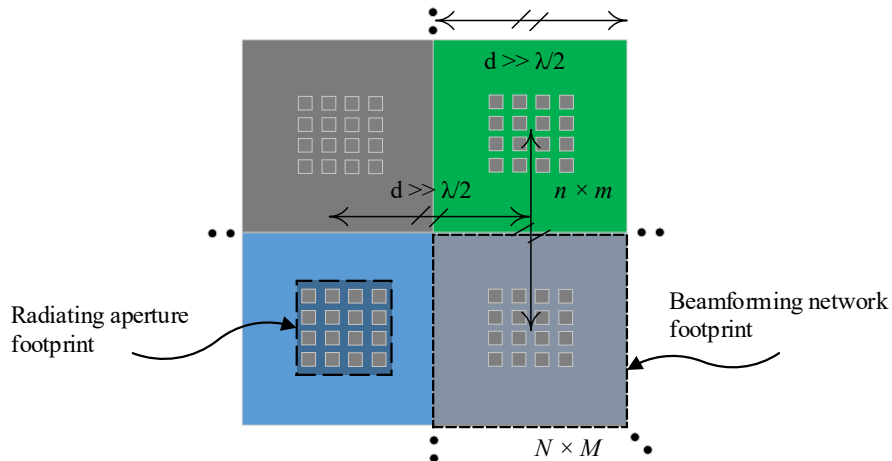


Figure 1-9. Discontinuous $N \times M$ array aperture due to subarray with larger beamforming network as compared to radiating aperture

multibeam subarray antenna implemented with these techniques on a printed circuit board (PCB) technology has a much larger beamforming network footprint as compared to the radiating aperture. Such as depicted in Figure 1-8 for longitudinal and 2-D beamforming network configurations [23], [24]. Therefore, their $n \times m$ arrangement within a large-scale $N \times M$ antenna frontend results in inter-subarray spacing much larger than $\lambda/2$. Furthermore, the integration of such subarrays to build an $N \times M$ antenna frontend also results in a discontinuous aperture as shown in Figure 1-9. Therefore, the existing multibeam antenna topologies are not practical for a wide-range beam scanning hybrid beamforming model.

B. Array Factor

The array factors (AFs) produced by a switched-beam subarray antenna are not identical, *i.e.*, from Figure 1-10 (a), $AF_1 \neq AF_2 \neq AF_3 \neq AF_4$. To perform beamspace digital beamforming, similar AFs are required that can be selected from the adjacent switched-beam subarrays, as shown in Figure 1-10 (b). However, as the radiating apertures producing such AFs are spaced much larger than $\lambda/2$, their AF is highly directional in all

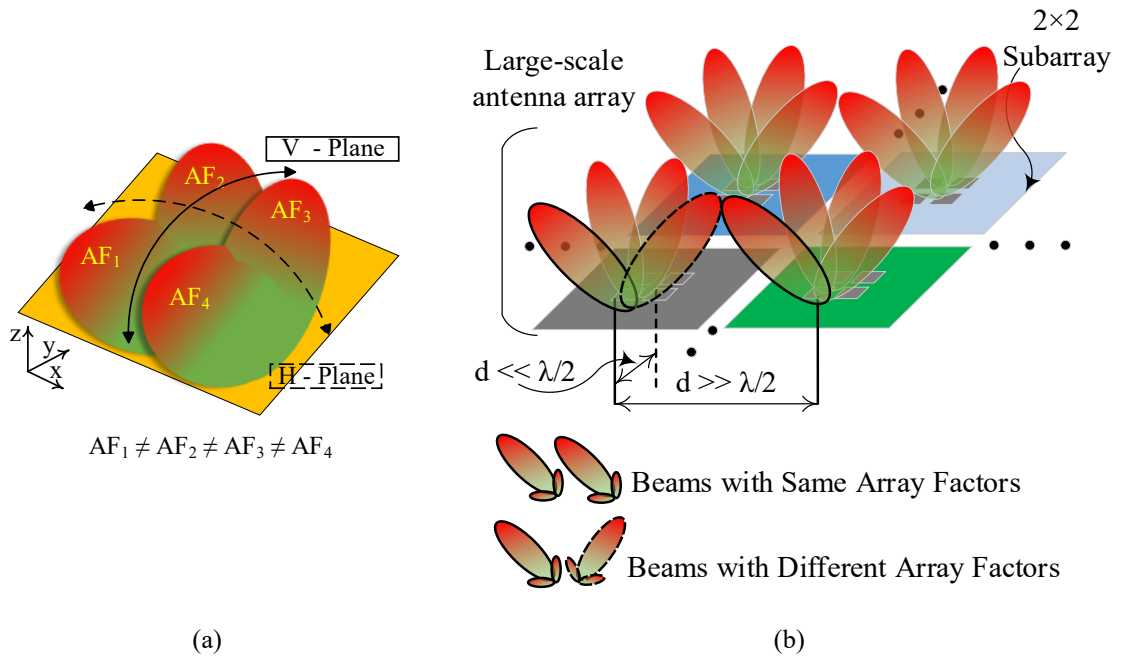


Figure 1-10. (a) A multibeam subarray radiation pattern AFs representation and (b) AFs of subarray-based $N \times M$ antenna frontend

ϕ -planes; therefore, it cannot be processed for digital beamspace beamforming. Thus, the large circuit layout and AF of the conventional multibeam subarray antenna are interrelated.

Recent literature on the multibeam antenna for mm-Wave communication shows that most of the studies have been conducted on single array designs with a limited order of $2^n \times 2^n$ only. As a constituent of an $N \times M$ antenna frontend configuration, their effect on the circuit layout and radiation characteristics have never been investigated. Furthermore, by predefining a specific mm-Wave hybrid beamforming scheme, the study of the required switched-beam subarray-based antenna frontend topology has not been found.

The problems mentioned above require a novel implementation of the multibeam subarray antenna to conceive a large-scale $N \times M$ antenna system for hybrid beamforming operation, proposed in

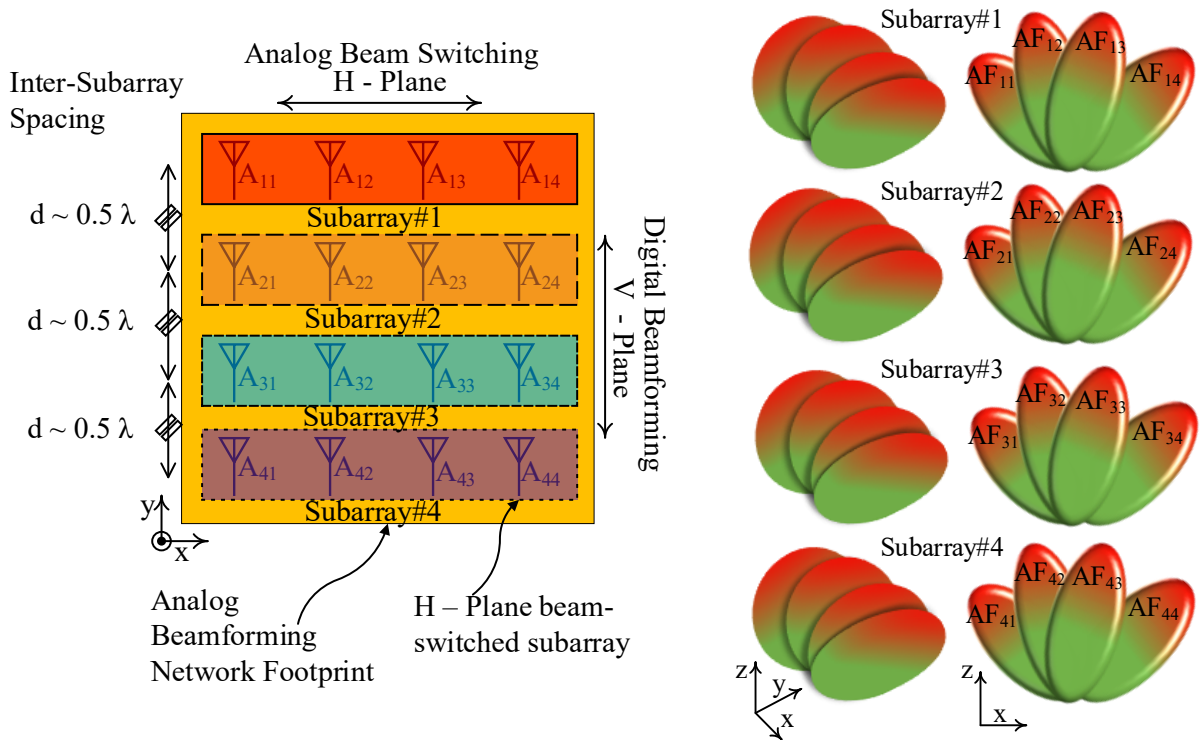


Figure 1-11. Proposed multibeam antenna frontend for mm-Wave hybrid beamforming

this thesis. In Figure 1-11, such topology is proposed in which the compact multibeam subarrays are arranged laterally with center-to-center spacing $\lambda/2$. For an array order of $N \times M = 4 \times 4$, each subarray's beamforming network could be accommodated beneath a 1×4 antenna distribution to make the circuit size compact. Furthermore, each subarray could produce four fan-shaped radiation patterns switched in the H-plane such that $AF_{1m} = AF_{2m} = AF_{3m} = AF_{4m}$, where $m = 1, 2, 3, 4$, are the beam-ports' indices. Thus, the proposed topology could address a large circuit layout and array factor for a multibeam antenna frontend for mm-Wave hybrid beamforming.

1.4 Objective

This work aims at developing a suitable multibeam antenna frontend for hybrid beamforming operation. In this regard, several subarray designs are critically analyzed with the implementation orders of $n \times m = 1 \times 4, 2 \times 2$, and 4×4 to reach the optimum ones. Within the allocated spectrum range for 5G NR FR2, the frequency band of 28 – 32 GHz is considered. As the subject matter demands fan-shaped directional beamspace subarray patterns with inter-subarray spacing around $\lambda/2$, therefore, it requires a thorough investigation of radiation characteristics and layout topologies. This includes the design and full-wave analysis of suitable antenna elements, beamforming components, subarray designs, and multibeam $N \times M = 4 \times 4$ antenna frontend in commercial software. The unidirectional radiation pattern antenna elements with directivity of 5-7 dBi are designed. To ensure subarrays performance within the bandwidth of 28-32 GHz, the beamforming components are designed with 25-30 % bandwidth at 30 GHz. The inadequacies of the fixed-beam over the switched-beam subarray design are critically analyzed. To control the transmission line losses at 30 GHz, a perfect magnetic conductor (PMC) packaged microstrip line technology is used. The PMC-packaged signal routing networks (SRNs) are investigated for four subarray antenna configurations. Finally, to perform two-dimensional (2-D) beamforming, two hybrid beamforming models are demonstrated by post-processing of the data obtained from the full-wave analysis of 4×4 multibeam antenna frontends.

1.5 Thesis Outline

This thesis is organized into six chapters. Chapter 2 covers the literature review of the recent advancements in mm-Wave beamforming. In Chapter 3, a concise review of pertinent PCB

packaging techniques and the principles of microstrip line PMC packaging are presented. In Chapter 4, four designs of multibeam subarray antennas with PMC packaged SRNs are presented along with a critical summary at the end of each section. In Section 4.1, a dual-polarized high-gain 4×4 fixed-beam subarray antenna is presented. Its effectiveness for a MIMO system and limitations for a hybrid beamforming architecture are also highlighted. In Section 4.2, a 2-D dual-polarized 2×2 switched-beam subarray antenna is presented. In Section 4.3, a 1-D multibeam subarray antenna with 1×4 fan-shaped beam-switched radiation patterns is presented. The problems of large circuit layout and AFs are addressed in Section 4.4, in which a compact 4×4 folded Butler matrix and 1×4 beam-switched subarray antenna are presented. In Chapter 5, two models of hybrid beamforming are presented where 4×4 antenna frontends are developed from the subarrays of Section 4.3 and Section 4.4. The data obtained from the CST MWS full-wave analysis is post-processed to conceptualize the DSP operation for 2-D hybrid beamforming. Finally, the work is concluded in Chapter 6 with expected research extensions as future work.

1.6 Contributions

A comprehensive case study of mm-wave hybrid beamforming is presented in which the task is divided into analog and digital beamforming in the H-plane and V-plane, respectively. However, the research emphasis is to propose an efficient $N \times M$ multibeam antenna frontend suitable for this purpose. This research is conducted to achieve this objective that results in several outcomes. The main contributions can be divided into the following three categories.

1.6.1 Fixed-beam versus Switched-beam Subarray Analysis

The $2^n \times 2^m$ fixed-beam and switched-beam subarrays are critically analyzed by defining their merits and demerits for an $N \times M$ hybrid beamforming antenna frontend. In this regard, a fixed-beam dual-polarized 4×4 subarray antenna with a packaged microstrip line feed on a single surface is presented. The subarray order $2^n \times 2^m$ could be scaled as per the requirements. However, it is found that the proposed design could better serve the MIMO system; therefore, a 2-D beam-switched subarray antenna is presented to achieve spatial diversity for beamforming systems.

1.6.2 Folded Butler Matrix Switched-beam Subarray

As the defined hybrid beamforming functionality requires fan-shaped switched-beam radiation patterns with lateral inter-subarray spacing $\lambda/2$; therefore, two Butler matrix-based switched-beam subarrays are developed with an order of $l \times 4$. However, based on the end-fire Butler matrix subarray, the hybrid beamforming model has performance limitations. This leads to developing a novel broadside $l \times 4$ folded Butler matrix switched-beam subarray, which is one of this research's main contributions. This solves two problems inherited from the conventional switched-beam designs: (1) large subarray layout and (2) array factors misalignment for beamspace beamforming.

1.6.3 Hybrid Beamforming System Demonstration

The operational principle of 2-D hybrid beamforming is demonstrated for the $N \times M = 16$ -antenna system. Two subarray-based multibeam antenna frontends are numerically solved. The digital beamforming post-processing is performed over the beamspace patterns obtained from the full-wave analysis. In these demonstrations, it is shown that as compared to full-analog 2-D beamforming, these models are capable of finetuned beam-steering in the V-plane because the complex beamforming coefficients are calculated dynamically by DSP. Furthermore, as compared to full-digital 2-D beamforming, it reduces the number of active RF chains from $N \times M$ to N .

Chapter 2

Literature Review

2.1 Hybrid Beamforming Systems

Beamforming capabilities are essential in modern mm-Wave BS/AP designs. Techniques, such as the Butler matrix, Blass matrix, Nolen matrix, and Rotman lens, have been commonly used for this purpose. In [23], their use for mm-Wave hybrid beamforming applications is presented comprehensively. A full-digital beamforming antenna array, also known as a smart antenna, requires the same number of RF chains as the number of radiating elements [25]. It might be affordable to develop such a laboratory test bench. However, a large number of chains could not be accommodated in a planar mm-Wave commercial antenna frontend with compact geometry. In hybrid beamforming architecture, instead of connecting dedicated RF paths directly to the radiating element, a single RF chain is assigned to an analog precoder, which groups a limited number of antenna elements at its array-ports. This precoder could be a switched-beam analog beamforming network or a fixed-beam [23], [26]. The subarrays can be arranged as a linear, rectangular, or square grid of radiating elements at the frontend, as per the design and performance requirements. For instance, a hybrid beamformer is analyzed using the Rotman lens as a switched-beam precoder [27]. To minimize hardware complexity and energy consumption, a fully-connected hybrid (digital and analog) receiver with eight antenna elements has been developed on CMOS technology for 25-30 GHz [28].

As a fixed-beam, an active array environment is studied for a hybrid beamforming transmitter with a 2×2 subarray antenna at 29 GHz [29]. In [30], it is shown that with a less complicated hybrid beamformer, the performance similar to a fully-digital array could be achieved for the angle of arrival estimation. Similarly, it is demonstrated that a sub-degree steering resolution could be achieved with a hybrid array [31]. In [32], several aspects of the hybrid beamformer, such as its microwave architecture, algorithms, and measurements, have been presented for future BS/AP applications. A 16×16 phased array antenna is partitioned into a

configuration of 2×2 subarrays with inter-element spacing $\lambda/2$ [33]. The hardware cost and complexity are significantly reduced by performing hybrid beamforming operations to achieve specific radiation profiles. However, as the subarrays with fixed-beam radiation patterns are considered; therefore, it results in a limited scan range. Similarly, with a 2×2 subarray configuration, the designs of 8×8 phased array antennas have been investigated to evaluate system-level performance [34], [35]. On the same principles, a robust wide-angle scanning 8×8 phased array with 2×2 subarrays is presented for 28 GHz 5G MIMO applications [36]. Although it is demonstrated that the number of RF chains could be reduced substantially, these phased array designs are more suitable for MIMO operation due to a limited scanning capability.

2.2 ESPAR and Frequency Scanning Subarray Antennas

Similarly, a large-scale aperture array could be divided into electronically steerable parasitic array radiators (ESPAR) as a subarray to perform hybrid beamforming. In [37]–[39], the 5-elements ESPAR designs have been investigated. To be considered for hybrid beamforming, such subarrays could result in array factor misalignment within a large-scale array. Furthermore, their 2-D elements' arrangement results in high directivity with narrow 3-dB beamwidths in both principal planes. Thus, beam-space hybrid beaming could not be effectively performed for a wide scanning.

Nevertheless, such a multibeam antenna frontend is suitable for MIMO applications where impinging signals over the fixed beam-spaces are acquired to process for the multiple simultaneous wireless streams. On the other hand, a lattice of 1-D miniaturized longitudinal subarray can be designed by the concept of traveling wave antennas [40], [41]. Such a fan-shaped beam-scanning subarray antenna could be efficiently laid out with inter-subarray spacing $\lambda/2$. However, it might not be suitable for the fixed-frequency beamforming applications as they are, in principle, frequency scanning antennas.

2.3 PCB Antennas, Beamforming Components, and Multibeam Subarrays

As compared to CMOS and LTCC technologies [28], PCB technology is low-cost/low-profile, and it is highly suitable for the mass production of specific applications. In a multibeam wideband RF system, the antenna element design plays a pivotal role. The ideal radiator that needs to be used within a 2-D beamforming array requires a stable symmetrical radiation pattern in both (principle)

planes. In this context, the research on a complimentary class of antennas, such as magneto-electric (ME) dipole, has been performed extensively in recent years [42]–[47]. A Huygens’ source can be approximately realized by placing a passive electric dipole in front of a magnetic dipole (slot). In this way, the properties of a dipole antenna and a slot are combined to achieve a unidirectional symmetrical radiation pattern.

Furthermore, such complementary designs are capable of achieving wide bandwidth, low cross-polarization, and stable radiation pattern over the wide operational bandwidth. Such planar radiators are good candidates for the BS/AP broadside radiating arrays [48]. However, their integration with an end-fire array is challenging [49], [50]. Similarly, components, such as phase shifters, couplers, crossovers, and bridges are vital parts of the analog beamforming networks. As presented in [51], the multi-layer PCB implementation can be simplified by laying the design on a single surface [52]. The microstrip line beamforming SRNs on a single surface could be effectively augmented with the PMC packaging concepts [53].

PCB technology has been used to develop a mm-Wave hybrid beamformer, which consists of vertically stacked 16 multibeam subarray antennas [54]. Each subarray contains a pair of modified 4×8 substrate integrated waveguide (SIW) Butler matrices, which generate 8 analog switched-beams in one principle plane, and a fine-tuned digital beamforming is performed in the other orthogonal plane using this stack of 16 subarrays along with DSP operation. In such a subarray design, the end-fire layout has a radiating aperture followed by an extended analog beamforming network, as highlighted in Chapter 1, Figure 1-8 (a). As such, several longitudinal multibeam antenna layouts, in which a beamforming network followed by the radiating section, have been recently reported [49], [55]–[65]. For 2-D beamforming, the circuit is preferred to be implemented on the XY-plane with symmetrically extended dimensions. The radiating aperture is placed in the middle, as depicted in Figure 1-8 (b). In the latest literature, such topologies have been extensively studied and laid out on a PCB technology for a planar tiled multibeam antenna frontend [43], [44], [66]–[73]. However, it is observed that mostly the single subarray designs have been investigated, except for a hybrid beamforming system-level implementation presented in [54]. Therefore, if multiple such subarrays are arranged to build an $N \times M$ large-scale antenna aperture, then it may result in edge-to-edge discontinuities between the subarray apertures due to

a large beamforming network footprint of each subarray. Thus, for a 2-D beamforming network configuration as presented in [43], [44], [74]–[76], the inter-subarray spacing could be several half-wavelengths with aperture discontinuity. This could bar to perform subarray-based hybrid beamforming for a wide scan-angle. Table 2-1 compares the recently reported multibeam antennas to highlight the complexity of implementation technology, bandwidth, pattern directivity, and large circuit layout due to the beamforming network footprints. The PRGW requires an intensive full-wave analysis for each component, bend, and discontinuity.

On the other hand, SIW as a waveguide accumulates large circuit space. It can be seen that most of these layouts result in 2D directional radiation patterns and large circuit layout. Therefore, these antennas could exhibit radiation pattern limitation and large circuit space if used as a subarray within an $N \times M$ multibeam antenna frontend.

2.4 Layout Miniaturization

Although, techniques such as half-mode SIW [77] or folded C-type SIW [55] have been utilized to design the relatively compact beamforming networks. However, it does not result in a substantial size reduction of multibeam subarray to be arranged with $\lambda/2$ inter-subarray spacing. In this aspect, limited literature has been reported. At the same time, none has been found in designing an $N \times M$ array aperture that could be built from such multibeam subarrays. To achieve circuit miniaturization at 38 GHz, a compact Butler matrix multibeam antenna is designed on PCB technology. However, the circuit still has a larger-size beamforming network compared to the antenna array aperture [78]. To miniaturize the footprints of a lens-based beamforming network, a folded Cassegrain lens topology is implemented using SIW technology at 28 GHz in which the circuit dimensions are still extending several wavelengths [79]. Similarly, a highly compact folded

Table 2-1. State-of-the-art multibeam antennas

Ref.	Technology & Configuration	Frequency (GHz)	Gain (dBi)	# of beams	Layout (λ^2)
[44]	PRGW 2×2 Beamforming network	27-33 GHz	12 dBi	4	5.6×7.1
[55]	SIW 4×4 Beamforming network	28-32 GHz	8.9-14.15 dBi	4	11.1×2.84
[56]	PRGW 4×4 Beamforming network	27-33.6 GHz	8.4-11.35 dBi	4	9×5.4
[66]	SIW 16×16 Beamforming network	10 GHz	-	16	22×16.7
[69]	SIW 16×16 Beamforming network	54-66 GHz	10-14.7 dBi	16	Several λ
[71]	SIW 5 Ports design	27-29 GHz	14.1-15.3 dBi	5	7.4×6
[99]	SIW SISL 4×4 Beamforming network	24.5-26.5	12 dBi	4	3.21×3.20

Butler matrix has been developed using LTCC technology at 5 GHz, which consists of 40 LTCC layers [80]. To keep the lateral dimensions strictly $\lambda/2$, a good design of a 4×4 SIW folded Butler matrix has been presented for 30 GHz multibeam applications [81]. The circuit consists of four PCB layers that occupy an area of $3.8 \lambda \times 0.5 \lambda$. Therefore, this literature review shows that single multibeam subarray designs have been investigated in most recent research. Whereas their design and performance challenges for a subarray-based $N \times M$ hybrid beamforming multibeam antenna frontend have been overlooked.

2.5 Research Methodology

The system-level studies show that hybrid beamforming architecture is an optimum choice for the large-scale mm-Wave antenna system to achieve spectral and energy efficiency in which analog beamforming subarrays are the vital constituents [14]. However, the recent development of beam scanning antennas shows that the associated challenges, while using them as a subarray within a large-scale antenna frontend, have been overlooked. If such conventional designs are considered to build a hybrid beamforming antenna frontend, it could result in the array factor problem and discontinuous aperture due to individual subarray layout. To overcome these limitations, the subarray-based multibeam antenna frontends are investigated, and by using them, two hybrid beamforming models are demonstrated for mm-Wave BS/AP applications. In this regard, the following research methodology is adopted.

A. Frequency of Operation and System Design Aspects

The 3rd Generation Partnership Project (3GPP) has announced the FR2 (24.25 ~ 52.6 GHz) for 5G mm-Wave applications. As the lower spectrum range around 30 GHz has been targeted for the outdoor BS/AP communication [2]; therefore, the frequency band 28 – 32 GHz is considered for the multibeam antenna frontend designs. However, the individual antenna elements and beamforming components are designed for a broader bandwidth of ~ 25 – 35 %.

For the analog beam switching in the H-plane, the Butler matrices are designed at 30 GHz to produce the excitation vectors as $[1, e^{-i\psi}, e^{-i2\psi}, \text{ and } e^{-i3\psi}]$, where $\psi \in [-135^\circ, -45^\circ, 45^\circ, \text{ and } 135^\circ]$ for four switched-beam spaces 2R, 1R, 1L, and 2L,

respectively. Similarly, the sets of complex weights \mathbf{W} are applied over the beam spaces $\mathbf{X} = [x_1, x_2, x_3, x_4]^T$ to generate beams B_V digitally. For the first and second hybrid beamforming models, $B_V \times B_H = 3 \times 4$ and $B_V \times B_H = 4 \times 4$, respectively.

B. Selection of Technology and Subarray Order

As the compact circuits could be efficiently laid out using quasi-TEM transmission lines, therefore, microstrip line technology is used. The SRNs are augmented with the PMC packaging concepts to minimize the radiation losses at mm-Wave. In Chapter 3, the PMC packaging principle is detailed, along with a brief review of other counterpart packaging techniques. These principles are used in developing PMC packaged designs in the subsequent chapters. The microstrip line circuits are designed with packaging in mind. The subarrays are designed with the order of $n \times m = 1 \times 4, 2 \times 2$, and 4×4 , for an $N \times M = 4 \times 4$ antenna frontend. However, the $n \times m$ order could be scaled as per the frontend design requirements as long as the losses from the analog beamforming network are within a defined range. The circuits are realized on Rogers laminates [82]. According to the requirement, the metallic and printed AMC packaging layers are designed for the circuits.

C. Full-Wave Analysis

CST MWS suite is used for the circuits' full-wave analysis [83]. Its Eignemode solver is used for the unit cell analysis to realize an AMC surface. For some designs, the Time Domain Solver's simulation results are also verified by the Frequency Domain Solver.

D. Fabrication and Measurement

The 1.85-mm end-launch (1893-03A-5) connectors provided by Southwest Microwave Inc., Tempe, AZ, USA, are used for circuit measurement [84]. The circuits are fabricated at the Poly-Grams research center, Polytechnique Montréal, using CNC and LPKF fabrication facilities. Their Keysight PNA (N52248) and compact range facility are used for the S-parameters and radiation pattern measurement. The circuits are also tested at Concordia University by using the Agilent PNA 65 GHz (N52271A) and the anechoic chamber facility.

Chapter 3

PCB Packaging Techniques for mm-Wave Applications

PCB technology has been widely used to realize analog beamforming networks such as Butler Matrix, Blass Matrix, Nolen Matrix, Rotman Lens, and delay lines due to their low profile. High-frequency laminates, such as Rogers [82] and Taconic [85], are very suitable for circuits' mass-production by using these low-cost materials. Furthermore, the fundamental theory of RF and microwave circuit components is well established to be used for design purposes [86]. However, the quasi-TEM microstrip line circuit inherits three types of losses at higher frequencies: the radiation-, conductor-, and dielectric-loss, as illustrated in Figure 3-1 [87]. It is well known that radiation loss can be avoided by using SIW technology. Thus, it has been used in several mm-Wave analog beamforming networks [23], [49], [67], [68], [88], [89]. Furthermore, air-filled SIW reduces dielectric losses [90], [91]. Despite the waveguide merits, quasi-TEM transmission lines are still preferably considered for compact mm-Wave frontend devices [92]–[94]. Therefore, this technology needs to be facilitated with the packaging to perform at higher frequencies.

In the following sections, three packaging technologies are discussed, which have emerged recently to package the low-cost PCB technology to make it useful for the higher frequency circuit designs, *e.g.*, mm-Wave planar circuits.

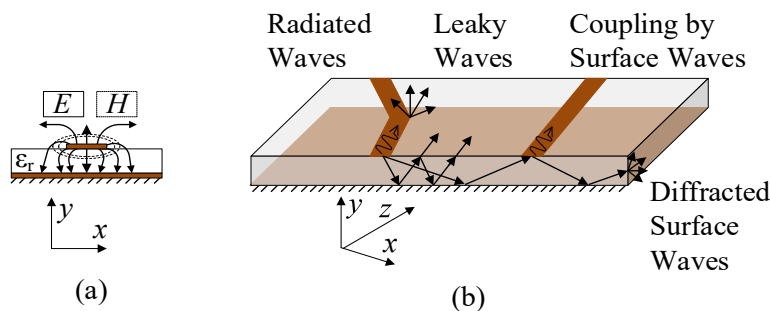


Figure 3-1. Microstrip circuit (a) Cross-sectional view and field distribution and (b) Three different kinds of waves in quasi-TEM structures

3.1 Substrate Integrated Suspended Lines (SISLs)

The concept of Substrate Integrated Suspended Lines (SISLs) has been introduced in [95]–[98] for the design of packaged microwave components by using multiple layers of PCB laminates. The cross-section view of the SISL along with quasi-TEM field distribution is shown in Figure 3-2 (a). By using the SISL technique, the design must consist of five PCB layers (Sub1 to Sub5) having metal on each side (M1 to M10), as shown in the exploded model view of Figure 3-2 (b). It requires

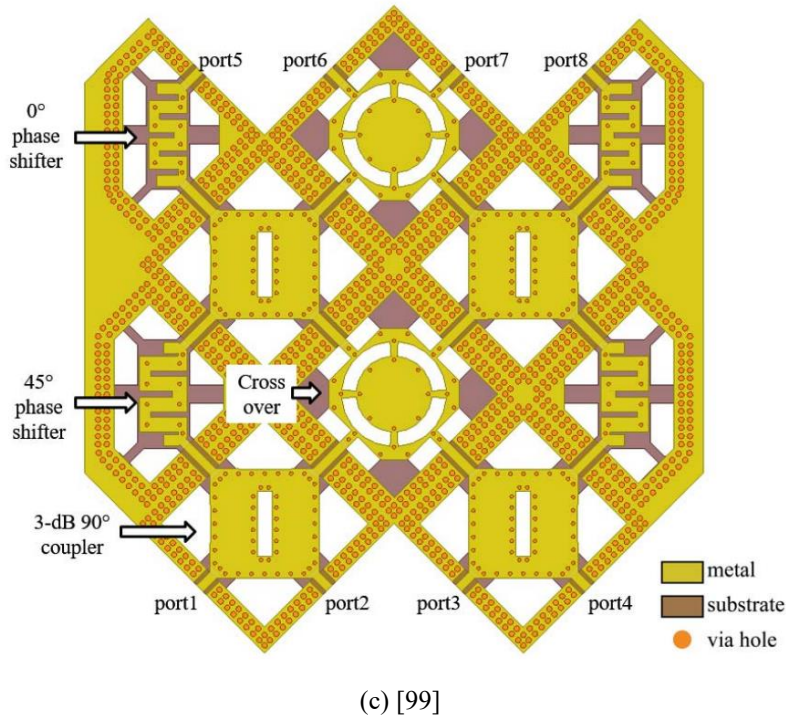
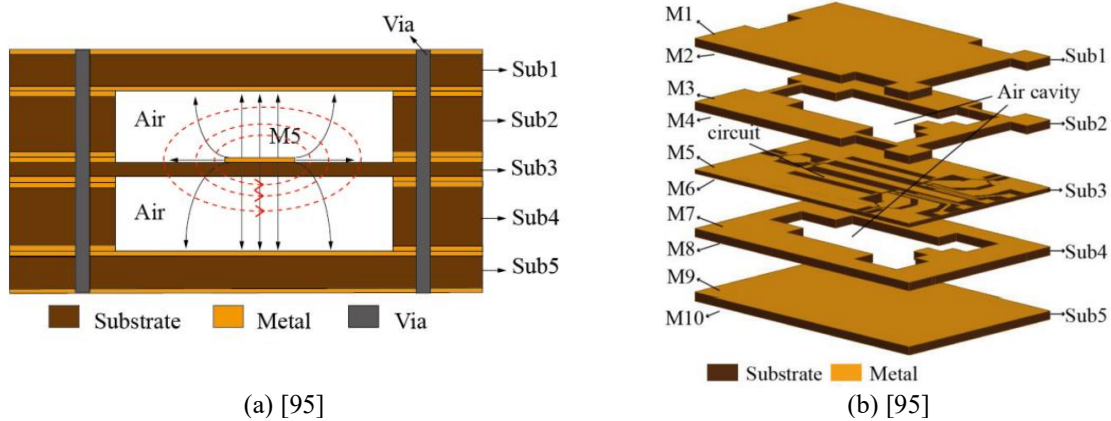


Figure 3-2. (a) SISL cross-section view, (b) Exploded model view of multi-layer SISL circuit assembly, and (c) 4 × 4 SISL Butler Matrix (only Sub3 layer is shown)

a large assembly of plated via holes connected to all the layers electrically. This self-packaging mechanism results in low loss transmission lines as the signal partially propagates in the air regions created by the packaging cavity. The technique is used to design a self-packaged self-shielded planar 4×4 Butler matrix, as shown in Figure 3-2 (c) [99].

As device shielding is typical, SISL could be a favorable planar circuit board technology due to its self-packaging mechanism. However, its circuit complexity is relatively high as a large number of substrate-integrated via holes are required to create housing for each component by using multiple substrate layers. Similarly, due to the spurious radiation at mm-Wave, shielding enclosures with complete perfect electric conductor (PEC) interior could support higher-order cavity modes within the circuit's operational bandwidth [100]. It is undesired that these cavity resonances be coupled to other neighboring circuit components on a device level. Besides, due to the compact geometry at mm-Wave, components are more close to each other physically, and the use of conventional cavity damping methods are not practical either [101].

3.2 Printed Ridge Gap Waveguide (PRGW)

Gap waveguide is another self-packaged emerging technology to facilitate the printed circuit designs [102], [103]. In this technique, a parallel plate waveguide – with PEC/PMC boundary conditions – is conceived with the extended upper PEC plate, and the lower one is a PEC ridge surrounded by a so-called PMC boundary. When the gap between the upper PEC boundary and the lower PEC/PMC boundary regions is less than the quarter of a wavelength ($\lambda/4$), the signal can propagate between PEC-PEC surfaces only, whereas it is suppressed out within the PEC-PMC bounded region. Thus, the fundamental concept of hard (go) and soft (stop) surfaces is utilized [104]. In a simplified way, a grid of PEC/PMC parallel strips covered with a PEC lid at height $\lambda/4$ could provide the hard and soft regions in which the metal groves with $\lambda/4$ depth represent the PMC strips. The wave propagates in the longitudinal direction along the PEC strips and attenuates rapidly transverse to the grid of strips, which represent hard and soft phenomena, respectively.

On a planar PCB, an artificial magnetic conductor (AMC) can be realized by a 2-D distribution of the electromagnetic bandgap (EBG) unit cells covered by a PEC plate at height $\lambda/4$ as shown in Figure 3-3 (a). The wave propagation region is the PEC ridge, which is electrically

connected with the PEC on the other side of the substrate through the via holes. The cross-section view illustrated in Figure 3-3 (a) shows the wave propagation region (Go) and the forbidden region (Stop). Recently, for higher frequency components and devices, this technology has been widely adopted since a compact size AMC could be designed at mmWave and higher frequency bands [91], [105]. A 4×4 Butler matrix is designed at 30 GHz by using printed ridge gap waveguide (PRGW) technology, as shown in Figure 3-3 (b) [56].

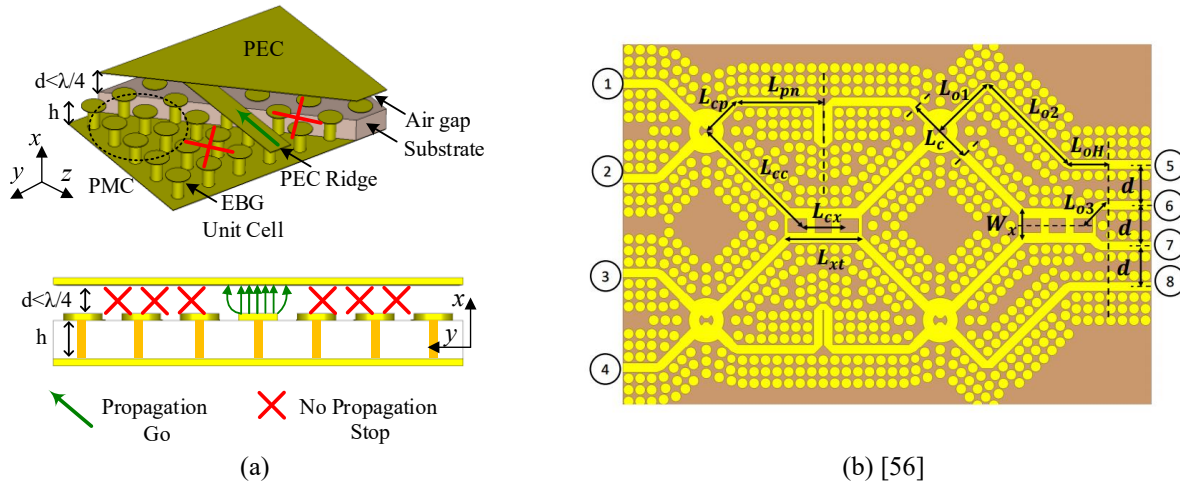


Figure 3-3. (a) Printed ridge gap waveguide and (b) 4×4 Butler Matrix

3.3 Perfect Magnetic Conductor (PMC) Packaged Microstrip Lines

The PMC packaging of the microstrip line circuit is similar to the printed ridge gap waveguide concept. However, the microstrip line guiding networks of certain devices, such as beamforming networks, are complex structures that consist of several components with bends and discontinuities. With the aforementioned techniques, beamforming components and devices are constructed in a mainly empirical way, depending on the experience of the designer. A simple analytical procedure could be followed to design a PMC packaged beamforming network. In such a case, the PMC textured surface can be elevated from the level of metallic strips to a higher level while considering the microstrip line ground-layer as a PEC cover. Rather than naming it inverted microstrip line [106], it is called a packaged microstrip line [107] because the signal still propagates within the microstrip line on a substrate. It has been demonstrated that the high impedance property of a textured surface can still be preserved by deploying PMC on a separate

layer. This trait could be exploited to design complex microstrip line designs on a separate layer without making a ground connection for the microstrip line traces (as in the case of PRGW) in the presence of the PMC covering layer. Thus, the EBG surface and the planar microstrip circuit's ground layer forming a parallel plate waveguide having a specific cut-off. Only the regions with microstrip line trace experience PEC-PEC path with the ground layer and PMC-PEC cavities elsewhere. This packaged environment reduces microstrip line radiation losses and suppresses the higher-order modes within a cavity, which consists of a substrate and an air gap.

PMC packaging is an effective technique [102], [108]–[110]. At mm-Wave frequencies, a compact size AMC texture-lid can be realized by miniaturizing the EBG unit cell. In [110], [111], such a lid of nails is used over a microstrip transmission line to improve the insertion loss and suppress the packing cavity modes within the operating bandwidth, as shown in Figure 3-4 (a). Later on, it has been successfully used in several mm-Wave printed circuit components [107], [112]–[114]. As the miniaturized EBG unit cells comparable to the microstrip line's width can be

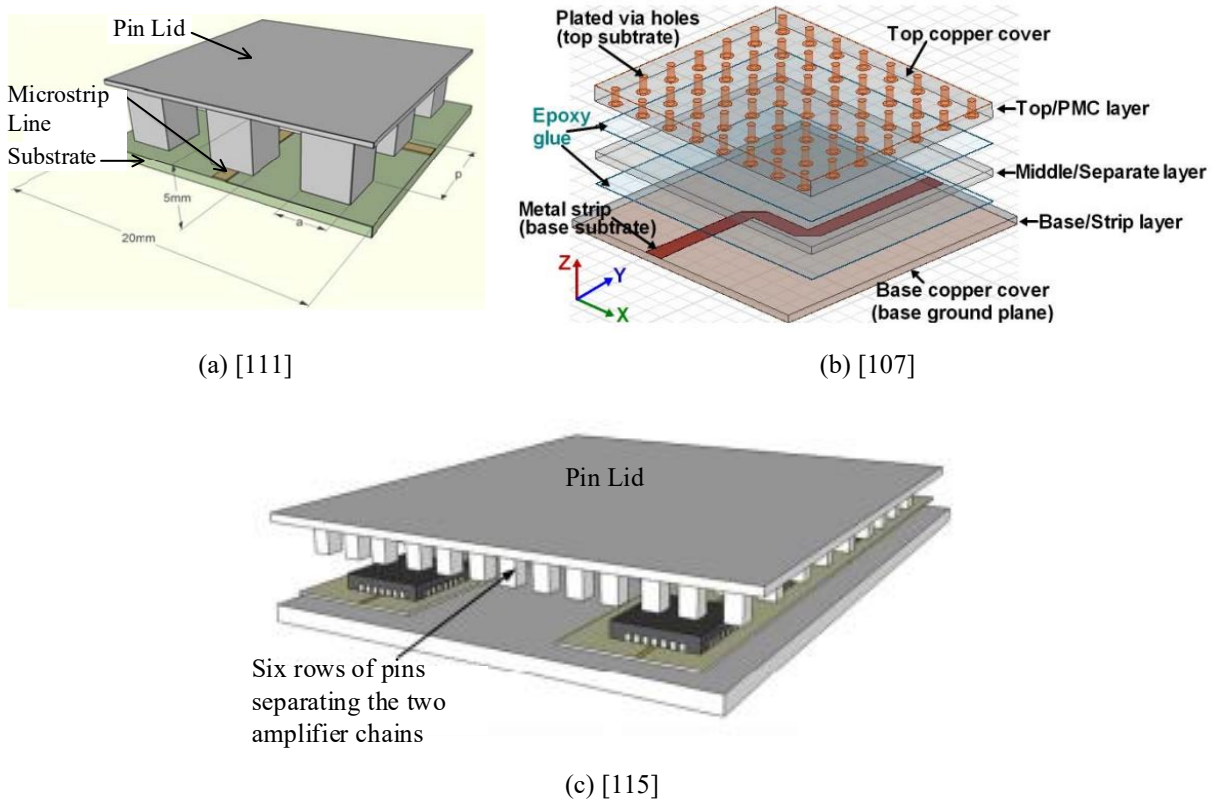


Figure 3-4. (a) Microstrip circuit design including PMC packaging, (b) AMC realization on printed circuit board, and (c) Isolation improvement among microwave components by using PMC packaging

designed at higher frequency bands, therefore, it is found more attractive for cm-/mm-Wave applications, as shown in Figure 3-4 (b). It is demonstrated that the isolation among various components significantly improves the overall circuit's performance [115]. Furthermore, this mechanism eliminates the need for separate compartments for each component/module. Only one pin lid could cover the whole circuit, which needs to be packaged, as shown in Figure 3-4 (c).

3.3.1 Principles of Microstrip Line PMC Packaging

The notion of the following analysis is to formulate and compare the cavity mode resonances in the case of (a) PEC and (b) PMC covering lid at the top of a planar microstrip line circuit; and, to analyze the influence of packaging lids over the characteristic impedance of the line [111]. The XZ cross-section views of the packaged microstrip line circuit are shown in Figure 3-5 (a, b). A PCB circuit is sandwiched between the PMC boundaries along the x-axis. The thickness of the packaged laminate is denoted as “t” with a gap “h-t” having a relative permittivity ϵ_1 and ϵ_2 , respectively, where “h” is the total height from the microstrip line ground to the top cover. The PEC or PMC boundary conditions can be achieved at “h” by placing a packaging lid at the top.

The PMC boundary beneath the PCB ground is omitted to simplify the analysis. Thus, a perspective view of a grounded cavity with a PEC or PMC boundary at the top is shown in Figure 3-5 (c). This forms an inhomogeneous cavity with two regions along the x-axis, having base dimensions of $a \times b$ (mm^2). Three boundaries can be defined along the x-axis (at $x = -t$, $x = 0$, and $x = h - t$). The wave propagation is considered in the direction of the z-axis with $e^{-j\beta z}$ propagation factor and no variation along the y-axis ($\partial/\partial y = 0$) [116].

Cavity resonances may support TE_z and/or TM_z modes. The fields' general solutions are expressed in (3-1) for the two regions. By applying boundary conditions, the transcendental equations for PEC and PMC at “ $x = h - t$ ” are derived in (3-2) and (3-3), where k_{x1} and k_{x2} are the propagation constants in medium-1 and -2, respectively. By considering a homogeneous cavity, (3-4) can be simplified for k_x as given in (3-5) to express the closed forms. Thus, for the PEC and PMC packaging at “ $x = h - t$,” the resonance frequencies are expressed in (3-6) and (3-7), respectively. The lowest cavity mode ($l = 0$, $m = n = 1$) is calculated (for $\epsilon_r = 1, 2$, and 3) with the cavity height “ $h=1$ mm ($h-t \approx 3 \times t$)”. The resonances with PMC-lid are occurring at far higher

frequencies than the PEC-lid, as shown in Table 3-1. It is worth mentioning that for “ $l = 0$ ”, the height of the cavity is playing its role only in the case of PMC packaging. The explicit values given in Table 3-1 are the approximations close to the numerical ones, as very thin substrate ($t = 0.254$ mm) and packaging gap ($h - t = 0.75$ mm) are considered. Thus, the closed forms may provide a reliable approximation.

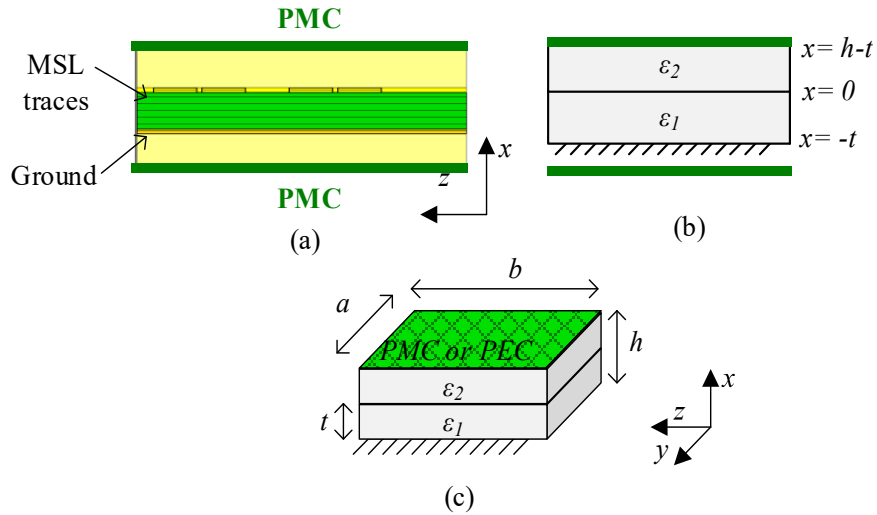


Figure 3-5. (a) XZ cross-section view of a PMC-PMC bounded region with microstrip line circuit in the middle, (b) Boundaries along x-axis for a cavity, and (c) Simplified cavity model covered with a PEC or PMC at the top

The eigenmodes correspond to all the possible field distributions within a structure. The Eigenmode solver of CST-MWS can be used to approximate these distributions. Some or all eigenmodes are excited when a nonzero projection exists between the incident fields on a field distribution associated with the eigenmodes. Therefore, in a planar design with the quasi-TEM propagation, the spurious radiation may trigger the TE/TM modes inside the packaging environment. It is essential to perform the eigenmode investigation of an EBG unit cell used to design an AMC lid in a full-wave environment to get bandgap characteristics. In Figure 3-6, a full-height-pin (EBG unit cell) and its design parameters are shown, which is used to form an AMC textured surface (pin lid) for PMC packaging. The first three modes extracted from the Eigenmode analysis are plotted in Figure 3-6 in which a bandgap of 20 GHz (22 ~ 42 GHz) is obtained.

$$e_{z1}(x, y) = A \sin k_{x1} x + B \cos k_{x1} x \quad (3-1)$$

$$e_{z2}(x, y) = C \sin k_{x2} x + D \cos k_{x2} x$$

$$\frac{k_{x1}}{\varepsilon_1} \tan k_{x1} t = -\frac{k_{x2}}{\varepsilon_2} \tan k_{x2} (h - t) \quad (3-2)$$

$$\frac{k_{x1}}{\varepsilon_1} \tan k_{x1} t = \frac{k_{x2}}{\varepsilon_2} \cot k_{x2} (h - t) \quad (3-3)$$

$$k_{x1}^2 = \left[\omega^2 \varepsilon_1 \mu - \left(\frac{n\pi}{a} \right)^2 - \left(\frac{m\pi}{b} \right)^2 \right] \quad (3-4)$$

$$k_{x2}^2 = \left[\omega^2 \varepsilon_2 \mu - \left(\frac{n\pi}{a} \right)^2 - \left(\frac{m\pi}{b} \right)^2 \right]$$

$$k_x^2 = \left[\omega^2 \varepsilon_r \mu_r - \left(\frac{n\pi}{a} \right)^2 - \left(\frac{m\pi}{b} \right)^2 \right] \quad (3-5)$$

$$f_{mnl}^{PEC} = \frac{c}{2\pi\sqrt{\varepsilon_r\mu_r}} \sqrt{\left[\left(\frac{n\pi}{a} \right)^2 + \left(\frac{m\pi}{b} \right)^2 + \left(\frac{l\pi}{h} \right)^2 \right]} \quad (3-6)$$

$$f_{mnl}^{PMC} = \frac{c}{2\pi\sqrt{\varepsilon_r\mu_r}} \sqrt{\left[\left(\frac{n\pi}{a} \right)^2 + \left(\frac{m\pi}{b} \right)^2 + \left(\frac{(2l+1)\pi}{2h} \right)^2 \right]} \quad (3-7)$$

where $l = 0, 1, 2 \dots; m = 1, 2 \dots; n = 1, 2 \dots$

Table 3-1 Cavity resonances with PEC/PMC packaging lids

Cavity base $a \times b$ (mm ²)	Dielectric constant (ε_r)	$h = 1 \text{ mm}$	
		PEC lid f_{110}^{PEC} (GHz)	PMC lid f_{110}^{PMC} (GHz)
23×45	1	7.33	75.36
	2	5.18	53.29
	3	4.23	43.51

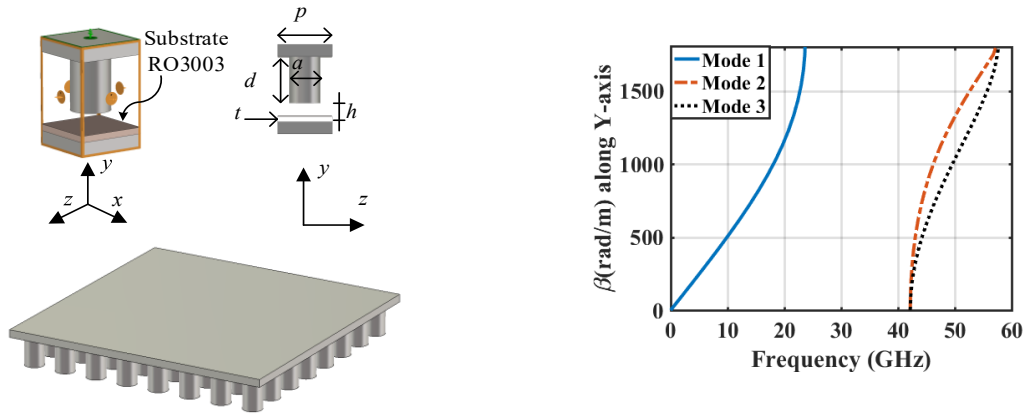


Figure 3-6. Full-height-pin EBG unit cell design parameters (in mm), and its dispersion diagram. (Parameters $t = 0.254$, $h = 1$, $a = 1.5$, $d = 2.25$, and $p = 2.6$)

In Figure 3-7 (a), a microstrip line with 90° double-bend is packaged with the PEC and AMC lids at height “ $h = 1 \text{ mm}$ ($h - t \approx 3 \times t$)” to perform a full-wave analysis. With PEC packaging,

the E-field distribution shows that packaging cavity modes exist, as shown in Figure 3-7 (b). Whereas, with the AMC lid made of pins, no cavity modes exist within a frequency span (27 ~ 40 GHz), as shown in Figure 3-8 for a few frequency points. This full-wave analysis is in concordance with the closed-form approximation of Table 3-1 for the case of $\epsilon_r = 2 \sim 3$.

The characteristic impedance of the microstrip line trace increases as the PMC is closer to the line because line impedance is inversely proportional to the effective width. The closer the packaging pin lid, the smaller the effective width as the *E*-fields becomes more confined. In Figure 3-9 (a), this effect is plotted for different values of “*h - t*.” In Figure 3-9 (b), it can be seen that the characteristics impedance is nearly the same as for the bare microstrip line with the gap of “*h - t = 3 × t*” and higher [111].

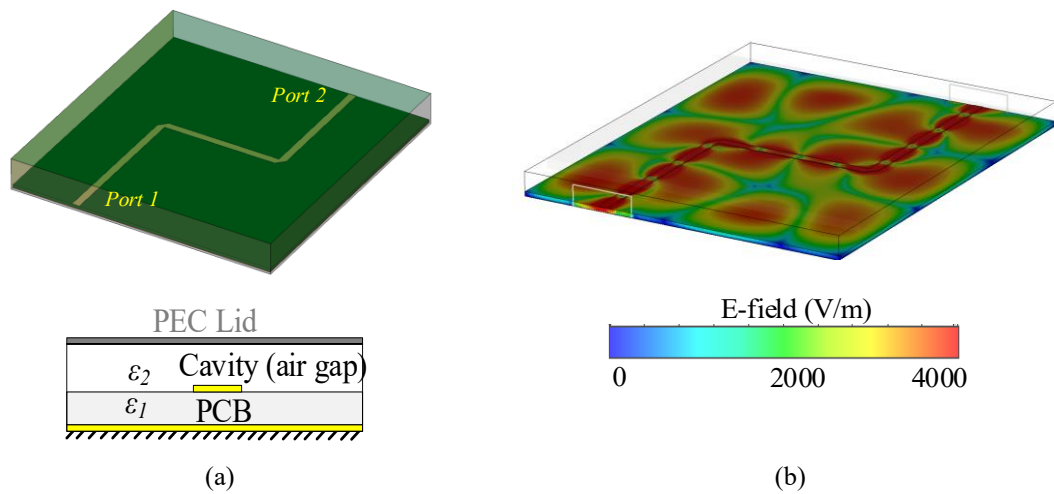


Figure 3-7. (a) PEC packaging at height $h = 1$ mm ($h - t \approx 3 \times t$) and (b) Absolute E-fields distribution at 30 GHz

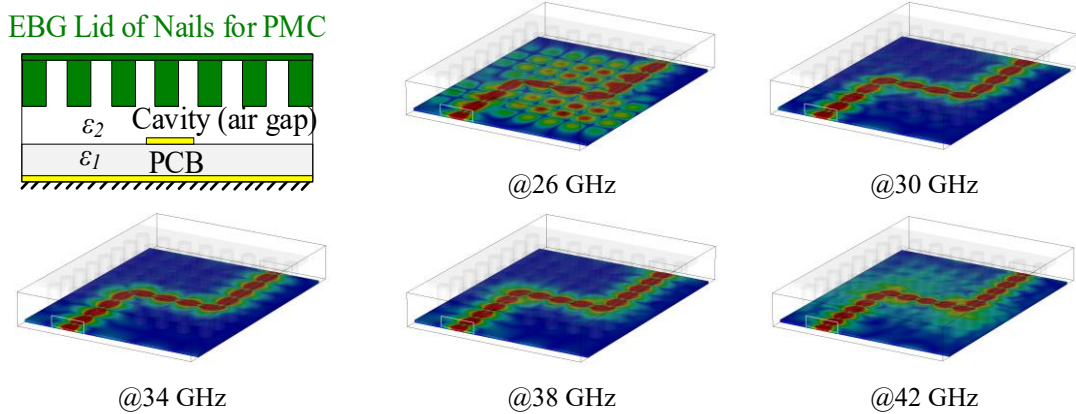


Figure 3-8. PMC packaging using EBG lid of nails at height $h = 1$ mm ($h - t \approx 3t$) and absolute E-fields distribution at five frequency points

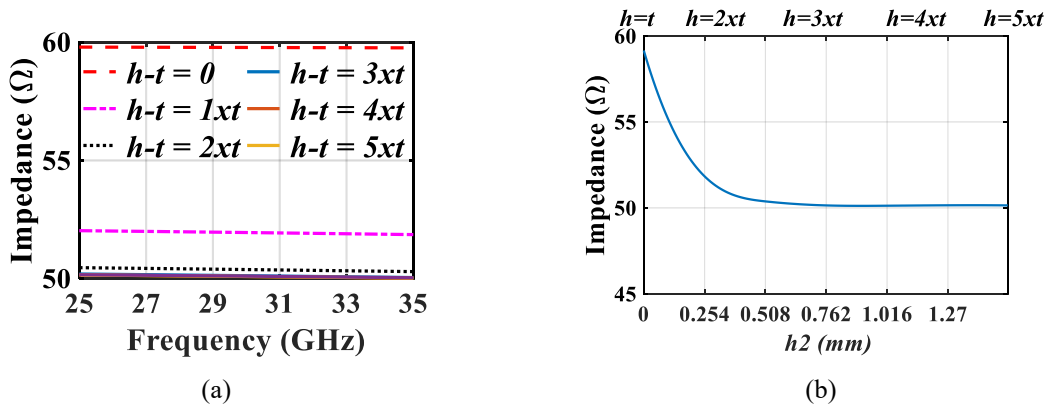


Figure 3-9. Effect of PMC packaging over the line impedance of microstrip line circuit with different packaging gaps $h - t$. (a) across frequency and (b) at 30 GHz

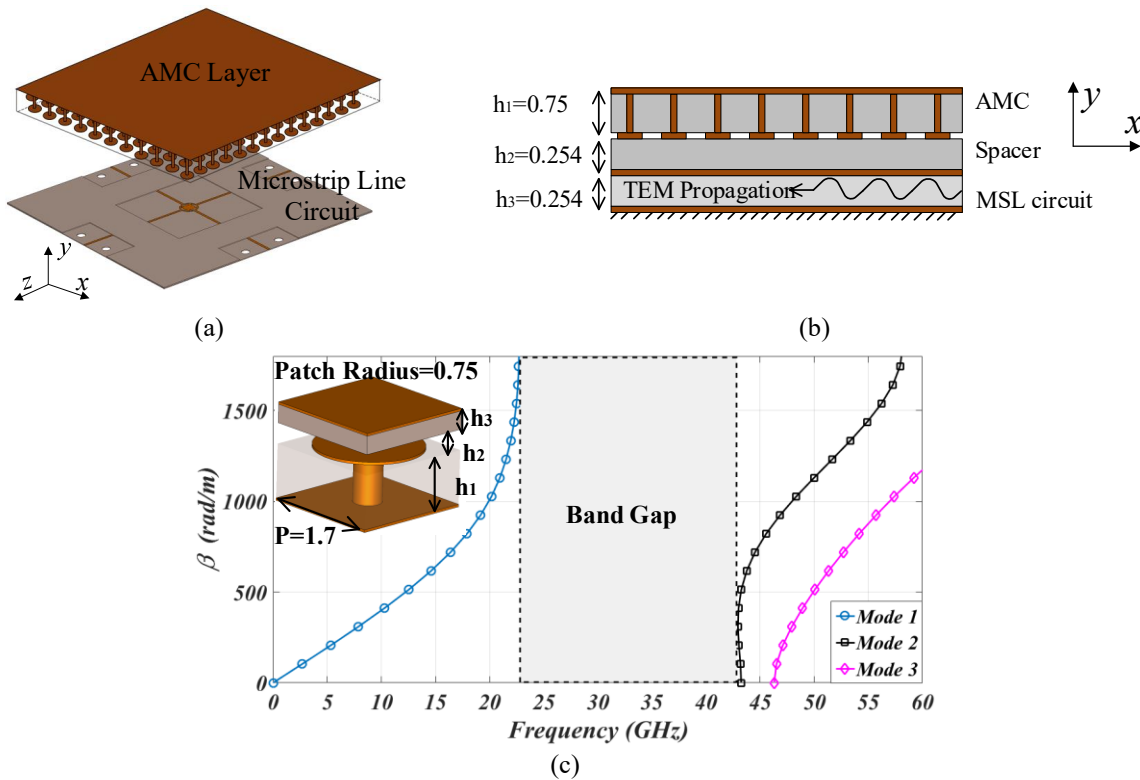


Figure 3-10. (a) Exploded model view of a three-layered AMC packaged structures (RO3003 substrates), (b) Cross-section view, and (c) EBG unit cell design parameters (units in mm), and dispersion diagram

The PMC lid can be realized on a printed circuit board as well. Figure 3-10 shows that, the EBG mushrooms are designed on separate layers [107], [113]. As mentioned earlier, this approach provides design flexibility while having the merits of gap waveguide (in ridge gap waveguide, a

ridge is electrically short-circuited with the ground by metalized via holes, which may disturb the current distribution of the propagating signal on the narrow-width ridge). By designing a separate AMC layer for packaging, the microstrip line design traces' position can be easily adjusted/optimized, and there is no electrical contact between the ridgeline and the PEC on the other side of the substrate. Thus, the PMC packaging technique could be more favorable for designing the large-scale analog beamforming networks as compared to the PRGW design rules.

3.3.1.1 Design Examples

A PMC packaged crossover and a hybrid coupler are presented as design examples. The components are designed on a single surface and packaged to minimize radiation losses. As these microwave components are used within an analog beamforming network; therefore, the use of the PMC packaging technique results in designing ease as well as a performance enhancement [113]. In Figure 3-11, the top layer consists of 2-D distributions of EBG mushroom-like unit cells in which 0.75 mm thick RO3003 substrate ($\epsilon_r=3$, $\tan\delta=0.001$) with a copper cladding of 17 μm . The

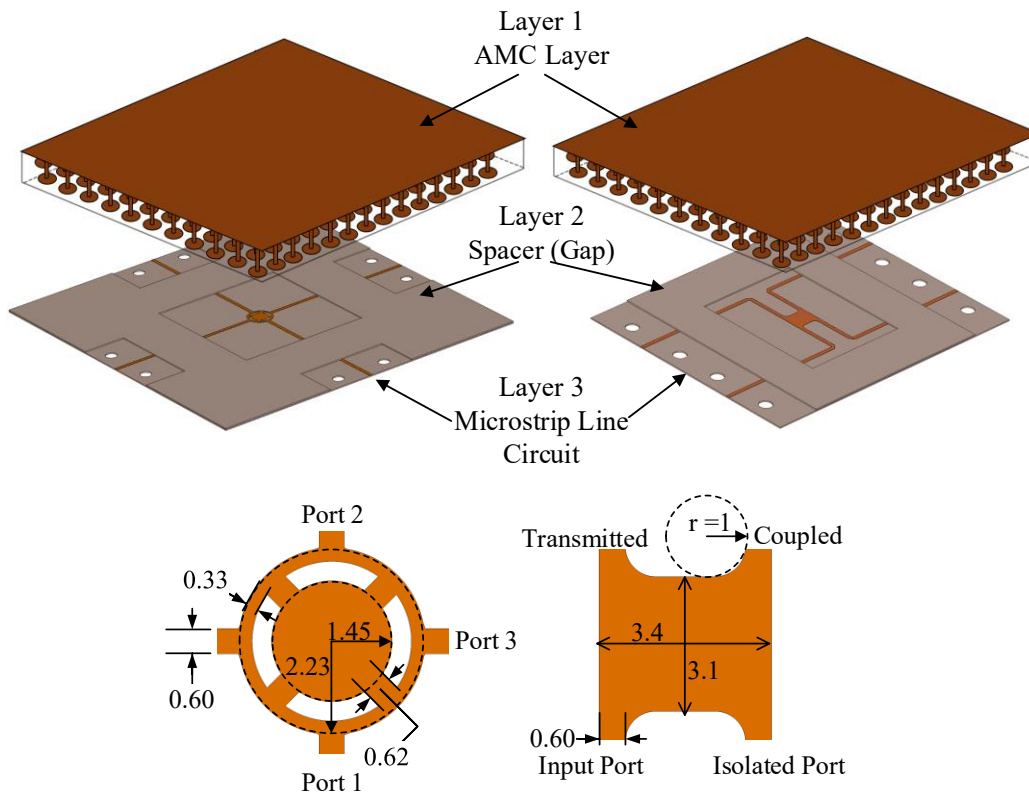


Figure 3-11. Exploded model view and design parameters of crossover and coupler (units in mm)

mushroom patch diameter and the metalized via are chosen to have an aspect ratio of 1.875 (1:1.875). The period of EBG cells is 1.7 mm. The components are designed on layer 3 (RO3003), having a thickness of 0.254 mm. Layer 2 is a spacer (RO3003) between the AMC and microstrip line circuit. The crossover and hybrid coupler prototypes and S-parameters measurement setup are shown in Figure 3-12.

The measured and simulated S-parameters for the crossover and hybrid coupler are shown in Figure 3-13 (a, b), respectively. The crossover reflection coefficient (S_{11}) is less than -10 dB from 25 to 35 GHz, with a center frequency of 30 GHz (30% fractional bandwidth). The insertion loss (S_{21}) is 0.5 dB with a variation of ± 0.15 dB across the frequency range. The isolated ports have shown transmission coefficient levels (S_{31} , S_{41}) less than -15 dB. It is to be noted that due to the symmetry of the structure, only port#1 excitation results are included. The hybrid coupler S-parameters magnitude and the phase difference between transmitted and coupled ports are shown in Figure 3-13 (b). The same impedance bandwidth (S_{11}) of 30% is achieved for the hybrid coupler as well. The input power is divided into transmitted (S_{21}) and coupled ports (S_{31}) by 3.5 dB with the variation of ± 0.25 dB as a magnitude imbalance over the frequency band. The isolated port

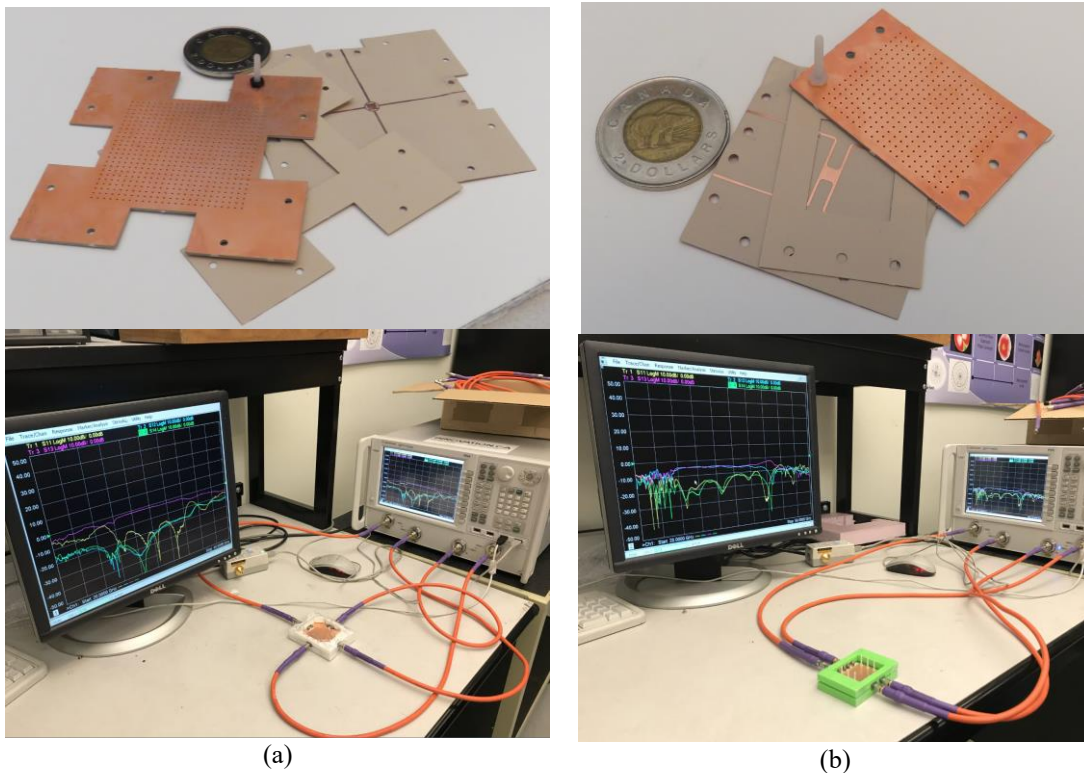


Figure 3-12. Prototypes and measurement setup: (a) Crossover and (b) Hybrid Coupler

shows the S_{41} level of less than -15 dB. The output (transmitted/coupled) ports phase difference ($\angle S_{31} - \angle S_{21}$) is 90° with $\pm 3^\circ$ variation. The measured and simulated results are in good agreement. However, measured results show some fluctuations at the start and end of the frequency band.

The component's performance is compared with AMC and without AMC packaging to quantify the packaging effect. The transmission is improved by more than 28 %, with AMC packaging at the crossover's center frequency. Similarly, in the 90° hybrid coupler case, the packaging enhanced the transmission and coupling by more than 14 % and 8 %, respectively, as shown in Figure 3-13 (c) simulated results.

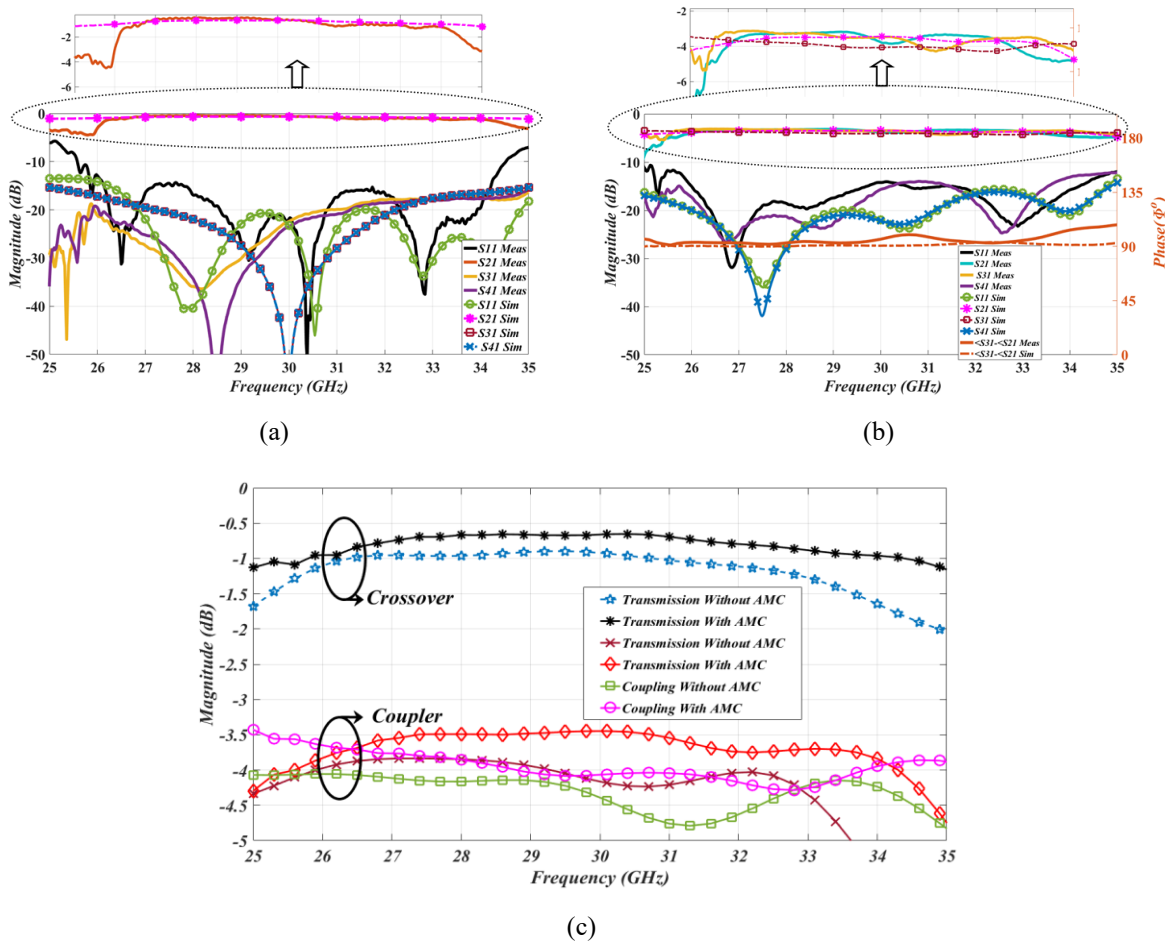


Figure 3-13. S-parameters (measured/simulated): (a) Crossover, (b) Hybrid Coupler, and (c) Performance comparison with/without AMC

3.4 Summary

In this chapter, the literature review of state-of-the-art microstrip line packaging techniques has been presented. Microstrip line circuits have been facilitated with these packaging techniques to use it effectively at cm-/mm-Wave frequency bands. To achieve design simplicity along with performance enhancement of microstrip line circuits, a PMC packaging technique is preferred. The principles of PMC packaging have been presented along with design examples. In the next chapters, these principles are used in designing signal routing networks of multibeam subarray antennas.

Chapter 4

Fixed-Beam and Switched-Beam Subarray Antenna Designs

4.1 Fixed-Beam Dual-Polarized Subarray Antenna

MIMO-enabled transceivers require multi-stream transmissions. For this purpose, high gain fixed-beam antennas could be designed as a multibeam frontend. Furthermore, the antenna polarization property can be exploited to enhance the channel capacity. For the sake of device compactness and efficient RF signal routing, a tile-based (planar multi-layer stacked) RF frontend is preferred. In such architecture, the radiating panel (dual-polarized antenna array) is integrated at the top, and the signal is routed down to the RF circuitry, which is stacked beneath the antenna array for MIMO RF precoding, as shown in Figure 4-1. In [35], it is shown that a fixed-beam 2×2 subarray is the

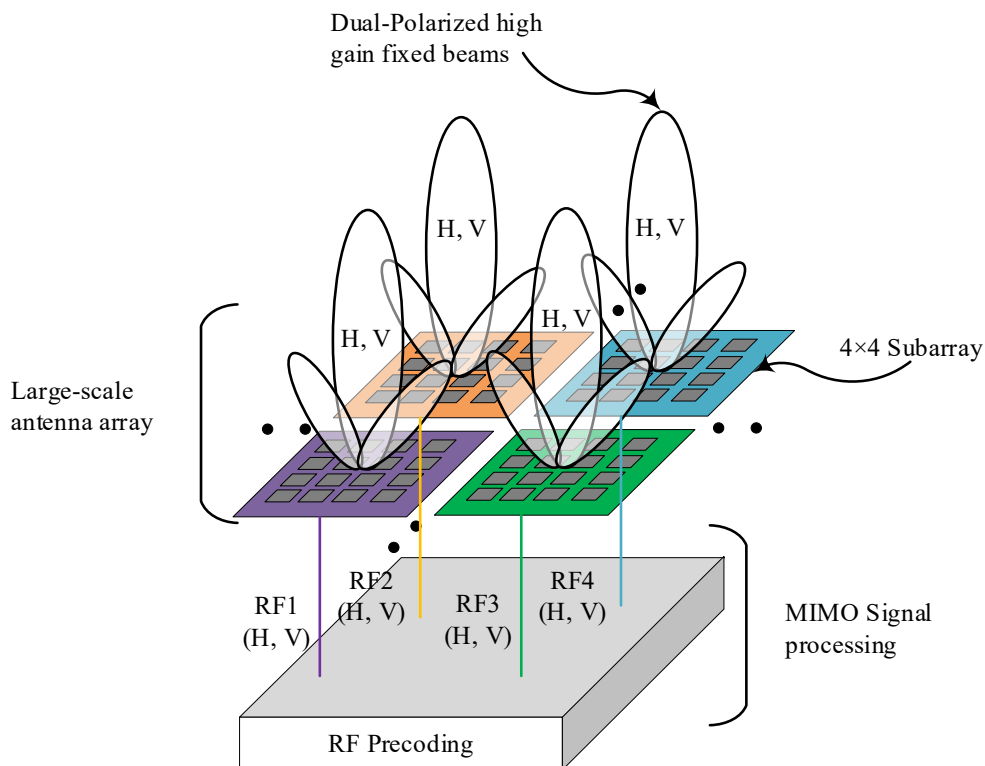


Figure 4-1. Fixed-beam dual-polarized antenna subarray within large-scale antenna frontend

building block of the large-scale $N \times M = 8 \times 8$ antenna frontend. MIMO precoding could be performed over the RF chains of horizontal (H) and vertical (V) polarization from each subarray.

4.1.1 Design Challenges

Efficient SRN is one of the vital design concerns of mm-Wave circuits. It becomes more challenging for an array with a single element of shared single-cross-slot-aperture (SCSA) that is highly preferred for the compact dual-polarized applications. Various cross-coupling (isolation) mechanisms between the orthogonal polarizations are discussed [117]. High isolation could be achieved either by placing the radiating apertures separately (cross-coupling reduction) and/or by deploying the SRN at different layers for each polarization (port-coupling reduction). In arrays, the former case may produce orthogonal patterns with different phase centers, and it could increase the size of the radiating part [118]. Similarly, for the latter scenario, more than one layer of feed-network is required [119].

The SCSA technique has been widely used for dual-polarized applications at lower frequency bands [120]–[124]. For mm-Wave, a PCB-based ME dipole antenna is a promising SCSA candidate that could provide symmetric radiation [76], [125]. The antenna with a unidirectional radiation pattern could be realized by combining the electric and magnetic dipoles [42], [126]. The properties of a dipole antenna and a slot could be combined to achieve a unidirectional symmetrical radiation pattern. Such complementary designs are capable of achieving wide bandwidth, low cross-polarization, and stable radiation pattern over the wide operational bandwidth. Thus, making this antenna class well-suited for mm-Wave base stations/access points [48]. As reported in [76], high-isolation can be achieved for dual-polarization by exciting the ME-dipole with orthogonal slots engraved within the SIW layers. Microstrip line technology can keep SRN footprints compact as compared to the SIW. However, it needs to be packaged at mm-Wave [107], [110], [113]. The microstrip line SRN could be backed by the AMC. This should not be confused with the concept of AMC as a reflector beneath the radiating elements, as presented in [127]. Recently, this technique has been effectively used for several mm-Wave antenna designs. For instance, the single-polarized ME-dipole antenna elements are reported with low back-radiation and having the capability to tune the reflection properties [128]–[130]. Similarly, packaged microstrip line corporate-feed is used to excite the linear arrays

[131], [132], a planar 4×4 ME-dipole array [133], a 4×4 dual-mode horn array [134], and 8×8 slot arrays [135], [136], for high-gain applications with a single polarization.

4.1.2 Proposed Subarray Implementation

For dual-polarization, a dual-channel corporate-feed SRN is presented to excite the dual-polarized ME-dipole array of any order $2^n \times 2^m$, where n and m are integer numbers larger than 1. First, a single-layer microstrip line feed mechanism is exploited to design a wideband dual-polarized antenna element having tunable port-to-port coupling. Hook-shaped and fork-shaped packaged microstrip line feeds are designed to excite the shared SCSA ME-dipole antenna. Second, this single element – having cross-polarization (x-pol) < -25 dB within the main beam view-range of 30° is used to build a 4×4 array. With these antenna properties, a dual-channel AMC-packaged SRN is also designed on a single-surface with port-to-port coupling > 30 dB; thus, the overall dual-polarized array is maintaining a bandwidth of 16.7% at 30 GHz with a maximum gain of 19.3 dBi and measured x-pol < -20 dB within the main beam view-range of 30° of beamwidth. The proposed topology could be scaled to any order of $2^n \times 2^m$, provided that the PCB losses within the acceptable range for the intended application [137], [138].

4.1.2.1 Antenna Element Design and Performance Analysis

The proposed SCSA-coupled dual-polarized ME-dipole antenna configuration is illustrated in Figure 4-2, which consists of four layers. The $\lambda_g/2$ dipole is implemented on Layer # 1 RT5880 ($\epsilon_r = 2.2$, $\tan\delta = 0.0009$) with thickness $h_1 = 1.524$ mm. Thick laminate, $h_1 \approx \lambda_g/4$, with low permittivity, is used to have a low Q-factor for the radiator. The SCSA is engraved in the ground plane of Layer # 2 RO3003 ($\epsilon_r = 3$, $\tan \delta = 0.001$). The microstrip feedlines are designed within the packaged environment and printed on the bottom side of Layer # 2 for H/V-polarizations. The metallic cylinders, shown in Figure 4-2 (c) connecting the dipole patches to the ground, act as vertical walls to couple fields to the dipole via SCSA. The dipole is divided into four patches having an electrical connection in the middle to achieve optimum matching. Thus, for each polarization, it forms a $\lambda_g/2$ electric dipole and two $\lambda_g/4$ magnetic dipoles. For V/H-polarization, the antenna is excited through Port # 1 (hook-shaped microstrip feedline) and Port # 2, respectively. Port#2-feed consists of a fork-divider that excites the slot symmetrically and reduces

the coupling with the single stub of Port#1. The physical lengths of the fork-feed stubs are shortened by mitering the 90° -bent corners, and the stubs are extended in opposite directions to

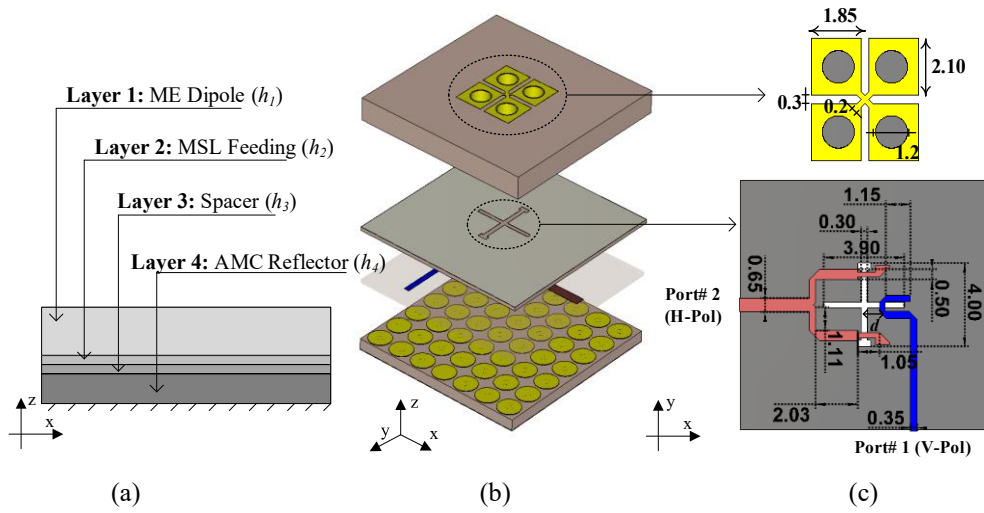


Figure 4-2. (a) Stacked structure of four layers, (b) Multilayer exploded model view, and (c) ME-dipole aperture's front and back view of SCSA along with feedlines

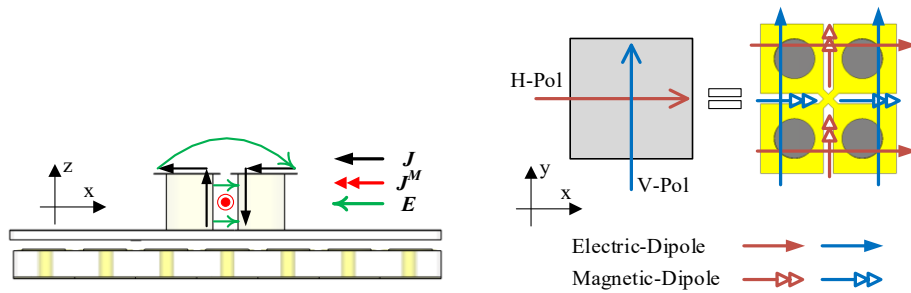


Figure 4-3. Current/field vectors' presentation, and H/V-polarization identification

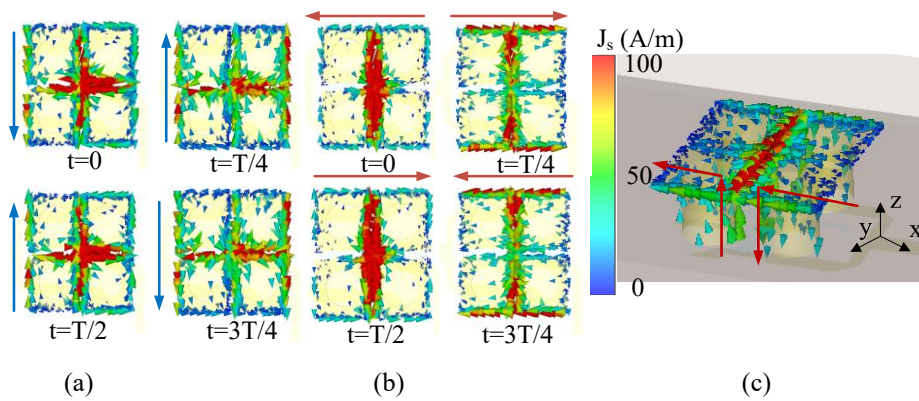


Figure 4-4. Surface current distributions: (a) Port#1 excitation, (b) Port#2 excitation, and (c). Perspective view for Port#2 excitation

minimize coupling. Stepped-slot sections are added on both sides of the slot to form a dog bone slot shape. This is to improve S_{22} impedance matching and to tune the resonance dip at the center frequency. Port # 1-feed is displaced by a factor of “d” from the center of the SCSA, as shown in Figure 4-2 (c). This is to achieve better isolation by suppressing the possible induced voltages from the H-polarized excitation.

In Figure 4-3, the formation of electric/magnetic dipoles and the electric current (J), magnetic current (J^M), and the electric field vectors (E) are illustrated. In Figure 4-4, the surface electric current distributions are shown for a period (T) of the excitation signal at 30 GHz. The dimensions and placements of the metallic cylinders (via holes) are very critical. The primary purpose of the current distribution for port#1 and port # 2 orthogonal excitations is that for a complete period, the orientation of the current vectors remains linear, *i.e.*, it does not form a curl. This guarantees the antenna orthogonal polarizations’ linearity. The absolute surface current distributions are shown in Figure 4-5. As the fields are time-varying with a period $t = T/2$. Therefore, the absolute surface electric current distributions (J) are shown for $t=0$ and $t=T/4$ for port#1 and port#2 excitations. At $t=0$, the surface current mainly gathers on the inner sides of the

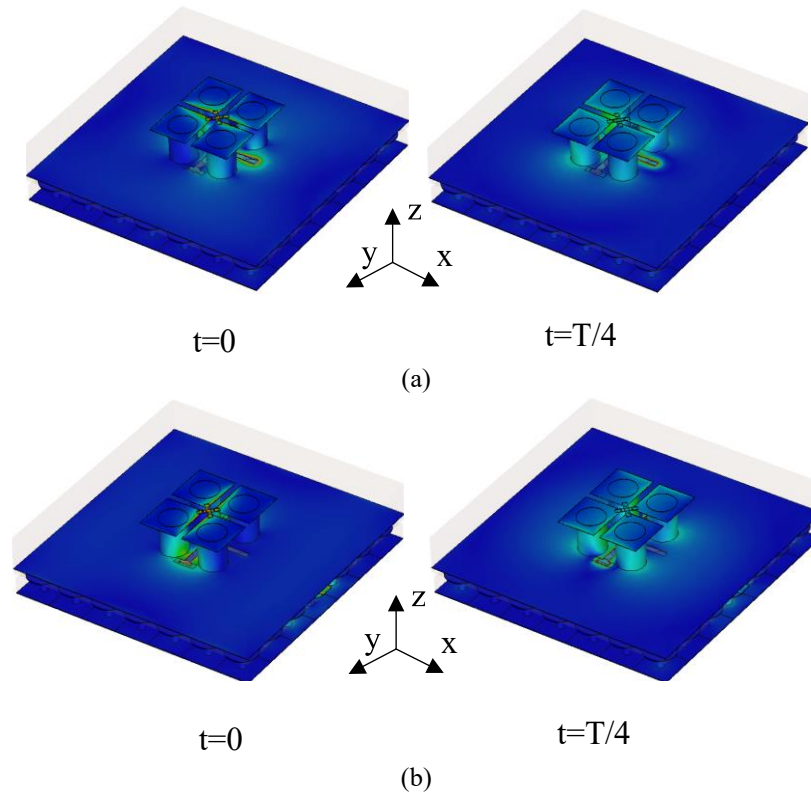


Figure 4-5. Absolute surface current distribution at $t=0$ and $t=T/4$ for (a) Port #1 and (b) Port#2

metallic cylinders for both excitations. This means that J^M (magnetic dipole) is excited. Similarly, at $t=T/4$, the surface current is distributed all over the dipole that satisfies the electric dipole functionally.

The S-parameters and gain values are shown in Figure 4-6. All material losses are considered within the simulation environment. S_{22} is a result of a single resonance behavior as the ME-dipole structure is excited uniformly through Port#2. Whereas, for S_{11} , more than one resonance may appear within the structure. This is because of Port#1 feed mechanism. The parameter “d” variation of Port#1 excitation affects the antenna resonance. An asymmetric aperture illumination – due to the offset feed – changes the effective antenna length/aperture of the vertical ME-dipole, as shown in the magnitude of electric fields distribution as a source, in Figure 4-7.

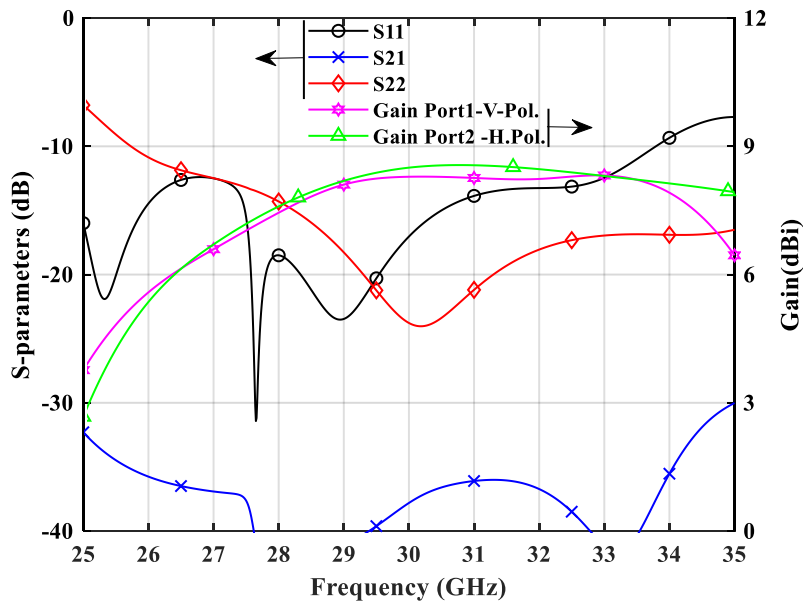


Figure 4-6. Antenna element S-parameters and gain

In Figure 4-8, the effect of parameter “d” on S_{11} and S_{21} is presented, which is a critical design parameter to achieve a proper level of port isolation. First, for all the parametric values, S_{11} is under -10 dB. It is to be noted that with a minimum value of $d = 0.25$ mm, a resonance around 32.5 GHz is prominent that shifts to a lower frequency of 29 GHz with $d = 0.75$ mm. Second, the isolation, S_{21} , is found to be -22 dB with $d = 0.25$ mm $\approx 0.04\lambda_g$ (where λ_g is the guided wavelength

in Layer # 3), which improves by a factor of about 5 dB with every increment of $d \approx 0.02\lambda_g$. Optimum results are achieved with $d = 0.75 \text{ mm} \approx 0.11 \times \lambda_g$. The antenna bandwidth is 20% at 30 GHz (28~34 GHz) by defining the performance parameters as $S_{11}, S_{22} < -10 \text{ dB}$, ports' isolation $> 35 \text{ dB}$.

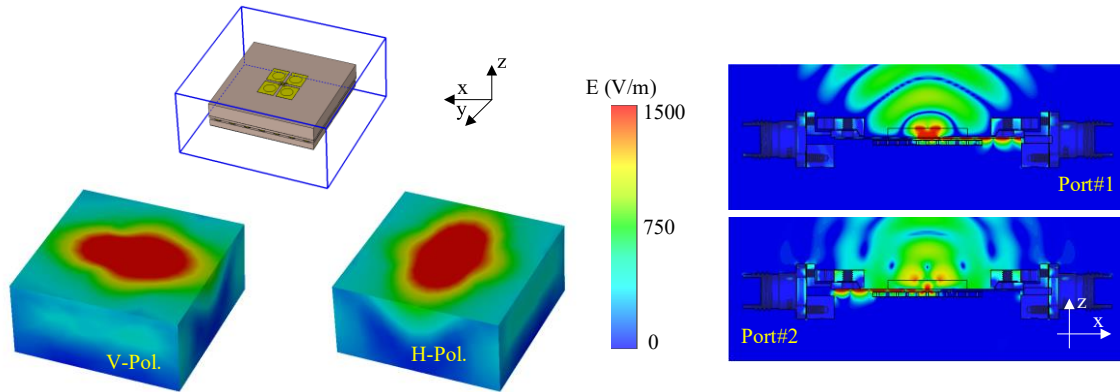


Figure 4-7. (a) Electric field-source over the boundary box around the antenna for V- and H-polarization and (b) Cross-section view of electric fields along with the end-launch connectors

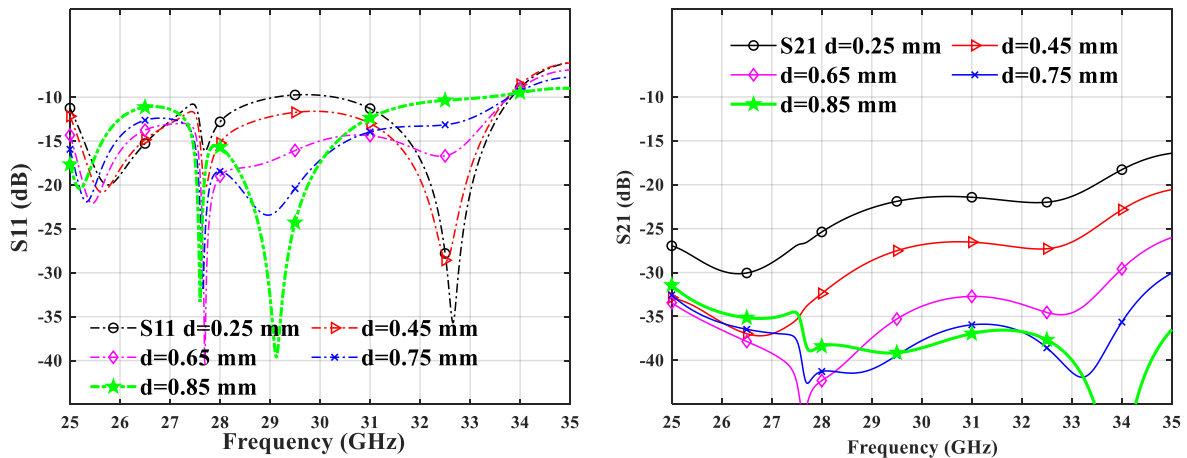


Figure 4-8. Impact of offset parameter “d” on port-to-port coupling (S_{21}) and Port 1 reflection coefficient (S_{11}). Port 2 reflection coefficient (S_{22}) is not plotted as it remains unaffected by this parametric variation

The normalized radiation patterns for each polarization are plotted in Figure 4-9 at the center frequency. The x-pol levels are less than -25 dB within the main beam view-range of 30° . The radiation patterns are symmetrical within the view range of $\theta = \pm 30^\circ$. The V-polarization feed mechanism introduces a marginal beam-squint in the H-plane that can be compensated in the array.

In the off-boresight view-range, the V-polarization also induces a high level of x-pol as compared to the H-polarization.

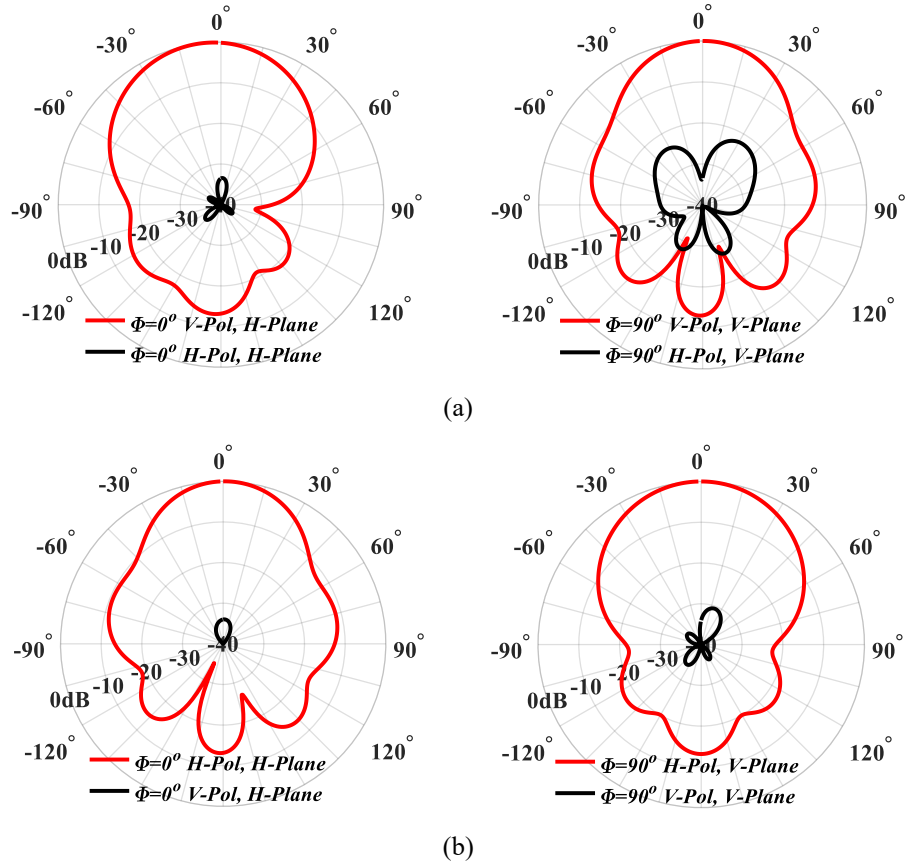


Figure 4-9. Antenna element radiation pattern for (a) V-Polarization and (b) H-Polarization

4.1.2.2 $2^n \times 2^m$ Dual-polarized Subarray

A schematic layout of a scalable dual-channel SRN for an array of any order $2^n \times 2^m$ is shown in Figure 4-10. The basic lattice of Figure 4-10 (a) is repeating within the larger lattices of order $m = n > 1$. To demonstrate the concept, a 4×4 array is considered. In Figure 4-11, PMC packaged feed-networks for 2×2 and 4×4 dual-polarized arrays are presented in which microstrip feedlines are implemented on a single surface. A cross-section view of the 1-to-16 packaged microstrip line feed network is shown in Figure 4-12. The constituents of the AMC packaging Layer # 4 are the EBG unit cells [113].

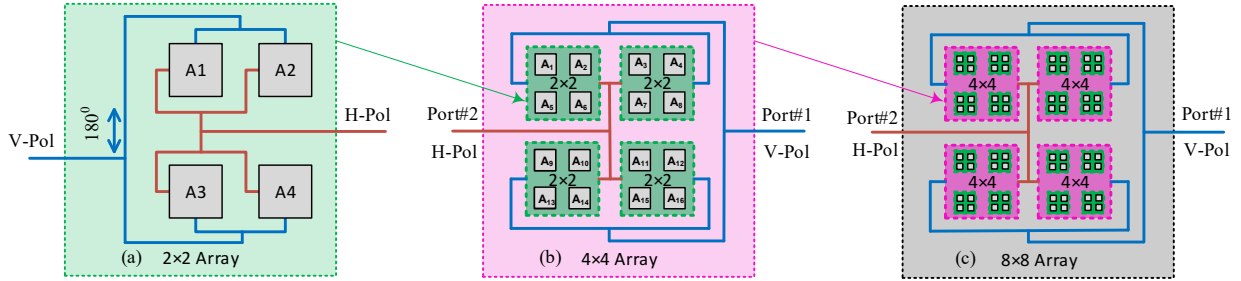


Figure 4-10. Scalable, dual-channel SRN topology-layout on a single surface for dual-polarized $2^n \times 2^m$ array

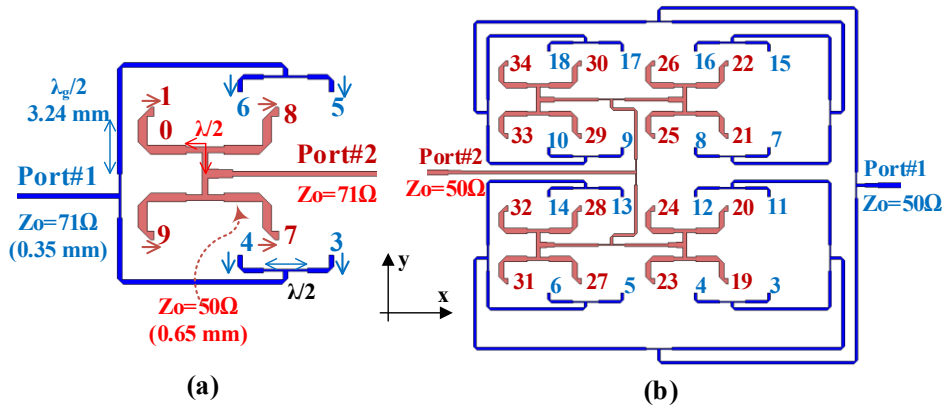


Figure 4-11. Microstrip line feed networks for 2×2 and 4×4 dual-polarized arrays

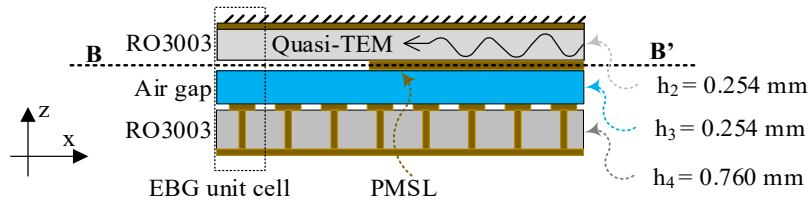


Figure 4-12. Cross-section view of packaged microstrip line signal routing network

The reflection (S_{NN}) and transmission coefficients (S_{N1} , S_{N2}) for 2×2 and 4×4 feed networks are plotted in Figure 4-13 (a – d). The reflection coefficients are less than -10 dB for both cases. The transmission coefficients are around -6 dB and -12 dB for 2×2 and 4×4 feed networks. However, the transmission coefficients are more dispersive for the 4×4 network due to losses.

The impedance bandwidth decreases with an increase in the array-order. The important performance parameters are the coupling coefficients between the H/V-polarizations, as shown in

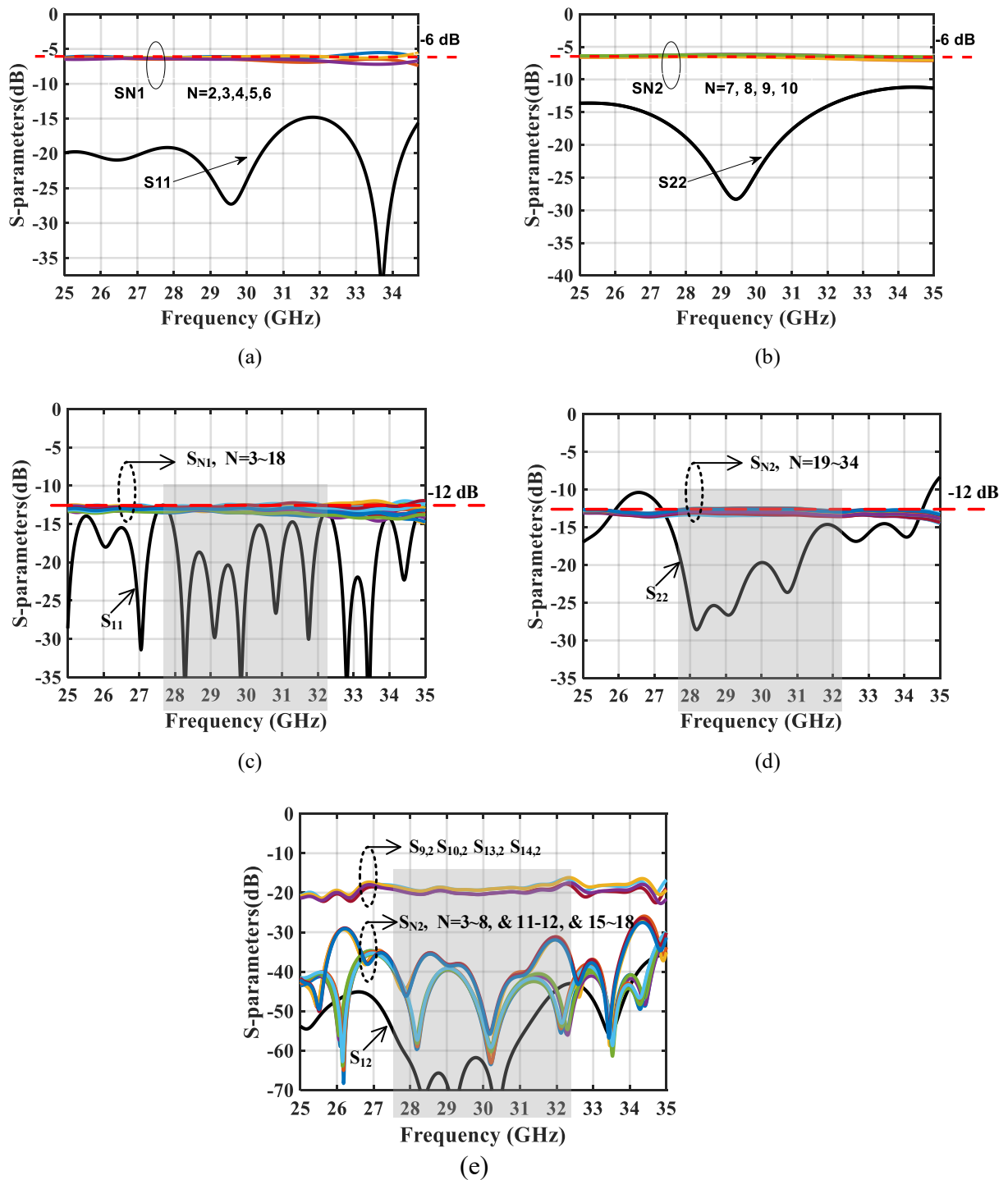


Figure 4-13. Reflection and transmission coefficients (a) Port#1, 2×2 feed network, (b) Port#2, 2×2 feed network, (c) Port#1, 4×4 feed network, (d) Port#2, 4×4 feed network, and (e) Coupling coefficients for 4×4 array feed network

Figure 4-13 (e) for a 4×4 network. All ports' coupling coefficients are less than -30 dB, except S_{N2} ($N = 9, 10, 13, 14$), which is around -20 dB. It is expected that within the array environment, these couplings could contribute to the x-pol of the antenna array. Therefore, along with port-to-port coupling, it is essential to analyze the x-pol of the antenna elements within the array environment. The minimum spacing between the adjacent microstrip feedlines of H/V-polarization is 0.6 mm, as shown in Figure 4-14. In this case, the ports' isolation decreases to a level of 27 dB.

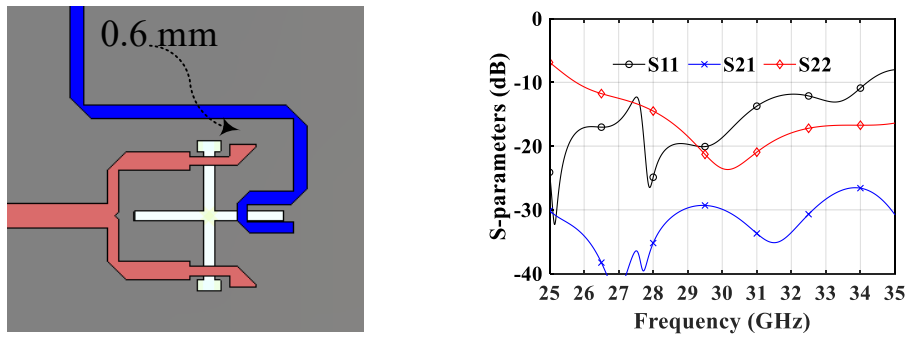


Figure 4-14. Feed arrangement within an array environment and S-parameters

A complete feed network arrangement is shown in Figure 4-15, along with the vital design parameters. The exploded model view of the array is shown in Figure 4-16, where the inter-element spacing (9 mm) is less than λ at the upper frequency of 33 GHz. The spacing between the AMC

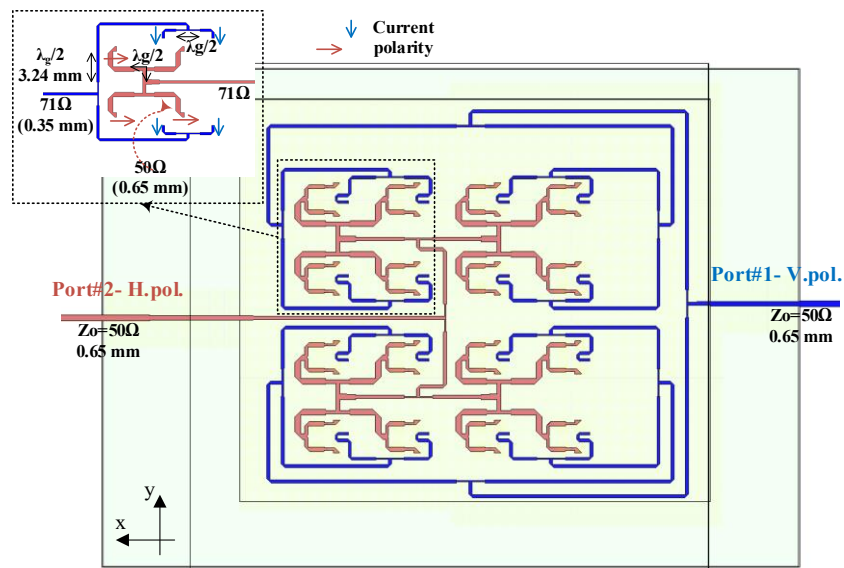


Figure 4-15. Corporate dual-channel feed network for 4×4 dual-polarized ME dipole antenna array

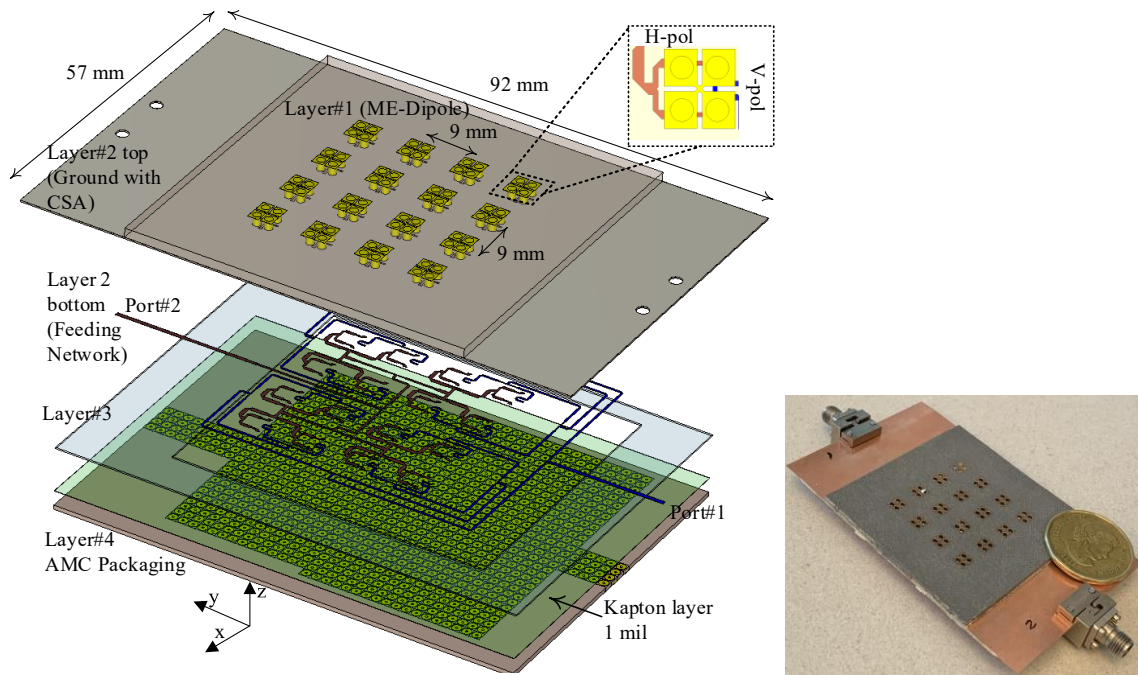


Figure 4-16. PCB multi-layer exploded model of a 4×4 dual-polarized ME dipole antenna array

Layer # 4 and the microstrip line SRN is kept as " $h_2 = 0.254 \text{ mm}$ ", where the characteristic impedance of the microstrip line is not affected substantially. Additionally, Kapton's one-mil layer is also deposited at the top of Layer#1 to guarantee insulation between the EBG patches and the feed-network (SRN).

For verification purposes, the array is fabricated and tested. The measured/simulated results are compared in Figure 4-17 for S-parameters and gain. From the full-wave analysis, the maximum gain value is found to be 19.30 dBi at 31 GHz that is 0.70 dB less than the theoretical value of 8

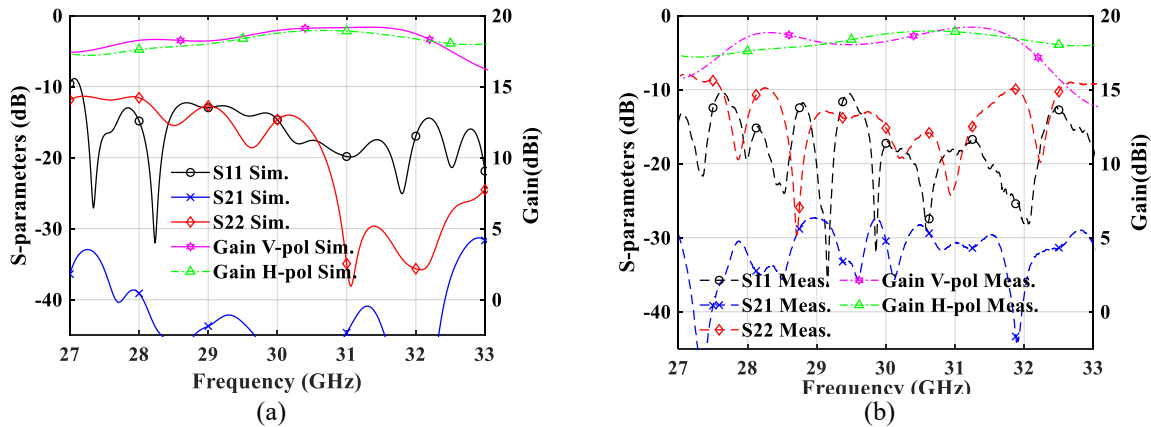


Figure 4-17. S-parameters and gain (a) Simulated and (b) Measured

dBi (single element) +12 (due to array size) = 20 dBi. This is due to the conductor losses in packaged microstrip line SRN's narrow traces. The measurements are fairly matching with the simulation. The array gain is consistent within the 28.5 ~ 31.5 GHz range that drops drastically at the frequency band's edges. By imposing limits on the measured results as $S_{11}, S_{22} < -10$ dB, and $S_{21} < -27$ dB, the 4×4 array maintains a bandwidth of 16.7%, which is expected to be reduced for the higher-order array, *i.e.*, $m = n > 2$.

The measured and simulated co-/x-pol radiation patterns are shown in Figure 4-18 and Figure 4-19 for V-pol and H-pol excitations, respectively, at 29 GHz and 31.5 GHz. The array exhibits symmetrical radiation patterns with nearly 14° 3-dB beamwidths for each polarization.

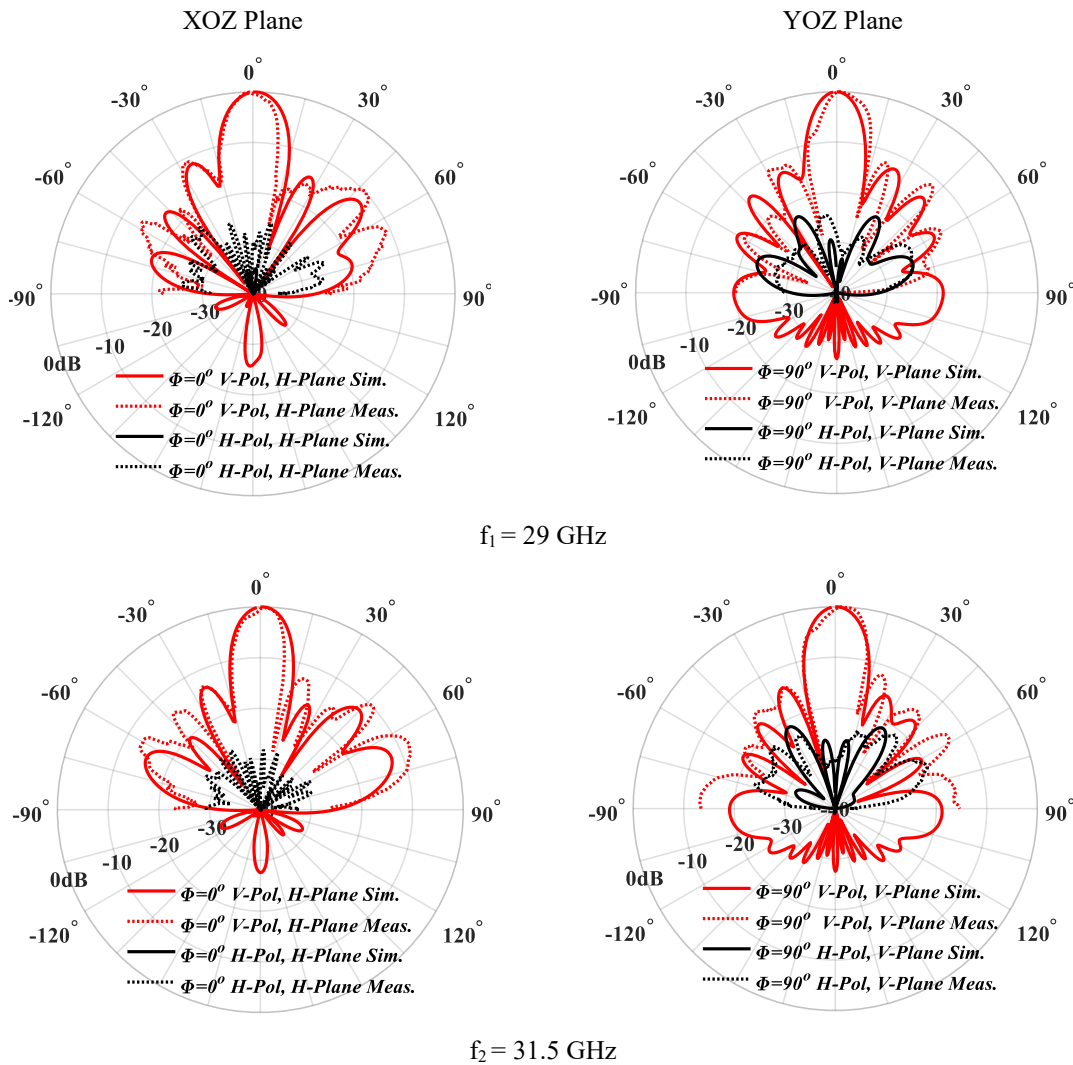


Figure 4-18. Measured and simulated radiation patterns for V-pol excitation

Over the whole frequency range, the SLLs are less than -10 dB. The AMC packaging resulted in extremely low back radiation. The measured x-pol levels are under -20 dB within the view-range of 30° . A disagreement between the measured and simulated SLLs could be due to fabrication tolerance, material properties, and/or layers' misalignment. It is also possible that improper via-holes milling in RT5880 PTFE laminate and metallization might have affected the aperture field distribution that results in slight beam-squinting/-shaping as well. A mm-Wave directional link's channel capacity could be doubled by utilizing the antenna's orthogonal polarizations having symmetrical radiation patterns.

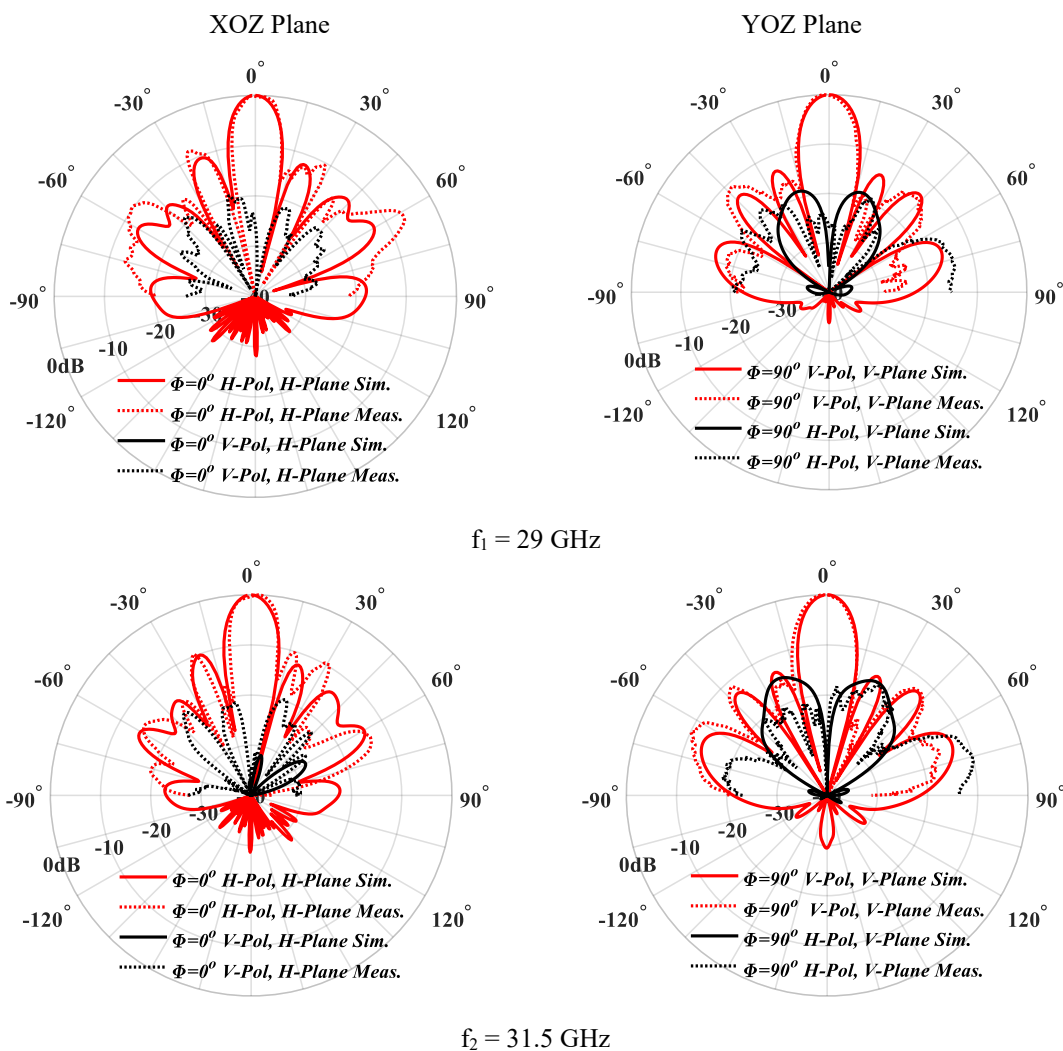


Figure 4-19. Measured and simulated radiation patterns for H-pol excitation

4.1.3 Summary

A concept of dual-polarized fixed-beam subarray for any order $2^n \times 2^m$ has been presented in which a packaged microstrip line SRN, implemented on a single PCB surface, is used to excite the antenna array. A dual-polarized ME-dipole is used as an SCSA antenna element. For demonstration purposes, a 4×4 array is designed for the operational bandwidth of 27.5 ~ 32.5 GHz. An mm-Wave directional link's channel capacity could be doubled by utilizing the subarray antenna's symmetrical radiation patterns having dual polarization.

However, the presented subarray antenna's radiation patterns are highly directional in all ϕ -planes. Furthermore, the inter-subarray spacing is much greater than $\lambda/2$ due to its physical size, as shown in Figure 4-20. With such electrical characteristics and physical layout, the proposed design could be efficiently used as a subarray within the MIMO large-scale antenna systems [34], where multiple RF streams are required for the same information simultaneously. However, such subarray characteristics could bar us from performing digital beamspace beamforming. Therefore, by using the proposed subarray antenna within a large-scale antenna frontend, MIMO postprocessing could be effectively performed, whereas hybrid beamforming could not be performed.

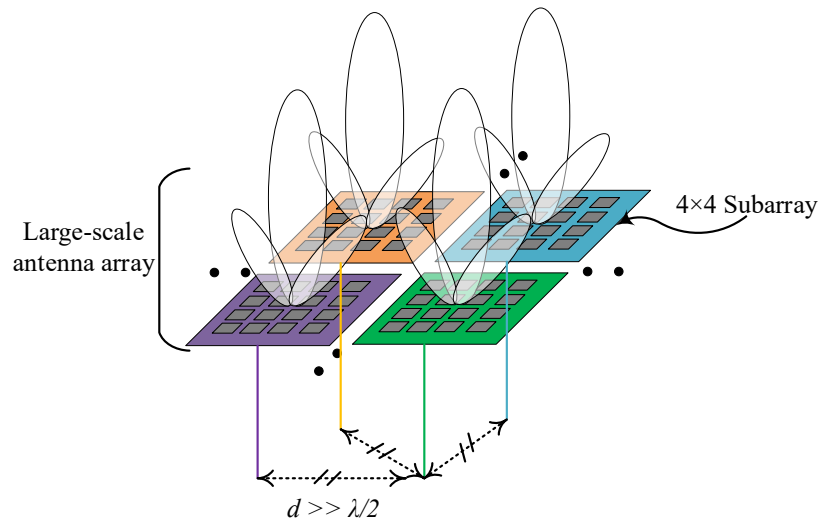


Figure 4-20. Inter-subarray spacing and directional radiation patterns highlighted

4.2 Switched-Beam Dual-Polarized Subarray Antenna

In this section, a 2×2 beam-switched subarray antenna, along with the dual-polarization capability. For this purpose, a packaged microstrip line beamforming network on a single PCB surface is under consideration. For dual-polarized applications, orthogonal signals can be guided within a single physical transmission line, such as a metallic waveguide. For instance, a Butler matrix is proposed in which two orthogonal polarizations are excited within a waveguide for the dominant mode operation [139]. However, in the case of substrate integrated waveguides, two orthogonal signals cannot be routed within the same waveguide transmission line path due to the substrate thickness limitations. Therefore, multiple layers of substrates are used for each channel in which dedicated SIW transmission lines are responsible for each polarization that are used to excite the dual-polarized antennas [43], [69], [76], [78]. For a single channel, the beamforming networks can be designed on a single substrate layer, as reported in [44], [66], [68]. Similarly, because of the quasi-TEM nature of the microstrip line technology, dedicated transmission lines could be used for each polarization (channel), and crossovers and bridges are used to transfer the RF signal from one PCB layer to another [70], [123], [140]. Except for metallic waveguides based designs [139], all other PCB based implementations, such as SIW and microstrip line, result in multi-layer layouts. However, for the dual-polarized applications, it is perceived that a dual-channel microstrip line beamforming network can be realized on a single surface of a PCB with the help of single layer couplers and crossovers. A large-scale antenna frontend can be constructed

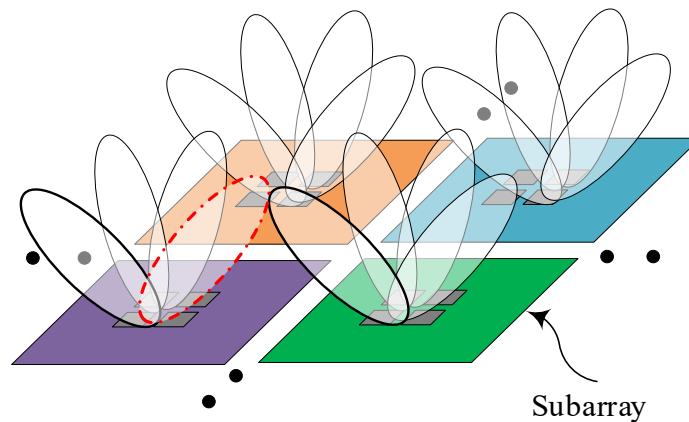


Figure 4-21. Large-scale antenna frontend with 2D beam-switched subarray antenna

by using such a 2-D beam-switch subarray antenna for hybrid beamforming operation, as shown in Figure 4-21.

An analog beamforming network is designed for 2-D beam-switched mm-Wave applications operating in the range of 28–32 GHz. Two identical 2×2 networks, one for each polarization (H-pol. and V-pol.), are integrated on the single surface of a substrate. The 90° hybrid couplers are used to achieve a 2-D progressive phase shift at two stages. A highly isolated crossover is used to cross the RF signal for each polarization. To avoid spurious radiation, the microstrip line circuit is packaged with the AMC. The beamforming network has four beam-ports for each polarization. Therefore, for H-/V-pol., eight beams can be generated simultaneously.

4.2.1 Beamforming Network for Dual-Polarized 2-D Scanning

Figure 4-22 shows a schematic for a 2×2 beamforming network consisting of eight hybrid couplers, four crossovers, four dual-polarized antennas, and four beam-ports (P_n and P_m) for each polarization. The array of four antennas (2×2) could be simultaneously excited horizontally and vertically from the beam-ports P_n and P_m , respectively, where $m = n = 1, 2, 3, \text{ and } 4$, in this case. In the case of P_n excitation (H-pol), the RF signal follows the solid line path, and the required phase shift is achieved by the 90° hybrid coupler (black blocks). Similarly, the RF signal for P_m excitation (V-pol) is guided through dashed line paths. The RF signals cross at four cross-points (RF crossovers) while being highly isolated from each other.

The proposed schematic of Figure 4-22 is realized in low-cost PCB technology. The microstrip line circuit and the AMC packaging are shown in Figure 4-23. The XZ cross-section view of Figure 4-23 (a) shows that the circuit consists of two layers. The first layer is the microstrip line beamforming circuit, where quasi-TEM wave propagation is shown, and an AMC packaging layer is placed at the height of h_2 from the microstrip line circuit. The laminates RO3003 ($\epsilon_r = 3$, $\tan\delta = 0.001$) are used in both layers. The XY cross-section plane at BB' of Figure 4-23 (a) is shown in Figure 4-23 (b). The width of 50Ω microstrip line traces is 0.65 mm. The crossover design (denoted as C) is obtained by cascading the two wideband hybrid couplers (denoted as H).

The beamforming components' design details and the AMC packaging can be found in [113], [137].

For the port P_1 excitation, the signal has a phase difference of 0° , 90° , 90° , and 180° at array-ports A_1 , A_2 , A_3 , and A_4 . For instance, to reach array-port A_1 , the signal is guided via $H_1 \rightarrow C_4 \rightarrow H_8$ path. The lattice provides progressive phase shifts φ_x and φ_y at the array-ports in X and Y dimensions. The phase distribution is given in Table 4-1 for horizontal polarization only. In response to this progressive phase shift, the beam is switched at (θ_0, ϕ_0) coordinate location, which can be calculated by using (4-1) (4-2) [44], [68]. A similar operation can be shown for the four

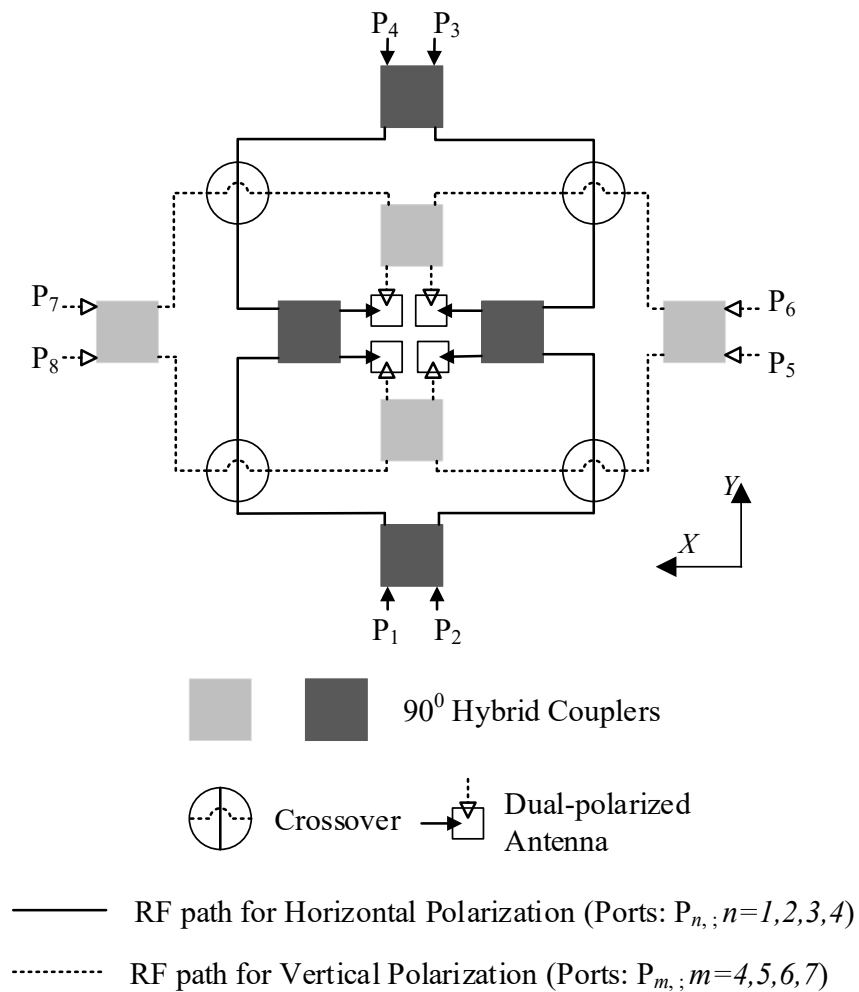


Figure 4-22. Layout schematic for a 2×2 dual-channel beamforming network

vertically polarized beams. Therefore, in eight simultaneous beams, a set of four beams is polarized horizontally and four vertically.

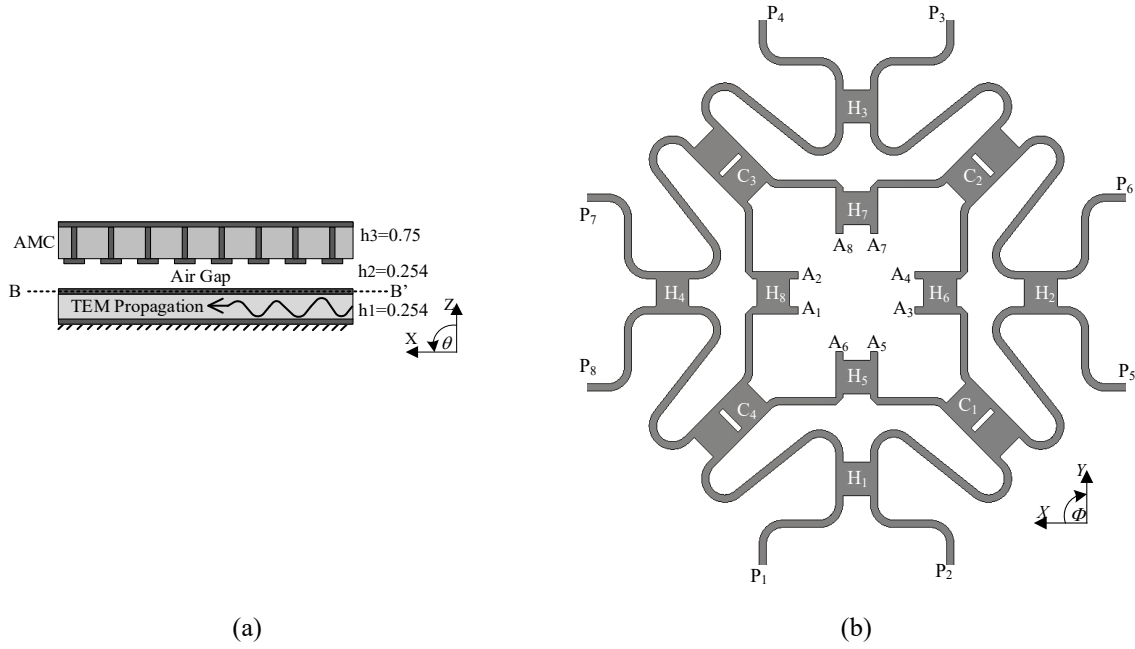


Figure 4-23. (a) XZ cross-section view of packaged beamforming network and (b) Microstrip beamforming network on single surface of XY-plane at BB' cross-section level

Table 4-1. Progressive phase shift for horizontal polarization

Port Excitation	Phase Distribution at Array-Ports		$\varphi_x = \angle A_1 - \angle A_3 = \angle A_2 - \angle A_4$ $\varphi_y = \angle A_1 - \angle A_2 = \angle A_3 - \angle A_4$
Port#1	$A_1 = 0^\circ$	$A_2 = 90^\circ$	$\varphi_x = -90^\circ, \varphi_y = -90^\circ$
	$A_3 = 90^\circ$	$A_4 = 180^\circ$	
Port#2	$A_1 = 90^\circ$	$A_2 = 180^\circ$	$\varphi_x = 90^\circ, \varphi_y = -90^\circ$
	$A_3 = 0^\circ$	$A_4 = 90^\circ$	
Port#3	$A_1 = 180^\circ$	$A_2 = 90^\circ$	$\varphi_x = 90^\circ, \varphi_y = 90^\circ$
	$A_3 = 90^\circ$	$A_4 = 0^\circ$	
Port#4	$A_1 = 90^\circ$	$A_2 = 0^\circ$	$\varphi_x = -90^\circ, \varphi_y = 90^\circ$
	$A_3 = 180^\circ$	$A_4 = 90^\circ$	

$$\theta_0 = \sin^{-1} \sqrt{\left(\frac{\varphi_x}{kd_x}\right)^2 + \left(\frac{\varphi_y}{kd_y}\right)^2} \quad (4-1)$$

$$\phi_0 = \tan^{-1} \left(\frac{\varphi_y d_x}{\varphi_x d_y} \right) \quad (4-2)$$

4.2.2 Subarray Antenna Performance

Full-wave simulation is performed for the packaged dual-channel beamforming network of Figure 4-23 in CST MWS Time Domain Solver. All dielectric and metallic losses are considered in the simulation setup. The beamforming network is a passive symmetric circuit; therefore, simulation results for Port # 1 excitation are analyzed only. Figure 4-24 shows that the -15 dB impedance bandwidth is 28-32 GHz. In this frequency range, the adjacent ports are isolated by a level of more than 15 dB. However, it reaches up to 12 dB at the band's edges. All other ports are isolated by more than 25 dB. Therefore, isolation results are presented for the adjacent ports only. Beamport#1 to array-ports (A_1 , A_2 , A_3 , and A_4) transmission level is -6.5 dB with ± 0.25 dB variation in the magnitude. The progressive phase shifts are also plotted in Figure 4-24. As given in Table 4-1, the simulated values show that for port#1 excitation, 90° phase shifts are achieved in both X- and Y-direction (φ_x, φ_y) with a variation of $\pm 5^\circ$.

A 2×2 array of the dual-polarized antennas could be used at the proposed beamforming network's array-ports. A study of a suitable antenna for such applications is presented in [137], [138]. Here, the dual-polarized ME-dipole antenna element presented in the previous section is used for 2×2 array factor calculation to observe the beam switching mechanism according to the phase distributions given in Table 4-1. The inter-element spacing is considered to be $d_x = d_y = \lambda/2$ at 30 GHz. Therefore, $k \times d = \pi$. The radiation directivity pattern for the single antenna element and 2×2 beams switching array are shown in Figure 4-25. The 2-D beam scanning array factors

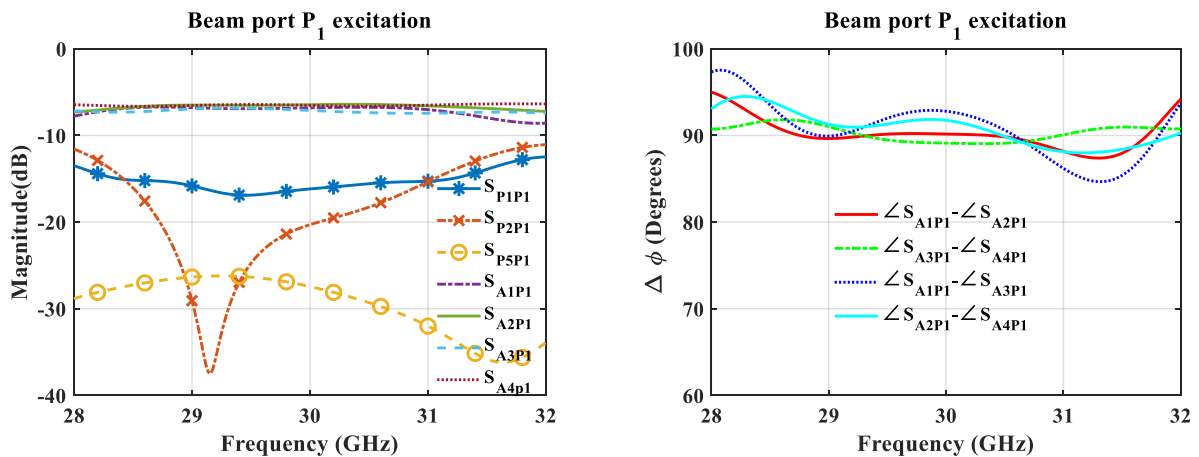


Figure 4-24. S-parameters (magnitudes and phase distribution) for port#1 excitation

are calculated and shown for the H-pol phased distribution. Similarly, the other four switched beams could also be generated for the V-pol excitations (Port # 5 to Port # 8).

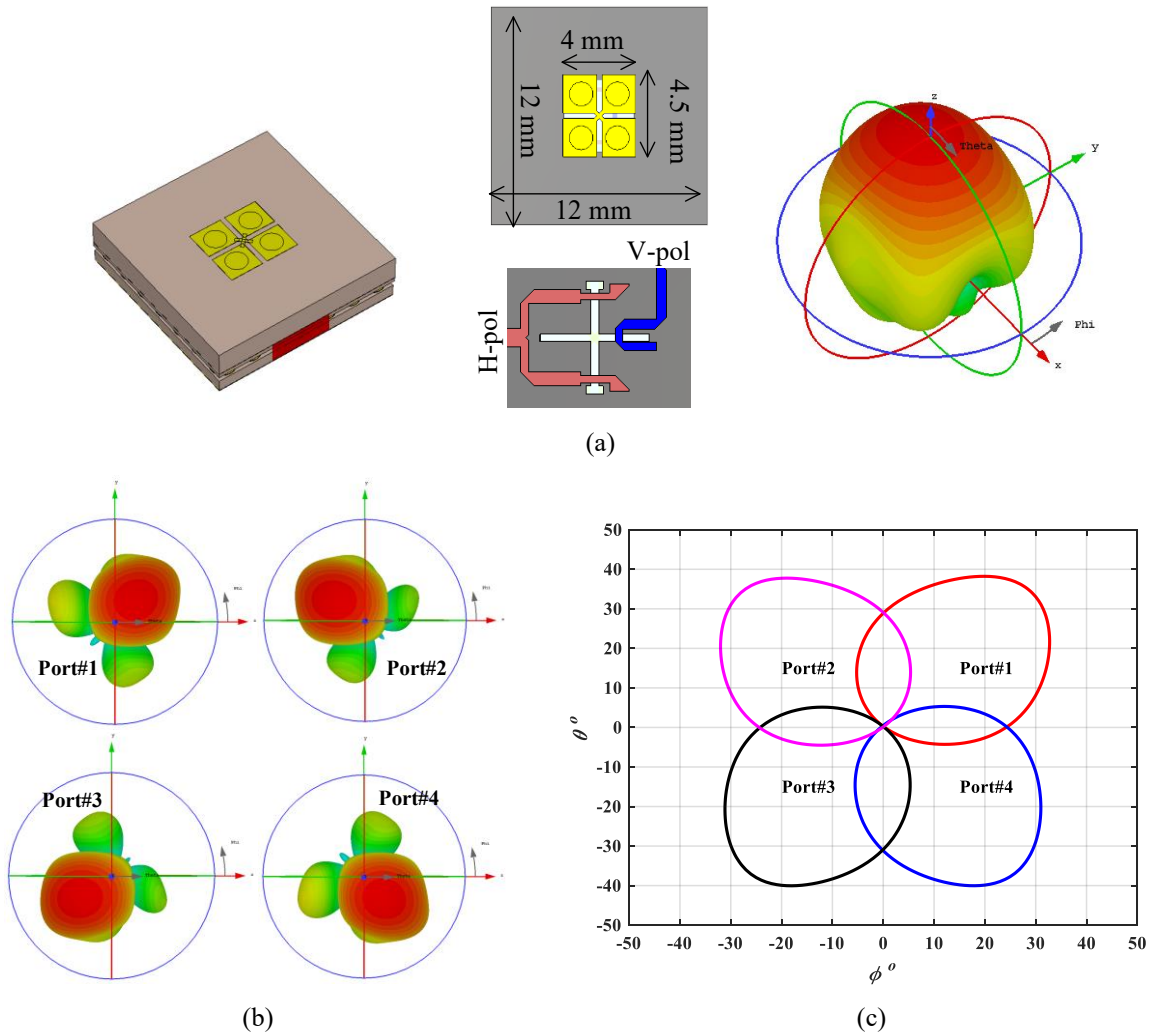


Figure 4-25. (a) Dual-polarized antenna element – ME-dipole, (b) 2-D beam switching, and (c) 3-dB contours

4.2.3 Summary

The presented dual-polarized 2-D beam switching network is simple to design and fabricate. It merely consists of hybrid couplers and crossovers, which are implemented on the single surface of a PCB and augmented with the PMC packaging to minimize the radiation losses. Four directional beams could be formed simultaneously for each polarization (H- and V-pol). The 2-D

beam switching capability, along with the added functionality of dual-polarization, could substantially enhance an mm-Wave wireless link capacity.

To address the limitations of Section 4.1 fixed-beam subarray antenna, a switched-beam subarray antenna with the wider beamwidth radiation patterns has been presented. However, while considering it as a subarray within a large-scale antenna frontend for hybrid beamforming, still there are two associated shortcomings. First, due to the beamforming network's large footprint, the subarray accumulates a large circuit area, as depicted in Figure 4-26. The radiating antenna

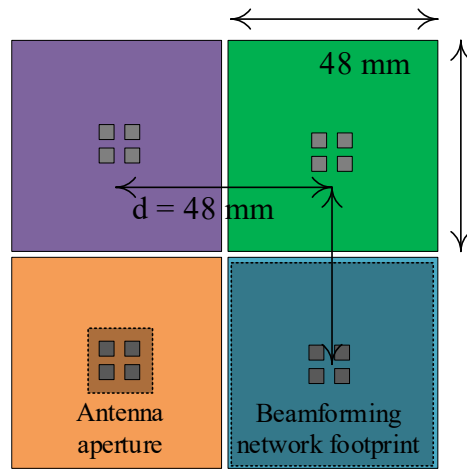


Figure 4-26. Footprint of antenna aperture compared to beamforming network

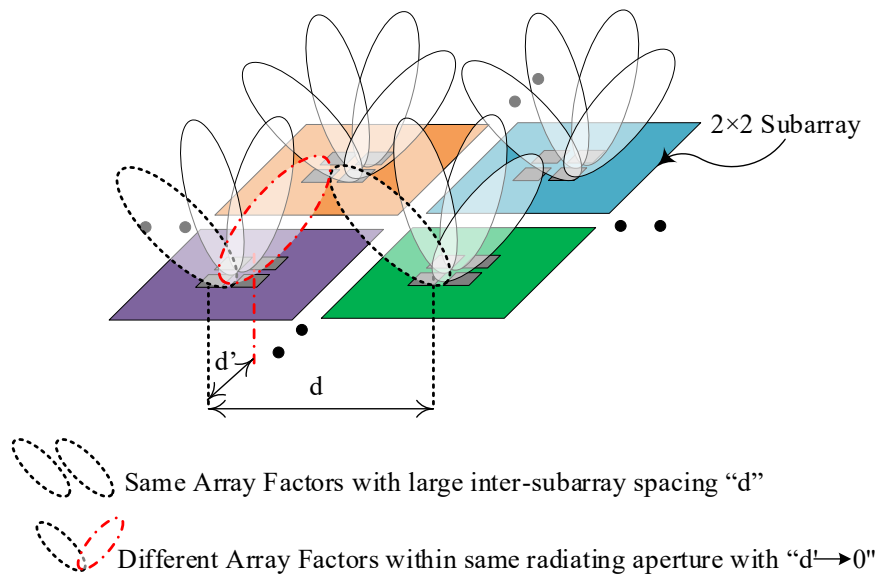


Figure 4-27. Array factors of 2×2 subarray antenna

aperture of the subarray is much smaller than the beamforming network, which results in a discontinuous large-scale antenna aperture. Therefore, the inter-subarray separation “ d ” among the radiation beams with similar array factors would be much larger than $\lambda/2$, as shown in Figure 4-27. As a result, digital beamforming could not be applied over the radiation patterns with the subarrays’ similar array factor. Second, each of the four beams within a subarray has different array factors. Therefore, these switched beams could not be processed for the digital beamforming. Thus, such subarray design might not be suitable for hybrid beamforming architecture as the radiation beams from the analog beamforming are not overlapping within their 3-dB beamwidths due to the aforementioned design limitations. Certainly, it requires a novel multibeam subarray implementation to address these challenges.

4.3 1-D Switched-Beam End-fire Subarray Antenna

An end-fire multibeam antenna subarray that consists of a wideband 4×4 Butler matrix is presented in Section 4.3.1. To perform hybrid beamforming, a 16-port multibeam antenna frontend could be conceived by stacking four such subarray antennas, as presented in the summary Section 4.3.2. Thus, the analog beam-switching could be performed in the H-plane and the digital beam-space beamforming in the V-plane.

4.3.1 Butler Matrix Subarray with Longitudinal Layout

In Figure 4-28, a hypothetical multibeam frontend is depicted to perform hybrid beamforming. The task of beamforming is appropriately divided between the analog and digital stages. An $N \times M$ antenna array frontend is considered and partitioned into N -subarrays. An end-fire switched-beam subarray is required for the H-plane beam-switching with M number of array-ports (here $M = 4$ elements, $E_1 - E_4$) fed by a beamforming network of the order $M \times M = 4 \times 4$. A vertical stack of N such subarrays could provide $N \times M$ fan-beams that are switched (directive) in the H-plane and having wider 3-dB beamwidth – same as the single antenna element – in the V-plane. The digital beamspace precoding (beamforming) can be applied over the set of beams for a fine-tuned coverage in the V-plane. For the model depicted in Figure 4-28, the order of $N = M = 4$ is under consideration.

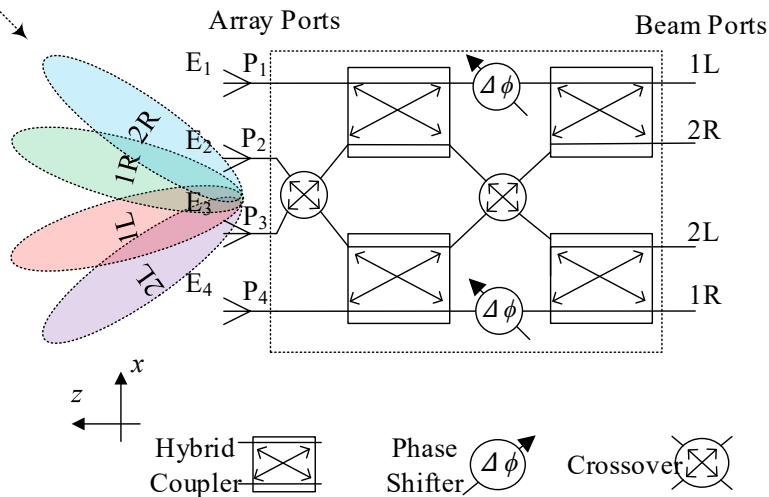
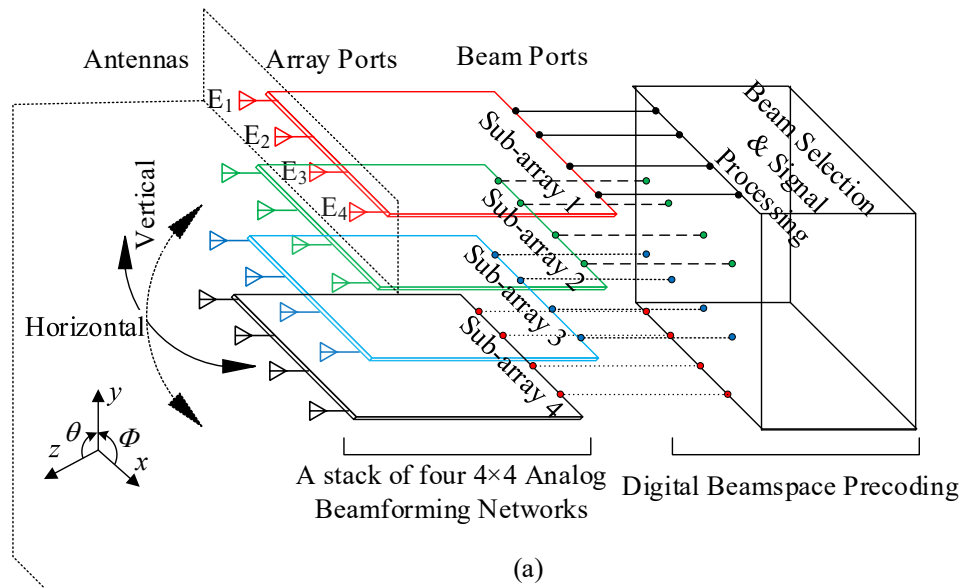


Figure 4-28. (a). A hypothetical multibeam frontend for hybrid beamforming, and (b). End-fire multibeam subarray antenna

Within this architecture, the vital part is the subarray antenna design. The present study is conducted for such subarray to achieve the predesignated requirements of (1) self-shielded, (2) single-substrate, (3) via-less, and (4) wideband analog beamforming network to perform azimuth wide-range beam-switching with reduced scan-loss within 28-33 GHz. The beamforming network is a single-layer microstrip line 4×4 Butler Matrix synthesized within a PMC packaged environment to minimize the radiation loss and suppress the cavity modes and surface waves. A

device model and its packaging boundary conditions are shown in Figure 4-29. The multibeam antenna subarray consists of Butler matrix (phase shifters, couplers, and crossovers). A technique of open-circuit multi-stubs loaded delay-line is used to achieve wideband phase shifters – phase coherent with the reference-line of crossover. Solid patch-shape couplers and crossovers are designed to minimize microstrip line metallic losses. An efficient transition region is designed to connect the beamforming network with the radiating part. The beamforming network is made from the packaged microstrip lines, and the double ridge gap waveguide (DRGW) concepts are used for the antenna designs. The symmetric DRGW transmission lines at Butler matrix array-ports are profiled in the E-plane to conceive a 1×4 H-plane horn antenna array. The motivation behind

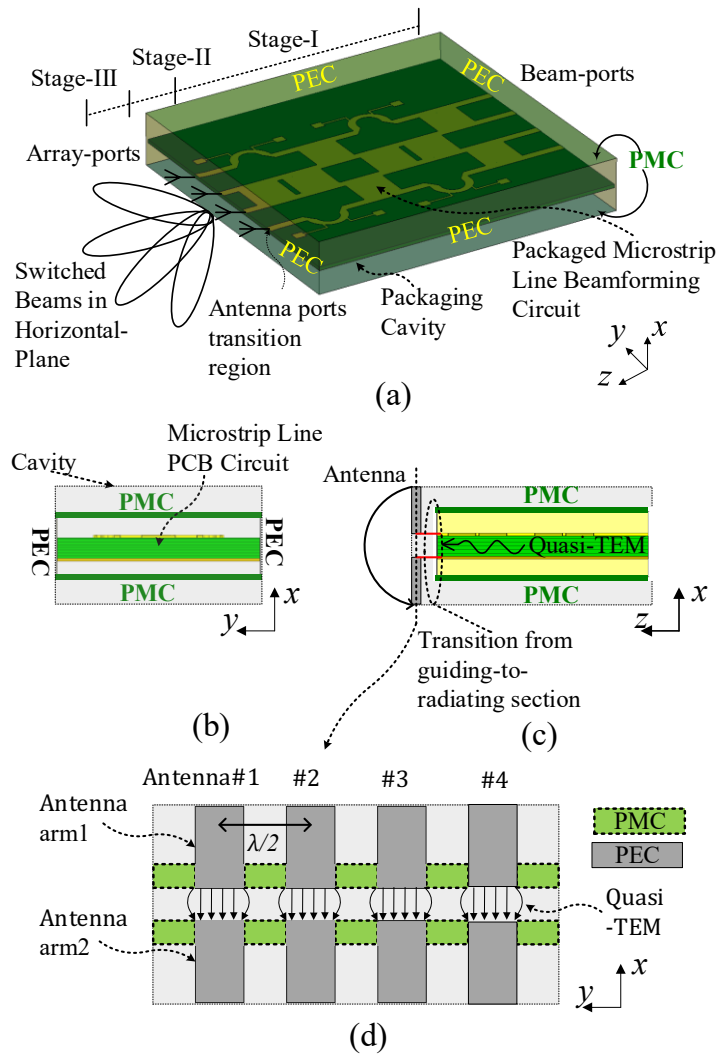


Figure 4-29. (a) Three stages of multibeam subarray antenna, (b) XY cross-section view, (c) XZ cross-section view, and (d) Front view of 1×4 array aperture

designing an end-launched horn antenna is to avoid interconnects such as adaptors and cables between the Butler matrix and the antenna array.

Furthermore, the symmetric double-ridge transmission lines are augmented with a row of half-height EBG unit cells between them forming DRGW to restrict the quasi-TEM signal propagation along the ridge only. In this way, a higher level of isolation can be achieved among the H-plane antennas to enhance the array's scanning performance. The design is self-shielded/self-packaged because the metallic enclosure is used to integrate the H-plane end-fire array, and it incorporates the AMC textured-surfaces within itself.

Section 4.3.1 is organized as follows. Synthesis of a single-substrate wideband 4×4 Butler matrix (Stage-I of Figure 4-29 (a)) is presented in Section 4.3.1.1. In Section 4.3.1.2, the development of DRGW and the transition region is presented (denoted as Stage-II). The DRGW horn antenna array's design procedure is presented in Section 4.3.1.3 (Stage-III). Finally, in Section 4.3.1.4, all the components are integrated, and the overall multibeam antenna performance is discussed.

4.3.1.1 Stage I: Synthesis of PMC Packaged 4×4 Butler Matrix

The theory of PMC packaging is applied at Stage-I of the multibeam antenna. Here, a layout of a single substrate microstrip line of 4×4 Butler matrix is under consideration for a fractional bandwidth $\geq 16\%$ at 30 GHz. Four beam-ports (#1, 2, 3, and 4) can produce the excitation vectors as $[1, e^{-i\psi}, e^{-i2\psi}, \text{ and } e^{-i3\psi}]$, where $\psi \in [-135^\circ, -45^\circ, 45^\circ, \text{ and } 135^\circ]$ for switched-beam 2R, 1R, 1L, and 2L, respectively [17], [141], [142]. A component-by-component study is presented to build a complete PMC packaged Butler Matrix in the subsequent sub-sections. For a better overall Butler matrix performance, wideband ($\geq 30\%$) single-substrate components are designed (25 ~ 35 GHz) by using Rogers laminate RO3003 ($\epsilon_r = 3, \tan \delta = 0.001$) with 0.254 mm thickness and copper cladding of 17 μm . Components are designed within a PMC packaged environment and then cascaded together to conceive a 4×4 Butler matrix. A standard of $h - t = 3 \times t$ is followed throughout Stage-I design, where $t = 0.254$ mm.

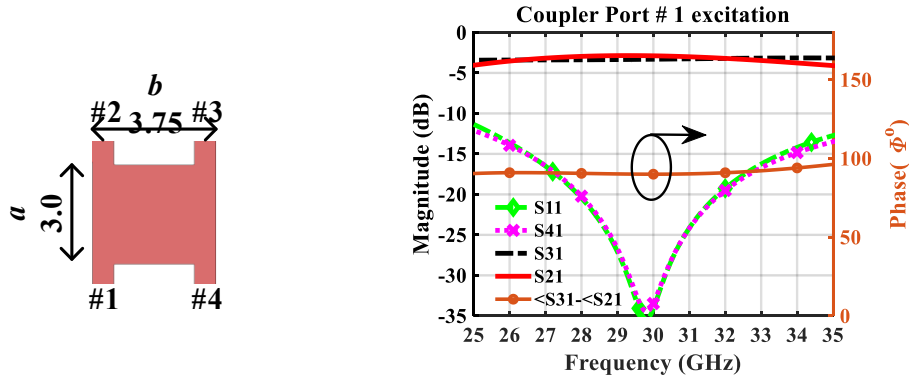


Figure 4-30. Design parameters and performance of a patch-shape hybrid coupler

A. 3-dB Quadrature Coupler

A branch line coupler's performance in terms of power division with the quadrature-phase is about 10%. Such design consists of narrow microstrip line traces, which may produce high metallic loss at mm-Wave. A solid patch-shape is presented [143], which provides wideband flat coupling with a 90° phase-shift. The coupler's design parameters and performance are shown in Figure 4-30. A matching of -15dB level, 15 dB port-isolation, and quadratic phase variation within $\pm 1^\circ$ are achieved from 26.5 to 33.5 GHz (23.5%). Within this range, the coupling is -3 ± 0.4 dB. The microstrip line ports are 50Ω with a line width of 0.65 mm. Parameters a and b are responsible for controlling the reflection/coupling coefficient and quadrature phase-shift, respectively. The presented layout could be further optimized by shape perturbation, such as a transverse slot in the middle or external matching subs. However, it is restricted to have minimum discontinuities and a solid metallic shape to minimize the metallic losses [143]–[145].

B. Crossover

Two wideband hybrid couplers are cascaded to design a crossover having length L and width W , as shown in Figure 4-31 [146]. Here, the objective is to keep the solid-patch layout to

$$S = e^{j\varphi} \begin{bmatrix} 0 & 0 & 1 & 0 \\ 0 & 0 & 0 & 1 \\ 1 & 0 & 0 & 0 \\ 0 & 1 & 0 & 0 \end{bmatrix} \quad (4-3)$$

minimize microstrip line spurious effects due to junctions parasitic. Therefore, the individual coupler's geometries are not modified. However, the structure is perturbed by a transverse slot engraved between the two hybrids, having length L_s and width W_s . Contrary to the annular ring-shaped or patch-shaped crossovers [52], [113], the present design is capable of controlling the characteristics of isolation in the forward (S_{21}) and backward (S_{41}) manners differently. For this purpose, the slot plays a vital role in adjusting the reflection (S_{11}), transmission (S_{31}), and isolation coefficients (S_{21} , S_{41}). To elaborate on the operational principle, a crude equivalent circuit model for the crossover is also given to understand the slot perturbation effect on the junctions' inductance (L_2) and capacitance (C_2) that are exploited to achieve optimum S-parameters.

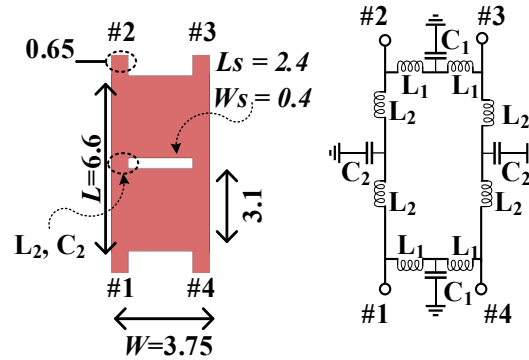


Figure 4-31. Crossover design and its crude equivalent circuit model

The ideal condition of a crossover is given in (4-3). However, different isolation levels (S_{21} , S_{41}) can be obtained by tuning the slot parameters. The slot length L_s mainly influences the S-parameters, whereas W_s has no substantial impact. By increasing the length, the microstrip line junctions' widths at the edges of the crossover (at $L/2$) decreases as marked in Figure 4-31, thus, increasing the series inductance L_2 and decreasing the shunt capacitance C_2 of the equivalent circuit. A parametric study is given in Figure 4-32 for the slot length parameter $L_s = 2 \sim 3$ mm. By increasing length, the second resonance of the return loss gets closer to the first one, thus, improving the $|S_{11}|$ level within the desired bandwidth of 23 %, as shown in Figure 4-32 (a). The isolation $|S_{21}|$ deteriorates rapidly after L_s reaches 2.4 mm, as shown in Figure 4-32 (b). Similarly, Figure 4-32 (c) shows that by increasing L_s , the isolation

$|S_{41}|$ can be better tuned toward a lower frequency band. However, it deteriorates when L_S becomes larger than 2.8 mm.

The advantage of the proposed design is that the isolation level and their variations are different for each of $|S_{21}|$ and $|S_{41}|$. However, in the case of annular or circular patch crossover design, the behavior of $|S_{21}|$ and $|S_{41}|$ remains the same [52]. As the crossover needs to be used within the Butler matrix as a reference transmission line, which is parallel to the phase shifters, L_S impact over the insertion loss phase $\angle S_{31}$ is shown in Figure 4-32 (d). It can be seen that

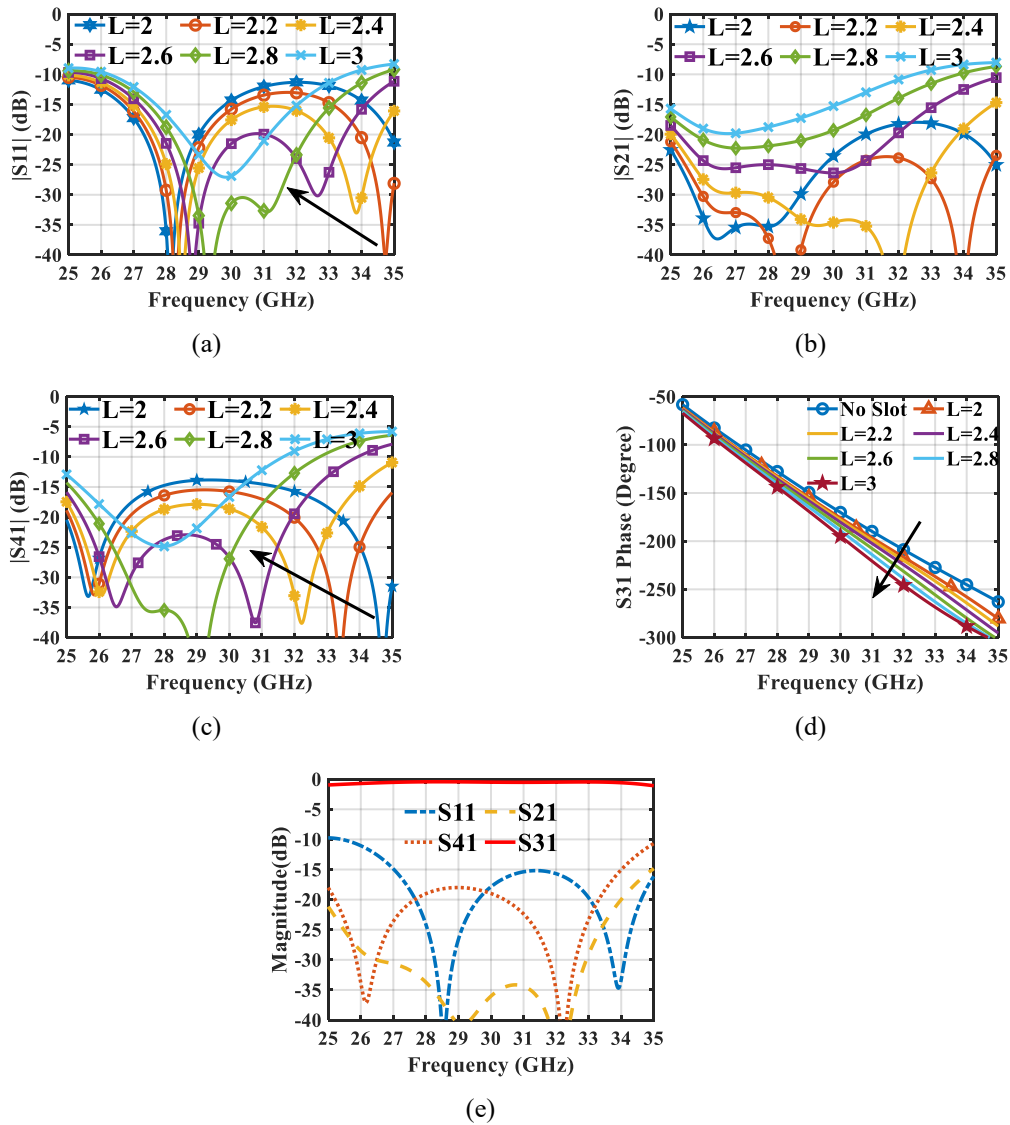


Figure 4-32. Crossover parametric study: (a) Return loss, (b) Isolation $|S_{21}|$, (c) Isolation $|S_{41}|$, (d) Phase variation, and (e) S-parameters for $L_S=2.4$, $W_S=0.3$ mm

the slope of $\angle S_{31}$ increases by increasing L_S , which is the smallest for the structure without a slot. This capability is highly desired and can be used to achieve a phase coherence between the crossover and phase shifters, which is a vital performance parameter to design wideband Butler Matrix components with similar phase dispersion characteristics. However, the phase variation is prominent at the higher frequency band, and with $L_S > 2.4$ mm, the magnitude of the insertion loss $|S_{31}|$ starts deteriorating rapidly away from the center frequency. Therefore, the parameters, $L_S = 2.4$ and $W_S = 0.3$ mm, are the optimized values to achieve $S_{11}, S_{41} < -15$ dB, and $S_{21} < -30$ dB to highly isolate $|S_{21}|$ and $|S_{31}|$ within 23.5% bandwidth.

C. Open-Circuit Multi-Stub Loaded-Line Phase Shifter

Within the lattice of a 4×4 Butler Matrix, the crossover transmission line, presented in the previous sub-Section (B), has to be placed in parallel along with the 0° and 45° phase shifters. Therefore, it is mandatory to have coherent phase variation for both types of transmission lines over the required fractional bandwidth. To obtain such phase coherence, a delay-line is considered that provides 0° phase difference ($\Delta\phi$) between the reference-line, *i.e.*, crossover

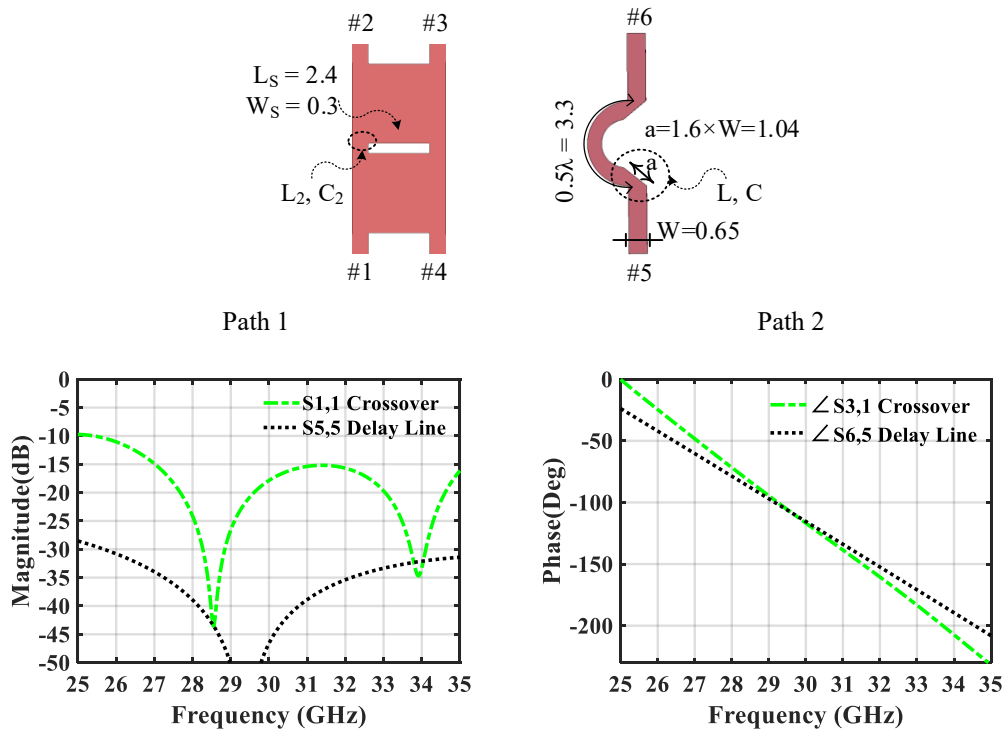


Figure 4-33. Reflection coefficient and phase variation of Path 1 (Crossover) and Path 2 (Delay-line)

(named as Path 1 in Figure 4-33) and the delay-line (Path 2), at center frequency 30 GHz. The reflection coefficients S_{11} , S_{55} , and phase variation of Path 1 and Path 2 are plotted in Figure 4-33.

It can be seen that the slope of the phase-variation for Path 1 is higher than Path 2, which results in phase incoherence. However, the slope difference ($\Delta\phi$) is not very large because of mitering the bend's corner with a length of $a = 1.6 \times W = 1.04$ mm of Path 2, where $W = 0.65$ mm is the width of $Z_0 = 50 \Omega$ transmission line to reduce the shunt capacitance of Path 2 microstrip line to achieve phase variation similar to Path 1.

For a broader bandwidth, the $\lambda/2$ section of Path 2 delay-line is loaded with two $\lambda/2$ open circuit stubs to conceive a phase shifter for a bandwidth of 30% at 30 GHz [70], [147]. Path 2 and the loaded-line configurations are shown in Figure 4-34, having electrical lengths of θ_1 and θ_3 with impedances Z_1 and Z_3 , and double open circuit stubs of length θ_2 with impedance Z_2 , respectively. For all Paths, the input/output characteristic impedance of the transmission lines is Z_0 , which is considered non-dispersive. The impedances and electrical lengths of each section of the transmission lines can be expressed in terms of Z_0 and frequency f , respectively.

$$Z_1 = a.Z_0 \quad Z_2 = b.Z_0 \quad Z_3 = c.Z_0$$

$$\theta_1(f) = \theta_{10} \frac{f}{f_0}, \quad \theta_2(f) = \theta_{20} \frac{f}{f_0}, \quad \theta_3(f) = \theta_{30} \frac{f}{f_0}$$

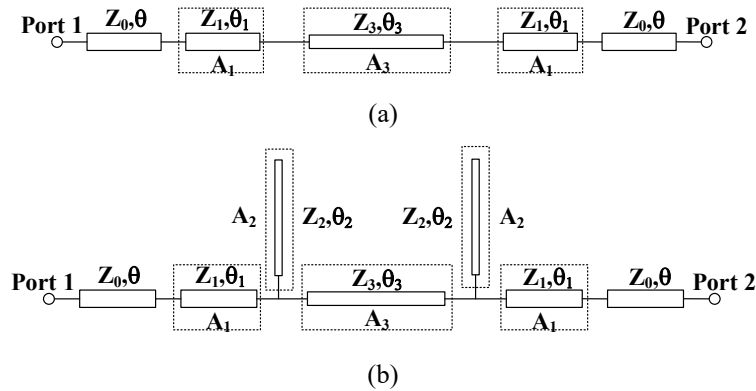


Figure 4-34. Circuit configuration of (a) Path 2 and (b) Loaded line with double open circuit stubs of half-wavelength

where a, b, and c are the normalized impedances, and θ_{10} , θ_{20} , and θ_{30} are the electrical lengths at center frequency f_0 .

The S-parameter of a five-sectioned transmission line of Figure 4-34 (b) can be obtained from the combined ABCD_c matrix expression that is given in (4-4). The normalized form of a matrix A is expressed as a. The magnitude of transmission S_{c21} is expressed in (4-5) with the corresponding phase shift in (4-6). Here, θ_{10} is the reference length (θ_r) to achieve the required phase shift. One of the possible parameters-sets for a 0° and 45° phase shifter is given in Table 4-2. The desired phase shifts can be obtained by adjusting the impedance and the electrical length of section A₁ ($a, \theta_{10} = \theta_r$) of the loaded-line phase shifter shown in Figure 4-34 (b).

$$\begin{bmatrix} a_c & b_c \\ c_c & d_c \end{bmatrix} = [a_1][a_2][a_3][a_2][a_1]$$

$$\begin{bmatrix} a_c & b_c \\ c_c & d_c \end{bmatrix} = \begin{bmatrix} \cos \theta_1 & ja \sin \theta_1 \\ j\frac{1}{a} \sin \theta_1 & \cos \theta_1 \end{bmatrix} \begin{bmatrix} 1 & 0 \\ j\frac{1}{b} \tan \theta_2 & 1 \end{bmatrix}$$

$$\begin{bmatrix} \cos \theta_3 & jc \sin \theta_3 \\ j\frac{1}{c} \sin \theta_3 & \cos \theta_3 \end{bmatrix} \begin{bmatrix} 1 & 0 \\ j\frac{1}{b} \tan \theta_2 & 1 \end{bmatrix} \begin{bmatrix} \cos \theta_1 & ja \sin \theta_1 \\ j\frac{1}{a} \sin \theta_1 & \cos \theta_1 \end{bmatrix} \quad (4-4)$$

$$S_{c21} = \frac{2}{a_c + b_c + c_c + d_c} \quad (4-5)$$

$$\text{Arg}(S_{c21}) = \tan^{-1} \frac{\text{Im}(S_{c21})}{\text{Re}(S_{c21})} = \tan^{-1} \frac{E_1}{E_2}$$

$$\frac{d(\text{Arg}(S_{c21}))}{df} = \frac{E_2 \cdot E_1' - E_1 \cdot E_2'}{E_1^2 + E_2^2} \quad (4-6)$$

Table 4-2. Design parameters for 0° (Path 4) and 45° (Path 5) phase shifters

Paths	a	b	c	$\theta_{10}=\theta_r$	θ_{20}	θ_{30}
Path 4	1.20	1.85	1.18	0.5π	π	0.5π
Path 5	1.15	1.85	1.18	0.75π	π	0.5π

This theory of loaded-line phase shifter is tested by simulating a 0° and 45° phase shifter in the full-wave environment.³³² The loaded-line is named Path 3 in Figure 4-35. Akin behavior of reflection coefficient and phase-variation for Path 1 and Path 3 is achieved, as

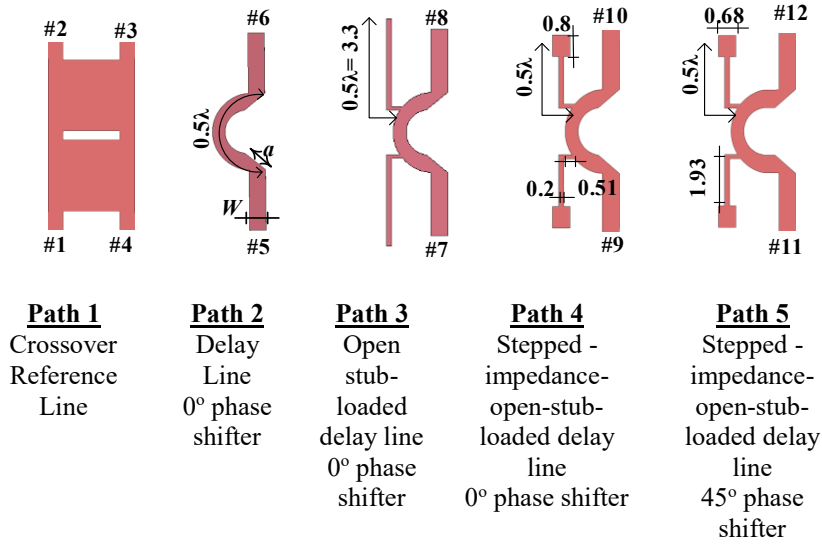


Figure 4-35. Crossover reference line, a delay-line, and double open stub loaded delay-lines to conceive wideband phase shifter coherent with reference line

shown in Figure 4-36 (a) and (b), respectively. Therefore, coherence in the phase variation is achieved, *i.e.*, $\Delta\phi = \angle S_{31} - \angle S_{87} = 0$, for 30% bandwidth at the center frequency, and any value of phase shift can be achieved by adjusting the parameters a , θ_{10} .

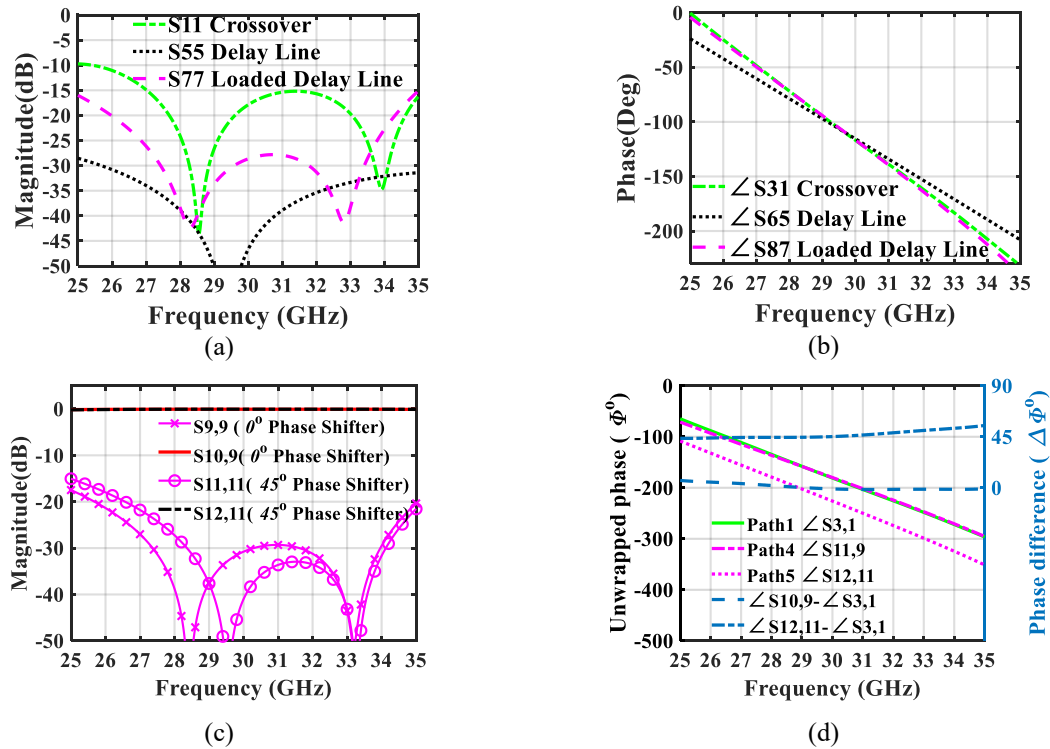


Figure 4-36. (a) Reflection coefficients, (b) Phases, (c) 0° and 45° phase shifters S-parameters, and (d) Phase variations and phase differences

By integrating these components within a compact lattice of a 4×4 Butler matrix, it is observed that the open circuit stubs of 0° and 45° phase shifters become very close to one another. The components' unwanted coupling due to the fringing field may deteriorate Butler matrix performance. Therefore, the open circuit stubs' physical lengths are shortened by introducing a stepped-impedance, as shown in Figure 4-35 Path 4 [147]. However, it does not affect the performance of the loaded-line phase shifter as the stubs are still half-wavelength long electrically. The updated design of a 0° and 45° phase shifters, named as Path 4 and Path 5 in Figure 4-35, are designed as per the numerical values provided in Table 4-2. The S-parameters (magnitude) are shown in Figure 4-36 (c). In Figure 4-36 (d), the phase variation and $\Delta\phi$ w.r.t. Path 1 reference-line (crossover transmission line) are plotted for 0° and 45° phase shifters. The phase deviation is $\pm 1^\circ$ within the bandwidth of 17%.

D. Components' Integration: PMC-Packaged 4×4 Butler Matrix

A 4×4 PMC-packaged Butler matrix is realized by integrating three types of components, as shown in Figure 4-37. To achieve a phase distribution of $\psi \in [-135^\circ, -45^\circ, 45^\circ, \text{ and } 135^\circ]$, the lattice consists of four wideband hybrid couplers, two 0° phase shifters, two 45° phase shifters, and two crossovers. The microstrip line circuit has a lid of full-height pins as an AMC cover. For measurement, the microstrip lines are extended to

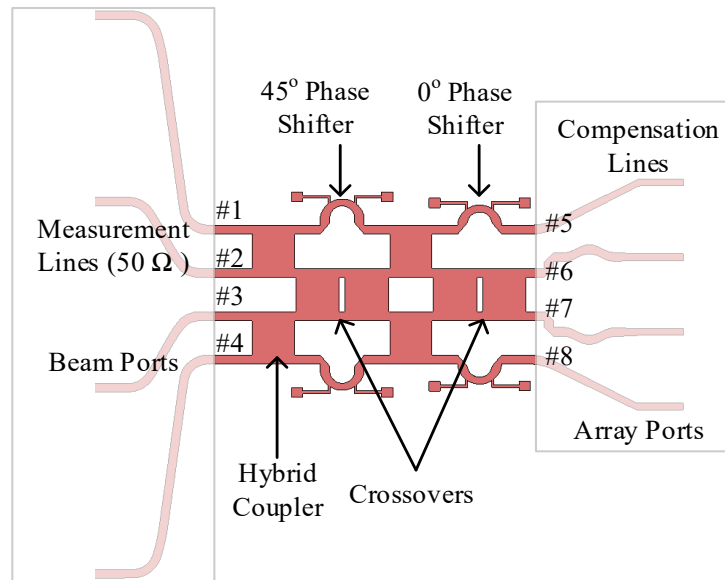


Figure 4-37. 4×4 packaged Butler Matrix with extended measurement and phase compensation lines

accommodate 50 Ω Southwest Microwave® connectors (1092-03A-5) at the beam-ports (#1, 2, 3, and 4). Similarly, at the array-ports (#5, 6, 7, and 8), the phase compensation lines are adjusted for the 1×4 array.

The Butler matrix circuit's symmetry is sufficient to analyze beam-Port # 1(1R) and # 2(2L) excitations. Figure 4-38 shows that the magnitude and phase of the Butler matrix S-parameters are shown. It exhibits an excellent performance within the range of 28 ~ 33 GHz. The reflection coefficient at each port is less than -15 dB, and the isolation level among the beam-ports is higher than 15 dB. At 30 GHz, the insertion loss is 0.8 dB, with a variation of ± 0.3 dB. Similarly, the phase distribution at the beam-ports 1R and 2L is $45^\circ \pm 3^\circ$ and $-135^\circ \pm 3^\circ$, respectively, which is reasonably flat within the bandwidth of 16%.

To observe the PMC packaging effect, the Butler matrix is simulated with and without any packaging (bare microstrip lines). The transmission coefficient magnitudes for beam-port#1 (1R) excitation are compared and shown in Figure 4-39. It is observed that, with the AMC packaging, the mean of the Butler Matrix's transmission is improved from -8.2 dB to -

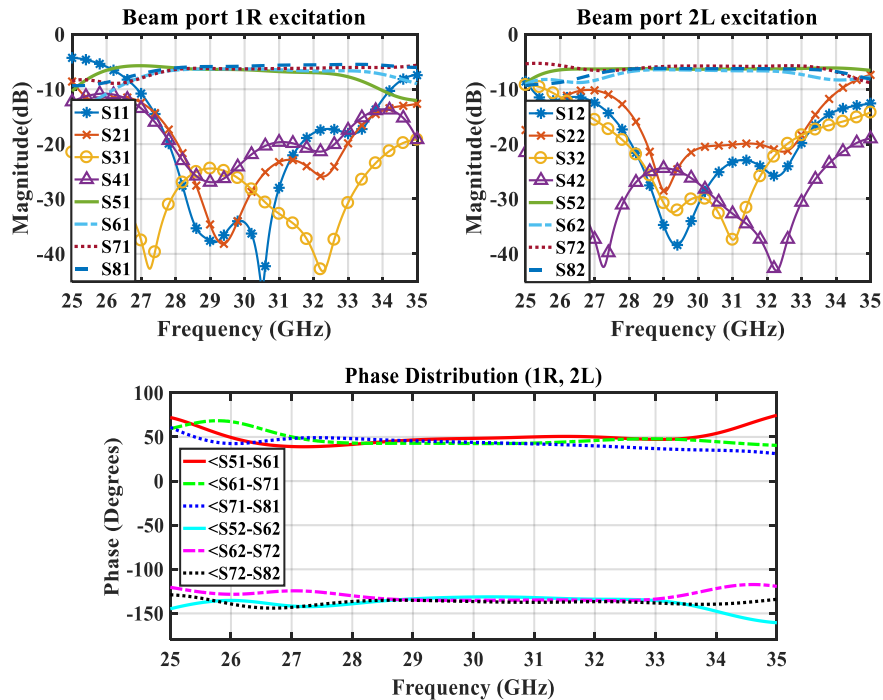


Figure 4-38. S-parameters: magnitude and phase distributions for beam-port#1 (1R) and #2 (2L) excitation of a 4×4 Butler Matrix

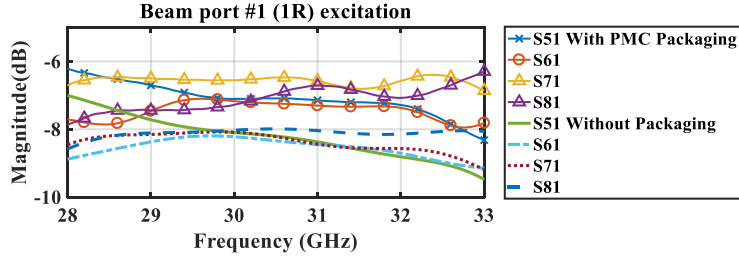


Figure 4-39. Comparison of transmission coefficient with/Without AMC packaging

6.8 dB at the center frequency. The calculated power loss factor ($1 - S_{11}^2 - S_{51}^2 - S_{61}^2 - S_{71}^2 - S_{81}^2$) is found to be 0.1558 and 0.3722 with AMC-lid and without any packaging, respectively. Whereas, beam-ports are almost equally isolated in both cases (*i.e.*, the factor, $S_{21}^2 + S_{31}^2 + S_{41}^2$, is the same). However, off from the center frequency, the transmission coefficients deviate more in AMC packaging, comparatively.

4.3.1.2 Stage II: DRGW Quasi-TEM Transmission Line

In this section, Stage-II of the multibeam subarray antenna is implemented. The objective is to develop the isolated symmetrical transmission lines within a packaged environment for the transition region that could be extended into a radiating structure (antenna array). Thus, the antennas could be integrated within the metallic enclosure. It could provide ease to conceive an E-plane flared horn antenna that requires two conductors to be flared symmetrically. The H-plane mutual coupling is always less than the E-plane [148]. The proposed configuration is advantageous because the scanning horn antenna array could be arranged in the H-plane. Furthermore, to restrict the double ridge's signal propagation, this symmetric transmission line is augmented with the half-height EBG unit cells. Therefore, a procedure to develop a quasi-TEM DRGW is presented in the following sub-sections.

A. Quasi-TEM Double-Ridge Gap Waveguide

A parallel plate waveguide in which two PEC conductors are separated by a gap, g , having width S represents a quasi-TEM transmission line, as shown in Figure 4-40. The transmission line's characteristic impedance can be approximated as

$$Z_{TEM} \approx \eta \frac{g}{S} \quad (4-7)$$

where η is the free space intrinsic impedance [91].

A double-ridge waveguide is formed by inserting this parallel plate structure into the metallic waveguide, as shown in Figure 4-40 (b). Except for the fringing fields region at the double-ridge transmission line's edges, the overall structure supports only vertical E-field distribution. The objective is to maintain the TEM propagation and the double-ridge transmission line and suppress the vertical field components elsewhere to achieve isolation between the adjacent transmission lines separated by a distance of $\lambda/2$. This requires symmetrical PMC-PMC boundary conditions, as shown in Figure 4-40 (c). In this XY cross-section view, the double-ridge is shown as a PEC-PEC region surrounded by PMC-PMC lateral walls on both sides. To achieve it, the double-ridge of Figure 4-40 (b) is packaged with the half-height EBG unit cells (pins), thus transforming the double ridge waveguide into a DRGW, as reported in [91], [149].

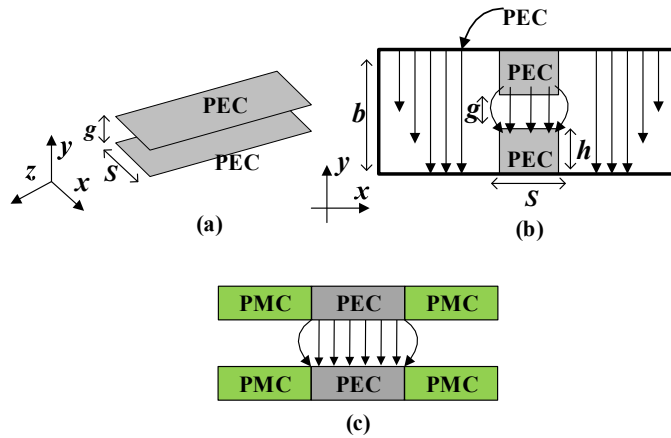


Figure 4-40. Parallel plate quasi-TEM transmission line, (b) Double-ridge waveguide, and (c) Desired boundary conditions

The half-height EBG unit cell's design principle for the DRGW is based on a full-height pin fundamentally (where a textured surface of full-height pins is covered by PEC with a gap less than $\lambda/4$ so that no vertical E-field component could propagate in this region). Similarly,

the reactance of the half-height pins provides a high impedance boundary. The bandgap characteristics of the half-height and full-height pins are nearly the same. However, the two back-to-back textured surfaces of half-height-pins along the y-axis could provide symmetrical boundary conditions that are highly desired in our case. Furthermore, the wide bandgap can be achieved by tailoring the upper and lower pins for different bandgaps and combining two bandgaps [91]. However, the identical half-height pins are assembled to achieve symmetrical PMC-PMC boundary conditions.

The half-height pin's design parameters are shown in Figure 4-41 (a). CST-MWS Eigenmode solver is used for the bandgap analysis. The unit cell boundaries are periodic in the XZ-plane. Similarly, the double-ridge is surrounded by the three pins on each side along the x-axis with magnetic boundary conditions and periodicity along the z-axis. Each pin with PEC on the top and bottom (parallel-plate waveguide) and a gap in the middle represents an admittance that is presented by jb . The equivalent circuit is drawn in Figure 4-41 (b) with periodicity in the direction of the z-axis. This textured surface forbids the propagation of any x- or z-directed wave. Because of symmetry, a phase sweep (0-180°) is performed only along the x-axis for the first ten modes. The dispersion diagram has a bandgap of 18 ~ 37 GHz, as shown in Figure 4-41 (c). The dispersion diagram is shown for the extended frequency range to classify modes' polarizations. The cross-sectional views for the E-field distribution on the unit cell structure for the first four modes are shown in Figure 4-41 (d). From Figure 4-41 (b), the equivalent circuit

$$\begin{bmatrix} V_n \\ I_n \end{bmatrix} = \begin{bmatrix} A & B \\ C & D \end{bmatrix} \begin{bmatrix} V_{n+1} \\ I_{n+1} \end{bmatrix} \quad (4-8)$$

$$\begin{bmatrix} A & B \\ C & D \end{bmatrix} = \begin{bmatrix} \cos \frac{\theta}{2} & j \sin \frac{\theta}{2} \\ j \sin \frac{\theta}{2} & \cos \frac{\theta}{2} \end{bmatrix} \begin{bmatrix} 1 & 0 \\ jb & 1 \end{bmatrix} \begin{bmatrix} \cos \frac{\theta}{2} & j \sin \frac{\theta}{2} \\ j \sin \frac{\theta}{2} & \cos \frac{\theta}{2} \end{bmatrix} \quad (4-9)$$

$$\begin{aligned} \frac{A+D}{2} &= \left| \cos \theta - \frac{b}{2} \sin \theta \right| > 1 \\ \left| \cos \theta - \frac{\omega C}{2Z_0} \sin \theta \right| &> 1 \end{aligned} \quad (4-10)$$

where $\omega=2\pi f$, and gap capacitance, $C = \frac{\epsilon_0 A}{g} + \delta = \frac{\epsilon_0 \pi \left(\frac{d}{2}\right)^2}{g} + \delta$.

represents a periodic distribution of the unit cells in the x - and z -direction; the n^{th} unit cell represents a two-port network having voltage and current V_n, V_{n+1} , and I_n, I_{n+1} at the input and

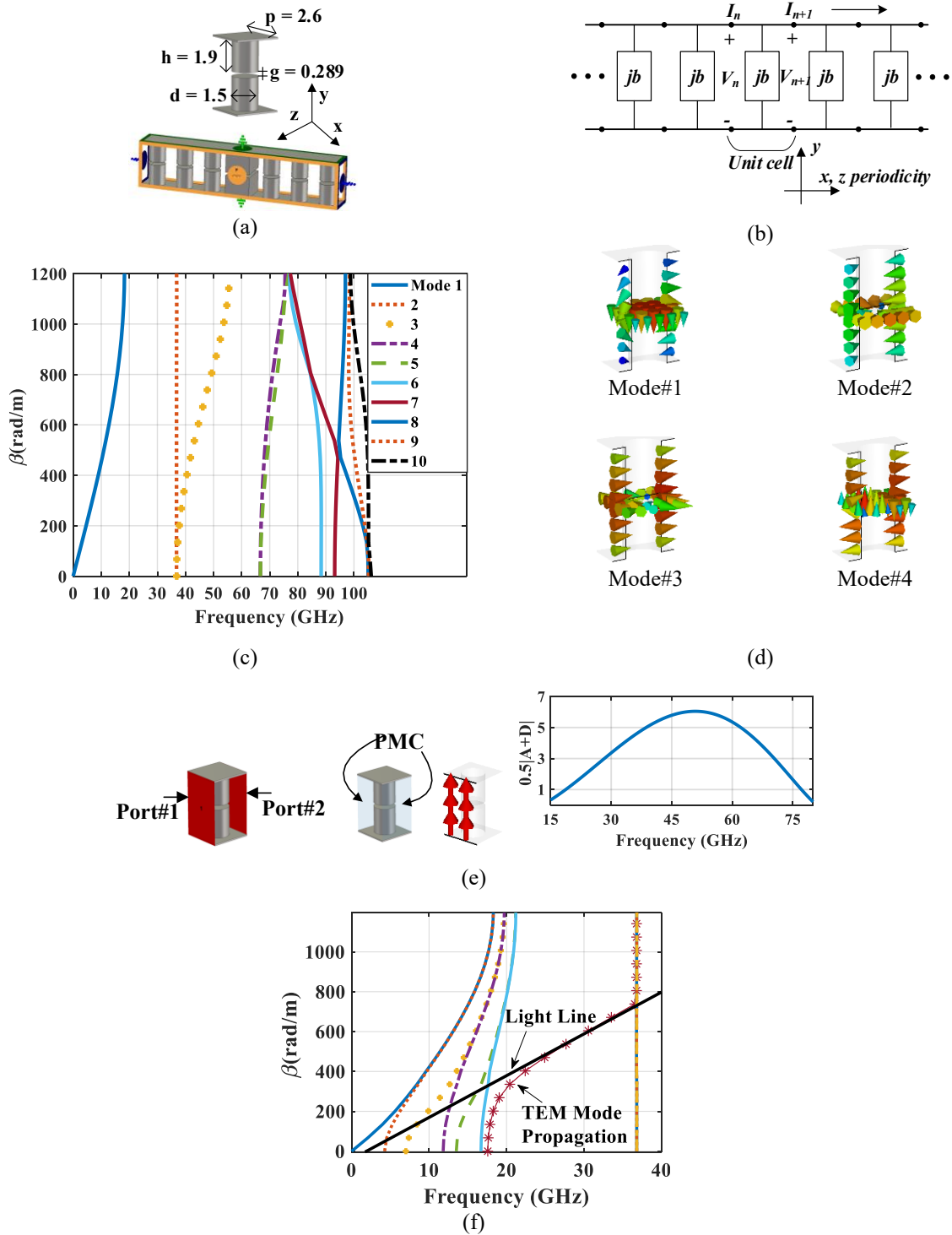


Figure 4-41. (a) Half-height EBG unit cell design parameters, (b) Equivalent circuit model, (c) Dispersion diagram, (d) Modes' E-fields, (e) Bandgap condition, and (f) DRGW dispersion diagram

the output terminals, respectively, that can be written in terms of ABCD matrix as given in (4-8) – (4-9). The unit cell is a cascaded network of a transmission line with length $p-d$, expressed as $\theta = k(p-d)$ and an admittance circuit of the pin. The bandstop condition is defined in (4-10).

In (4-10), the fringing field effect around the pin gap (g) is denoted by δ . For the optimum value of $\theta = k(p-d) \approx \frac{2\pi f}{c}(2 \text{ mm})$, this effect is neglected, *i.e.*, $\delta = 0$. As the value of gap (g) is much smaller than the pin diameter d , only the dominant capacitive effect is incorporated (4-10). Here, $\epsilon_0 = 8.85 \times 10^{-12}$, $c = 3 \times 10^8 \text{ m/s}$, and $Z_0 = 120\pi \Omega$.

Data extracted from the CST MWS full-wave analysis is plotted in Figure 4-41 (e) that satisfies the analytical expression given in (4-10). However, contrary to the dispersion diagram bandgap (18 ~ 37 GHz) of the Eigenmode analysis given in Figure 4-41 (c), this plot shows a bandgap of 18 ~ 76 GHz, which is the bandgap between Mode#1 and Mode#4 as per Figure 4-41 (c). Thus, it is important to notice from Figure 4-41 (d) that the field distributions for Mode#2 and Mode#3 are horizontally polarized. Floquet port excitation in Figure 4-41 (e) is vertically polarized. Therefore, Mode#2 and Mode#3 are not excited; and the next vertically polarized mode is Mode#4.

However, for the DRGW transmission line, the propagating mode is quasi-TEM. The horizontally polarized modes may also get excited due to the fringing fields. Therefore, considering all possible polarizations, the bandgap is considered 18 ~ 37 GHz. Figure 4-41 (f) shows that the dispersion behavior of the single quasi-TEM propagating mode is almost identical to the projected light-line with a bandwidth of 21.2 GHz ~ 36.8 GHz.

A double-ridge transmission line with $Z_{\text{TEM}} = 50 \Omega$ is simulated with/without half-height EBG cells, as shown in Figure 4-42. To capture all the fields around the port (including the fringing fields), the waveguide port is extended beyond the width of double-ridge by one EBG unit cell on each side, and the height of the port is six times the ridge gap g . The cross-sectional views (AA', BB') of the E-field distribution are also presented in Figure 4-42 (b) for both cases. It can be observed that even after one row of EBG pins, the field decays more than 60%.

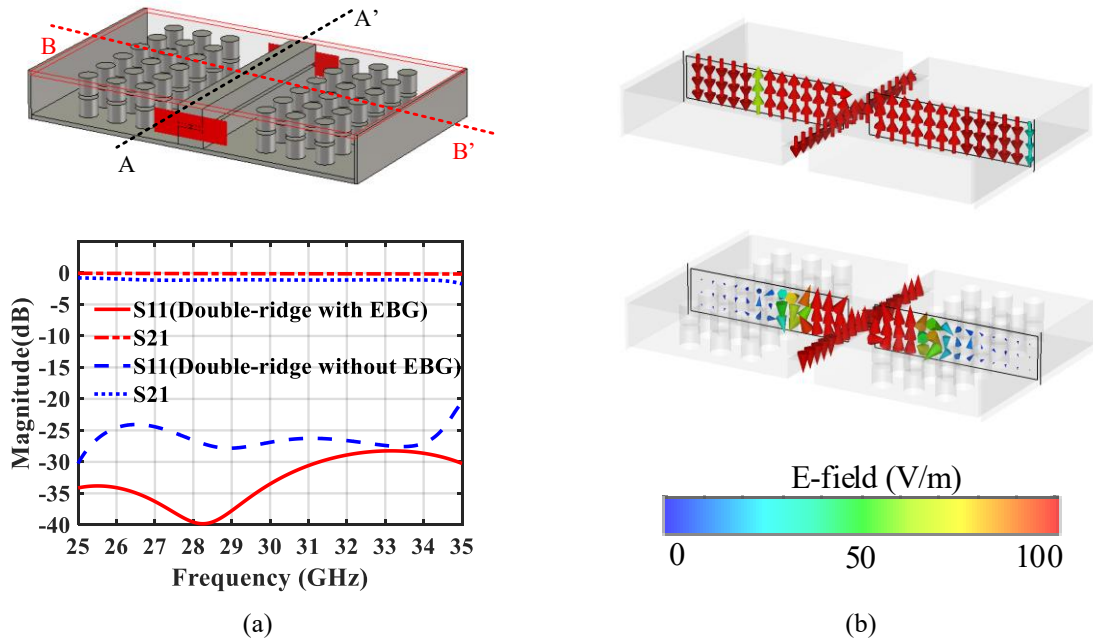


Figure 4-42. (a) DRGW transmission line and S-parameters and (b) E -field distributions on AA' BB' Cross-sections

B. Packaged-Microstrip Line-to-DRGW Transition

The transition region – from beamforming network to radiating section – of the multibeam antenna is a very sensitive part. Microstrip line-to-DRGW transitions are shown in Figure 4-43 and Figure 4-44. A 50Ω microstrip line, on a Rogers laminate (RO3003, $\epsilon_r = 3$, $\tan \delta = 0.001$) of thickness 0.254 mm with line-width of $W = 0.65$ mm, is used to excite DRGW. It is worth mentioning that the transition is a mechanical-touch design. Soldering or conductive epoxy is not used in this region. The lower ridge is connected to the ground, as the MSL is inserted into the gap of the double-ridge. However, for matching purposes, the upper ridge is extended in length to cover the microstrip line. A flared DRGW with width $S = 4$ mm in the middle is excited. The transition model and its S-parameters are shown in Figure 4-43.

Additionally, the normalized electric field distributions across the x-axis over the DRGW at $z = 0, 5,$ and 10 mm, in the middle of the gap height ($y = 0$), are also shown and have a quasi-TEM behavior. The H-plane antenna array with $\lambda/2$ inter-element spacing and is excited by these transmission lines. Therefore, two such transmission lines having ridge width $a = 2.2$ mm (same as the width of antenna aperture in the H-plane), separated by a row of EBG cells, are stimulated to observe its cross-talk. The S-parameters for Port#1 excitation are plotted in Figure 4-44, showing $S_{11} < -20$ dB with a back-to-back insertion loss of 0.3 dB at 30 GHz. From 28 GHz and up, S_{41} is monotonically decreasing below -20 dB.

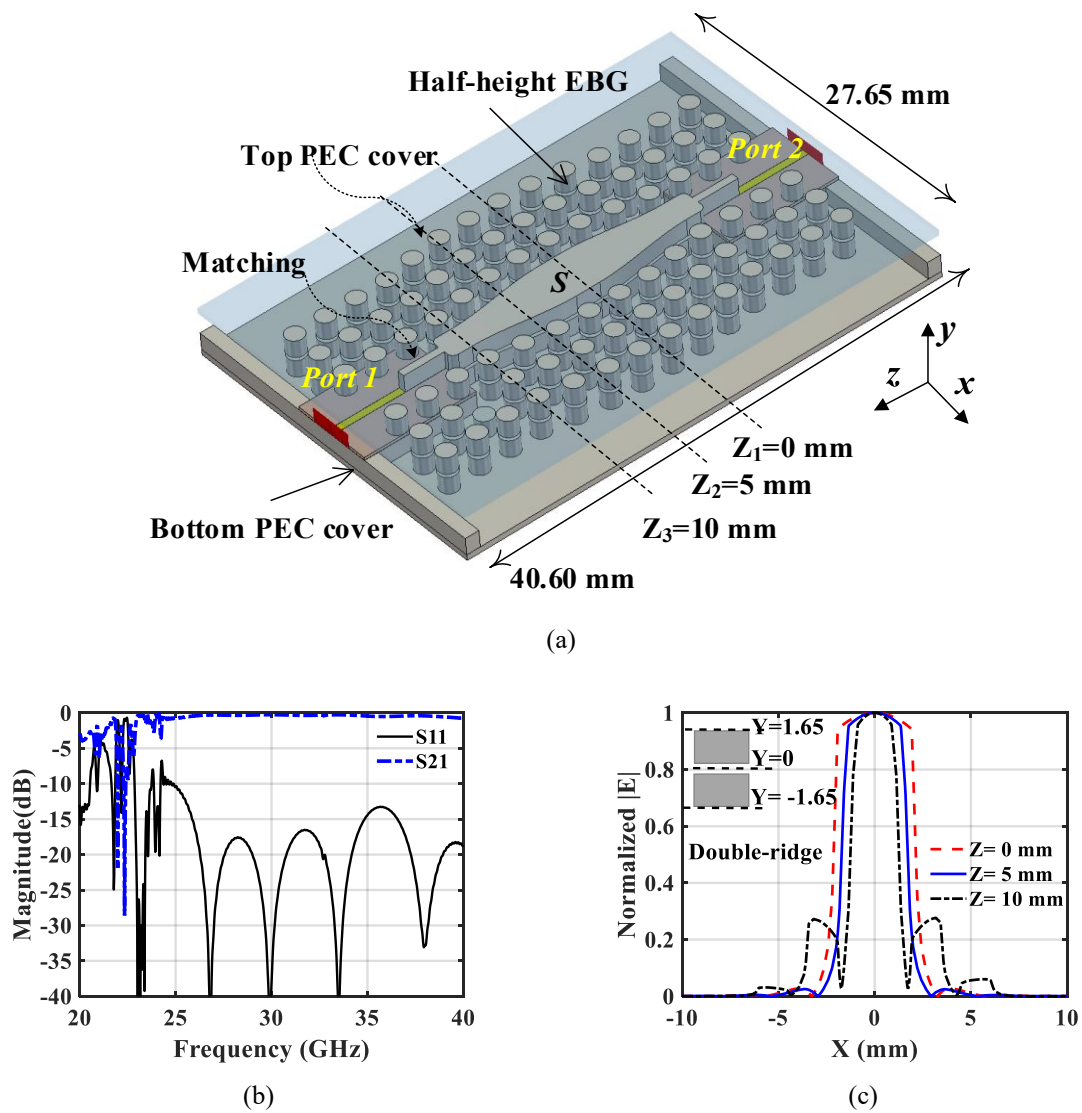


Figure 4-43. (a) Microstrip line to DRGW transition, (b) S-parameters, and (c) E-fields distributions across x-axis

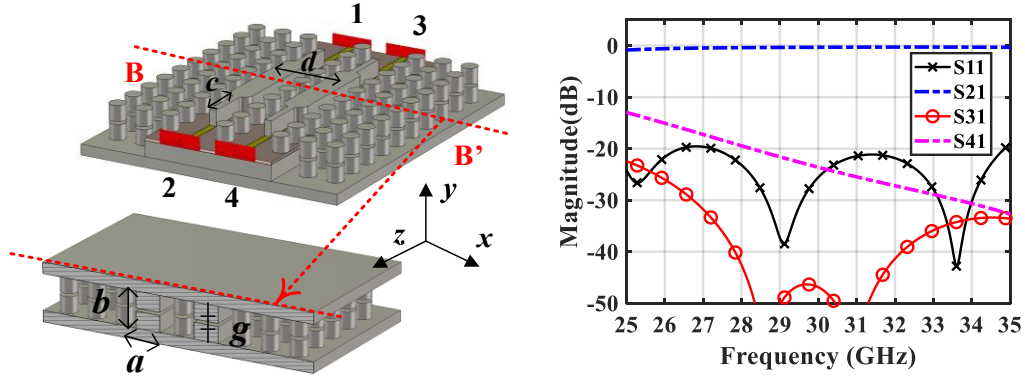


Figure 4-44. Design parameters and simulated S-parameters

4.3.1.3 Stage III: DRGW Horn Antenna Array

For a wideband operation and design compatibility with packaged microstrip line Butler Matrix, a horn antenna is chosen. Cables and adapters are commonly used to connect antennas at the array-ports. However, at mm-Wave, such interconnects may not be feasible for the proposed beamforming network design. Furthermore, rather than introducing a separate structure for the radiating part, an E-plane horn could easily be integrated within the shielding cover as compared to any other antenna type. Therefore, the DRGW transmission line is extended and exponentially flared. In this way, a 50Ω input impedance is matched to the intrinsic impedance of the air (377Ω) [150], [151]. The flared-profile represents a multi-section impedance matching transformer. The expression for the E-plane tapered horn antenna is given as

$$Y(z_i) = c_1 e^{Rz_i} + c_2 \quad (4-11)$$

where, c_1 , c_2 and R are calculated to be 2.46×10^{-3} , 0.141 , and 0.8 , respectively, and the antenna is profiled along the z -axis. Similarly, the corresponding expression for the impedance profile is formulated as

$$Z(l) = (Z_o - 10) + Y(l)e^{4.4} \quad (4-12)$$

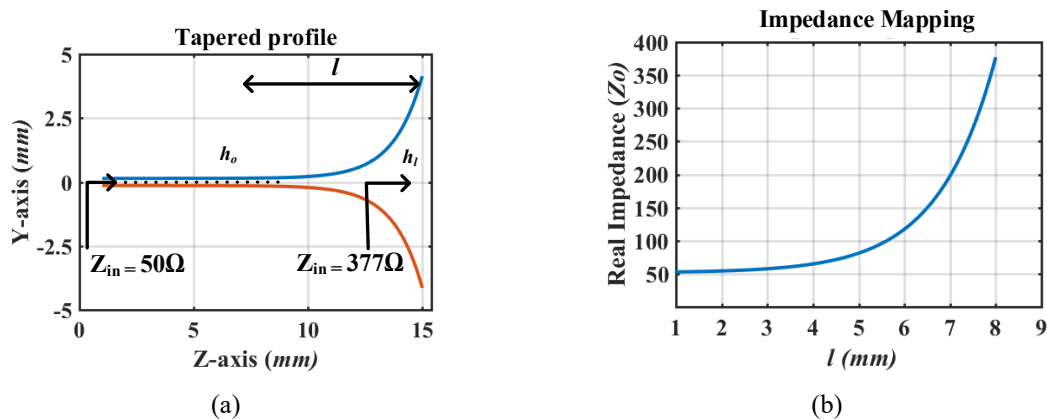
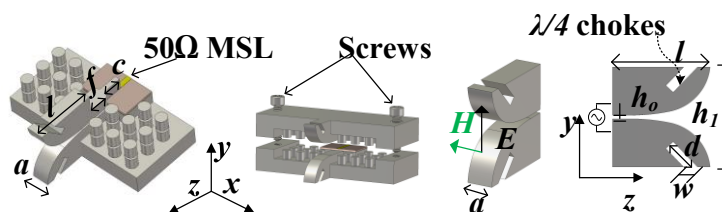


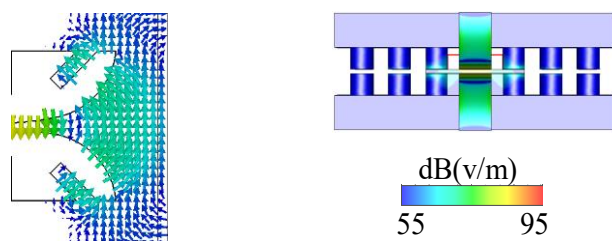
Figure 4-45. (a) E-plane exponentially tapered profile and (b) Corresponding impedance mapping.

where $Z_0 = 50\Omega$, and l is the flaring length. The physical profile and impedance mapping are plotted in Figure 4-45 [152]. The antenna consists of two removable metallic parts with a microstrip line feed that is sandwiched between the ridges, as shown in Figure 4-46 (a).



Design parameters: $a = 2.2$, $h_0 = 0.289$, $h_l = 8$, $l = 7.74$, $d = 2.5$, $w = 1.1$, $c = 2.31$, $f = 3$; units in mm

(a)



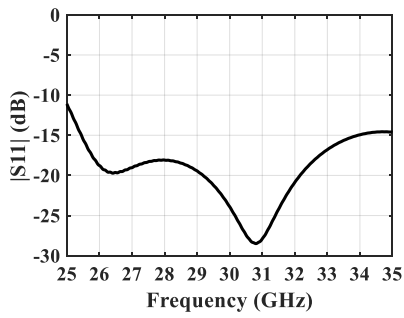
(b)

Figure 4-46. (a) DRGW Horn antenna design parameters and (b) E-fields distribution onto the antenna aperture

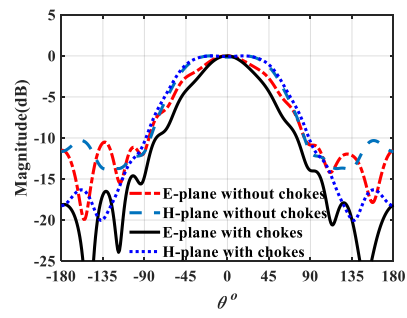
The design parameters such as the antenna neck f and the length l control the resonance frequency. Similarly, E-plane flaring and H-plane width, a , are responsible for controlling the radiation pattern beamwidths in the respective planes [153]. As microstrip line-to-DRGW transition introduces a small unbalance factor in the surface current. Therefore, chokes having depth $d = \lambda/4$ and width $w = \lambda/10$ at the center frequency are engraved at the antenna exterior. Contrary to the corrugation engraved inside the horn antenna aperture [154], the chokes are engraved on the outer face. This is for the ease of fabrication and to achieve the desired performance. These $\lambda/4$ corrugations balance the current distribution on the horn's two arms by limiting any amount of backward current propagation. The electric field distribution on the antenna aperture is shown in Figure 4-46 (b).

The antenna has a -15-dB impedance matching level within 25.5 ~ 35 GHz, as shown in Figure 4-47 (a), with a gain of 6.7 dBi. Figure 4-47 (b) shows that the $\lambda/4$ chokes reduce the E-plane's antenna back radiation by about 7 dB. Furthermore, the E-plane radiation pattern becomes more symmetric in both half-planes, *i.e.*, $\theta = \pm 0 \sim 180^\circ$. The radiation patterns in the E- and H-plane at four different frequencies are shown in Figure 4-47 (c, d, e, and f). In the H-plane, the cross-polarization is less than -30 dB within the operational bandwidth, whereas E-plane cross-polarization is extremely low. Therefore, it is not shown in the plots. It is important to note that the horn antenna element's H-plane radiation pattern is wider than the E-plane. The 3-dB beamwidth in the E- and H-plane are 70° and 117° , respectively. A wider 3-dB beamwidth in the H-plane is synthesized to achieve maximum flat-beam-switching for the multibeam antenna. Such antenna design could be highly suitable for a dual-polarized waveguide Butler matrix [139]. The proposed geometry also provides a balanced current distribution on the antenna aperture as the packaged microstrip line and the DRGW are quasi-TEM transmission lines [93], [94]. However, by feeding such (TEM) antenna with another type of transmission line (TE or TM), such as SIW, it could unbalance the current distribution due to TE-to-TEM mode conversion. Therefore, the E-plane radiation pattern are asymmetric, as observed in [155].

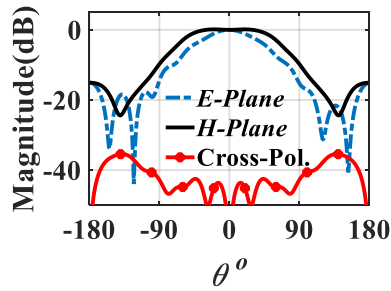
In Figure 4-48 (a), four standalone DRGW antennas are arranged in the H-plane without beamforming network. After a full-wave analysis, the radiation patterns are processed for four sets



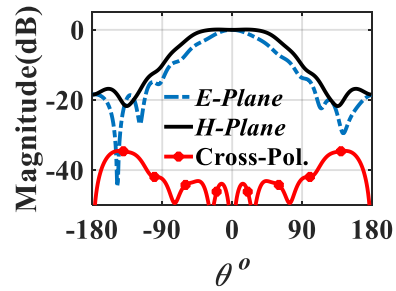
(a)



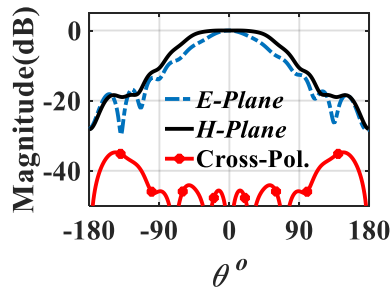
(b)



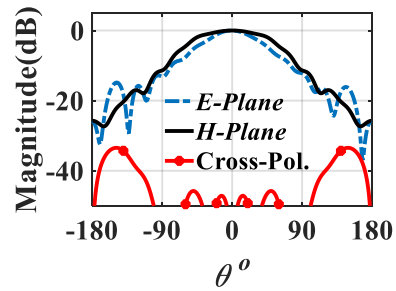
(c)



(d)



(e)



(f)

Figure 4-47. (a) S-parameters, (b) Effect of chokes on antenna back radiation, and radiation patterns at: (c) 28 GHz, (d) 30 GHz, (e) 32 GHz, (f) 34 GHz

of phase distributions 2L, 1L, 1R, and 2R. Radiation patterns obtained by applying following sets of phase distributions:

$$2L \Rightarrow [1\angle 0^\circ + 1\angle +135^\circ + 1\angle +270^\circ + 1\angle +45^\circ]$$

$$1L \Rightarrow [1\angle 0^\circ + 1\angle +45^\circ + 1\angle +90^\circ + 1\angle +135^\circ]$$

$$1R \Rightarrow [1\angle 0^\circ + 1\angle -45^\circ + 1\angle -90^\circ + 1\angle -135^\circ]$$

$$2R \Rightarrow [1\angle 0^\circ + 1\angle -135^\circ + 1\angle -270^\circ + 1\angle -45^\circ]$$

In Figure 4-48 (b), the beams are switched at $\theta = -43^\circ, -14^\circ, +14^\circ,$ and $+43^\circ$, with a gain of 12 dBi. The flat-gain scan profile of the array in the H-plane is a result of antenna element radiation pattern, inter-element spacing, and the extended AMC at the antenna/array aperture that consists of half-height EBG unit cells. With the aperture width $a = 2.2$ mm surrounded by half-height EBG cells, the H-plane element radiation pattern provides two humps off-boresight and a valley in the middle. However, at the higher edge of the frequency band, the H-plane pattern is flat at the top.

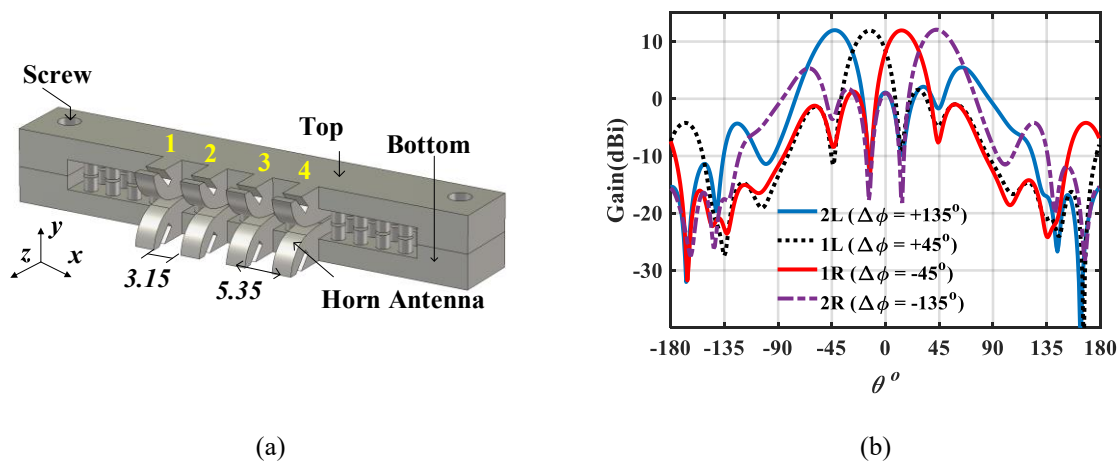


Figure 4-48. (a) 1×4 H-plane DRGW antenna array and (b) Radiation patterns by applying a set of phase distributions

4.3.1.4 Multibeam Antenna Prototype

A. Device Integration

All the design stages are integrated to build a self-shielded multibeam antenna device having the beam-switching capability in the H-Plane. In a full-wave simulation environment, all possible losses (metallic, dielectric, discontinuities) are considered. The prototype assembly is shown in Figure 4-49. The overall design consists of three parts – Two parts of the metallic casing and a single-layer substrate.

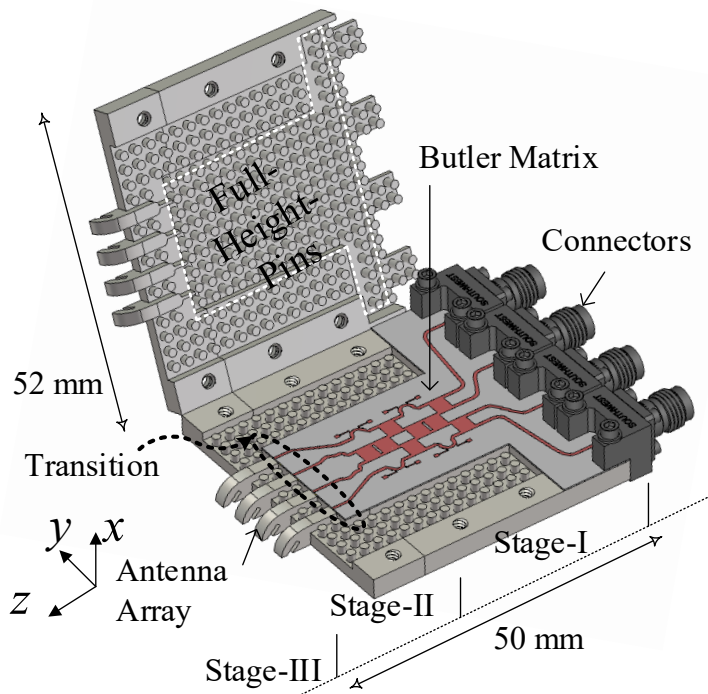
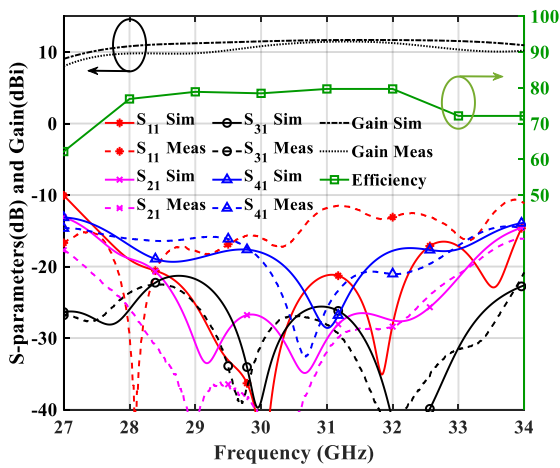


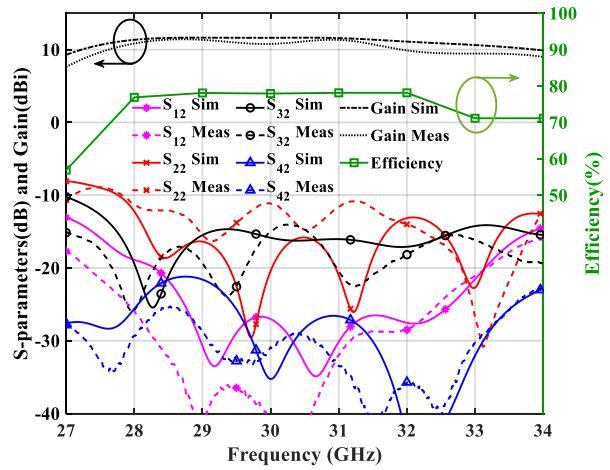
Figure 4-49. H-plane beam-switched multibeam antenna design interior

B. Fabrication, Measurement and Discussion

The simulated and measured S-parameters of the multibeam antenna prototype are shown in Figure 4-50 (a) and (b). Therefore, as the device is symmetric, the results for beam-port#1 (1R) and #2 (2L) are presented only. A bandwidth of 5 GHz (28~33 GHz) is maintained for both ports. Within this bandwidth, the beam-ports are isolated by more than 15 dB. The simulated results are verified with the measurements. The maximum values of the gain for beam-port 1R and 2L are found to be 11.7 dBi, and 11.2 dBi, respectively. Similarly, the antenna efficiency is 78 ~ 80% within 28 ~ 32 GHz, which deteriorates rapidly at the frequency band's edges.

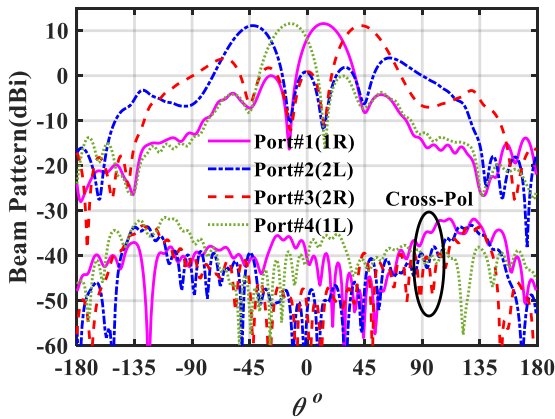


(a)

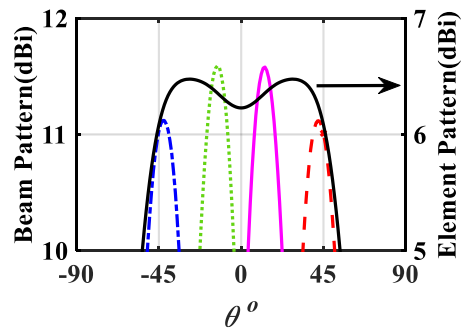


(b)

Figure 4-50. Measured/Simulated S-parameters, gain and efficiency for (a) Beam-port#1 (1R) and (b) Beam-port#2 (2L) excitations



(a)



(b)

Figure 4-51. (a) Simulated co-/cross-beam patterns and (b) Beam patterns and single antenna element pattern 2-dB zoomed view

Far-field radiation patterns of the realized gain are plotted in Figure 4-51 (a) at 30 GHz that is covering a scan-range of $\phi = \pm 42^\circ$ with four switched-fan-beams. The H-plane cross-polarization is below -30 dB in all four beam directions. In Figure 4-51 (b), a 2-dB view is shown for the beam patterns and the antenna element pattern. The H-plane element pattern has a dip of 0.25 dB in the boresight direction ($\theta = 0^\circ$), which contributes to reducing the scan-loss, and it is further supported by the AMC of the half-height EBG unit cells extended

in the H-plane at the array aperture. Thus, the magnitude-decrease for the 2nd beams (2R, 2L) is maintained under 0.5 dB with respect to the 1st beams (1R, 1L).

The measured normalized radiation patterns compared to the simulated patterns are shown in Figure 4-52 (a), (b), and (c) at 29, 30, and 31 GHz, respectively. At 30 GHz, beams are switched at $\pm 14^\circ$, and $\pm 42^\circ$ with the crossing points at -3.5 dB and -3.8 dB, and maximum gain of 11.7 and 11.2 dBi, respectively. The adjacent beams are 28° apart. The measured beam switching performance is in excellent agreement with the simulation. The gain is measured by comparison to the standard horn gain. The values are plotted in Figure 4-50 (a) and (b) for beam-ports 1R and 2L. A drop in the measured gain of about 0.5 ~ 1

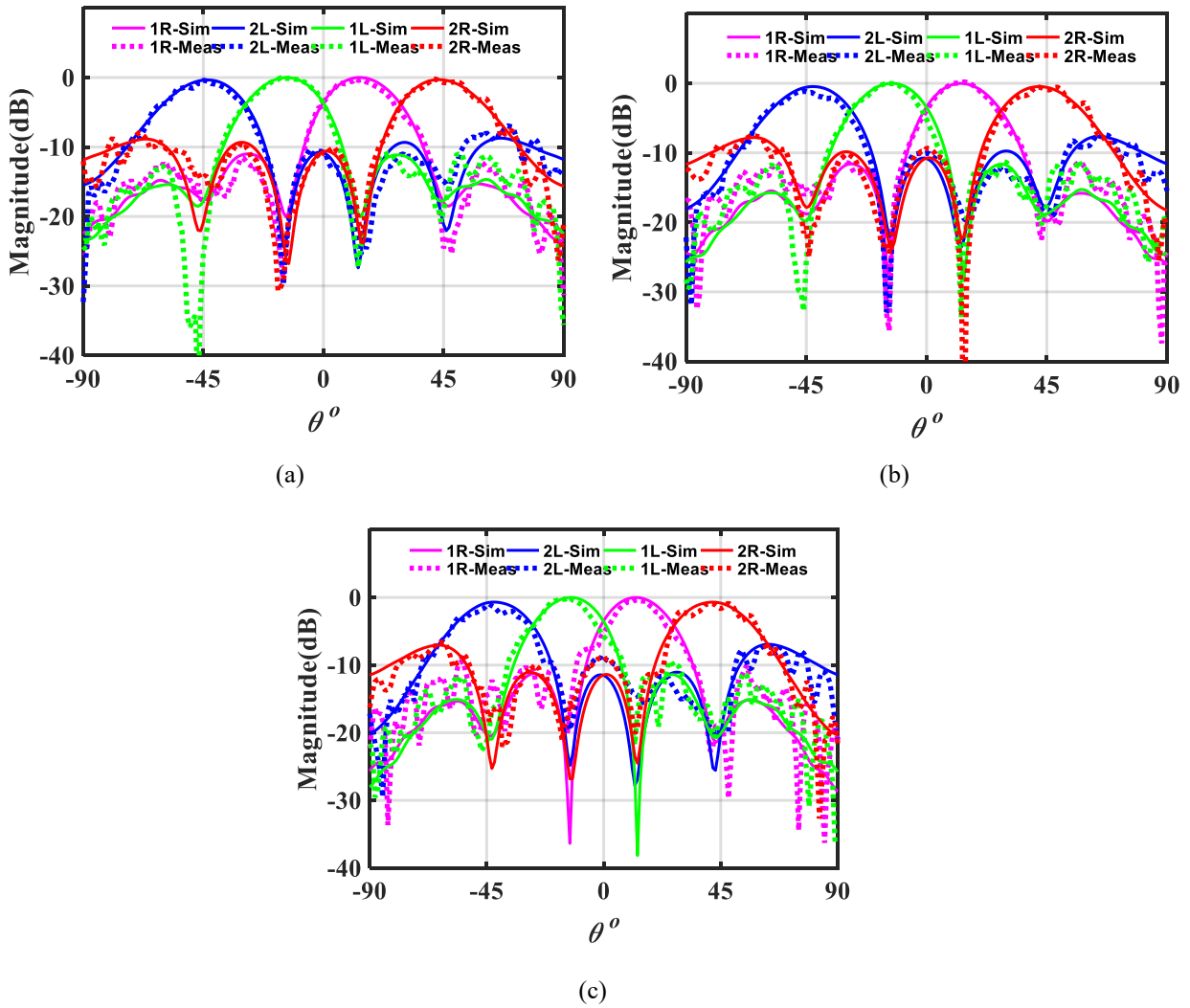


Figure 4-52. Simulated and measured radiation patterns at (a) 29 GHz, (b) 30 GHz, and (c) 31 GHz

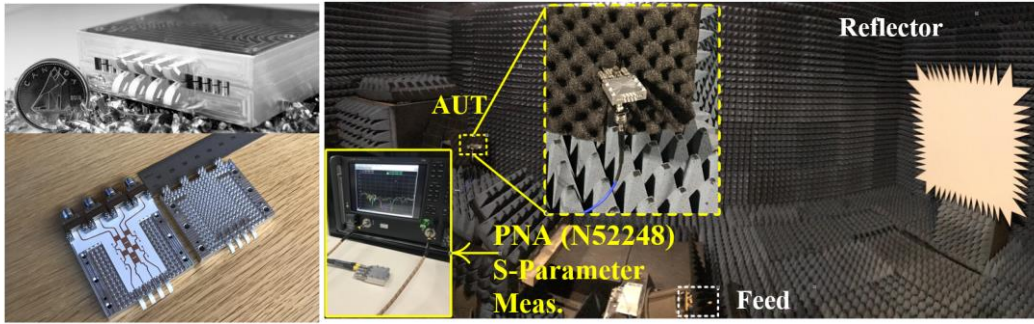


Figure 4-53. Multibeam antenna prototype and the measurement setup. Keysight PNA (N52248) and compact range anechoic chamber

dB is observed at the band edges. The metallic parts of the device are fabricated by CNC machining, whereas the microstrip line Butler matrix is fabricated by standard PCB laser prototyping technology. The prototype photographs and the measurement setup are shown in Figure 4-53.

4.3.2 Summary

PMC packaged single-substrate layer Butler matrix has been presented. The wideband components of a 4×4 Butler matrix have been designed on a single-substrate within a packaged environment. The open-circuit multi-stub-loaded delay-line has been used to enhance the phase shifter bandwidth. The Butler Matrix's antenna ports are terminated by an E-plane-flared horn antenna array designed to provide smaller scan-loss. The Butler Matrix bandwidth is 5 GHz (28~33 GHz) with return loss < -15 dB and isolation > 15 dB. At 30 GHz, insertion loss is 0.8 ± 0.3 dB, and antenna-ports' phase distributions are $\pm 45^\circ$ and $\pm 135^\circ$. The H-plane fan beam-switching covers $\pm 42^\circ$ azimuth range with a maximum gain of 11.7 and 11.2 dBi for 1R and 2R beams, respectively; thus, limiting the scan-loss under 0.5 dB. The self-shielding/packaging concept has simplified the overall device, as two parts of the casing incorporate the AMC textures as well as the antenna array. To utilize microstrip line technology at the higher frequencies, this technique has eliminated the requirement of packaging each component in individual compartments (as reported in [99]). Therefore, the complete circuit has been packaged with a single lid of nails. Excellent 1×4 beam-switching capabilities have been achieved in the H-plane.

The presented switched-beam subarray antenna addresses radiation characteristics and physical geometry limitations, which were highlighted in Section 4.1 and 4.2 subarray designs. As the radiation patterns are fan beams, therefore, it is suitable for beamspace digital beamforming in the plane of wider beamwidths. The subarray antennas could be stacked in the elevation plane with $\approx \lambda/2$ inter-subarray spacing to perform signal processing for digital beamspace beamforming, while the beams are already switched by the analog transformation (Butler matrix) in the azimuth plane. Therefore, the operation of hybrid beamforming, as depicted in Figure 4-28, could be achieved. Such a model is shown in Figure 4-54, in which four switched-beam subarray antennas are stacked vertically, resulting in a frontend of 16 antenna system.

Despite the merits of fan-shaped switched-beams and nearly half-wavelength inter-subarray spacing, the overall prototype is bulky, and it functions in an end-fire fashion. It would be quite challenging to integrate such a bulky design with a compact RF frontend where a multilayer PCB tile-based implementation is needed. Although the aforementioned problems of radiation patterns and inter-subarray spacing have been significantly addressed in this Chapter, Section 4.3; however, it still required a low-profile switched-beam subarray antenna with broadside radiation, which could be efficiently integrated with a compact tile-based multilayer PCB RF frontend for 5G applications.

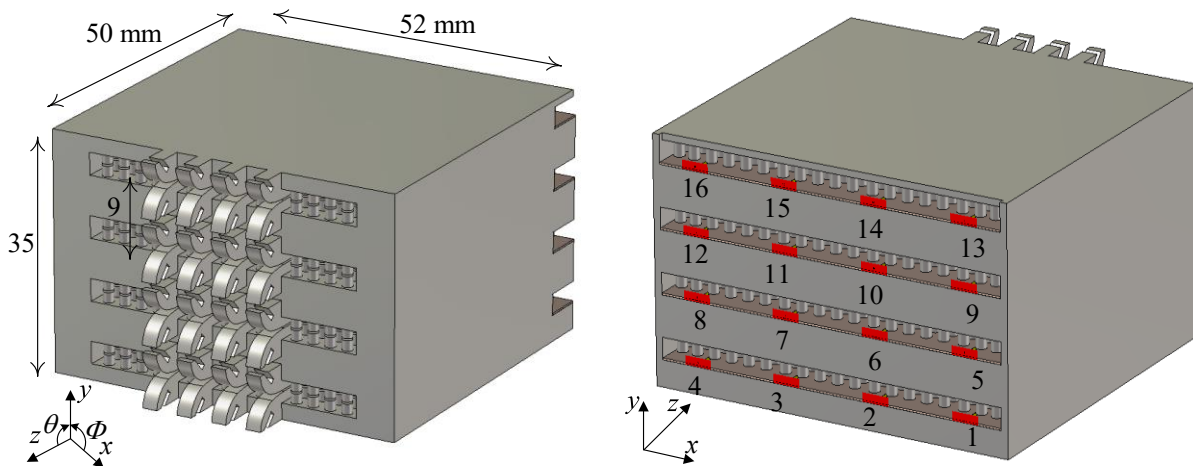


Figure 4-54. 16 – antenna element frontend by stacking four switched-beam subarray antennas in elevation plane

4.4 1-D Switched-Beam Broadside Subarray Antenna

As concluded in Section 4.3.2, the antenna frontend conceived of the fan-beam subarray with end-fire radiation characteristics switched in the H-plane is bulky, and its implementation mechanism might not be suitable for multilayer PCB RF circuitry. Therefore, a novel topology of the folded Butler matrix is presented in this section. Butler matrix's traditional is modified by implementing each hybrid coupler stage on a separate PCB layer. Thus, routing the signal among the vertically stacked SRN layers coupled with the radiating structure to radiate in a broadside fashion. In this regard, this section includes the designs of (1) a 4×4 folded Butler matrix, (2) a single antenna element, and (3) a 1×4 multibeam subarray antenna. The PMC packaged microstrip line technology is used to implement the proposed layouts.

4.4.1 Folded Butler Matrix Layout

The folded Butler matrix can be efficiently laid out on the multilayer PCB technology to accommodate the beamforming network underneath the antenna array arrangement, which is comparatively low-cost and less complicated. The proposed topology is depicted in Figure 4-55. It requires all the fundamental components of conventional design, such as couplers, phase shifters, and crossovers. However, each stage of couplers and phase shifters is stacked vertically, and the RF paths are established through the aperture coupled transition. To effectively utilize the microstrip line PCB technology at 30 GHz, the circuit is developed within a PMC packaged environment, as shown in Figure 4-56. Substrate 1 (Sub1) and substrate 4 (Sub4) are used for the AMC packaging. Whereas the folded Butler matrix is implemented on substrate 2 (Sub2) and substrate 3 (Sub3). The subarray can be extended linearly for the higher-order $n \times n$ implementation; however, here, it is limited to an order of 4×4 . In this way, the beamforming network is hidden under the antenna array. Therefore, due to the compact circuit space, the lateral subarray size could be accommodated around $\lambda/2$ footprints along the y-axis. The subarray design and full-wave analysis are presented in the following Sections.

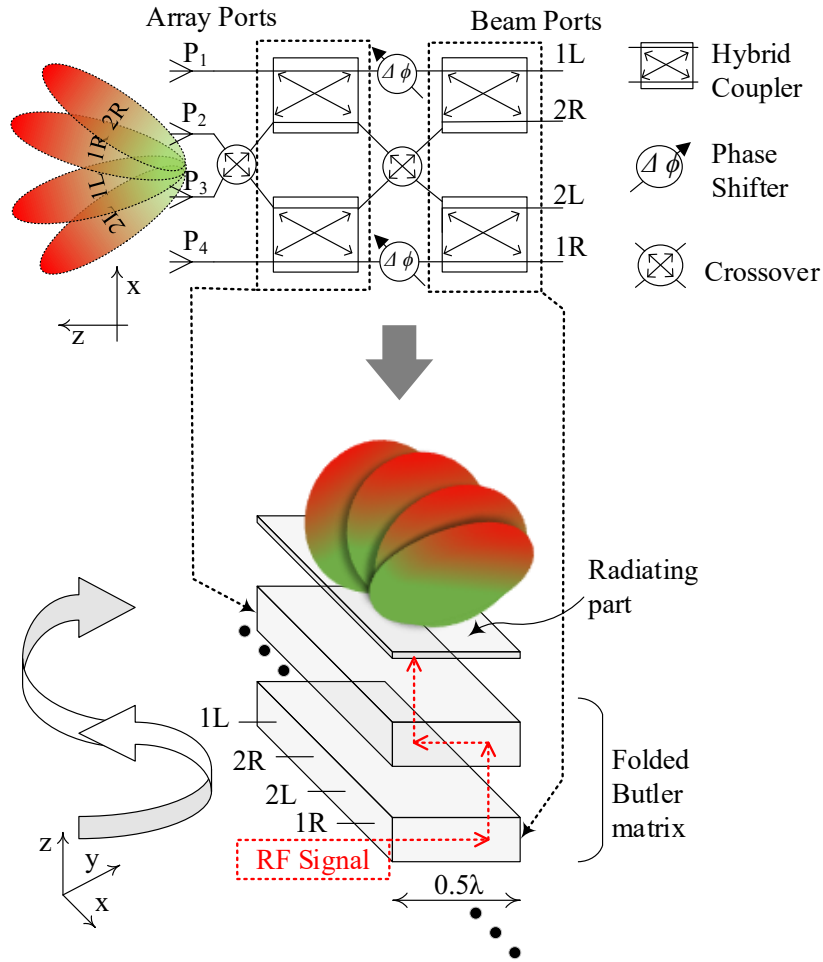


Figure 4-55. Folded Butler Matrix topology layout

The folded Butler matrix circuit is designed at 30 GHz to produce the excitation vectors as $[1, e^{-i\psi}, e^{-i2\psi}, \text{ and } e^{-i3\psi}]$, where $\psi \in [-135^\circ, -45^\circ, 45^\circ, \text{ and } 135^\circ]$ for switched-beam ports 2R, 1R, 1L, and 2L, respectively. For better overall performance, wideband components are designed. The proposed topology is implemented on four PCB layers. Same substrate, Rogers laminate RO3010 ($\epsilon_r = 11.2$, $\tan \delta = 0.002$, at 16 GHz), is used for all the layers with thickness defined as (Sub1) $t_1 = 0.64$ mm, (Sub2) $t_2 = 0.254$ mm, (Sub3) $t_3 = 0.254$ mm and (Sub4) $t_4 = 0.64$ mm, and with the copper cladding of $17 \mu\text{m}$. Full-wave solver CST-MWS is used in which all the dielectric and metallic losses are considered for the simulation. In the following sections, the

design principles and performance are given for each component, which is integrated altogether to conceive a folded Butler matrix switch-beam antenna subarray, as shown in Figure 4-56.

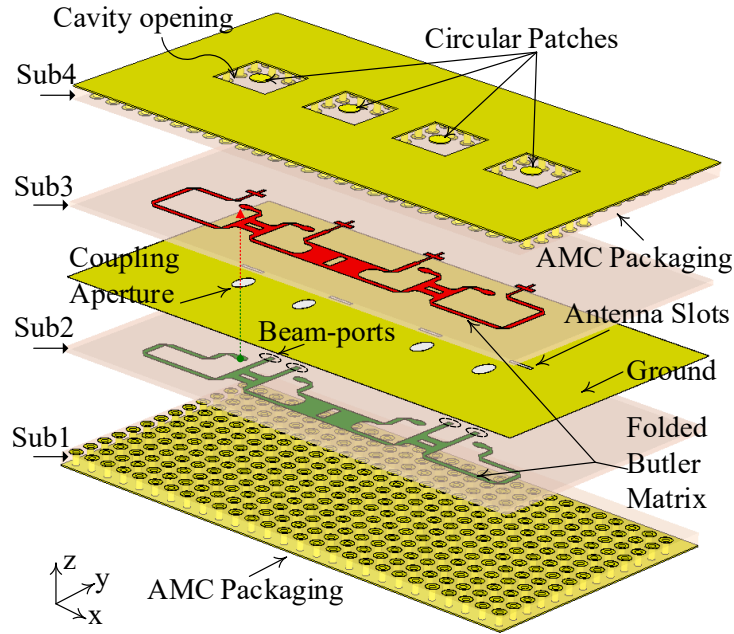


Figure 4-56. Folded Butler Matrix implementation with packaged microstrip line technology

A. Packaged Microstrip Line

The PMC packaging concept, elaborated in Chapter 3, is utilized for packaging the microstrip line. An AMC packaging layer is realized by the 2-D distribution of an EBG

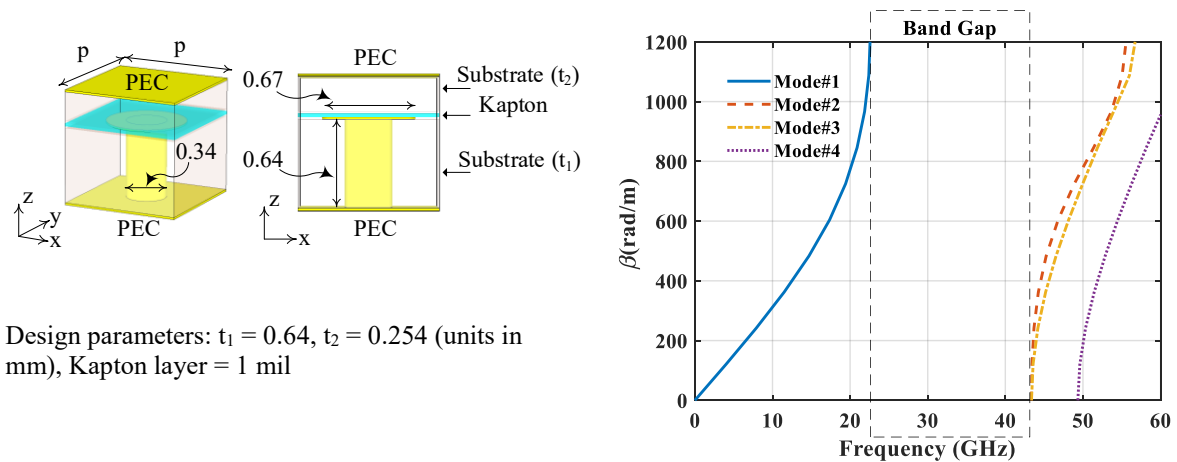


Figure 4-57. EBG unit cell design parameters (units in mm) and its bandgap characteristics

unit cell. The EBG unit cell's design parameters and its bandgap characteristics are shown in Figure 4-58. . It consists of two substrates, RO3010 (Sub1 and Sub2), with one mil thick layer of Kapton in between them. The unit cell is designed in the Eigenmode solver of CST-MWS with periodicity in the x – and y- directions. The propagation constants' phase variation along the x-axis is extracted for the first four modes and plotted in Figure 4-58. A bandgap of 21 GHz is achieved from 22.5 to 43.5 GHz.

In the previous sections, the AMC packaging lid has been positioned away from the microstrip line by a distance that does not affect its characteristics impedance substantially. However, here it is kept just 1 mil away from the microstrip line to utilize the packaging concept more effectively. Furthermore, it is beneficial in terms of broad bandgap characteristics, as the gap between AMC and the microstrip line traces is small, and the bandgap is wide. Ideally, if the gap is kept infinitesimal, the maximum possible bandgap could be extracted from the structure. Therefore, in the present design of Figure 4-58, the transmission line is designed within the packaged environment in which a 1 mil layer of Kapton is used to insulate the microstrip traces from the AMC conductor. The optimum

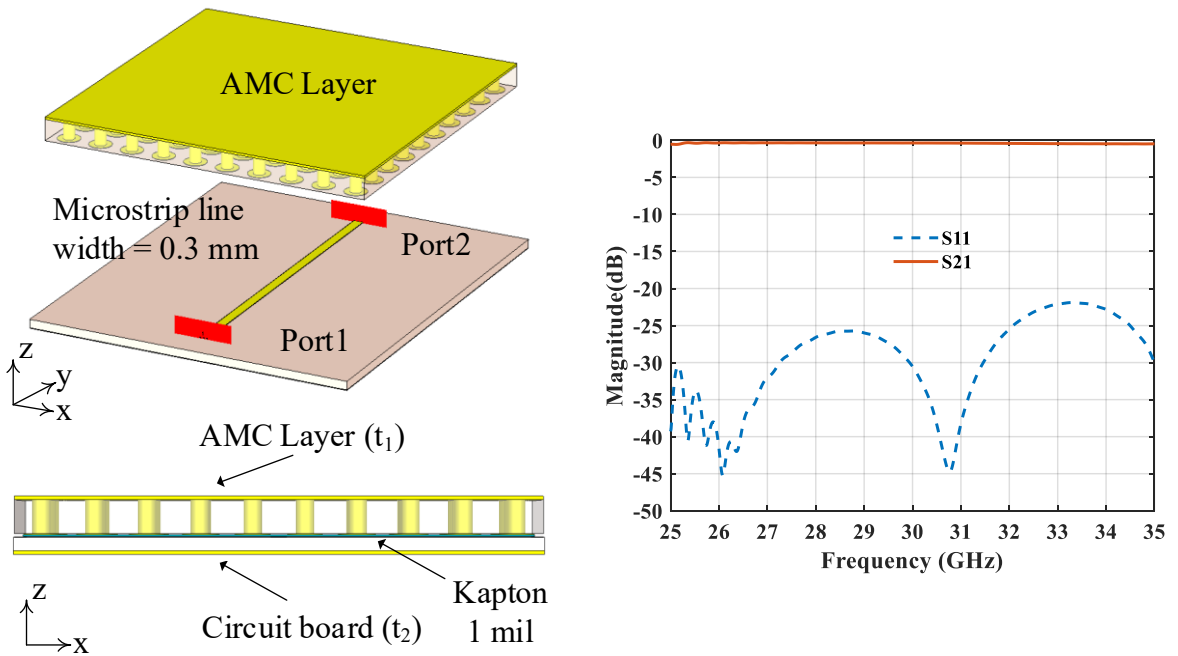


Figure 4-58. AMC packaged microstrip line (exploded model view and cross-section view), and S-

reflection and transmission characteristics are achieved with the trace width of 0.3 mm within a packaged environment, as shown in Figure 4-58.

B. 3-dB Quadrature Coupler and Crossover

The coupler's design parameters and performance are shown in Figure 4-59. With coupler width, $A = 1.3$ mm, length $B = 1.25$ mm, and $r = 0.3$ mm, a matching of -15 dB along with 15 dB port-isolation and quadratic phase variation within $\pm 1^\circ$ are achieved from 27 to 32 GHz. Within this range, the coupling is -3.3 ± 0.1 dB. Furthermore, the slit parameters "a" and "b" play a critical role in controlling the S-parameters. The length parameter "a"

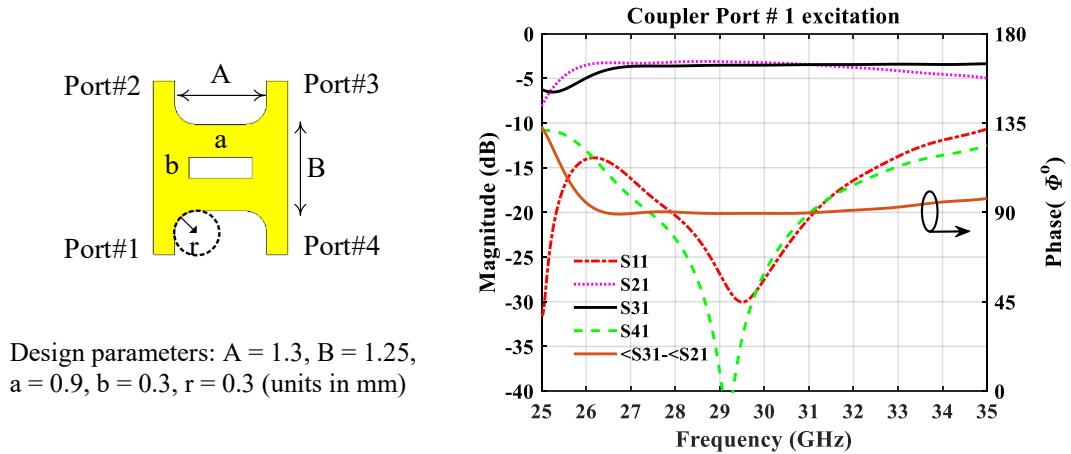


Figure 4-59. Coupler's design and S-parameters

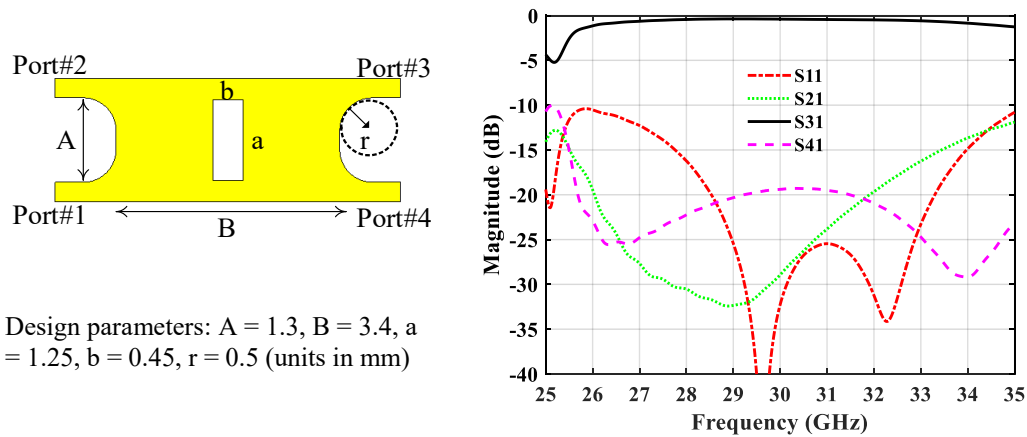


Figure 4-60. Crossover's design and S-parameters

is inversely proportional to the resonance adjustment, whereas its width “b” is responsible for tuning the isolation (S_{41}). The coupling coefficients (S_{21} , S_{31}) are also highly influenced by the slit length. The optimum design parameters are given in Figure 4-59.

On similar principles, a crossover transmission line having width “A” and length “B” is designed as shown in Figure 4-60. In this case, the slit width “b” has no substantial effect on the crossover’s performance. However, its length parameter “a” plays a critical role in optimizing its reflection and isolation characteristics, and it is observed that length is inversely proportional to the tuning frequency for reflection coefficient (S_{11}) and isolation levels (S_{21} , S_{41}). The crossover bandwidth is 28 ~ 32 GHz with -15 dB reflection coefficient and isolation ≥ 20 dB. The level of maximum transmission coefficient is -0.3 dB at the center frequency.

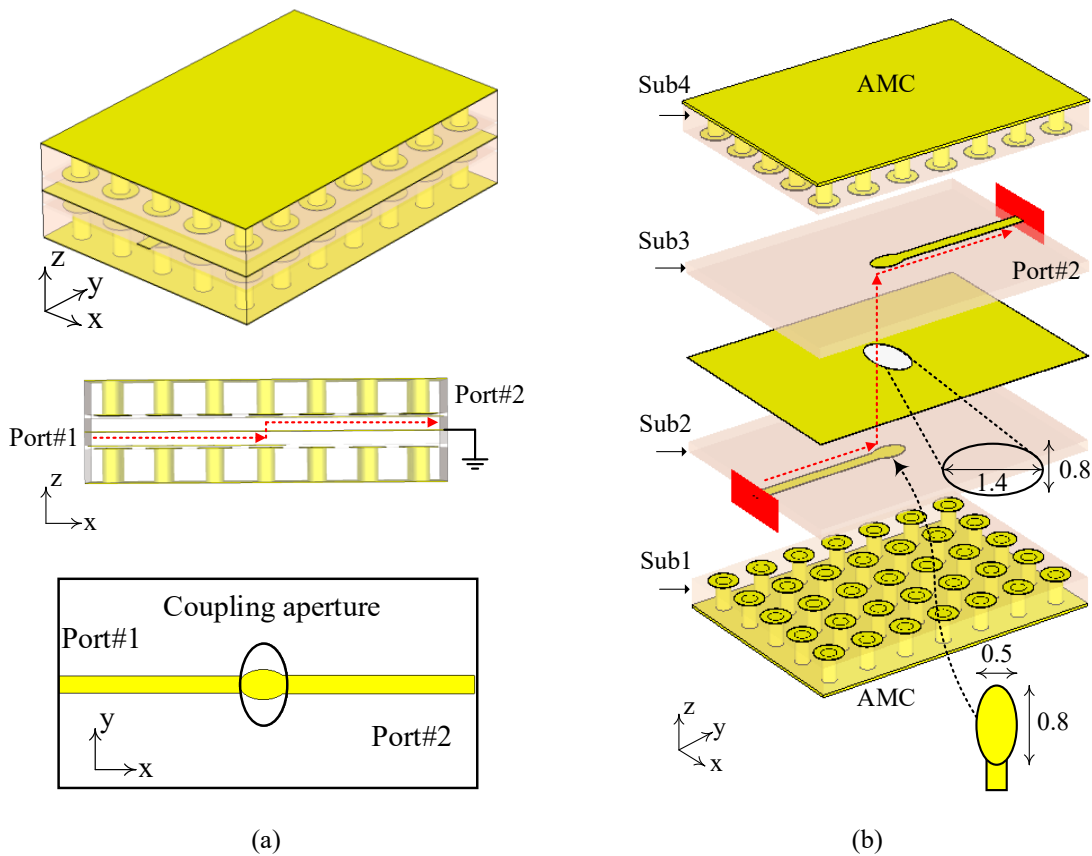


Figure 4-61. Two-layer packaged microstrip line transition: (a) Isometric and cross-section views and (b) Exploded model view

C. Two-Layer Packaged Microstrip Line Transition

To route the RF signal from one layer of the Butler Matrix to another, a PMC packaged microstrip transition is designed. The isometric and cross-section views are shown in Figure 4-61 (a). The multilayer transmission line is a symmetric structure in the XY-plane with the common ground in the middle. The vertically stacked microstrip transmission lines end up with elliptic-shape patches which couple the signal through an elliptical aperture engraved within the common ground, as shown in Figure 4-61 (b). For instance, the excited Port#1, marked in the red dotted line, reaches Port#2 after transit through the coupling aperture. The optimum design parameters are given in Figure 4-61 (b). The transmission line S-parameter shows a wideband performance from 27 ~ 34 GHz with a maximum transmission coefficient of -0.3 dB and a reflection coefficient < -30 dB, as shown in Figure 4-62.

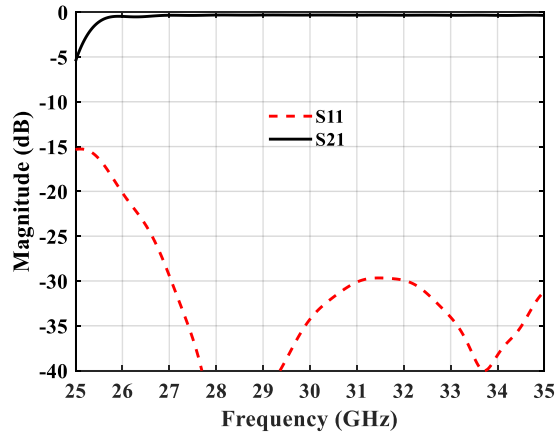


Figure 4-62. Two-layer packaged microstrip line transition S-parameters

D. 4×4 Butler Matrix

To obtain the phase distribution $\psi \in [-135^\circ, -45^\circ, 45^\circ, \text{ and } 135^\circ]$ for four switched-beams 2R, 1R, 1L, and 2L with an order of 4×4 Butler matrix, a PMC packaged folded Butler matrix is developed by using beamforming components presented in the previous Sections. As compared to the conventional layout, the lateral dimensions are substantially reduced in the y-axis in the present design. Butler Matrix dimensions and its isometric view

are shown in Figure 4-63 (a). The phase distribution network is implemented in two stages. Beam-ports (Port#1 ~ Port#4) and antenna array-ports (Port # 5 ~ Port # 8) are defined at the first level and second level, respectively, as shown in Figure 4-63 (b). To incorporate the 45° phase shifts, the delay lines are accommodated at the first stage. The front and back views of microstrip line traces of folded Butler Matrix in the XY – plane are shown in Figure 4-63 (c).

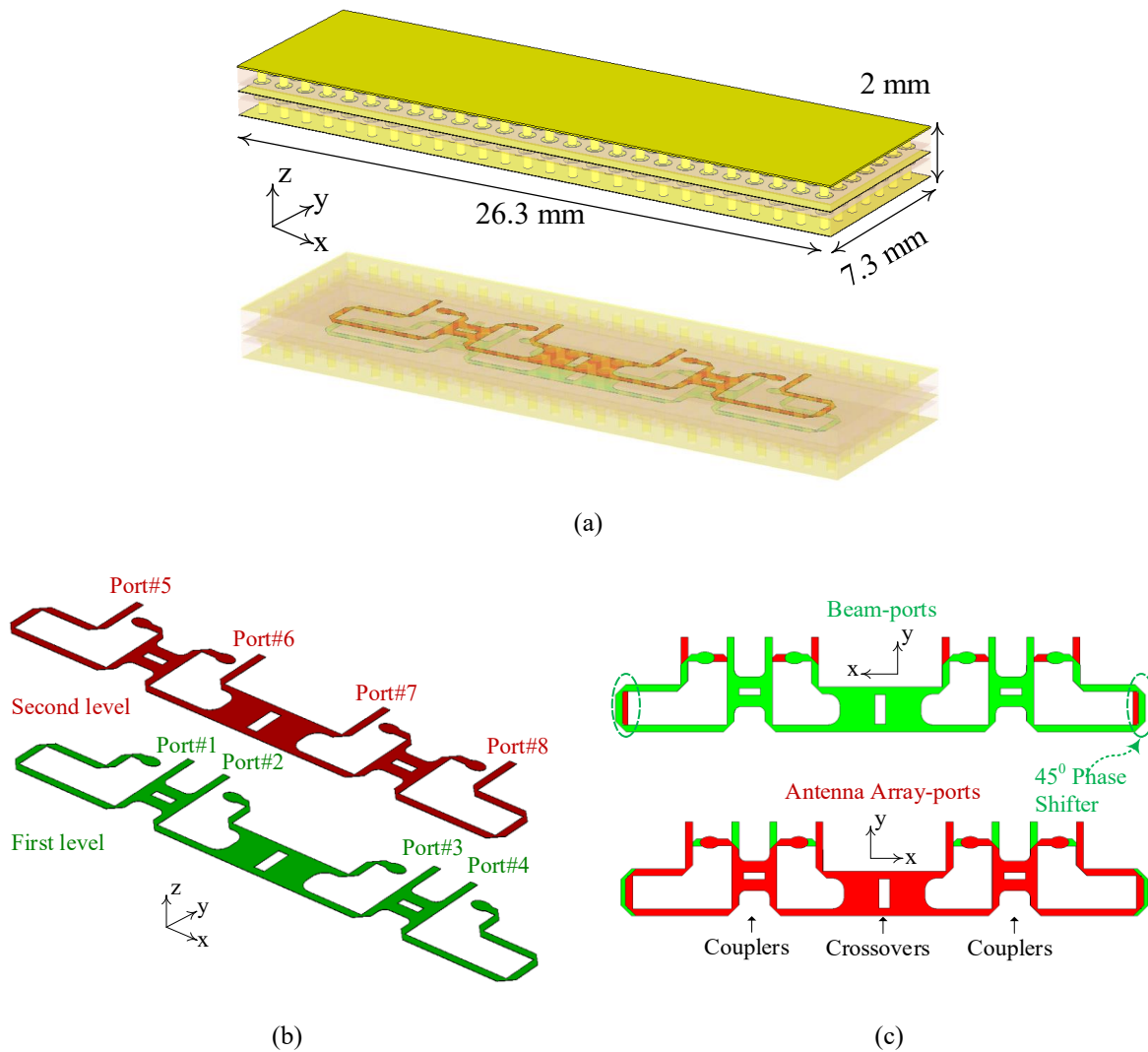


Figure 4-63. PMC packaged 4×4 folded Butler matrix: (a) Geometry and dimensions, (b) First and second stage, and (c) Front and back views of folded microstrip traces

The 4×4 Butler matrix design is simulated in CST MWS. Therefore, as the design is symmetric, the analysis for two ports (Port#1 and Port#2) is considered sufficient. The performance is verified by comparing the simulation results obtained from the Transient Time Domain Solver and Frequency Domain Solver. The Time Domain 3D full-wave solver of CST MWS comes with both finite integration technique (FIT) and transmission line matrix (TLM) implementations included in a single package. The Time Domain Solver performs broadband simulations in a single run with the classical finite-difference time-domain (FDTD) method [156].

Similarly, the Frequency Domain Solver is based on the finite element method (FEM), that offers excellent simulation performance for many types of component and subsystems.

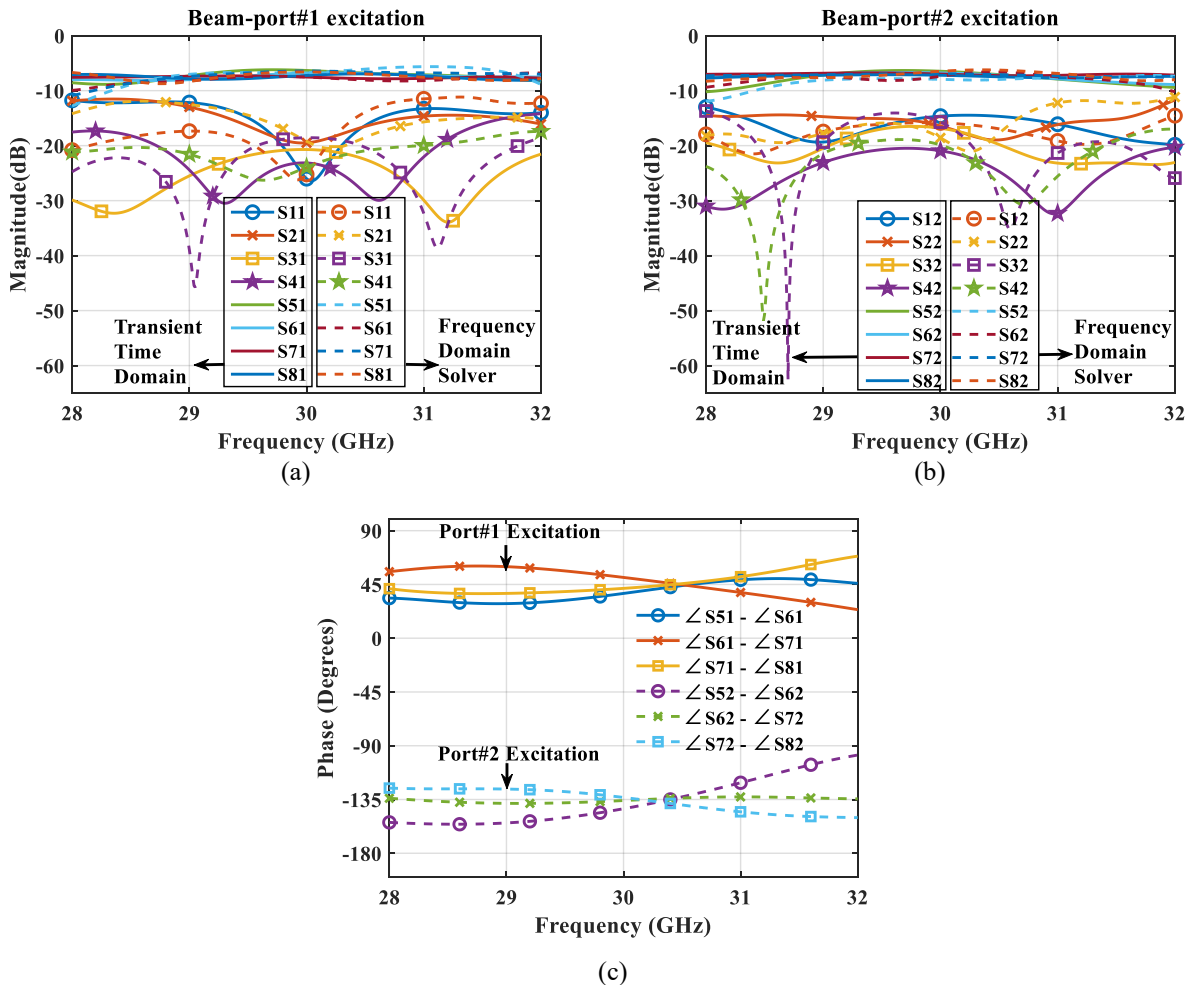


Figure 4-64. Folded Butler matrix S-parameters. Magnitude (a) Port#1 excitation, (b) Port#2 excitation, and (c) Phase difference at array-ports for Port#1 and Port#2 excitation

The CST MWS suite also incorporates the Integral Equation Solver, based on the method of moment (MOM) technique [157]. As CST MWS can provide full-wave Time Domain and Frequency Domain analysis by solving Differential and Integral Equations using different methods such as FIT and FEM, therefore the results of the 4×4 Butler matrix design obtained from the Time Domain Solver are also verified by its Frequency Domain Solver [157].

Figure 4-64 (a) shows that the magnitude of S-parameters for Port#1 excitation is shown. From 28 to 32 GHz, the level of reflection coefficients and ports' isolation is less than -10 dB and -15 dB, respectively. At the center frequency, the transmission coefficient's magnitude is -6.5 dB, with a variation of ± 0.5 dB. A reasonably similar performance is observed for Port#2 excitation as well. Butler matrix's transmission performance degrades at the edges of the frequency band. The comparison of Time Domain and Frequency Domain full-wave analysis shows a good agreement. The phase differences among the array-ports are plotted in Figure 4-64 (c) for Port # 1 (1R) and Port # 2 (2L) excitations. Ideally, the Butler matrix should produce $\psi = 45^\circ$ and -135° for an order of 4×4 Butler matrix, which is observed at 30.5 GHz in Figure 4-64 (c). However, within the band away from this single frequency point, a variation of $\pm 10^\circ$ is observed as an extreme scenario.

4.4.2 Antenna Element

While keeping in mind the AMC packaging used for the folded Butler matrix topology, an antenna element is designed accordingly, which could be efficiently integrated within this environment. In Figure 4-65, the design parameters are defined by showing a 3-D view and the isometric view in which only the metal parts are highlighted. Same as the design of Butler matrix, the antenna element consists of four layers of substrates (Sub1, Sub2, Sub3, and Sub4) having $17 \mu\text{m}$ copper cladding. For all four layers, Rogers laminate RO3010 ($\epsilon_r = 11.2$, $\tan \delta = 0.002$) is used, and the thickness of Sub1, Sub4, and Sub2, Sub3 is 0.64 mm and 0.254 mm, respectively. A 1 mil Kapton layer is deposited between the AMC layer and the microstrip line circuit to guarantee insulation. A slot is engraved in the ground, exposed to the microstrip feed line at the top and AMC underneath.

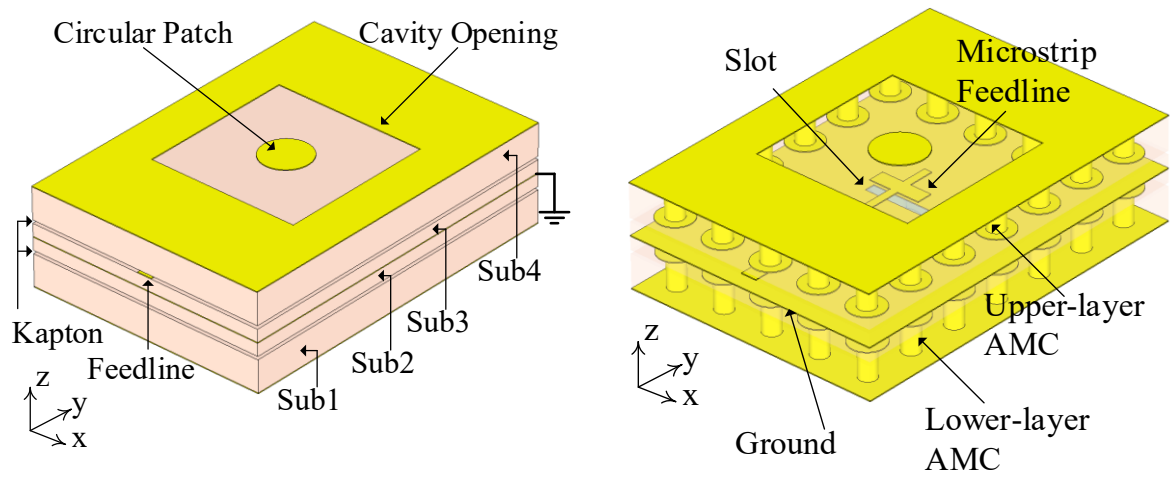


Figure 4-65. Defining antenna element design parameters in its perspective and isometric view

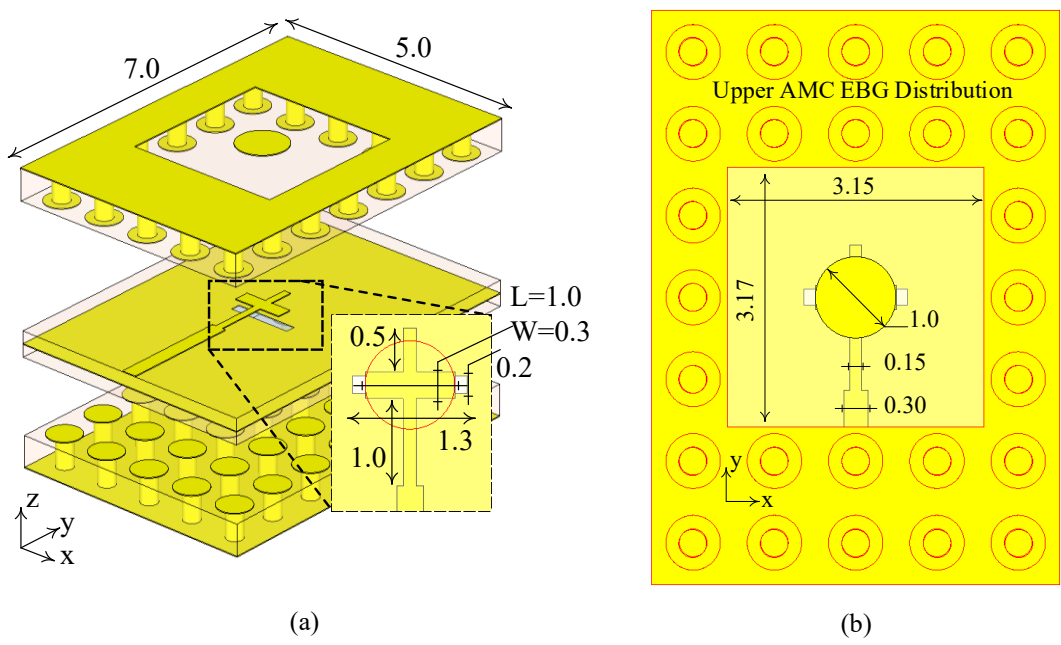


Figure 4-66. Antenna design parameters: (a) 3D exploded model view and (b) Front view

The antenna is designed in a four-layer structure as it needs to be integrated into this fashion within the Butler matrix subarray. The upper AMC has a cavity opening where a circular patch is placed in the middle. This slot-coupled patch is excited through the cross-shaped microstrip feedline for broader bandwidth. Therefore, the cross-shaped structure parameters, along with the

stub, are vital in tuning the antenna's desired reflection coefficient. With a line width of 0.3 mm, the port impedance of the antenna is set to be the same as the Butler matrix array-ports impedance. Close to the slot coupling region, the line width is decreased to 0.15 mm for a section of length 1 mm. This is to achieve better matching. For more design details of the packaged interior and the antenna design parameters, an exploded model view and a front view are shown in Figure 4-66.

The length (L) and width (W) of the cross-shaped structure along with the transverse-to-the-slot stub section are vital tuning parameters. The effect of “L” and “W” over the impedance bandwidth is shown in Figure 4-67 (a) and (b), respectively. It can be seen that -10 dB impedance bandwidth increases as “L” increases by flattening the resonance curve. Whereas “W” plays a role as a part of the stub length for resonance frequency tuning. In Figure 4-68, the optimum results are plotted for “L = 1 mm” and “W = 0.3 mm” with -10 dB impedance bandwidth of 4 GHz (28 ~ 32 GHz). For verification purposes, the S₁₁ results obtained by time domain and frequency domain solvers of CST MWS are also compared. At center frequency, the absolute electric field distributions at the antenna aperture cross-sections are plotted in Figure 4-69.

The antenna directivity 3-D plot is shown in Figure 4-70 (a) with a maximum value of 5.22 dBi at the center frequency. The normalized radiation patterns at two principle planes ($\phi = 0^\circ$, and $\phi = 90^\circ$) are shown in Figure 4-70 (b). At $\phi = 90^\circ$, the x-pol are less than -40 dB, therefore, it is not visible in the plot. Whereas, at $\phi = 0^\circ$, the x-pol are under -35 dB. The 3-dB beamwidth of the

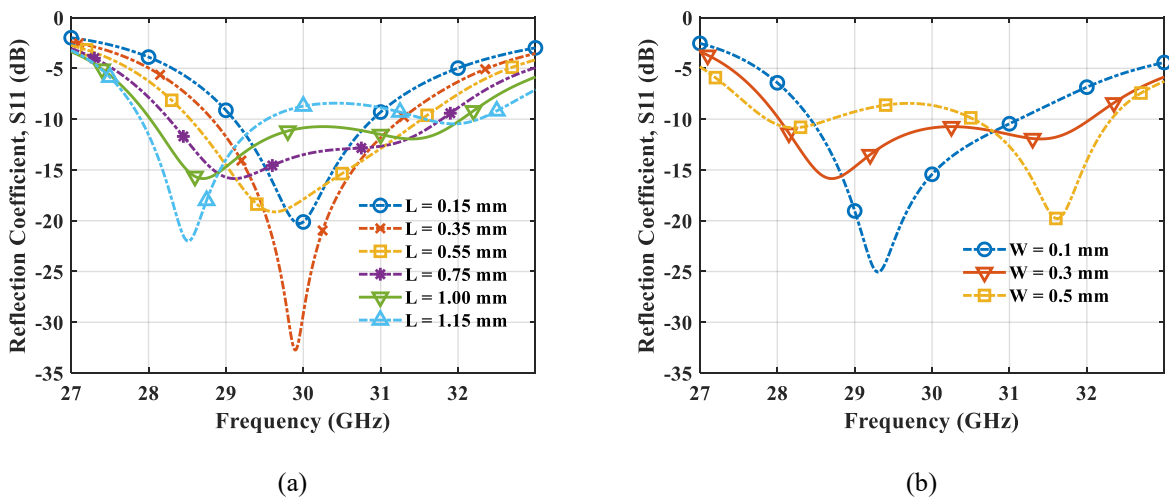


Figure 4-67. Reflection coefficient parametric study for (a) Length “L” and (b) Width “W”

antenna is 120° and 94° at $\phi = 90^\circ$ and $\phi = 0^\circ$, respectively. The radiation patterns are symmetric within a 90° view range.

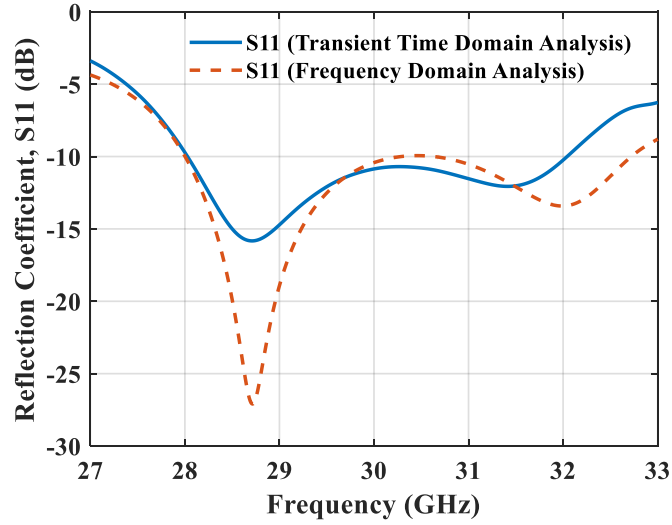


Figure 4-68. Reflection coefficient (S_{11}) performance comparison

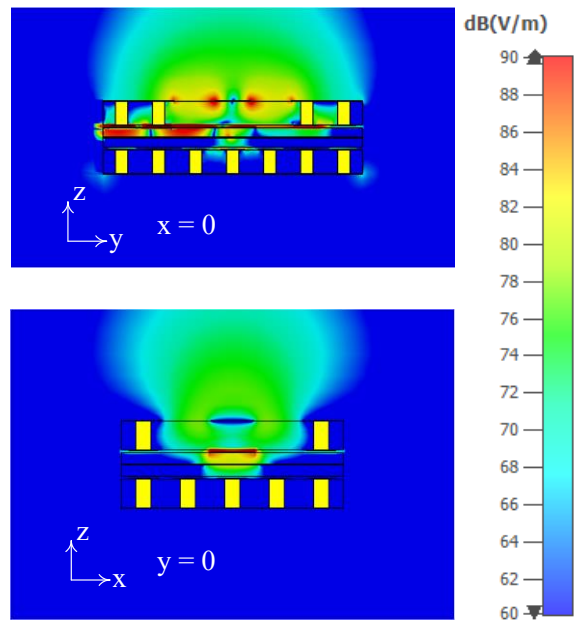


Figure 4-69. Cross-section views of absolute electric field distribution at antenna aperture

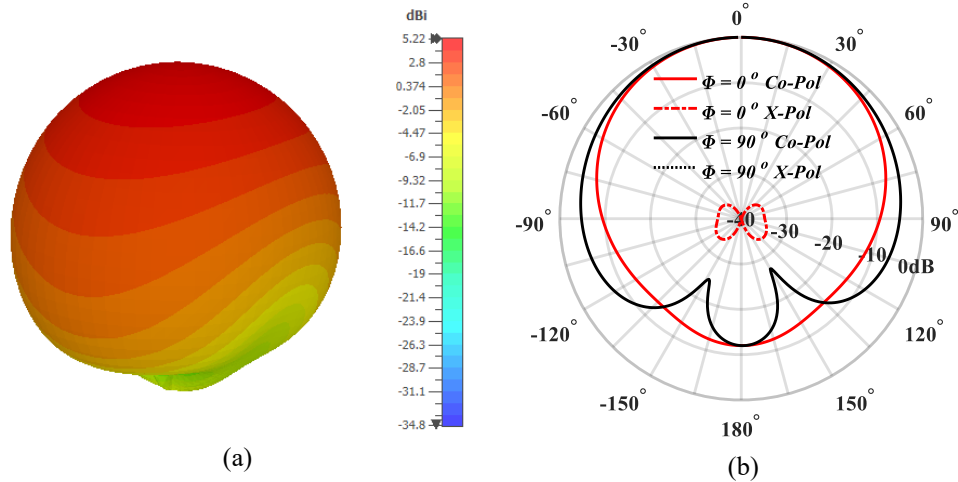


Figure 4-70. Antenna directivity: (a) 3D plot and (b) Polar plot at two principle planes

4.4.3 Broadside 1×4 Switched-beam Subarray

The folded Butler matrix and the antenna element developed in the previous sections are integrated to conceive a 1×4 multibeam subarray antenna. Figure 4-71 (a, b) shows the exploded model and subarray front view. The inter-element spacing is 5.47 mm, nearly half wavelength at 28 GHz. The multibeam antenna beam-ports are highlighted in the isometric view of Figure 4-71 (c). Therefore,

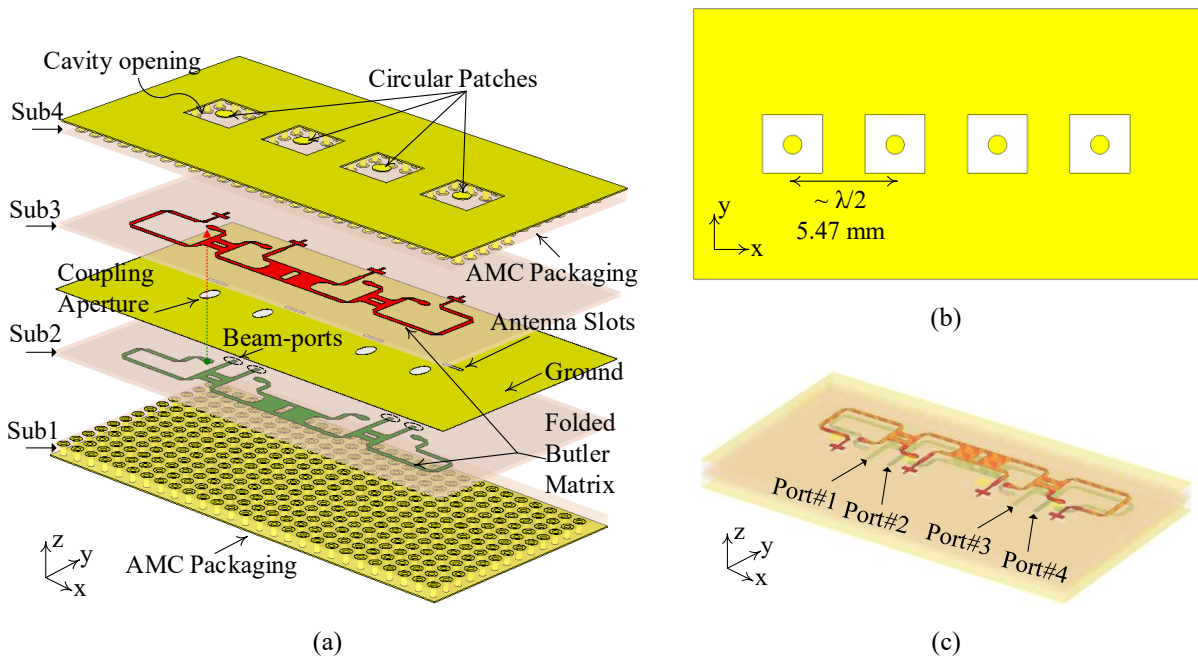


Figure 4-71. Packaged folded Butler matrix: (a) Exploded model view, (b) Antenna array aperture view, and (c) Beam-ports identification in isometric view

as the design is symmetric, the S-parameters for Port # 1 and Port # 2 excitations are plotted only. Figure 4-72 shows that the reflection coefficients (S_{11} , S_{22}) are less than -10 dB from 27 to 32 GHz, and all ports are isolated by more than 10 dB within this range. The normalized cartesian plots and 3D radiation patterns are shown in Figure 4-73 for all four beam-ports. The maximum directivities for the inner (1R, 1L) and outer (2R, 2L) radiation beams are found to be 11.1 dBi and 10.6 dBi, respectively. The beams are switched at $\theta = \pm 15^\circ$ and $\theta = \pm 38^\circ$.

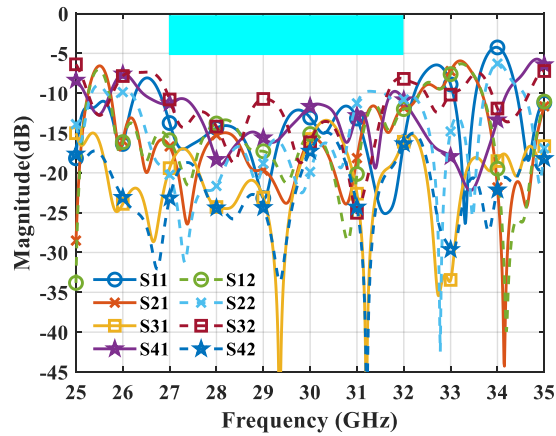


Figure 4-72. S-parameters for Port #1 and Port #2 excitation

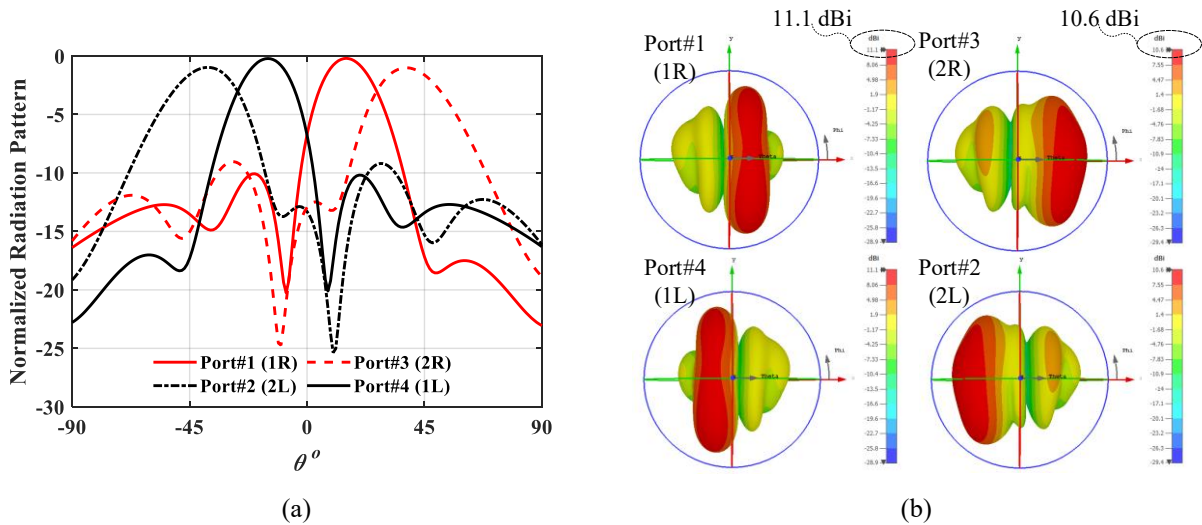


Figure 4-73. Beam switching performance. (a) Cartesian plots at plane $\phi = 0^\circ$ and (b) 3D radiation patterns

4.4.4 Summary

A modified design of the folded Butler matrix has been presented to accommodate the microwave beamforming network under the antenna array's physical footprints. Butler matrix lattice size is reduced by more than 50 %. Furthermore, the PCB aperture-coupled antenna elements are integrated within the AMC packaged environment for a broadside radiation characteristic. The Butler matrix and antenna element are designed for a 28 ~ 32 GHz operation frequency band. The directivity of the single antenna element is 5.22 dBi. For a 1×4 beam-switched subarray antenna, the directivities are 11.1 dBi and 10.6 dBi for the inner and outer radiation beams, respectively.

All the problems mentioned above were summarized in the previous sections were related to subarray antenna radiation characteristics and geometry layouts, which have been addressed in this section. The present subarray antenna design has the following merits: (1) switched multibeam, (2) PCB implementation as a whole, (3) compact size to accommodate the number of subarrays of a large-scale antenna frontend, and (4) aperture-coupled integrated antenna design for broadside radiation. The folded Butler matrix multibeam subarray antenna is the right candidate for a compact size tile-based multilayer PCB RF frontend for hybrid beamforming with all these merits.

Chapter 5

Hybrid Analog-Digital Beamforming

In this Chapter, two models of hybrid beamforming are presented. In the first model, the multibeam subarray antenna of Section 4.3 is used to construct a 16-element antenna frontend. Similarly, in the second model, the folded Butler matrix subarray antenna of Section 4.4 is used. The objective is to arrange the subarray antennas efficiently to perform beamspace beamforming. Thus, the overall multibeam frontend should be capable of performing digital beamspace beamforming in one plane (V-plane) and analog beam-switching in the other plane (H-plane).

5.1 First Model

The hybrid beamforming model depicted in Figure 5-1 can be realized by using the H-plane beam-switched subarray antenna presented in Chapter 4, Section 4.3, previously. The subarray antennas

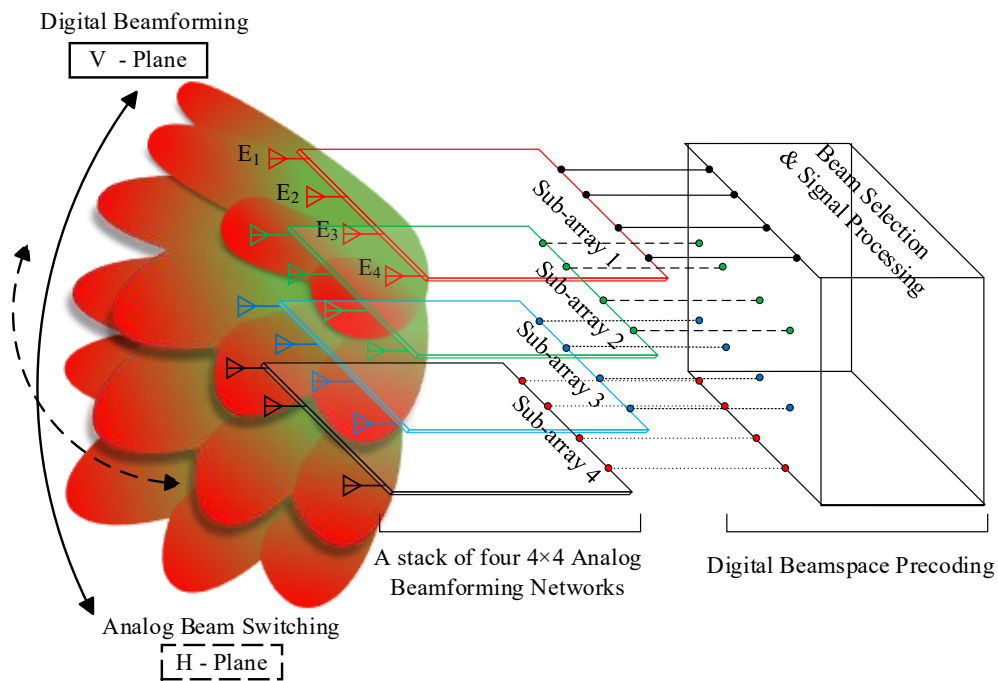


Figure 5-1. First model of hybrid beamforming based on H-plane beam-switched subarray antenna

can be stacked in the vertical plane to perform digital beamforming in the Vertical E-plane. This concept is demonstrated in Figure 5-2. Four subarray antennas, with H-plane beam switching, are stacked in the vertical plane with an inter-subarray spacing of $9\text{ mm} < \lambda$ at 28 GHz. The 16 DRGW horn antenna array's overall dimensions, which consists of four packaged beamforming networks,

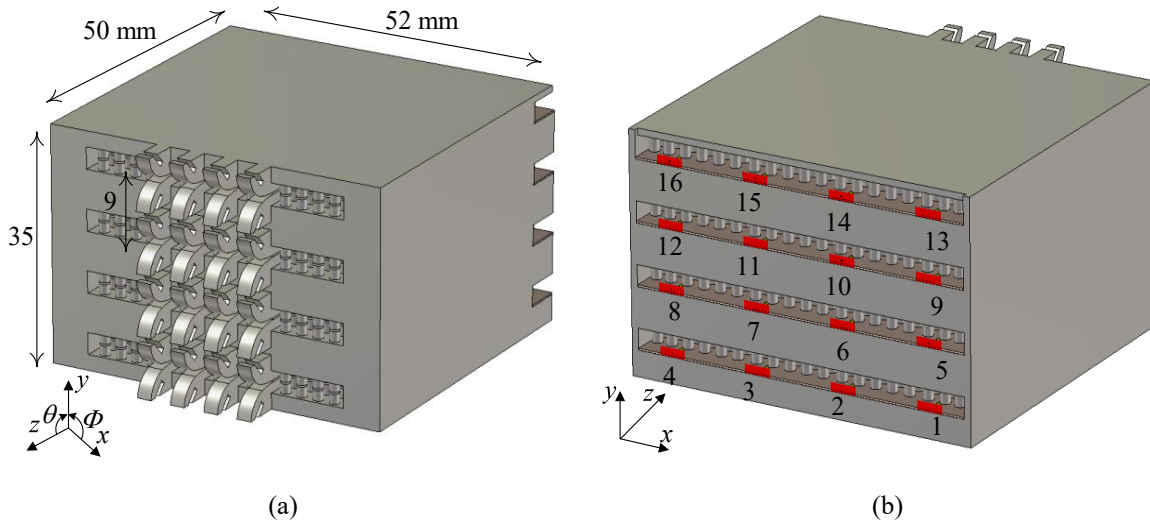


Figure 5-2. Vertically stacked subarrays to build a 4×4 antenna frontend for hybrid beamforming. Perspective views showing (a) Front and (b) Back

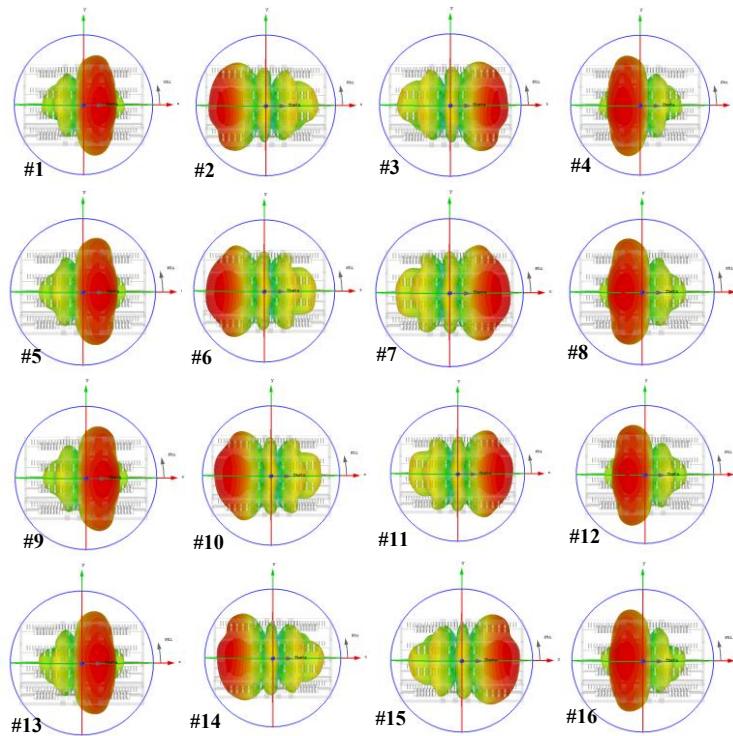


Figure 5-3. Directivity patterns from full-wave analysis of a 16-ports antenna system of first model

are given in Figure 5-2 (a). It is a 16-port network, as shown in Figure 5-2 (b). The full-wave analysis is performed in the Time Domain Solver of CST – MWS. In Figure 5-3, 3-D radiation patterns are given in the spherical coordinate system.

For a better understanding, the 3-dB contours of the radiation pattern are plotted on Azimuth/Elevation-plane as shown in Figure 5-4. The beams at 2L (second left), 1L (first left), 1R (first right), and 2R (second right) are switched at $\theta = -42^\circ$, -14° , 14° , and 42° , respectively, with wider 3-dB beamwidths in the V-plane.

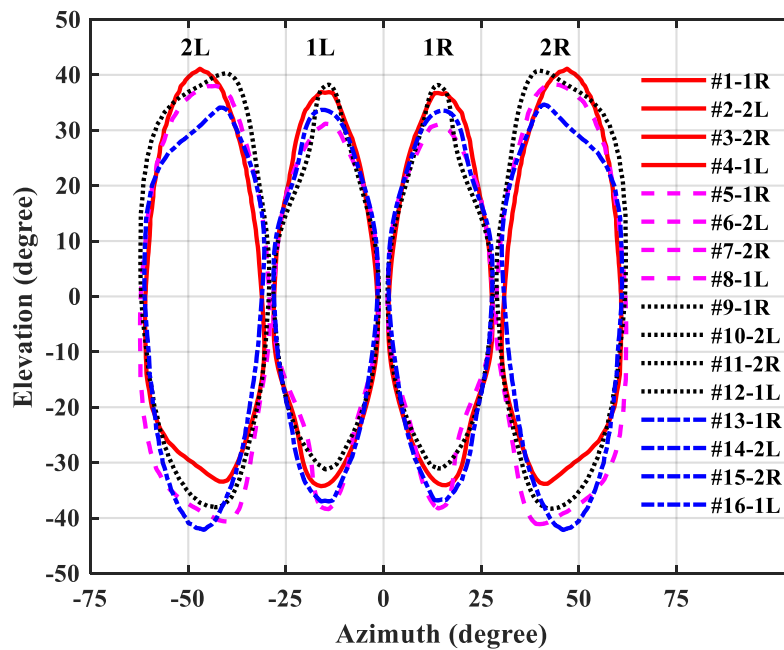


Figure 5-4. 3-dB radiation beams' contours of the first model 16-ports antenna system at 30 GHz

From the radiation pattern characteristics of all four subarray antennas plotted in Figure 5-4, the 3-dB beamwidths toward a specific θ -switched directions (2L, 1L, 1R and 2R) are nearly covering the same Azimuth/Elevation-plane. Therefore, digital beamforming can be applied in the V-plane. For instance, a multibeam frontend is considered in a receiving mode. Among the four H-plane beams (2L, 1L, 1R, and 2R), a single beam can be selected from each subarray by using a single-pole four throw (SP4T) switch as shown in Figure 5-5. These selected signals in the received mode can be represented as X_m , where $m = 1, 2, 3,$ and 4 in the given scenario of Figure

5-6. Therefore, as given in (5-1), the received signals from each subarray antenna can be represented in the vector notation as $\mathbf{X} = [x_1, x_2, x_3, x_4]^T$. For beamforming in the V-plane, each signal is multiplied with a complex coefficient W_{nm} function and added to generate “n” number of $Y_n(\theta_n)$ digital beams in the direction of arrival.

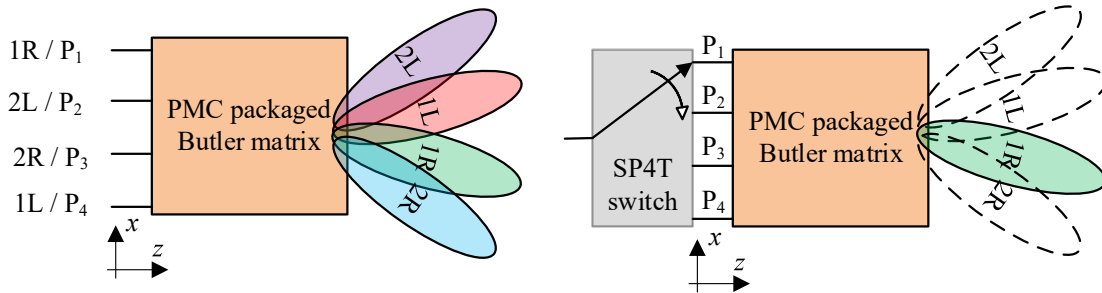


Figure 5-5. Switched-beams in H-plane (H-Plane) and beam selection through SP4T switch

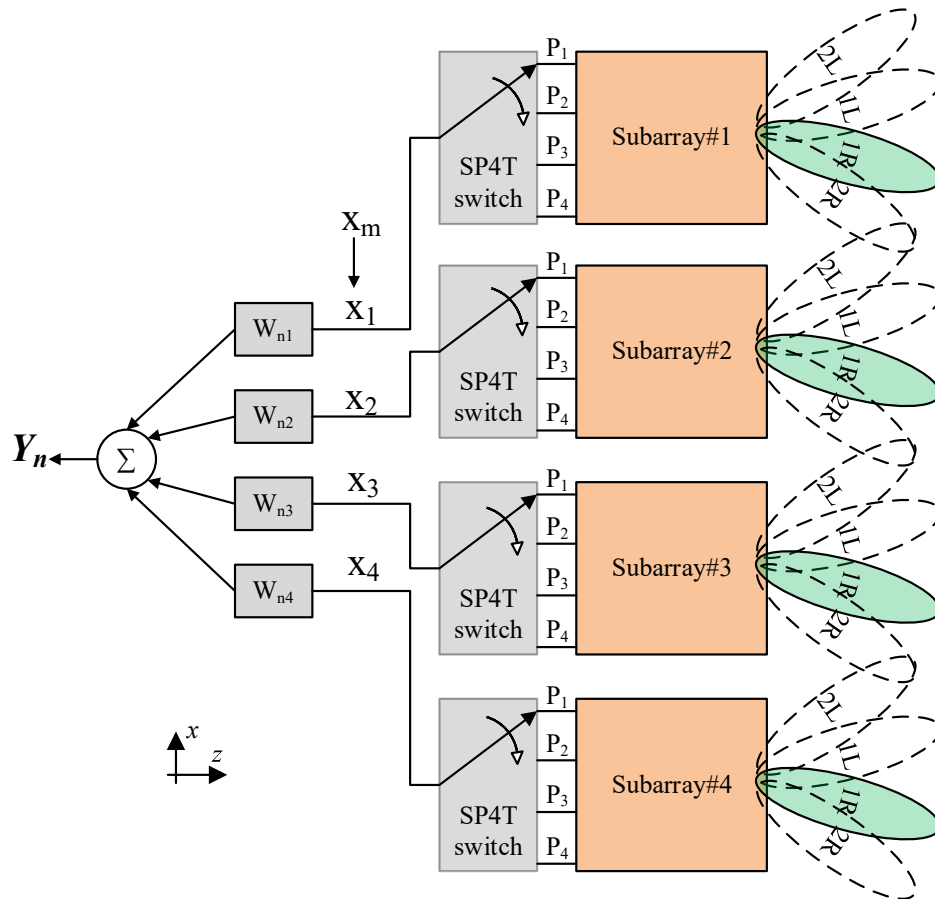


Figure 5-6. Beamspace digital beamforming operation over the H-plane beam-switched signals

The n -number of weighting vectors $\mathbf{W}_n = [W_{n1} \ W_{n2} \ W_{n3} \ W_{n4}]$ can be generated by DSP, as given in (5-2) and (5-3), to multiply with the received signals X_m to generate beams of (5-4). The complex beamforming coefficient, $W_{nm} = a_{nm}e^{-jkd \sin \theta_n}$, consists of magnitude a_{nm} and phase $\Delta\phi^0 = -jkd \sin \theta_n$ part, where $d = 9$ mm is the inter-subarray spacing in the vertical plane. The magnitudes can be distributed for the beams' amplitude tapering, whereas the phases are responsible for beamforming to steer the beam in a specific direction. Here, in this thesis, beam steering performance is studied by applying the phase distributions only with equal amplitudes (a_{nm}) distribution.

$$\mathbf{X} = [x_1, x_2, x_3, x_4]^T \quad (5-1)$$

$$\mathbf{W} = \begin{bmatrix} \mathbf{W}_1 \\ \mathbf{W}_2 \\ \mathbf{W}_3 \\ \vdots \\ \mathbf{W}_n \end{bmatrix} = \begin{bmatrix} W_{11} & W_{12} & W_{13} & W_{14} \\ W_{21} & W_{22} & W_{23} & W_{24} \\ W_{31} & W_{32} & W_{33} & W_{34} \\ \vdots & \vdots & \vdots & \vdots \\ W_{n1} & W_{n2} & W_{n3} & W_{n4} \end{bmatrix} \quad (5-2)$$

$$\mathbf{W}_n = [1, e^{-jkd \sin \theta_n}, e^{-j2kd \sin \theta_n}, e^{-j3kd \sin \theta_n}] \quad (5-3)$$

$$\mathbf{Y}_n(\theta) = \mathbf{W}_n \mathbf{X} \quad (5-4)$$

To achieve a $B_V \times B_H = 3 \times 4$ multibeam frontend, *i.e.*, four analog switched beams (B_H) and three digital beams (B_V), three beamforming complex coefficient vectors \mathbf{W}_1 , \mathbf{W}_2 , and \mathbf{W}_3 are calculated to switch the beams in $\theta_1 = 20^\circ$, $\theta_2 = 0^\circ$ and $\theta_3 = -20^\circ$ directions. The progressive phase shifts $\Delta\phi^0$ for each beamspace (2L, 1L, 1R, and 2R) are given in Table 5-1. The inter-subarray

Table 5-1. Beamforming coefficients calculated for the E-plane beamspace digital beamforming

$\Delta\phi^0 = -jkd \sin \theta_n$				
$(Y_n) \theta_n$	2L	1L	1R	2R
$(Y_1) \theta_1 = 20^\circ$	-103.5	-103.5	-103.5	-103.5
$(Y_2) \theta_2 = 0^\circ$	0	0	0	0
$(Y_3) \theta_3 = -20^\circ$	103.5	103.5	103.5	103.5

spacing in the elevation plane is “ $d = 9$ mm,” which is less than a wavelength $\lambda = 10.7$ mm at 28 GHz, as shown in Figure 5-2.

The corresponding 3-dB radiation pattern contours of the hybrid beamforming are plotted in Figure 5-7. The required beamforming performance is well-achieved for the inner beams at 1L and 1R positions having symmetric 3-dB beamwidth of $\sim 28^\circ$. However, the outer beams at 2L and 2R positions are asymmetric, comparatively. The subarray antenna's H-plane radiation characteristics can be called a beamspace factor.

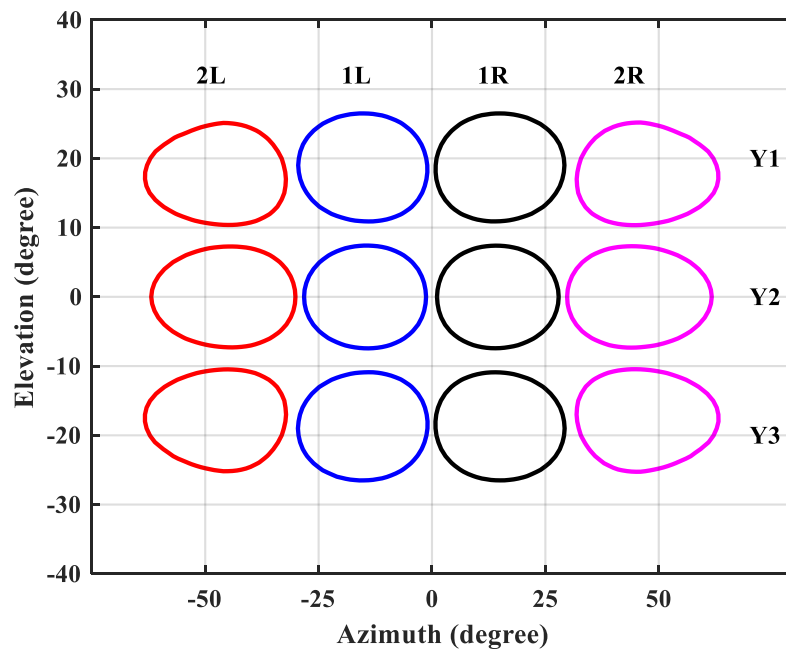


Figure 5-7. 3-dB radiation pattern contours of hybrid beamforming for first model

5.2 Performance Limitations of First Model

The presented design has certain limitations. First, the subarray implementation and the overall multibeam antenna frontend are in end-fire topology. Therefore, the prototype could be bulky for some applications as it has a footprint of $52 \times 50 \times 35$ mm³. Thus, the integration of such an antenna frontend might not be feasible for a compact multilayer PCB RF circuitry. Second, with the H-plane horn antenna subarray, the inter-subarray spacing in the elevation plane could not be

reduced to less than 9 mm, limiting the digital beamforming scan range in the V-plane. For instance, for a broad scanning view, the beamforming weights are calculated with a progressive phase shift of $\Delta\phi^0 = 150^0$, to steer the beam towards $\theta = -30^0$. The corresponding digital beamforming results are plotted in Figure 5-8 for the 2L beam location. It shows that the grating lobe in the direction of $\theta = 40^0$ also starts to appear within a 3-dB bandwidth level on the Azimuth/Elevation-plane. Therefore, this subarray antenna results in a limited scan-range for digital beamspace beamforming.

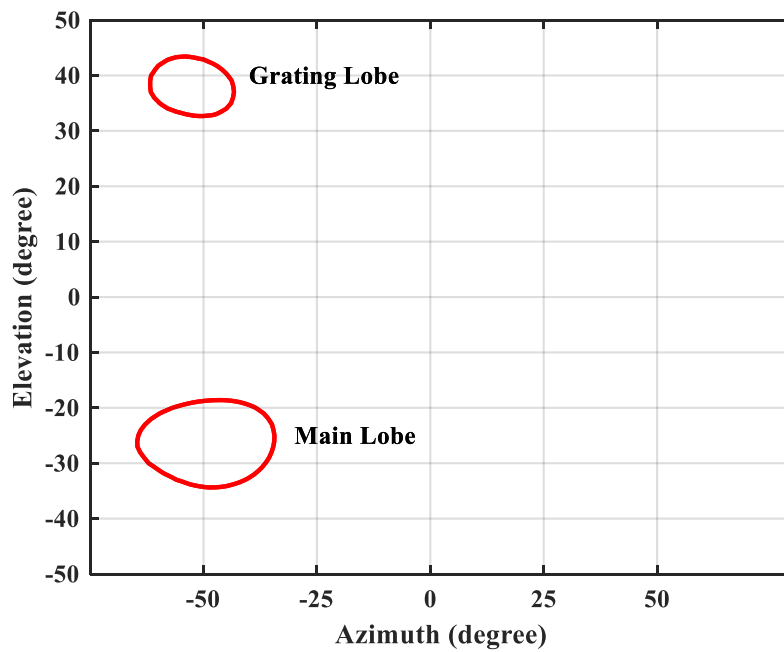


Figure 5-8. Appearance of the grating lobe within 3-dB contour level

5.3 Second Model

Based on the limitations discussed above for the first model, the second model of hybrid beamforming implementation is the improvised version in terms of radiation characteristics and physical layout of the individual subarray antenna that would help to perform overall hybrid analog-digital beamforming operation efficiently. In Figure 5-9, the operational principle is presented, which is similar to the scenarios given in Figure 5-5 and Figure 5-6. However, the multibeam antenna system with broadside radiation characteristics is considered here.

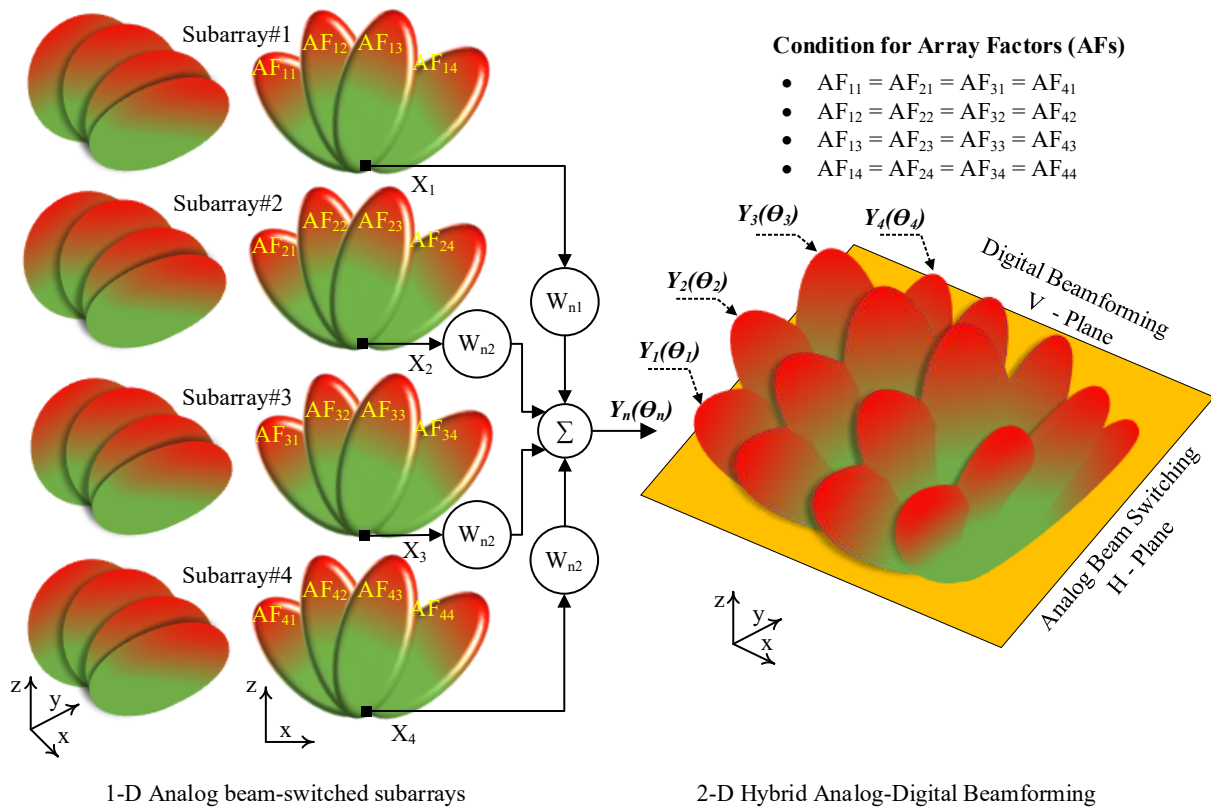


Figure 5-9. Second model of hybrid beamforming based on planar folded Butler Matrix subarray topology

The depicted model of Figure 5-9 is implemented by using four folded Butler matrix subarray antennas presented in Chapter 4, Section 4.4. The 4×4 implementation is shown in Figure 5-10, which consists of four subarrays denoted as Subarray#1, #2, #3, and #4. Each subarray is a 1×4 beam-switched multibeam antennas. The center-to-center inter-subarray spacing is 6 mm along the y-axis, and antenna elements are separated by 5.47 mm at the array ports. These physical dimensions are around $\sim \lambda/2$ at 28 GHz. The four-layer structure has a thickness of 2 mm. The design interior of a 16- antenna frontend implemented with PMC packaged microstrip line technology is detailed in Figure 5-10.

A full-wave analysis is performed for this 16-beam-ports antenna system by using the Time Domain solver of CST MWS. The front and back views of the design are shown in Figure 5-11. The total number of 16 beam-ports is marked in Figure 5-11 (b). The 3D radiation patterns of

antenna directivity and their corresponding 3-dB contour plots on the Azimuth/Elevation-plane are shown in Figure 5-12 and Figure 5-13, respectively.

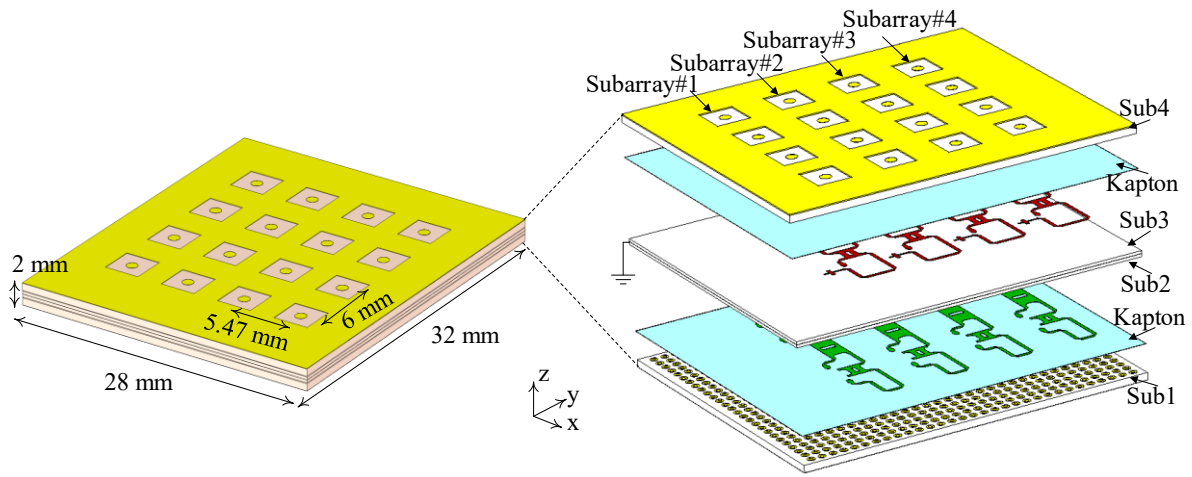


Figure 5-10. Arrangement of four folded Butler matrix subarray antennas for the second model of hybrid beamforming

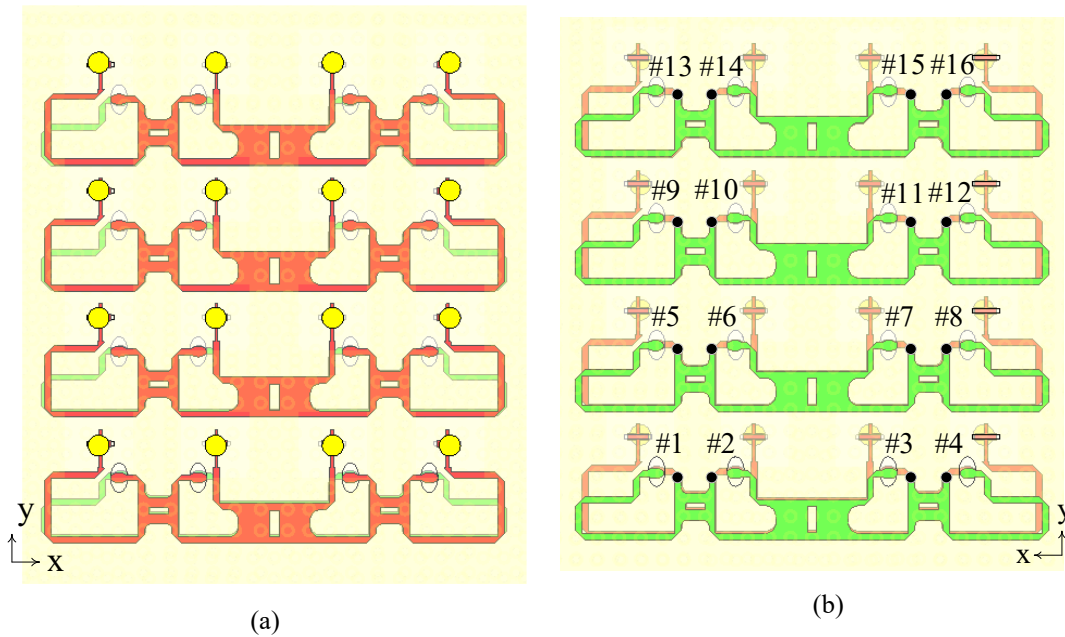


Figure 5-11. (a) Front-view and (b) Back-view of the second model of 16-antenna system

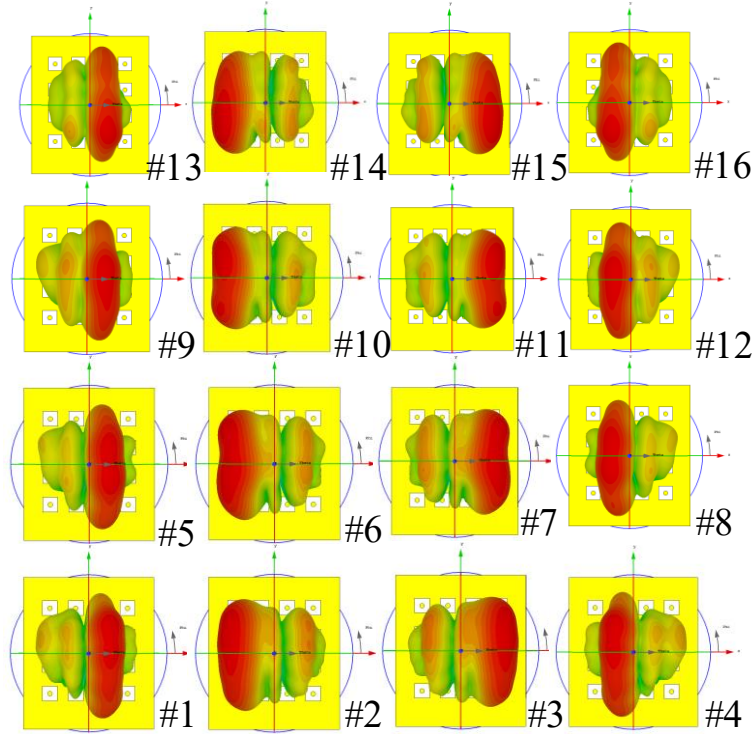


Figure 5-12. Directivity patterns from full-wave analysis of the second model of 16-ports antenna system

In Figure 5-14, a complete hybrid beamforming frontend module is presented. It consists of 16 beam-ports and four SP4T RF switching chips. This tile-based multibeam antenna system implementation could be backed by a module that performs DSP, and it has power control to switch the RF paths among four beam-ports (RF#1 to RF#4) for each subarray. Among the four H-plane beams (2L, 1L, 1R, and 2R), a single beam can be selected from each subarray represented as X_m , where $m = 1, 2, 3, \text{ and } 4$. Therefore, as given in (5-1), the received signals from each subarray antenna can be represented in the vector notation as $\mathbf{X} = [x_1, x_2, x_3, x_4]^T$. For beamforming in the V-plane, each signal is multiplied with a complex coefficient W_{nm} function and added to generate “n” number of $Y_n(\theta_n)$ digital beams in the direction of θ_n . Design and full-wave analysis are performed for 16-port multibeam frontend antenna, whereas the RF switches and signal processing blocks are shown to elaborate analytical postprocessing.

To achieve a $B_H \times B_V = 4 \times 4$ analog-digital multibeam frontend, four beamforming complex coefficient vectors, $\mathbf{W}_1, \mathbf{W}_2, \mathbf{W}_3$ and \mathbf{W}_4 as given in (5-5), are applied over the X_m beam spaces for each of the four RF streams (2L, 1L, 1R, and 2R). This data postprocessing results in

2-D beamforming, as shown in Figure 5-15, where four digital beams $Y_1 - Y_4$ are steered in the V-plane for each analog RF stream switched in the H-plane. At 1L and 1R Azimuthal plane locations, the digital beams $Y_1, Y_2, Y_3,$ and Y_4 are steered at $\theta = 40^\circ, 13.5^\circ, -13.5^\circ,$ and -40° in the V-plane, respectively. The beams are approximately symmetric. However, the beams are deformed at 2L and 2R locations, comparatively. This phenomenon is due to the digital beamforming phase distribution ($\Delta\phi$) and beamspace patterns at 2L and 2R locations.

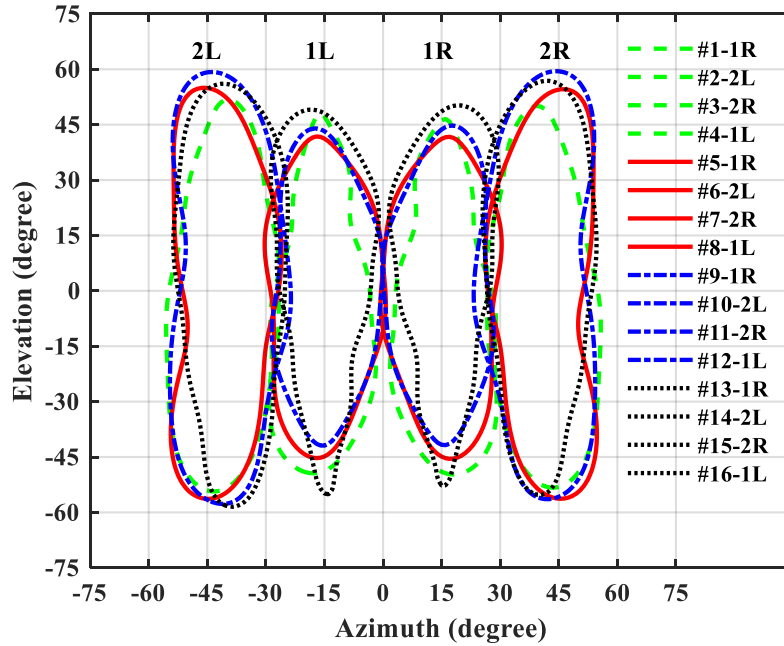


Figure 5-13. 3-dB radiation beams' contours of the second model of 16-ports antenna system at 30 GHz

$$W = \begin{bmatrix} W_1 \\ W_2 \\ W_3 \\ W_4 \end{bmatrix} = \begin{bmatrix} 1 & e^{j135} & e^{2j135} & e^{3j135} \\ 1 & e^{j45} & e^{2j45} & e^{3j45} \\ 1 & e^{-j45} & e^{-2j45} & e^{-3j45} \\ 1 & e^{-j135} & e^{-2j135} & e^{-3j135} \end{bmatrix} \quad (5-5)$$

5.4 Summary

In this chapter, two models of the 16-antenna system have been presented in which the data extracted from the full-wave analysis is processed to demonstrate analog-digital beamforming. Limitations on the first model, such as the size of the hardware, implementation topology, and scan-range, are addressed in the second model. For the first model, as grating lobes start to appear

after $\pm 20^\circ$ scan-range; therefore, the hybrid beamforming operation is limited to $B_V \times B_H = 3 \times 4 = 12$ beams. The second model is a complete PCB design which is highly suitable to be integrated with the compact multilayer PCB tile-based RF frontend. The second model is a $B_V \times B_H = 4 \times 4 = 16$ beams antenna system in which a set of $\pm 45^\circ$ and $\pm 135^\circ$ phase distributions ($\Delta\phi$) are applied for the analog beam-switching and digital beamspace beam-steering in the Azimuth and Elevation planes, respectively. The flow of the hybrid beamforming process is mapped in Figure 5-16.

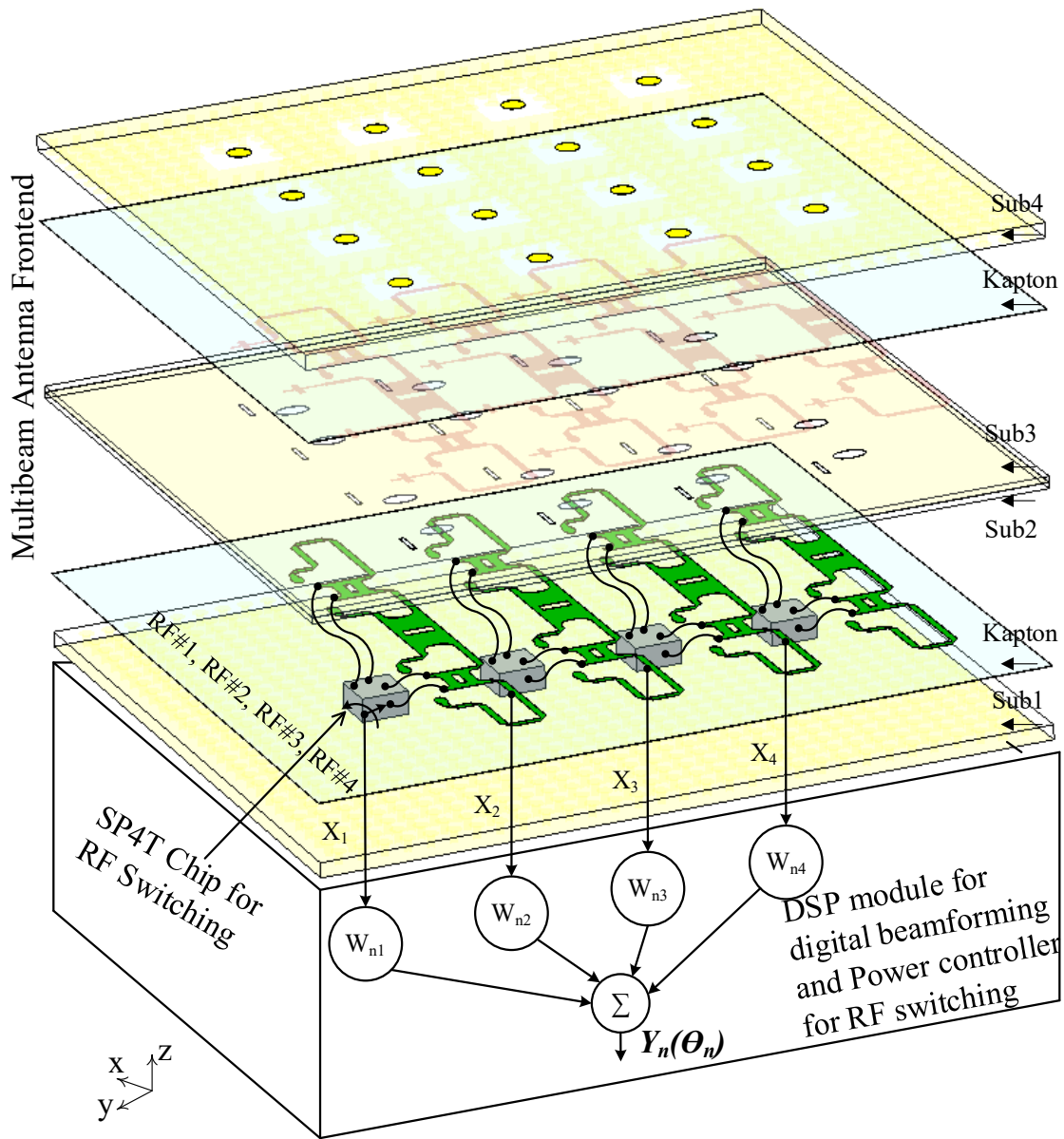


Figure 5-14. A complete multibeam frontend for hybrid analog-digital beamforming

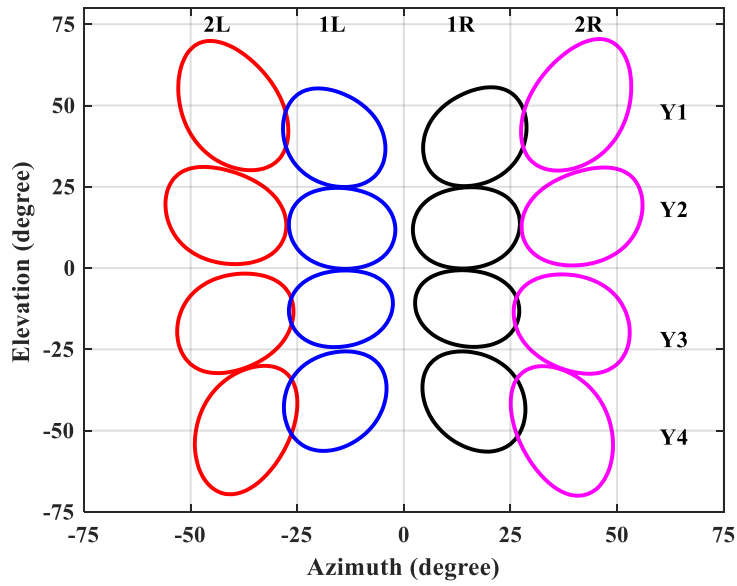


Figure 5-15. 3-dB radiation pattern contours of hybrid beamforming for second model

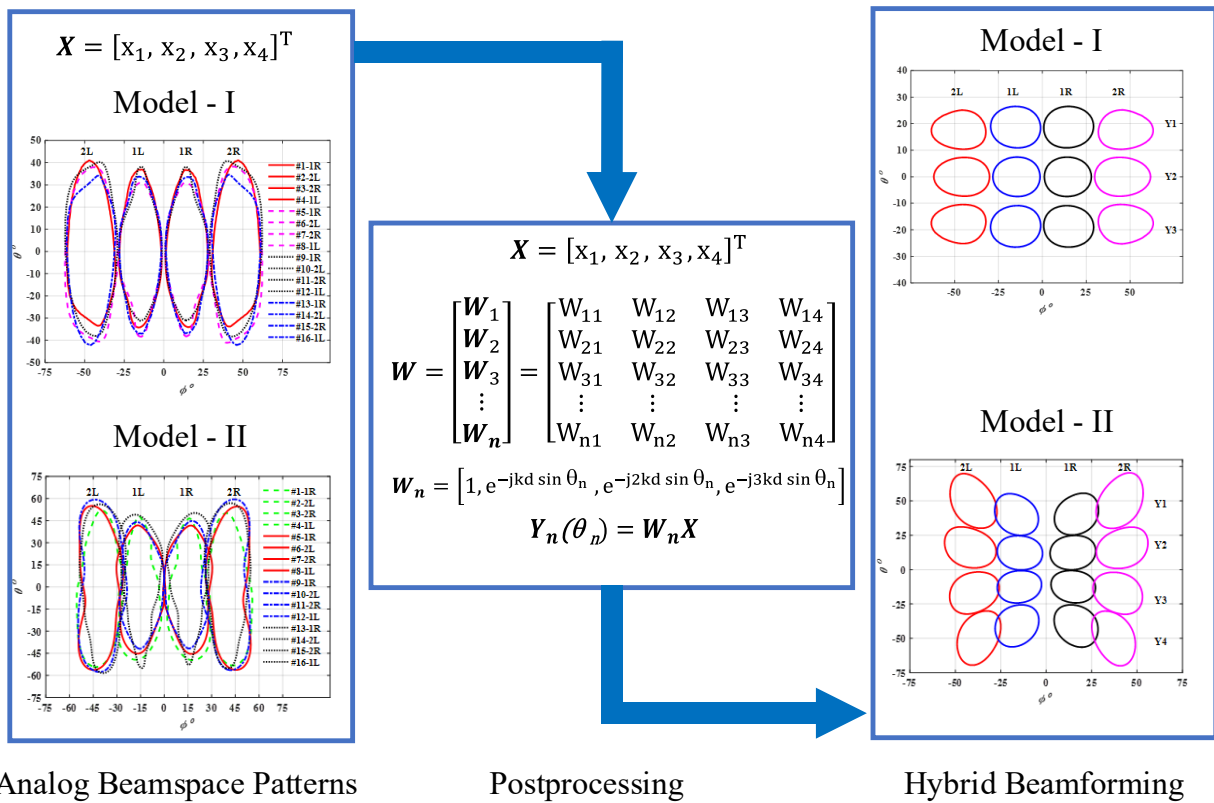


Figure 5-16. Process mapping of Hybrid Analog-Digital beamforming

Chapter 6

Conclusion and Future Work

6.1 Conclusion

In this thesis, the concepts of multibeam antenna subarrays that need to be used within a large-scale $N \times M$ antenna frontend have been presented for partially-connected hybrid beamforming at 30 GHz. The subarray orders $n \times m = 2 \times 2$, 1×4 , and 4×4 have been under consideration with fixed-beam, one-dimensional, and two-dimensional switched-beam radiation patterns. Key factors have been under research investigation, such as the selection of technology, design layout, and radiation characteristics, and these factors are analyzed critically for the desired application. Microstrip line technology has been used to design these subarray antennas. This choice has been made because a compact, low-cost circuitry could be efficiently realized and augmented with the PMC packaging at mm-Wave. A simplified hybrid beamforming model, where analog beam-switching could be defined in one principle plane (H-plane) and fine-tuned digital beamspace beamforming in the other (V-plane), it required a novel implementation of multibeam subarray antenna. The desired radiation characteristics are the fan-shape switched multibeam patterns in the H-plane with the arrangement of $\lambda/2$ inter-subarray layout spacing vertically to perform digital beamspace beamforming in the V-plane. These characteristics have not been achieved by a 4×4 fixed-beam and 2×2 switched-beam subarray antennas presented in Chapter 4, Section 4.1, and Section 4.2, respectively. The 4×4 fixed-beam subarray has a gain of 19.3 dBi and symmetrical radiation patterns. Such highly directional beam spaces could not be used in the defined model of hybrid beamforming. Similarly, a 2×2 dual-polarized beam-switched subarray has a large circuit size as compared to its radiating part. Being used as a constituent of an $N \times M$ large-scale antenna frontend for hybrid beamforming, it has resulted in the aperture discontinuity and the associated problem of array factor.

In Section 4.3, these properties have been achieved by a 1×4 switched-beam subarray antenna, which consists of a 4×4 PMC packaged Butler matrix and a DRGW horn antenna array

with an end-fire operation. Wideband components with 30 % bandwidth at 30 GHz have been designed on a single substrate within a PMC packaged environment. The open-circuit multi stub-loaded delay line has been used to enhance the phase-shifter bandwidth. The PMC packaging lid of nails has been positioned away from the microstrip line circuit by a distance that does not affect its characteristics impedance substantially. The self-shielding/packaging concept has simplified the overall device, as two parts of the casing incorporate the AMC textures as well as the antenna array. This technique has eliminated the requirement of packaging each component in individual compartments. Therefore, the complete circuit has been packaged with a single lid of nails. A 5 GHz (28-33 GHz) bandwidth with return loss and isolation, both better than 15 dB has been achieved with insertion loss 0.8 ± 0.3 dB, and antenna-ports' phase distributions $\pm 45^\circ$ and $\pm 135^\circ$. Excellent 1×4 beam-switching capabilities have been achieved in the H-plane with a maximum gain of 11.7 and 11.2 dBi for the inner (1R) and outer (2R) fan-shaped radiation beams covering $\pm 42^\circ$. However, its metallic enclosure has resulted in a bulky structure. Therefore, a novel 4×4 multi-layer PCB folded Butler matrix has been designed to improve the PMC packaging technique further. In Section 4.4, the folded Butler matrix designs and the antenna element have been presented for a bandwidth of 4 GHz (28-32 GHz). The directivity was calculated to be 5.22 dBi; whereas, for 1×4 switched-beam subarray antenna, it has been found 11.1 dBi and 10.6 dBi for 1R and 2R fan-shaped beams, respectively. Thus, to be more compatible with the multi-layer miniaturized RF circuitry, an improvised compact 1×4 subarray antenna has been presented with broadside radiation patterns switched in the H-plane; $\sim \lambda/2$ inter-subarray layout spacing in the vertical direction.

Two hybrid beamforming models have been presented in Chapter 5. For each model, A 16-antenna system has been constructed for each model, which is made up of four 1-D beam-switched multibeam subarrays presented in Section 4.3 and 4.4. Data from the full-wave analysis has been extracted for a 16-port multibeam antenna system, which includes a mutual coupling effect. In the first model, the DSP post-processing of the extracted radiation patterns has resulted in a limited 2-D beam-scanning of Azimuth \times Elevation = $42^\circ \times 28^\circ$ with $B_V \times B_H = 3 \times 4 = 12$ beams. By increasing the scan-range with more digital beams B_V , the grating lobes have been starting to appear within a 3-dB level, resulting from radiation pattern performance and inter-subarray spacing. This has been rectified in the second model where an approximate scan-range of Azimuth

\times Elevation = $38^\circ \times 40^\circ$ is covered by $B_V \times B_H = 4 \times 4 = 16$ switched beams. This has been achieved by improving the radiation characteristics and minimizing the inter-subarray spacing.

Under hybrid beamforming architecture, the number of RF chains could be reduced. Furthermore, the planar low-cost/low-profile multibeam antenna system's proposed topology could be highly suitable to integrate with a tile-based multilayer RF frontend module. The presented prototype is highly suitable for a low-cost multibeam system where a finetuned beam switching is required in one principle plane with a set of predefined switched beams in the other.

6.2 Future Work

As future work, the present study could be extended into or made a part of the following possible research directions:

A. Higher-Order Multibeam Subarray

Here, a 4×4 folded Butler matrix has been considered to realize a 1×4 multibeam subarray antenna. For a better analog beam-switching resolution in the Azimuth plane, the Butler matrix could be designed for an order greater than 4×4 . The presented topology of the folded Butler matrix, which is implemented on multiple PCB layers, could provide this design flexibility while keeping the lateral physical dimensions around \sim half wavelength ($\lambda/2$), a requirement for hybrid beamforming.

B. Transceiver Test Bench

The analytical process of digital beamforming and the post-processing block represented in Chapter 5 could be tested by using a DSP chip. Similarly, for the functionality of RF switching at beam-ports, the mm-Wave SP4T switching chips could be integrated into a packaged microstrip line circuit at the antenna beam-ports' locations. The RF chains would be required between the multibeam subarray antennas and the DSP chip for transmission and reception to have a complete hybrid beamforming transceiver test bench. A digital-to-analog-converter (DAC), phase shifter, and power amplifier would be

required in the transmitting mode. A low noise amplifier, phase shifter, and ADC would be needed in the receiving mode.

C. Energy Efficiency Analysis

One of the main objectives of the hybrid beamforming architecture is to minimize the RF chains. A wireless system's total power consumption is the sum of the effective transmit power and power loss in the circuit (RF chains). The energy efficiency analysis could be performed for the hybrid beamforming transceiver test bench by measuring the number of bits that could be reliably transmitted/received per unit of energy [158].

Bibliography

- [1] E. Dahlman, S. Parkvall, and J. Skold, *5G NR: The Next Generation Wireless Access Technology*, 1st ed. New York, NY, USA: Academic Press, 2018.
- [2] T. S. Rappaport *et al.*, “Millimeter wave mobile communications for 5G cellular: It will work!,” *IEEE Access*, vol. 1, pp. 335–349, 2013.
- [3] T. S. Rappaport, R. W. Heath Jr., R. C. Daniels, and J. N. Murdock, *Millimeter Wave Wireless Communications*. Englewood Cliffs, NJ, USA: Prentice-Hall, 2014.
- [4] M. Xiao *et al.*, “Millimeter wave communications for future mobile networks,” *IEEE Journal on Selected Areas in Communications*, vol. 35, no. 9, pp. 1909–1935, 2017.
- [5] R. J. Mailloux, *Phased Array Antenna Handbook*, 2nd ed. Norwood, MA, USA: Artech House, 2005.
- [6] 3rd Generation Partnership Project, *5G NR Base Station (BS) Radio Transmission and Reception 3GPP Technical Specification 38.104 Version 15.5.0*, Release 15. Sophia Antipolis, France: 3GPP, 2019.
- [7] C. A. Balanis and P. Ioannides, *Introduction to Smart Antennas*. San Rafael, CA, USA: Morgan & Claypool, 2007.
- [8] F. Gross, *Smart Antennas for Wireless Communications with MATLAB*. USA: McGraw-Hill, 2005.
- [9] B. R. Jackson, S. Rajan, B. J. Liao, and S. Wang, “Direction of arrival estimation using directive antennas in uniform circular arrays,” *IEEE Transactions on Antennas and Propagation*, vol. 63, no. 2, pp. 736–747, 2015.
- [10] J. Litva and T. K. Lo, *Digital Beamforming in Wireless Communications*. Boston, MA: Artech House, 1996.
- [11] J. C. Libert and T. S. Rappaport, *Smart Antennas for Wireless Communications: IS-95 and Third Generation CDMA Applications*. Englewood Cliffs, NJ, USA: Prentice-Hall, 1999.
- [12] S. Sun, T. S. Rappaport, R. W. Heath, A. Nix, and S. Rangan, “MIMO for millimeter-wave wireless communications: Beamforming, spatial multiplexing, or both?,” *IEEE Communications Magazine*, vol. 52, no. 12, pp. 110–121, 2014.
- [13] I. Ahmed *et al.*, “A survey on hybrid beamforming techniques in 5G: Architecture and system model perspectives,” *IEEE Communications Surveys and Tutorials*, vol. 20, no. 4, pp. 3060–3097, 2018.
- [14] S. Han, C. I, Z. Xu, and C. Rowell, “Large-scale antenna systems with hybrid analog and digital beamforming for millimeter wave 5G,” *IEEE Communications Magazine*, vol. 53, no. 1, pp. 186–194, 2015.
- [15] J. Zhang, X. Yu, and K. B. Letaief, “Hybrid beamforming for 5G and beyond millimeter-wave systems: A holistic view,” *IEEE Open Journal of the Communications Society*, vol. 1, no. January, pp. 77–91, 2019.

- [16] Z. Zhou, N. Ge, Z. Wang, and S. Chen, "Hardware-efficient hybrid precoding for millimeter wave systems with multi-feed reflectarrays," *IEEE Access*, vol. 6, pp. 6795–6806, 2018.
- [17] J. Butler and R. Lowe, "Beam-forming Matrix simplifies design of electronically scanned antennas," *Electronic Design*, vol. 9, pp. 170–173, 1961.
- [18] H. J. Moody, "The systematic design of the Butler Matrix," *IEEE Transactions on Antennas and Propagation*, vol. AP-12, no. 6, pp. 786–788, 1964.
- [19] J. Blass, "Multidirectional antenna - A new approach to stacked beams," in *IRE International Convention Record*, 1960, no. 1, pp. 48–50.
- [20] J. C. Nolan, "Synthesis of multiple beam networks for arbitrary illuminations," *Ph.D. dissertation, Baltimore, MD, Radio Division, Bendix Corp*, 1965.
- [21] W. Rotman and R. F. Turner, "Wide-angle microwave lens for line source applications," *IEEE Transactions on Antennas and Propagation*, vol. 11, no. 6, pp. 623–632, 1963.
- [22] R. C. Hansen, "Design trades for Rotman lenses," *IEEE Transactions on Antennas and Propagation*, vol. 39, pp. 464–472, 1991.
- [23] W. Hong *et al.*, "Multibeam antenna technologies for 5G wireless communications," *IEEE Transactions on Antennas and Propagation*, vol. 65, no. 12, pp. 6231–6249, 2017.
- [24] Y. J. Cheng, P. Chen, W. Hong, T. Djerafi, and K. Wu, "Substrate integrated waveguide beamforming networks and multibeam antenna arrays for low-cost satellite and mobile systems," *IEEE Antennas and Propagation Magazine*, vol. 53, no. 6, pp. 18–30, 2011.
- [25] Y. Hu *et al.*, "A digital multibeam array with wide scanning angle and enhanced beam gain for millimeter wave massive MIMO applications," *IEEE Transactions on Antennas and Propagation*, vol. 66, no. 11, pp. 5827–5837, 2018.
- [26] K. Wu, Y. J. Cheng, T. Djerafi, and W. Hong, "Substrate-integrated millimeter-wave and terahertz antenna technology," *Proceedings of the IEEE*, vol. 100, no. 7, pp. 2219–2232, 2012.
- [27] Y. Gao, M. Khaliel, F. Zheng, and T. Kaiser, "Rotman lens based hybrid analog-digital beamforming in massive MIMO systems: Array architectures, beam selection algorithms and experiments," *IEEE Transactions on Vehicular Technology*, vol. 66, no. 10, pp. 9134–9148, 2017.
- [28] S. Mondal, R. Singh, A. I. Hussein, and J. Paramesh, "A 25-30 GHz fully-connected hybrid beamforming receiver for MIMO communication," *IEEE Journal of Solid-State Circuits*, vol. 53, no. 5, pp. 1275–1287, 2018.
- [29] P. Taghikhani, K. Buisman, and C. Fager, "Hybrid beamforming transmitter modeling for millimeter-wave MIMO applications," *IEEE Transactions on Microwave Theory and Techniques*, pp. 1–1, 2020.
- [30] S. F. Chuang, W. R. Wu, and Y. T. Liu, "High-Resolution AoA estimation for hybrid antenna arrays," *IEEE Transactions on Antennas and Propagation*, vol. 63, no. 7, pp. 2955–2968, 2015.
- [31] L. Xie, X. Yin, C. Lu, L. Yang, H. Zhao, and S. Li, "Hybrid analog-digital antenna array

- with built-in image injection calibration,” *IEEE Transactions on Antennas and Propagation*, vol. 62, no. 11, pp. 5513–5523, 2014.
- [32] V. Venkateswaran, F. Pivit, and L. Guan, “Hybrid RF and digital beamformer for cellular networks: Algorithms, microwave architectures, and measurements,” *IEEE Transactions on Microwave Theory and Techniques*, vol. 64, no. 7, pp. 2226–2243, 2016.
- [33] B. Rupakula, A. H. Aljuhani, and G. M. Rebeiz, “Limited scan-angle phased arrays using randomly grouped subarrays and reduced number of phase shifters,” *IEEE Transactions on Antennas and Propagation*, vol. 68, no. 1, pp. 70–80, 2020.
- [34] A. Nafe, M. Sayginer, K. Kibaroglu, and G. M. Rebeiz, “2 x 64-Element dual-polarized dual-beam single-aperture 28-GHz phased array with 2 x 30 Gb/s links for 5G polarization MIMO,” *IEEE Transactions on Microwave Theory and Techniques*, vol. 68, no. 9, pp. 3872–3884, 2020.
- [35] K. Kibaroglu, M. Sayginer, and G. M. Rebeiz, “A low-cost scalable 32-element 28-GHz phased array transceiver for 5G communication links based on a beamformer flip-chip unit cell,” *IEEE Journal of Solid-State Circuits*, vol. 53, no. 5, pp. 1260–1274, 2018.
- [36] Y. Yin, B. Ustundag, K. Kibaroglu, M. Sayginer, and G. M. Rebeiz, “Wideband 23.5–29.5 GHz phased arrays for multistandard 5G applications and carrier aggregation,” *IEEE Transactions on Microwave Theory and Techniques*, no. Early Access, 2020.
- [37] M. R. Nikkhah, P. Lohmannia, J. Rashed-Mohassel, and A. A. Kishk, “Theory of ESPAR design with their implementation in large arrays,” *IEEE Transactions on Antennas and Propagation*, vol. 62, no. 6, pp. 3359–3364, 2014.
- [38] R. Movahedinia, M. R. Chaharmir, A. R. Sebak, M. Ranjbar Nikkhah, and A. A. Kishk, “Realization of large dielectric resonator antenna ESPAR,” *IEEE Transactions on Antennas and Propagation*, vol. 65, no. 7, pp. 3744–3749, 2017.
- [39] R. Movahedinia, A. R. Sebak, M. R. Chaharmir, M. Ranjbar Nikkhah, and A. A. Kishk, “X-Band circularly polarized electronically steerable parasitic array radiator of DRA,” *IEEE Transactions on Antennas and Propagation*, vol. 66, no. 2, pp. 721–728, 2018.
- [40] Y. Lin, Y. Zhang, H. Liu, Y. Zhang, E. Forsberg, and S. He, “A simple high-gain millimeter-wave leaky-wave slot antenna based on a bent corrugated SIW,” *IEEE Access*, vol. 8, pp. 91999–92006, 2020.
- [41] M. R. Rahimi, N. Bayat-Makou, and A. A. Kishk, “Millimeter-wave substrate integrated gap waveguide leaky-wave antenna for WiGig applications,” *IEEE Transactions on Antennas and Propagation*, vol. 67, no. 9, pp. 5790–5800, 2019.
- [42] K. M. Luk, H. Wong, K. Luk, and H. Wong, “A new wideband unidirectional antenna element,” *International Journal of Microwave and Optical Technology*, vol. 1, no. 1, pp. 35–44, 2006.
- [43] Y. Li and K. M. Luk, “60-GHz Dual-polarized two-dimensional switch-beam wideband antenna array of aperture-coupled magneto-electric dipoles,” *IEEE Transactions on Antennas and Propagation*, vol. 64, no. 2, pp. 554–563, 2016.
- [44] M. M. M. Ali and A. R. Sebak, “2-D Scanning magnetolectric dipole antenna array fed by

- RGW butler matrix,” *IEEE Transactions on Antennas and Propagation*, vol. 66, no. 11, pp. 6313–6321, 2018.
- [45] M. M. M. Ali, I. Afifi, and A.-R. Sebak, “A dual polarized magneto-electric dipole antenna based on printed Ridge Gap Waveguide technology,” *IEEE Transactions on Antennas and Propagation*, no. Early Access, 2020.
- [46] M. M. M. Ali and A. Sebak, “Printed RGW circularly polarized differential feeding antenna array for 5G communications,” *IEEE Transactions on Antennas and Propagation*, vol. 67, no. 5, pp. 3151–3160, 2019.
- [47] A. T. Hassan and A. A. Kishk, “Efficient procedure to design large finite array and its feeding network with examples of ME-dipole array and microstrip Ridge Gap Waveguide feed,” *IEEE Transactions on Antennas and Propagation*, vol. 68, no. 6, pp. 4560–4570, 2020.
- [48] Z. N. Chen and K. M. Luk, *Antennas for Base Stations in Wireless Communications*. New York, USA: McGraw-Hill, 2009.
- [49] J. Wang, Y. Li, L. Ge, J. Wang, and K. M. Luk, “A 60 GHz horizontally polarized magnetolectric dipole antenna array with 2-D multibeam endfire radiation,” *IEEE Transactions on Antennas and Propagation*, vol. 65, no. 11, pp. 5837–5845, 2017.
- [50] Q. Wu, J. Hirokawa, J. Yin, C. Yu, H. Wang, and W. Hong, “Millimeter-wave multibeam endfire dual-circularly polarized antenna array for 5G wireless applications,” *IEEE Transactions on Antennas and Propagation*, vol. 66, no. 9, pp. 4930–4935, 2018.
- [51] L. M. Abdelghani *et al.*, “Ultra-broadband 4×4 compact Butler matrix using multilayer directional couplers and phase shifters,” in *IEEE/MTT-S International Microwave Symposium Digest*, 2012, pp. 1–3.
- [52] Y. Wang, A. M. Abbosh, and B. Henin, “Broadband microwave crossover using combination of ring resonator and circular microstrip patch,” *IEEE Transactions on Components, Packaging and Manufacturing Technology*, vol. 3, no. 10, pp. 1771–1777, 2013.
- [53] N. Ashraf, A. A. Kishk, and A.-R. Sebak, “28–32 GHz dual-polarized single-layer microstrip line beamforming network for 2×2 beam switching,” in *IEEE MTT-S International Microwave Conference on Hardware and Systems for 5G and Beyond (IMC-5G)*, 2019.
- [54] Y. Hu, J. Zhan, Z. H. Jiang, C. Yu, and W. Hong, “An orthogonal hybrid analog-digital multibeam antenna array for millimeter-wave massive MIMO systems,” *IEEE Transactions on Antennas and Propagation*, no. Early Access, 2020.
- [55] Q. Sun, Y. L. Ban, J. W. Lian, Y. Liu, and Z. Nie, “Millimeter-wave multibeam antenna based on folded C-type SIW,” *IEEE Transactions on Antennas and Propagation*, vol. 68, no. 5, pp. 3465–3476, 2020.
- [56] I. Afifi and A. R. Sebak, “Wideband 4×4 Butler matrix in the printed ridge gap waveguide technology for millimeter wave applications,” *IEEE Transactions on Antennas and Propagation*, no. Early Access, 2020.

- [57] M. Farahani, M. Akbari, M. Nedil, A. R. Sebak, and T. A. Denidni, "Millimeter-wave dual left/right-hand circularly polarized beamforming network," *IEEE Transactions on Antennas and Propagation*, vol. 68, no. 8, pp. 6118–6127, 2020.
- [58] J. W. Lian, H. Zhu, Y. L. Ban, D. K. Karmokar, and Y. J. Guo, "Uniplanar high-gain 2-D scanning leaky-wave multibeam array antenna at fixed frequency," *IEEE Transactions on Antennas and Propagation*, vol. 68, no. 7, pp. 5257–5268, 2020.
- [59] W. F. Moulder, W. Khalil, and J. L. Volakis, "60-GHz two-dimensionally scanning array employing wideband planar switched beam network," *IEEE Antennas and Wireless Propagation Letters*, vol. 9, pp. 818–821, 2010.
- [60] Q. L. Yang, Y. L. Ban, J. W. Lian, Z. F. Yu, and B. Wu, "SIW Butler matrix with modified hybrid coupler for slot antenna array," *IEEE Access*, vol. 4, pp. 9561–9569, 2016.
- [61] L. H. Zhong, Y. L. Ban, J. W. Lian, Q. L. Yang, J. Guo, and Z. F. Yu, "Miniaturized SIW multibeam antenna array fed by dual-layer 8×8 Butler matrix," *IEEE Antennas and Wireless Propagation Letters*, vol. 16, pp. 3018–3021, 2017.
- [62] J. W. Lian, Y. L. Ban, Q. L. Yang, B. Fu, Z. F. Yu, and L. K. Sun, "Planar millimeter-wave 2-D beam-scanning multibeam array antenna fed by compact SIW beam-forming network," *IEEE Transactions on Antennas and Propagation*, vol. 66, no. 3, pp. 1299–1310, 2018.
- [63] J. W. Lian, Y. L. Ban, C. Xiao, and Z. F. Yu, "Compact substrate-integrated 4×8 Butler matrix with sidelobe suppression for millimeter-wave multibeam application," *IEEE Antennas and Wireless Propagation Letters*, vol. 17, no. 5, pp. 928–932, 2018.
- [64] J. W. Lian, Y. L. Ban, J. Q. Zhu, Y. Liu, and K. Kang, "SIW multibeam antenna based on modified horn beam-forming network," *IEEE Antennas and Wireless Propagation Letters*, vol. 17, no. 10, pp. 1866–1870, 2018.
- [65] J. W. Lian, Y. L. Ban, J. Q. Zhu, K. Kang, and Z. Nie, "Compact 2-D scanning multibeam array utilizing SIW three-way couplers at 28 GHz," *IEEE Antennas and Wireless Propagation Letters*, vol. 17, no. 10, pp. 1915–1919, 2018.
- [66] J.-W. Lian, Y.-L. Ban, H. Zhu, and Y. J. Guo, "Uniplanar beam-forming network employing eight-port hybrid couplers and crossovers for 2-D multibeam array antennas," *IEEE Transactions on Microwave Theory and Techniques*, no. Early Access, 2020.
- [67] T. Djerafi and K. Wu, "A low-cost wideband 77-GHz planar butler matrix in SIW technology," *IEEE Transactions on Antennas and Propagation*, vol. 60, no. 10, pp. 4949–4954, 2012.
- [68] A. B. Guntupalli, T. Djerafi, and K. Wu, "Two-Dimensional scanning antenna array driven by integrated waveguide phase shifter," *IEEE Transactions on Antennas and Propagation*, vol. 62, no. 3, pp. 1117–1124, 2014.
- [69] Y. Li, J. Wang, and K. M. Luk, "Millimeter-wave multiBeam aperture-coupled magnetoelectric dipole array with planar substrate integrated beamforming network for 5G applications," *IEEE Transactions on Antennas and Propagation*, vol. 65, no. 12, pp. 6422–6431, 2017.
- [70] K. Ding and A. A. Kishk, "2-D Butler matrix and phase-shifter group," *IEEE Transactions*

- on *Microwave Theory and Techniques*, vol. 66, no. 12, pp. 5554–5562, 2018.
- [71] S. P. Yan, M. H. Zhao, Y. L. Ban, J. W. Lian, and Z. Nie, “Dual-layer SIW multibeam pillbox antenna with reduced sidelobe level,” *IEEE Antennas and Wireless Propagation Letters*, vol. 18, no. 3, pp. 541–545, 2019.
- [72] R. J. Gong, Y. L. Ban, S. P. Yan, and J. W. Zheng, “Three-beam circularly polarized ME dipole antenna array fed by 3×3 Butler matrix,” in *IEEE MTT-S International Wireless Symposium*, 2019.
- [73] J. W. Lian, Y. L. Ban, J. Q. Zhu, J. Guo, and Z. Chen, “Planar 2-D scanning SIW multibeam array with low sidelobe level for millimeter-wave applications,” *IEEE Transactions on Antennas and Propagation*, vol. 67, no. 7, pp. 4570–4578, 2019.
- [74] I. M. Mohamed and A. R. Sebak, “60 GHz 2-D scanning multibeam cavity-backed patch array fed by compact SIW beamforming network for 5G applications,” *IEEE Transactions on Antennas and Propagation*, vol. 67, no. 4, pp. 2320–2331, 2019.
- [75] N. Ashraf, A. A. Kishk, and A. Sebak, “28-32 GHz dual-polarized single-layer microstrip line beamforming network for 2×2 beam switching,” in *IEEE MTT-S International Microwave Conference on Hardware and Systems for 5G and Beyond (IMC-5G)*, 2019.
- [76] Y. Li and K. M. Luk, “60-GHz Dual-polarized two-dimensional switch-beam wideband antenna array of magneto-electric dipoles,” in *IEEE International Symposium on Antennas and Propagation & USNC/URSI National Radio Science Meeting*, 2015, pp. 1542–1543.
- [77] E. T. Der, T. R. Jones, and M. Daneshmand, “Miniaturized 4×4 Butler matrix and tunable phase shifter using ridged half-mode substrate integrated waveguide,” *IEEE Transactions on Microwave Theory and Techniques*, vol. 68, no. 8, pp. 1–1, 2020.
- [78] Y. Cao, K. S. Chin, W. Che, W. Yang, and E. S. Li, “A compact 38 GHz multibeam antenna array with multifolded Butler matrix for 5G applications,” *IEEE Antennas and Wireless Propagation Letters*, vol. 16, pp. 2996–2999, 2017.
- [79] J. W. Lian, Y. L. Ban, Z. Chen, B. Fu, and C. Xiao, “SIW folded Cassegrain Lens for millimeter-wave multibeam application,” *IEEE Antennas and Wireless Propagation Letters*, vol. 17, no. 4, pp. 583–586, 2018.
- [80] G. Tudosie, R. Vahldieck, and A. Lu, “A novel modularized folded highly compact LTCC Butler matrix,” in *IEEE MTT-S International Microwave Symposium Digest*, 2008, pp. 691–694.
- [81] J. W. Lian, Y. L. Ban, Y. Q. Wu, and L. H. Zhong, “Miniaturized multibeam array antenna based on E-Plane Butler matrix for 5G application,” in *IEEE Antennas and Propagation Society International Symposium and USNC/URSI National Radio Science Meeting*, 2018, pp. 1031–1032.
- [82] “Rogers Corporation.” [Online]. Available: www.rogerscorp.com. [Accessed: 20-Aug-2020].
- [83] “CST Microwave Studio.” [Online]. Available: www.3ds.com. [Accessed: 01-Aug-2020].
- [84] “Southwest Microwave Inc.” [Online]. Available: www.mpd.southwestmicrowave.com.

[Accessed: 01-Aug-2020].

- [85] “Taconic.” [Online]. Available: www.4taconic.com. [Accessed: 20-Aug-2020].
- [86] R. Mongia, I. Bahl, and P. Bhartia, *RF and Microwave Coupled-Line Circuits*. Norwood, MA, USA: Artech House, 1999.
- [87] F. E. Gardiol, “Radiation from microstrip circuits: An introduction,” *International Journal of Microwave and Millimeter-Wave CAE*, vol. 1, no. 2, pp. 225–235, 1991.
- [88] T. Djerafi, N. J. G. Fonseca, and K. Wu, “Broadband substrate integrated waveguide 4×4 Nolen matrix based on coupler delay compensation,” *IEEE Transactions on Microwave Theory and Techniques*, vol. 59, no. 7, pp. 1740–1745, 2011.
- [89] C. J. Chen and T. H. Chu, “Design of a 60-GHz substrate integrated waveguide Butler matrix - A systematic approach,” *IEEE Transactions on Microwave Theory and Techniques*, vol. 58, no. 7, pp. 1724–1733, 2010.
- [90] F. Parment, A. Ghiotto, T. P. Vuong, J. M. Duchamp, and K. Wu, “Air-filled substrate integrated waveguide for low-loss and high power-handling millimeter-wave substrate integrated circuits,” *IEEE Transactions on Microwave Theory and Techniques*, vol. 63, no. 4, pp. 1228–1238, 2015.
- [91] N. Bayat-Makou and A. A. Kishk, “Realistic air-filled TEM printed parallel-plate waveguide based on ridge gap waveguide,” *IEEE Transactions on Microwave Theory and Techniques*, vol. 66, no. 5, pp. 2128–2140, 2018.
- [92] G. Hueber and A. M. Niknejad, *Millimeter-wave circuits for 5G and radar*. Cambridge, UK: Cambridge University Press, 2019.
- [93] A. Darvazehban, O. Manoochehri, M. A. Salari, P. Dehkhoda, and A. Tavakoli, “Ultra-wideband scanning antenna array with Rotman lens,” *IEEE Transactions on Microwave Theory and Techniques*, vol. 65, no. 9, pp. 3435–3442, 2017.
- [94] O. Manoochehri, A. Darvazehban, M. A. Salari, A. Emadeddin, and D. Erricolo, “A parallel plate ultrawideband multibeam microwave lens antenna,” *IEEE Transactions on Antennas and Propagation*, vol. 66, no. 9, pp. 4878–4883, 2018.
- [95] K. Ma, Y. Wang, W. Li, and Y. Chen, “A novel compact self-packaged SPDT switchable BPFs based on SISL platform,” *IEEE Transactions on Industrial Electronics*, vol. 66, no. 9, pp. 7239–7249, 2019.
- [96] Y. Wang, K. Ma, and S. Mou, “A compact branch-line coupler using substrate integrated suspended line technology,” *IEEE Microwave and Wireless Components Letters*, vol. 26, no. 2, pp. 95–97, 2016.
- [97] P. Zou, K. Ma, and S. Mou, “A low phase noise VCO based on substrate-integrated suspended line technology,” *IEEE Microwave and Wireless Components Letters*, vol. 27, no. 8, pp. 727–729, 2017.
- [98] Y. Wang and K. Ma, “Loss mechanism of the SISL and the experimental verifications,” *IET Microwaves, Antennas and Propagation*, vol. 13, no. 11, pp. 1768–1772, 2019.
- [99] Y. Wang, K. Ma, S. Member, and Z. Jian, “A low-loss Butler matrix using patch element

- and honeycomb concept on SISL platform,” *IEEE Transactions on Microwave Theory and Techniques*, vol. 66, no. 8, pp. 3622–3631, 2018.
- [100] F. Mesa, A. A. Oliner, D. R. Jackson, and M. J. Freire, “The influence of a top cover on the leakage from microstrip line,” *IEEE Transactions on Microwave Theory and Techniques*, vol. 48, no. 12, pp. 2240–2248, 2000.
- [101] P. Dixon, “Cavity-resonance dampening,” *IEEE Microwave Magazine*, vol. 6, no. 2, pp. 74–84, 2005.
- [102] P.-S. Kildal, E. Alfonso, A. Valero-Nogueira, and E. Rajo-Iglesias, “Local metamaterial-based waveguides in gaps between parallel metal plates,” *IEEE Antennas and Wireless Propagation Letters*, vol. 8, pp. 84–87, 2009.
- [103] P.-S. Kildal, “Three metamaterial-based gap waveguides between parallel metal plates for mm/submm waves,” in *2009 3rd European Conference on Antennas and Propagation*, 2009, pp. 28–32.
- [104] P.-S. Kildal, “Artificially soft and hard surfaces in electromagnetics,” *IEEE Transactions on Antennas and Propagation*, vol. 38, no. 10, pp. 1537–1544, 1990.
- [105] M. S. Sorkherizi and A. A. Kishk, “Fully printed gap waveguide with facilitated design properties,” *IEEE Microwave and Wireless Components Letters*, vol. 26, no. 9, pp. 657–659, 2016.
- [106] J. Liu, J. Yang, and A. U. Zaman, “Analytical solutions to characteristic impedance and losses of inverted microstrip gap waveguide based on variational method,” *IEEE Transactions on Antennas and Propagation*, vol. 66, no. 12, pp. 7049–7057, 2018.
- [107] J. Zhang, X. Zhang, D. Shen, and A. A. Kishk, “Packaged microstrip line: A new quasi-TEM line for microwave and millimeter-wave applications,” *IEEE Transactions on Microwave Theory and Techniques*, vol. 65, no. 3, pp. 707–719, 2017.
- [108] P.-S. Kildal, A. U. Zaman, E. Rajo-Iglesias, E. Alfonso, and A. Valero-Nogueira, “Design and experimental verification of ridge gap waveguide in bed of nails for parallel-plate mode suppression,” *IET Microwaves, Antennas & Propagation*, vol. 5, no. 3, p. 262, 2011.
- [109] A. Valero-Nogueira, E. Alfonso, J. I. Herranz, and P. S. Kildal, “Experimental demonstration of local quasi-TEM gap modes in single-hard-wall waveguides,” *IEEE Microwave and Wireless Components Letters*, vol. 19, no. 9, pp. 536–538, 2009.
- [110] E. Rajo-Iglesias, A. U. Zaman, and P. S. Kildal, “Parallel plate cavity mode suppression in microstrip circuit packages using a lid of nails,” *IEEE Microwave and Wireless Components Letters*, vol. 20, no. 1, pp. 31–33, 2010.
- [111] A. A. Kishk, A. U. Zaman, and P. S. Kildal, “Numerical prepackaging with PMC lid - Efficient and simple design procedure for microstrip circuits including the packaging,” *Applied Computational Electromagnetics Society Journal*, vol. 27, no. 5, pp. 389–398, 2012.
- [112] M. S. Sorkherizi and A. A. Kishk, “Self-packaged, low-loss, planar bandpass filters for millimeter-wave application based on printed gap waveguide technology,” *IEEE Transactions on Components, Packaging and Manufacturing Technology*, pp. 1–13, 2017.

- [113] N. Ashraf, A. A. Kishk, and A. Sebak, “Broadband millimeter-wave beamforming components augmented with AMC packaging,” *IEEE Microwave and Wireless Components Letters*, vol. 28, no. 10, pp. 879–881, 2018.
- [114] D. Sun *et al.*, “Gap waveguide with interdigital-pin bed of nails for high-frequency applications,” *IEEE Transactions on Microwave Theory and Techniques*, vol. 67, no. 7, pp. 2640–2648, 2019.
- [115] A. U. Zaman, M. Alexanderson, T. Vukusic, and P. S. Kildal, “Gap waveguide PMC packaging for improved isolation of circuit components in high-frequency microwave modules,” *IEEE Transactions on Components, Packaging and Manufacturing Technology*, vol. 4, no. 1, pp. 16–25, 2014.
- [116] D. M. Pozar, *Microwave engineering*, 4th Ed. New York, USA: Wiley, 2012.
- [117] M. Mirmozafari, G. Zhang, C. Fulton, and R. J. Doviak, “Dual-polarization antennas with high isolation and polarization purity: A review and comparison of cross-coupling mechanisms,” *IEEE Antennas and Propagation Magazine*, vol. 61, no. 1, pp. 50–63, 2019.
- [118] S. Gao and A. Sambell, “Dual-polarized broad-band microstrip antennas fed by proximity coupling,” *IEEE Transactions on Antennas and Propagation*, vol. 53, no. 1, pp. 526–530, 2005.
- [119] J. Lu, Z. Kuai, X. Zhu, and N. Zhang, “A high-isolation dual-polarization microstrip patch antenna with quasi-cross-shaped coupling slot,” *IEEE Transactions on Antennas and Propagation*, vol. 59, no. 7, pp. 2713–2717, 2011.
- [120] W. Yang, Q. Meng, W. Che, and S. Member, “Low-profile wideband dual-circularly polarized metasurface antenna array with large beamwidth,” *IEEE Antennas and Wireless Propagation Letters*, vol. 17, no. 9, pp. 1613–1616, 2018.
- [121] H. Li, L. Kang, F. Wei, Y. M. Cai, and Y. Z. Yin, “A low-profile dual-polarized microstrip antenna array for dual-mode OAM applications,” *IEEE Antennas and Wireless Propagation Letters*, vol. 16, pp. 3022–3025, 2017.
- [122] W. Wang, J. Wang, A. Liu, and Y. Tian, “A novel broadband and high-isolation dual-polarized microstrip antenna array based on quasi-substrate integrated waveguide technology,” *IEEE Transactions on Antennas and Propagation*, vol. 66, no. 2, pp. 951–956, 2018.
- [123] S. J. Yang, Y. M. Pan, Y. Zhang, Y. Gao, and X. Y. Zhang, “Low-profile dual-polarized filtering magneto-electric dipole antenna for 5G applications,” *IEEE Transactions on Antennas and Propagation*, vol. 67, no. 10, pp. 6235–6243, 2019.
- [124] R. Lian, Z. Wang, Y. Yin, J. Wu, and X. Song, “Design of a low-profile dual-polarized stepped slot antenna array for base station,” *IEEE Antennas and Wireless Propagation Letters*, vol. 15, pp. 362–365, 2016.
- [125] M. Li and K. M. Luk, “Wideband magneto-electric dipole antenna for 60-GHz millimeter-wave communications,” *IEEE Transactions on Antennas and Propagation*, vol. 63, no. 7, pp. 3276–3279, 2015.
- [126] B. Q. Wu and K. Luk, “A broadband dual-polarized magneto-electric dipole antenna with

- simple feeds,” *IEEE Antennas and Wireless Propagation Letters*, vol. 8, pp. 60–63, 2009.
- [127] B. Feng, S. Member, and X. He, “A low-profile differentially fed dual-polarized antenna with high gain and isolation for 5G microcell communications,” *IEEE Transactions on Antennas and Propagation*, vol. 68, no. 1, pp. 90–99, 2020.
- [128] J. Sun and K. M. Luk, “Wideband linearly-polarized and circularly polarized aperture-coupled magneto-electric dipole antennas fed by microstrip line with electromagnetic bandgap surface,” *IEEE Access*, vol. 7, pp. 43084–43091, 2019.
- [129] D. Shen, C. Ma, W. Ren, X. Zhang, Z. Ma, and R. Qian, “A low-profile substrate-integrated-gap-waveguide-fed magnetolectric dipole,” *IEEE Antennas and Wireless Propagation Letters*, vol. 17, no. 8, pp. 1373–1376, 2018.
- [130] A. Dadgarpour, M. S. Sorkherizi, and A. A. Kishk, “High-efficient circularly polarized magnetolectric dipole antenna for 5G applications using dual-polarized split-ring resonator lens,” *IEEE Transactions on Antennas and Propagation*, vol. 65, no. 8, pp. 4263–4267, 2017.
- [131] J. Zhang, X. Zhang, and A. A. Kishk, “Broadband 60 GHz antennas fed by substrate integrated gap waveguides,” *IEEE Transactions on Antennas and Propagation*, vol. 66, no. 7, pp. 3261–3270, 2018.
- [132] A. Dadgarpour, M. S. Sorkherizi, and A. A. Kishk, “Wideband low-loss magnetolectric dipole antenna for 5G wireless network with gain enhancement using meta lens and gap waveguide technology feeding,” *IEEE Transactions on Antennas and Propagation*, vol. 64, no. 12, pp. 5094–5101, 2016.
- [133] M. Sharifi Sorkherizi, A. Dadgarpour, and A. A. Kishk, “Planar high-efficiency antenna array using new printed ridge gap waveguide technology,” *IEEE Transactions on Antennas and Propagation*, vol. 65, no. 7, pp. 3772–3776, 2017.
- [134] E. Pucci, E. Rajo-Iglesias, J. L. Vázquez-Roy, and P. S. Kildal, “Planar dual-mode horn array with corporate-feed network in inverted microstrip gap waveguide,” *IEEE Transactions on Antennas and Propagation*, vol. 62, no. 7, pp. 3534–3542, 2014.
- [135] X. Jiang *et al.*, “Ka-band 8×8 low-sidelobe slot antenna array using a 1-to-64 high-efficiency network designed by new printed RGW technology,” *IEEE Antennas and Wireless Propagation Letters*, vol. 18, no. 6, pp. 1248–1252, 2019.
- [136] J. Liu, A. Vosoogh, A. U. Zaman, and J. Yang, “Design and fabrication of a high-gain 60-GHz cavity-backed slot antenna array fed by inverted microstrip gap waveguide,” *IEEE Transactions on Antennas and Propagation*, vol. 65, no. 4, pp. 2117–2122, 2017.
- [137] N. Ashraf, A. R. Sebak, and A. A. Kishk, “Packaged microstrip line feed network on a single surface for dual-polarized $2^N \times 2^M$ ME-dipole antenna array,” *IEEE Antennas and Wireless Propagation Letters*, vol. 19, no. 4, pp. 596–600, 2020.
- [138] N. Ashraf, A. A. Kishk, and A. R. Sebak, “Dual-linear or dual-circular polarized slot excited me-dipole antenna with single-layer feeding,” in *2019 IEEE International Symposium on Antennas and Propagation and USNC-URSI Radio Science Meeting*, 2019, pp. 27–28.
- [139] W. M. Dyab, A. A. Sakr, and K. Wu, “Dually-polarized Butler matrix for base stations with

- polarization diversity,” *IEEE Transactions on Microwave Theory and Techniques*, vol. 66, no. 12, pp. 5543–5553, 2018.
- [140] P. I. Bantavis, C. I. Kolitsidas, T. Empliouk, M. Le Roy, B. L. G. Jonsson, and G. A. Kyriacou, “A cost-effective wideband switched beam antenna system for a small cell base station,” *IEEE Transactions on Antennas and Propagation*, vol. 66, no. 12, pp. 6851–6861, 2018.
- [141] C. Leclerc, H. Aubert, A. Ali, A. Annabi, and M. Romier, “The close-form solution for symmetric Butler matrices,” *Progress In Electromagnetics Research C*, vol. PIER C 26, pp. 167–179, 2012.
- [142] A. K. Bhattacharyya, *Phased Array Antennas: Floquet Analysis, Synthesis, BFNs, and Active Array Systems*. Hoboken, NJ: Wiley, 2006.
- [143] S. Yang, W. S. Chan, S. H. Leung, and Q. Xue, “Broadband Butler matrix with flat coupling,” *Electronics Letters*, vol. 43, no. 10, pp. 576–577, 2007.
- [144] T. Kawai and I. Ohta, “Planar-Circuit-Type 3-dB Quadrature Hybrids,” *IEEE Transactions on Microwave Theory and Techniques*, vol. 42, no. 12, pp. 2462–2467, 1994.
- [145] S. Y. Zheng, S. H. Yeung, W. S. Chan, K. F. Man, and S. H. Leung, “Size-reduced rectangular patch hybrid coupler using patterned ground plane,” *IEEE Transactions on Microwave Theory and Techniques*, vol. 57, no. 1, pp. 180–188, 2009.
- [146] and S. P. Y. Jijun Yao, Cedric Lee, “Microstrip branch-line couplers for crossover application,” *IEEE Transactions on Microwave Theory and Techniques*, vol. 59, no. 1, pp. 87–92, 2011.
- [147] S. Y. Zheng, W. S. Chan, and K. F. Man, “Broadband phase shifter using loaded transmission line,” *IEEE Microwave and Wireless Components Letters*, vol. 20, no. 9, pp. 498–500, 2010.
- [148] S. Raffaelli, Z. Sipus, and P. S. Kildal, “Analysis and measurements of conformal patch array antennas on multilayer circular cylinder,” *IEEE Transactions on Antennas and Propagation*, vol. 53, no. 3, pp. 1105–1113, 2005.
- [149] F. Fan, J. Yang, V. Vassilev, and A. U. Zaman, “Bandwidth investigation on half-height pin in ridge gap waveguide,” *IEEE Transactions on Microwave Theory and Techniques*, vol. 66, no. 1, pp. 100–108, 2018.
- [150] C. A. Balanis, *Antenna Theory, Analysis, and Design*, 2nd ed. New York, USA, 1997.
- [151] R. S. Elliott, *Antenna Theory and Design*, Revised ed. New Jersey: IEEE Press, 2003.
- [152] A. R. Mallahzadeh and F. Karshenas, “Modified TEM horn antenna for broadband applications,” *Progress In Electromagnetics Research*, vol. 90, pp. 105–119, 2009.
- [153] J. Shin and D. H. Schaubert, “A parameter study of stripline-fed vivaldi notch-antenna arrays,” *IEEE Transactions on Antennas and Propagation*, vol. 47, no. 5, pp. 879–886, 1999.
- [154] A. A. Kishk and C. Lim, “Comparative analysis between conical and gaussian profiled horn antennas,” *Progress In Electromagnetics Research*, vol. PIER 38, pp. 147–166, 2002.

- [155] B. Yang, Z. Yu, Y. Dong, J. Zhou, and W. Hong, “Compact tapered slot antenna array for 5G millimeter-wave massive MIMO systems,” *IEEE Transactions on Antennas and Propagation*, vol. 65, no. 12, pp. 6721–6727, 2017.
- [156] G. A. E. Vandenbosch and A. Vasylychenko, “A Practical Guide to 3D Electromagnetic Software Tools,” in *Microstrip Antennas*, 1st ed., Hertfordshire, U.K.: InTech, 2011, pp. 507–540.
- [157] CST Microwave Studio Suite, “Electromagnetic Simulation Solvers,” *Dassault Systems*, 2021. [Online]. Available: <https://www.3ds.com/products-services/simulia/products/cst-studio-suite/solvers/>. [Accessed: 15-Jan-2021].
- [158] E. Björnson, J. Hoydis, and L. Sanguinetti, “Massive MIMO networks: Spectral, energy, and hardware efficiency,” *Foundations and Trends in Signal Processing*, vol. 11, no. 3–4, pp. 154–655, 2017.

Publications

A. Journal Articles

- J-1 N. Ashraf, A. R. Sebak, and A. A. Kishk, "PMC packaged single-substrate 4 x 4 Butler matrix and double-ridge gap waveguide horn antenna array for multibeam applications," *IEEE Transactions on Microwave Theory and Techniques*, vol. 69, no. 1, pp. 248-261, Jan. 2021.
- J-2 N. Ashraf, A. R. Sebak, and A. A. Kishk, "Packaged microstrip line feed network on a single surface for dual-polarized $2^N \times 2^M$ ME-dipole antenna array," *IEEE Antennas and Wireless Propagation Letters*, vol. 19, no. 4, pp. 596-600, 2020.
- J-3 N. Ashraf, A. A. Kishk, and A. R. Sebak, "Broadband millimeter-wave beamforming components augmented with AMC packaging," *IEEE Microwave and Wireless Components Letters*, vol. 28, no. 10, pp. 879-881, 2018.

B. Conference Papers

- C-1 N. Ashraf, A. A. Kishk, and A. R. Sebak, "Printed ridge gap waveguide Rotman Lens without dummy ports or matching loads for 5G," Presented in *IEEE APS/URSI*, Montreal, QC, Canada, 2020.
(IEEE AP-S 2020, Student Paper Competition Honorable Mention)
- C-2 N. Ashraf, A. A. Kishk, and A. R. Sebak, "Printed feed network on a single surface for dual-polarized antenna array," Presented in *2019 IEEE APS/URSI*, Montreal, QC, Canada, 2020.
- C-3 N. Ashraf, A. A. Kishk, and A. R. Sebak, "28-32 GHz dual-polarized single-layer microstrip line beamforming network for 2×2 beam switching," *2019 IEEE MTT-S*

International Microwave Conference on Hardware and Systems for 5G and Beyond (IMC-5G), Atlanta, GA, USA, 2019.

C-4 N. Ashraf, A. A. Kishk, and A. R. Sebak, "Dual-linear or dual-circular polarized slot excited ME-dipole antenna with single-layer feeding," *IEEE APS/URSI*, Atlanta, GA, USA, 2019.

(IEEE AP-S 2019, Student Paper Competition Honorable Mention)

C-5 N. Ashraf, A. A. Kishk, and A. R. Sebak, " Slot-excited wideband horn antenna with microstrip line feeding for Ka-band applications," *IEEE APS/URSI*, Atlanta, GA, USA, 2019.

C-6 N. Ashraf, A. R. Sebak, and A. A. Kishk, "End-launch horn antenna array for Ka-band 5G applications," *18th International Symposium on Antenna Technology and Applied Electromagnetics (ANTEM)*, Waterloo, ON, Canada, 2018.

(IEEE ANTEM 2018, Best Student Paper Award, 3rd Place)

C-7 N. Ashraf, A. A. Kishk, and A. R. Sebak, "Ridge Gap Waveguide quasi-TEM horn antenna for Ka-band applications," *IEEE APS/URSI*, Boston, MA, USA, 2018.

C-8 N. Ashraf, A. A. Kishk, and A. R. Sebak, " AMC-packaged Butler matrix for millimeter-wave beamforming," *IEEE APS/URSI*, Boston, MA, USA, 2018.